High spectral purity microwave sources based on optical resonators

Khaldoun Saleh

Université de Toulouse

THESIS

In partial fulfillment of the requirements for the degree of

DOCTOR OF PHILOSOPHY
FROM TOULOUSE UNIVERSITY

Delivered by Université Paul Sabatier – Toulouse III

Major : Microwaves, Electromagnetism and Optoelectronics

Presented and defended by Khaldoun SALEH

the 29th of November 2012

Title :

High spectral purity microwave sources based on optical resonators

---

JURY

Philippe ARGUEL, President (LAAS-CNRS)
Yanne CHEMBO, Reviewer (FEMTO-ST)
Patrice FÉRON, Reviewer (FOTON-ENSSAT)
Gilles CIBIEL (CNES)
Jacques GRAFFEUIL (LAAS-CNRS)
Olivier LLOPIS (LAAS-CNRS)
Loïc MORVAN (Thalès TRT)
Giorgio SANTARELLI (SYRTE, LP2N)
Invited: Angélique RISSONS (ISAE)

Doctoral school : GEET
Research unit : LAAS-CNRS, MOST team
Thesis supervisor : Olivier LLOPIS

Knowledge is a thousand doors…behind each, there is another thousand.

Ali Ibnu Abi Talib

To my mother and my father,
To my sister and my brothers,
To my beloved wife Jinan…
And to Syraj

Acknowledgements

I would like to thank the following for making this thesis possible:

The French national space center (CNES) and the regional council of Midi-Pyrénées for financing my studies.

Mr. Jacques Graffeuil for helping me to pursue my ambitions…

My thesis supervisor Mr. Olivier Llopis for accepting me in his research team, for sharing his knowledge and for providing me with encouragement during my research.

My technical CNES supervisor, Mr. Gilles Cibiel.

Mr. Patrice Féron and Mr. Yanne Chembo for accepting to examine and assess this work.

Mr. Philippe Arguel, for presiding the thesis jury, and all the jury members.

Everybody who has contributed to the creation of the unique and stimulating work environment in the laboratory: Aude, Pierre-Henri, Houda, Ayad, Pierre, Arnaud, Serge, Dina, Teddy, Amel, Olga, Tonio, Alessandro, Seraphin, Sawsen and all the members of MOST team and of the laboratory of analysis and architecture of systems (LAAS-CNRS).

Finally, no words would ever do justice to express my deepest appreciation and gratitude to my most wonderful family: my parents, my sister, my brothers and my beloved wife Jinan. I will be eternally grateful to them for being there for me at all times. Their continuous love, sacrifice, support and encouragement have allowed me to pursue my ambitions.

Last but not least, this is for you

Syraj, may your soul shine on heaven's grounds.

Table of contents

Glossary **1**

General Introduction **5**

Chapter I Generation of microwave sources using optics **9**

I.1 Introduction *9*

I.2 Microwave oscillators *10*

I.2.1 Frequency stability 10

I.2.1.a Phase noise and signal's short term stability 11

I.2.2 Noise in microwave oscillators 12

I.2.2.a Noise evaluation and conversion processes identification 12

I.2.2.b Noise characterization of microwave components 16

I.2.3 State of the art microwave oscillators 17

I.2.3.a Dielectric resonator based oscillators (DROs) 18

I.2.3.a.i Ceramic resonators 18

I.2.3.a.ii Sapphire WGM resonators 19

I.2.4 State of the art microwave oscillators – noise results comparison 19

I.3 Optoelectronic oscillators (OEOs) *20*

I.3.1 Principle of delay line based OEO 20

I.3.2 Principle of active cavity based coupled OEO (COEO) 24

I.3.3 Principle of passive cavity based OEO 25

I.3.3.a Pound-Drever-Hall (PDH) laser stabilization technique 27

I.3.3.b OEO experimental setup 28

I.3.3.c OEO based on whispering gallery mode (WGM) resonator 29

I.3.3.c.i WGM resonator coupling technique 29

I.3.3.c.ii OEO based on a CaF_2 WGM resonator 30

I.3.3.d OEO based on fiber ring resonator 31

I.3.4 State of the art optoelectronic oscillators – noise results comparison 32

I.4 Conclusion *33*

I.5 References *35*

Chapter II Modeling and characterization of the fiber ring resonator and the optoelectronic oscillator **39**

II.1 Introduction *39*

II.2 Fiber ring resonator (FRR) *40*

II.2.1 FRR principle and characteristics 40

II.2.2 Modeling of the FRR 43

II.2.2.a FRR simulation using Maple13 45

II.2.2.a.i Absorption transfer function 45

II.2.2.a.ii Intra-cavity power enhancement factor 47

II.2.2.a.iii Transmission transfer function 49

II.2.2.a.iv Effects of γ_1, γ_2, α_s and α_f on the FRR's transmission response 51

II.3 A CAD approach of the fiber ring resonator based OEO using a microwave software *51*

II.3.1 Modeling of the FRR using ADS 53

Table of contents

II.3.1.a FRR ADS model 53
II.3.1.a.i Optical fiber model 53
II.3.1.a.ii Optical coupler model 53
II.3.1.b Modeling of compound and complex architectures based on multiple FRRs 55
II.3.2 Resonator experimental characterization techniques 56
II.3.2.a Optical domain characterization techniques 57
II.3.2.a.i Narrow linewidth laser wavelength scanning method 57
II.3.2.a.ii Cavity ring down method 57
II.3.2.b Microwave domain characterization technique using a vector network analyzer 58
II.3.3 Modeling of the FRR based OEO using ADS 59
II.3.3.a Optical components modeling 60
II.3.3.a.i Laser model with its amplitude and phase noise 60
II.3.3.a.ii Mach-Zhender modulator model 63
II.3.3.a.iii The PDH loop 64
II.3.3.a.iv Photodiode model 64
II.3.3.b Microwave components modeling 65
II.3.3.b.i Modeling the RF filter, the RF phase shifter and the RF amplifier 66
II.3.3.c Simulation of the FRR response 66
II.3.3.d OEO phase noise modeling using ADS 66
II.3.3.d.i Open-loop phase noise simulations 67
II.3.3.d.ii Closed-loop phase noise simulations 68

II.4 Conclusion 69

II.5 References 71

Chapter III Optoelectronic oscillator based on fiber ring resonator: optimization studies 73

III.1 Introduction 73

III.2 OEO first realization based on a 10m-long polarization maintaining FRR 74
III.2.1 The 10m-long FRR architecture 74
III.2.2 The 10m-long FRR experimental characteristics 74
III.2.3 The 10m-long FRR based OEO experimental phase noise results 74
III.2.4 Results discussions 75

III.3 OEO optimization study 76
III.3.1 White frequency noise modeling following Leeson's approach 76
III.3.1.a White frequency noise model: validation and use 77
III.3.1.b Influence of the fiber ring length 78
III.3.1.c Influence of coupling coefficients, couplers' excess loss and the FRR loss 78
III.3.2 OEO based on the optimized 20m-long FRR 80
III.3.2.a The optimized 20m-long FRR 80
III.3.2.b The 20m-long FRR based OEO phase noise results 81
III.3.3 Results discussions 81

III.4 Laser amplitude and frequency noise conversions inside the OEO setup 82
III.4.1.a Laser noise conversions through fiber chromatic dispersion 82
III.4.1.b Laser noise conversions through the FRR 83
III.4.1.c Laser noise conversions through the photodiode nonlinearity 85

Table of contents

III.5 Conclusion 89

III.6 References 90

Chapter IV Nonlinear optical effects generated in the 20m-long FRR and OEO phase noise degradation 91

IV.1 Introduction 91

IV.2 The Brillouin scattering in the FRR based OEO 92

IV.2.1 Brillouin scattering in optical fibers and FRRs 92

IV.2.1.a Brillouin scattering theory 92

IV.2.1.b Stimulated Brillouin scattering (SBS) threshold definition 95

IV.2.2 SBS frequency shift and gain spectrum characterization in the 20m-long FRR 97

IV.2.3 SBS power characterization in the 20m-long FRR 99

IV.2.4 SBS spectrum characterization in the 20m-long FRR 100

IV.2.5 Laser RIN degradation caused by the SBS 102

IV.2.6 OEO phase noise degradation caused by the SBS and the Rayleigh scattering 103

IV.3 The Rayleigh scattering in the FRR based OEO 105

IV.3.1 Rayleigh scattering in optical fibers and FRRs 106

IV.3.2 STRS power characterization in the 20m-long FRR 106

IV.3.3 STRS spectrum characterization in the 20m-long FRR 107

IV.3.4 Laser RIN degradation caused by the STRS 108

IV.4 Other nonlinear optical effects and scattering mechanisms inside the FRR 110

IV.4.1 Fresnel back-reflection 110

IV.4.2 Raman scattering 111

IV.4.3 Two and four wave mixing 111

IV.5 High power and high spectral purity millimeter-wave (MMW) signals generation using the Brillouin selective sideband amplification inside the 20m-long FRR 113

IV.5.1 Millimeter-wave signals generation setup 114

IV.5.2 Optical characterization 115

IV.5.3 RF characterization 116

IV.5.4 Noise characterization 117

IV.6 New passive 100m-long FRR, optimized and immunized against nonlinear optical effects 119

IV.6.1 SBS and STRS suppression methods 119

IV.6.2 SBS suppression using optical isolators 120

IV.6.3 Optimized and immunized FRR (IFRR) 122

IV.6.3.a IFRR optimization using ADS 122

IV.6.3.b IFRR optical characterization 124

IV.6.3.c STRS behavior in the IFRR 125

IV.6.3.d Laser RIN behavior in the IFRR 126

IV.6.3.e IFRR RF characterization 127

IV.6.3.f Signal phase noise behavior through the IFRR 127

IV.7 OEO based on the new passive 100m-long IFRR 128

IV.7.1 OEO phase noise: theoretical expectations 128

IV.7.2 OEO phase noise: experimental results 131

IV.7.3 Comparison to a 756m delay line based OEO 132

Table of contents

IV.7.4 Effects of the PDH stabilization loop bandwidth 132

IV.8 Conclusion 133

IV.9 References 135

Chapter V FRR and OEO: thermal stability and tunability studies 139

V.1 Introduction 139

V.2 FRR and OEO thermal stability 140

V.2.1 Theoretical studies on the FRR and the OEO thermal stability 140

V.2.2 Experimental results on the FRR and the OEO thermal stability 144

V.3 FRR and OEO tunability 145

V.3.1 Theoretical studies on the tunability of the FRR 146

V.3.1.a Absolute frequency tuning using an optical phase-shifter 146

V.3.1.b Free spectral range tuning using a variable optical coupler 149

V.3.1.c All-tunable FRR 153

V.3.2 Experimental results of an all-tunable FRR 154

V.4 Conclusion 157

V.5 References 158

General Conclusion 159

Perspectives 163

Appendix A: Analytical expressions for FRR modeling 165

Appendix B: Characterization of the optical phase shifter (FPS-001 from general photonics) 169

Appendix C: Real images of the different experimental benches 171

List of publications 177

Glossary

Acronyms and Some of the Symbols Used in the Text

AM	amplitude modulation
ARF	anneau résonant fibré
BAW	bulk acoustic wave
BGS	Brillouin gain spectrum
BNA	baseband noise analyzer
BSSA	Brillouin selective sideband amplification
BSSA-SG	millimeter-wave signals generation using the Brillouin selective sideband amplification
C_1 and C_2	FRR's optical directional couplers
CAD	computer aided design
COEO	coupled optoelectronic oscillator
DFWM	degenerate four-wave mixing
DL	delay line
DL-OEO	delay line based OEO
DPC	direct propagating laser carrier
DRO	dielectric resonator based oscillator
EDFA	erbium doped fiber amplifier
ESA	electrical spectrum analyzer
FBG	fiber Brag grating
FC/APC	angled-polished optical fiber connector
FM	frequency modulation
FOSO	fiber-optic stabilized oscillator
FRR	fiber ring resonator
FRR-PS	fiber ring resonator including a phase-shifter
FRR-SM	fiber ring resonator including a Sagnac mirror
FSM	frequency-shifter modulator
FSR	free spectral range
FWHM	full-width at half-maximum
FWM	four-wave mixing
GAWBS	guided acoustic wave Brillouin scattering
GPS	global positioning system
IFRR	immunized fiber ring resonator
IL	insertion loss
IPEF	intra-cavity power enhancement factor
LO	local oscillator
LSB	modulation lower sideband

MLL	mode-locked laser
MMW	millimeter-wave
MZM	Mach-Zehnder modulator
NCR	noise-to-carrier ratio
OEO	optoelectronic oscillator
OSA	optical spectrum analyzer
PDH	Pound-Drever-Hall laser stabilization loop
PM	Phase modulation
P-M	polarization-maintaining
PS	phase shifter
$P_{th\text{-}SBS\text{-}IC}$	intra-cavity stimulated Brillouin scattering threshold
$P_{th\text{-}SBS\text{-}R}$	stimulated Brillouin scattering threshold at the resonator input
$P_{th\text{-}SBS\text{-}SPG}$	stimulated Brillouin scattering threshold in single-path-geometry optical fiber
PZT	piezoelectric actuator
RIN	relative intensity noise
ROF	RF over fiber
RUT	resonator under test
SAO	semiconductor optical amplifier
SAW	surface acoustic wave
SBS	stimulated Brillouin scattering
SBST	stimulated Brillouin scattering threshold
SDD	symbolically defined device
Si BJT	silicon bipolar junction transistor
SiGe HBT	silicon-germanium hetero-junction bipolar transistor
SM	Sagnac mirror
SPG	single-path-geometry
SRS	stimulated Raman scattering
SSA	signal source analyzer
SSB	single sideband
STRS	Stimulated Rayleigh scattering
TC	tunable optical coupler
TE	transverse electric mode
TFRR	all-tunable fiber ring resonator
TM	transverse magnetic mode
USB	modulation upper sideband
VNA	vector network analyzer
VOA	variable optical attenuator
WFN	white frequency noise contribution
WGM	whispering gallery modes
WGMR	whispering gallery mode resonator
YIG	yttrium iron garnet
λ_l	Laser carrier wavelength

General Introduction

Pursuing accurate standards for time measurement has been an ongoing emerging investigation from the early days of mankind. To be able to do so, time seekers first started using the natural oscillators surrounding them: Earth and sun movements (e.g. Egyptian shadow clocks; 3500 year BC). However, no other natural oscillators have been able to provide such accurate frequency standards. Therefore it was an imperative to find artificial alternatives such as water clocks, sand clocks and candle clocks. The investigations have finally directed to the invention of mechanical clocks. One can especially mention the mechanical clock using the regular swing of a pendulum which has been discovered by Galileo in 1580 and first built by Christiaan Huygens in 1656. A time error less than 10 seconds per day has been achieved in later improved versions of this clock.

It is not until 1880 that Jacques and Pierre Curie have discovered the remarkable piezoelectric properties of crystalline quartz. The first quartz oscillator (clock) was built in 1927 at Bell Telephone Laboratories in Canada, with a time error less than 0.01 second per day[1]. Due to its accuracy, the National Bureau of Standards (NBS) (now NIST: National Institute of Standards and Technology) has based the time standard of the United States from late 1929 until the 1960s[2] on a quartz oscillators' network until it eventually changed to atomic clocks[3].

Each chemical element in nature absorbs and emits electromagnetic radiations at particular resonant frequencies. These resonances are naturally stable over time and space. For example, an atom of hydrogen (or cesium) today is exactly the same one million years ago. The first atomic clock, invented in 1949, was using the absorption line of the ammonia molecule as a reference (resonant frequency at 23.8701 GHz). This clock used a stable 100 kHz quartz oscillator that drove a frequency multiplier chain to develop the signal that probed the ammonia resonance. The development of the ammonia clock was simply the first step into the age of atomic standards. Most of the later atomic clocks were based on the spin property of cesium (9.192631770 GHz; used nowadays to define the "second"), hydrogen or rubidium atoms.

Atomic clocks are currently considered as the most accurate timekeeping devices. The cesium atomic clock, currently maintained by the NIST, is accurate to 30 billionths of a second per year. This time accuracy is crucial for numerous time-frequency applications. For example, in the global positioning system (GPS) that provides critical capabilities to military, civil and commercial users around the world, a delay by even one millisecond means an error in positioning by 300 kilometers!

All things considered, we can see that two types of frequency standards therefore exist: natural primary standards (astronomical, atomic…) that have exceptionally long-term stability, and secondary artificial standards (e.g. the human made crystal-based oscillators) that can achieve very high short-term

[1] W. A. Marrison, "A high precision standard of frequency", Proc. IRE, 17, 1103 (1929); also Bell System Tech. J. 8, 493 (1929).
[2] E.L. Hall, V.E. Heaton, E.G. Lapham, "The national primary standard of radio frequency", J. Res. Natl. Bur. Stand., Vol. 14, No. 2, p. 85, (1935).
[3] D.B. Sullivan, "Time and frequency measurement at NIST: the first 100 years," Frequency Control Symposium and PDA Exhibition, 2001. Proceedings of the 2001 IEEE International, vol., no., pp.4-17, (2001).

stability ("high spectral purity" or "phase noise" terms are most frequently used) but an inferior long-term stability compared to primary standards. It is for that reason that both standards have to be used together to fabricate atomic clocks providing extremely accurate frequency standards.

Unfortunately, until now, genuine high spectral purity microwave sources near cesium's resonant frequency in the X band are even bulky or very complex. The high spectral purity is crucial principally if the atomic clock is intended to be used in space were electromagnetic immunity, weight and size do really count. The aim of using such a clock in space[4] is principally to increase the interaction period between the probe signal and atoms and therefore to further increase the clock stability.

Usually, in earth based atomic clocks, the probe signal originates from an ultra-stable quartz oscillator multiplied to the desired frequency. This is due to the fact that the highest frequency achieved with quartz oscillators is only of few hundreds of MHz. However, this multiplication process results in the degradation of the oscillator stability by at least 20log (M), where M is the frequency multiplication factor.

Besides their use to fabricate atomic clocks and in time-frequency metrology, high spectral purity sources are widely used today for other numerous applications. We can especially mention the communications systems (e.g. satellites and the onboard signals distribution to different antenna arrays) and radars. Such systems need high spectral purity sources featuring both close-to-carrier and far-from-carrier low phase noise levels.

Given the above reasons to tackle, this thesis investigates a new type of secondary frequency standards based on the one invented by researchers in 1994 at the NASA's Jet Propulsion Laboratory: the optoelectronic oscillator. This oscillator is able to provide very high spectral purity signal and it also features a good electromagnetic immunity and relatively compact size and low weight.

This thesis is a part of a research joint venture between the French National Space Center (CNES) in Toulouse, Thales Research & Technology in Paris and three laboratories of the CNRS: LAAS-CNRS (Toulouse), ENSSAT-FOTON (Lannion) and FEMTO-ST (Besançon).This project seeks the development of a high spectral purity microwave source in the X band. The stability specifications of this source are as follows:

- A close-to-carrier phase noise level lower than a multiplied quartz oscillator, for an eventual atomic clock application (the ultimate goal is to be as low as -68 dBc/Hz at 1 Hz offset frequency).
- A far-from-carrier low phase noise level, for radars or communications systems' applications.

The first chapter in this manuscript gives a brief review of the oscillator's frequency stability definition and the noise processes that can occur in a classical microwave oscillator. The different state of the art microwave oscillators are then listed and discussed together with the commonly used and

[4] Ch. Salomon, N. Dimarcq, M. Abgrall, A. Clairon, P. Laurent, P. Lemonde, G. Santarelli, P. Uhrich, L.G. Bernier, G. Busca, A. Jornod, P. Thomann, E. Samain, P. Wolf, F. Gonzalez, Ph. Guillemot, S. Leon, F. Nouel, Ch. Sirmain, S. Feltham, "Cold atoms in space and atomic clocks: ACES", Comptes Rendus de l'Académie des Sciences - Series IV - Physics, Volume 2, Issue 9, Pages 1313-1330, (2001).

state of the art different optoelectronic oscillators. These different optoelectronic oscillators are listed and described with their phase noise performance each. Specific attention is finally given to the optoelectronic oscillator scheme we are using in our laboratory which is based on either an optical micro-resonator or on a fiber ring resonator.

The fiber ring resonator's simplicity and the very high quality factors that can be achieved using this device have guided the concentrate of the second chapter. In Chapter II, the fiber ring resonator is extensively studied as well as its response which is modeled by different means, primarily using a microwave modeling software. This is done in order to get the highest quality factor and the best performance when the resonator is used as the frequency stability element in an optoelectronic oscillator setup. Furthermore, we have tried to model the overall oscillator system to understand the different noise contributions, especially those related to the noise processes in the resonator itself.

The optoelectronic oscillator is a complex system in which the resonator quality factor is not the only parameter to optimize in order to get a good phase noise performance. In addition, the oscillator setup may involve many noise conversion processes that have to be evaluated and understood. For this reason, in the third chapter of this manuscript we present a fiber ring resonator optimization study based on the evaluation of the white frequency noise contribution to the oscillator phase noise. Moreover, the different noise conversion processes that are likely to occur inside the optoelectronic oscillator have been thoroughly studied. Particularly, we have probed the laser noise conversion processes with respect to the RF amplitude and phase noise through the resonator itself and through the photodiode nonlinearity.

In optical fibers, many nonlinear optical phenomena can occur especially when high optical power levels are used. It has been found that nonlinear optical phenomena were the cause of an excess optical noise inside the optical resonator and therefore inside the oscillator setup. These findings have led us to deeply look into the nonlinear optical effects generated inside the fiber ring resonator, especially the stimulated Brillouin scattering and the stimulated Rayleigh scattering. In the fourth chapter of this manuscript, we first give a description about each of these nonlinear optical phenomena and their possible contributions to the noise in the optoelectronic oscillator. After the descriptions, we demonstrate how these nonlinear optical effects could be useful to generate high power and high spectral purity millimeter wave signals. We then present the different methods used in the literature to suppress these nonlinear optical effects in optical fibers and describe the suppression method we have chosen to be used in our optical resonator. Finally, an optimized and immunized fiber ring resonator has been fabricated and a significantly low oscillator's phase noise level has been measured.

The thermal stability is also an important parameter to scale in the optoelectronic oscillator, as it could affect its frequency stability. In addition, the oscillator tunability is a main desired feature for time-frequency and communications systems applications. The final chapter of this manuscript has been therefore dedicated to the study of these two characteristics of the oscillator. First, theoretical and experimental studies were made to determine precisely the oscillator thermal stability. Next, we have studied different techniques to make the optical resonator completely tunable. This has been found to

be possible using a specific structure based on the fiber ring resonator, which has been simulated, fabricated and experimentally tested.

Chapter I Generation of microwave sources using optics

I.1 Introduction

The first attempts of generating pure microwave signals using a photonic oscillator have been developed at the NASA's Jet Propulsion Laboratory (JPL). In the early 1980's, studies at JPL were focused on the distribution of a stable atomic clock reference signal over optical fibers towards multiple antenna sites located tens of kilometers apart. The aim was to benefit from optical fiber's extremely low loss compared to a coaxial cable. Subsequent work in the field has led the researchers at the same laboratory to take advantage of the properties of optical components and fabricate a microwave oscillator based on microwave-photonics, the so-called optoelectronic oscillator.

In this chapter, after reviewing the oscillator frequency stability definition and the noise processes that occur in classical microwave oscillators, the different state of the art microwave oscillators are discussed and we further focus on the features of dielectric resonator based oscillators.

The second part of this chapter is dedicated to the description of the most common optoelectronic oscillator's schemes, used to generate high spectral purity microwave signals. We start by describing the first demonstrated OEO based on a long optical fiber which was used as the delay element. After that, we list the other OEO schemes based on active and passive optical resonators. In particular, a specific attention is given to the one we use in our laboratory, which is based on either an optical micro-resonator or a fiber ring resonator. Finally, the different state of the art optoelectronic oscillators are listed with their noise performance for comparison.

I.2 Microwave oscillators

Oscillators are devices that produce periodic waves whose amplitude, phase and frequency can be precisely controlled. Oscillators are an essential element in any system that receives or transmits a signal. They are widely used in communications systems, radars, satellites, sensors, time and frequency metrology, radio astronomy, signal processing and different other applications where an electromagnetic signal is generated, received or processed.

A classical feedback oscillator design includes an amplifier with its output fed back into its input through a selective filter and a phase control element (see Fig. I. 1 (a)). The amplifier guarantees a sufficient gain in the loop (above unity) while the phase element (a phase shifter) is used to obtain a constructive phase-match, and the selective filter will be the main responsible of the oscillator stability.

Of course, the generated signal will not be perfect because it will be affected by the different random noise instabilities generated inside the oscillator loop: amplitude, phase and frequency instabilities (see Fig. I. 1 (b)). This in-loop noise is directly linked to the noise generated by the active element (the amplifier) and the selectivity of the filtering element (its quality factor *Q*).

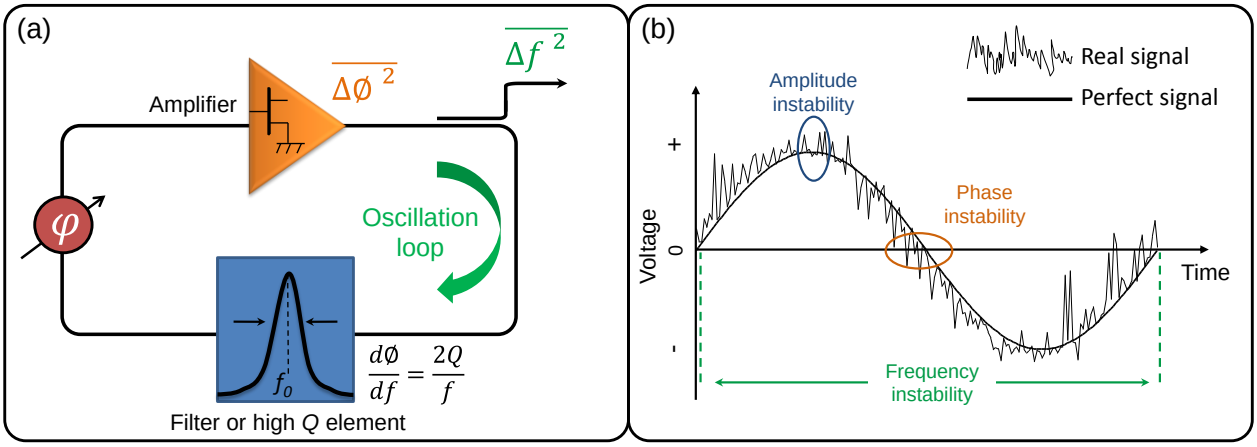

Fig. I. 1. (a) Classical feedback oscillator design and (b) generated sinusoidal signal affected by the different instabilities in the oscillator loop

As shown in Fig. I. 1 (b), a frequency instability results from fluctuations in the period of oscillation, fluctuations in the phase result in instability of the zero crossing and finally, fluctuations in the peak value of the signal result in amplitude instability.

I.2.1 Frequency stability

To evaluate the "ideality" of the signal generated by the oscillator and therefore the oscillator stability, two terms have to be measured: its short term stability, which is usually known as the phase noise or spectral purity (well described in [1]), and its long term stability versus time, which is the degree of uniformity of the oscillator frequency over time and is limited by the aging of the oscillator elements. Finally, it is the short term stability which will be used and evaluated all along our work in this thesis.

I.2.1.a *Phase noise and signal's short term stability*

The phase noise describes the short term stability of a frequency source [1]. It is therefore an important parameter to scale in order to evaluate the quality of this source. In a feedback oscillator, the phase fluctuations of the amplifier are directly converted into frequency fluctuations through the oscillator nonlinearity [2].

Mathematically, a perfectly sinusoidal signal is written as:

$$v(t) = V_0 \, sin(2\pi f_{Osc} t) \qquad \textit{(Eq. I. 1)}$$

where V_0 is the nominal peak voltage amplitude of the signal and f_{Osc} is the nominal frequency.

In reality, the microwave signal generated by the oscillator is affected by many random perturbations (Fig. I. 1). Therefore, the instantaneous output voltage of an oscillator can be expressed as:

$$v_{Osc}(t) = \big(V_0 + \Delta V_0(t)\big) \, sin\big(2\pi f_{Osc} t + \Delta\emptyset(t)\big) \qquad \textit{(Eq. I. 2)}$$

where $\Delta V_0(t)$ and $\Delta\emptyset(t)$ are time dependent random signals representing the deviation from the nominal amplitude and deviation from the nominal phase respectively (amplitude instability is not usually considered in most of microwave domain applications).

In the frequency domain, Fig. I. 2 (a) and Fig. I. 2 (b) respectively illustrate the power spectrums of a pure and a real signal. In addition, Fig. I. 2 (c) illustrates the typical phase fluctuations spectrum $\overline{\Delta\emptyset^2}$ (phase noise spectrum) of a real signal expressed in (rad²/Hz) versus the offset frequency (f_m) from the carrier.

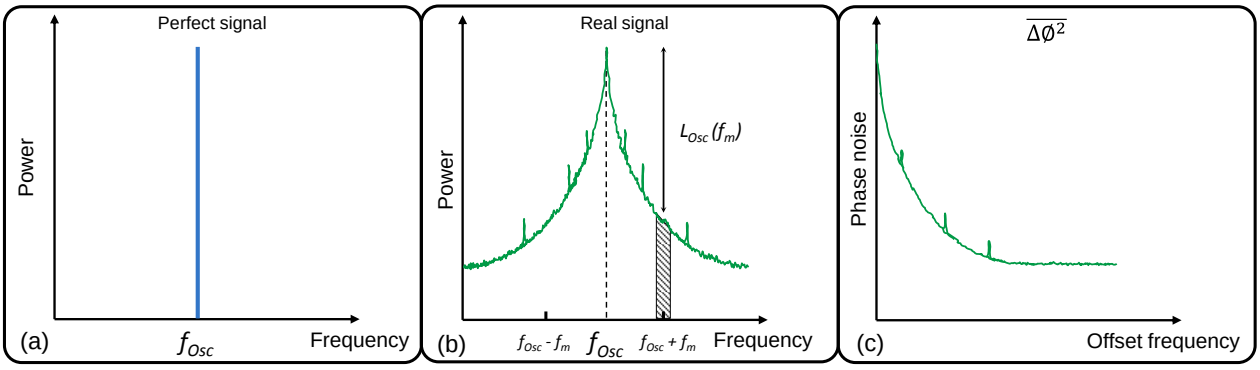

Fig. I. 2. Power spectrum of: (a) perfect signal and (b) real signal generated by an oscillator. (c) Illustration of a typical phase noise spectrum of a real signal

This phase noise has two origins: noise components of known sources (electrical ~ 50 Hz, mechanical, acoustic…) that can be identified in a phase noise spectrum as noise peaks (called spurious peaks) and noise generated by multiple random fluctuations inside the oscillation loop. Some causes of

these fluctuations are: thermal noise, white noise, flicker noise (characterized by its *1/f* noise slope) and high frequency noise.

The oscillator phase instability can be characterized by the spectral density of phase fluctuations, $S_{\emptyset_{Osc}}(f_m)$, given by:

$$S_{\emptyset_{Osc}}(f_m) = \frac{\overline{\Delta\emptyset^2}}{BW} \qquad rad^2/Hz \qquad \textit{(Eq. I. 3)}$$

where BW (in Hz) is the measurement system bandwidth.

This definition includes fluctuations from both upper and lower sidebands of the carrier and it is this quantity that is generally measured in frequency metrology. However, another quantity has been designated as the standard measure of phase instability in the frequency domain. It is defined as the ratio of the power in one sideband due to phase modulation by noise (in one Hz bandwidth) to the total signal power (carrier plus sidebands) [1] (see Fig. I. 2 (b)). This quantity is called the single sideband (SSB) phase noise. It is expressed in decibels (dBc/Hz) and linked to $S_{\emptyset_{Osc}}(f_m)$ by:

$$L_{Osc}(f_m) = S_{\emptyset_{Osc}}(f_m) - 3dB \qquad dBc/Hz \qquad \textit{(Eq. I. 4)}$$

Moreover, the spectral density of phase fluctuations $S_{\emptyset_{Osc}}(f_m)$ is linked to the spectral density of frequency fluctuations, $S_{f_{Osc}}(f_m)$ expressed in (Hz²/Hz), by the following relation:

$$S_{\emptyset_{Osc}}(f_m) = \frac{S_{f_{Osc}}(f_m)}{{f_m}^2} \qquad rad^2/Hz \quad or\ in \quad dBrad^2/Hz \qquad \textit{(Eq. I. 5)}$$

Finally, it is mainly $L_{Osc}(f_m)$ and $S_{\emptyset_{Osc}}(f_m)$ which are usually used in frequency metrology to specify the phase noise or the short term stability of frequency standards.

I.2.2 Noise in microwave oscillators

I.2.2.a *Noise evaluation and conversion processes identification*

The frequency fluctuations in a classical microwave oscillator are of various origins. We can particularly mention the phase fluctuations caused by the active element in the oscillator (the RF amplifier), the flicker noise of the resonator and the phase noise of the phase control element (e.g. phase shifter). In addition to these contributors, we can also add the mechanical vibrations, the thermal fluctuations and also the electrical network contribution (50Hz). It is therefore difficult to take into account all these noise contributions to model the oscillator's noise behavior. Despite that, a simple and well-known model has been proposed by D.B. Leeson [2] to describe the phase noise behavior in a classical feedback oscillator.

This model is based on the idea that the frequency instability of an oscillator can be estimated from the phase instability of the active element in the loop (the amplifier) ($\overline{\Delta\emptyset^2}_{Amp}$; representing the spectral density of phase fluctuations) while assuming the amplitude instability insignificant. This conversion process has been expressed as follows:

$$\overline{\Delta f^2}_{Osc} = \left(\frac{df}{d\emptyset}\right)^2 \overline{\Delta\emptyset^2}_{Amp} \qquad \textit{(Eq. I. 6)}$$

In (Eq. I. 6), $\overline{\Delta f^2}_{Osc}$ represents the spectral density of the oscillator's frequency fluctuations (in Hz²/Hz) and $\overline{\Delta\emptyset^2}_{Amp}$ the spectral density of the amplifier's phase fluctuations (in rad²/Hz); (see Fig. I. 1 (a)). Finally, $\left(\frac{df}{d\emptyset}\right)$ is the stability coefficient that can be computed from the loaded quality factor Q_L of the resonator (the Q_{RF} term will be used instead of Q_L in this manuscript for more clarity):

$$\frac{df}{d\emptyset} = \frac{f_{Osc}}{2Q_{RF}} \qquad \textit{(Eq. I. 7)}$$

where f_{Osc} is the oscillation frequency.

As illustrated in Fig. I. 3 (a), the quality factor of a resonator can be mathematically defined as the ratio of the resonant frequency (f_{Res}) to the resonant mode's full width at half maximum ($FWHM$):

$$Q = \frac{f_{Res}}{FWHM} \qquad \textit{(Eq. I. 8)}$$

Moreover, this quality factor can be directly calculated from the phase slope transition at the resonance, as demonstrated by (Eq. I. 7) and illustrated in Fig. I. 3 (b). The phase slope steepness is crucial for the oscillator stability and it reflects a high quality factor of the resonator.

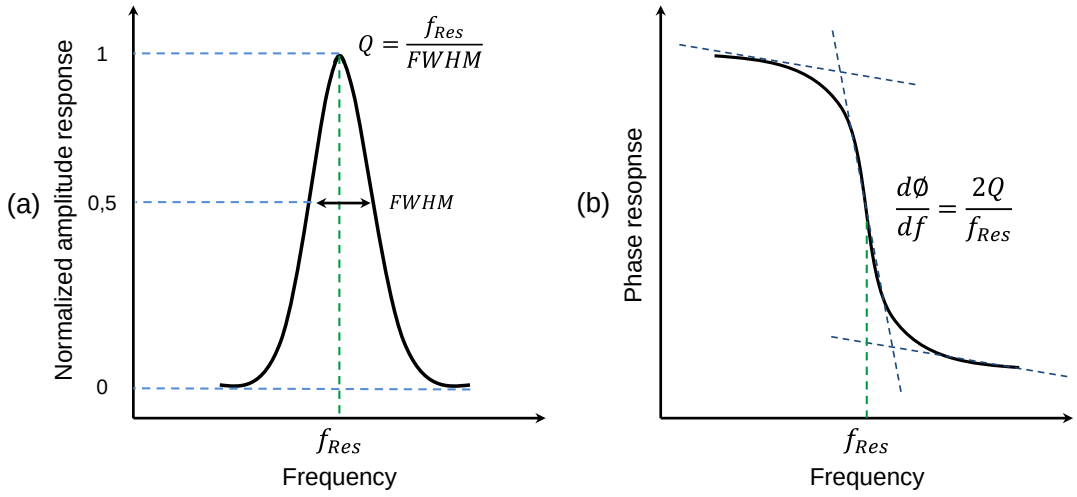

Fig. I. 3. Typical amplitude and phase responses of a resonator at a resonant frequency f_{Res}

The relation (Eq. I. 6) clearly shows the main noise conversion process in an oscillator: the amplifier's phase noise fluctuations are converted into oscillator's frequency fluctuations through the oscillation loop condition. Using equations (Eq. I. 4) - (Eq. I. 7), the oscillator's SSB phase noise can be finally expressed as follows:

$$L_{Osc}(f_m) = 20log\left(\frac{f_{Osc}}{2\sqrt{2}Q_{RF}f_m}\right) + 10log\left(\overline{\Delta\emptyset^2}_{Amp}\right) \qquad dBc/Hz \qquad \textit{(Eq. I. 9)}$$

This relation clearly explains the conversion of the amplifier flicker noise (with a -10 dB/dec slope) into oscillator phase noise with a -30 dB/dec noise slope.

Other than this noise conversion description, Lesson has proposed a complete noise model of the amplifier and therefore of the oscillator. The model included a description of both additive and multiplicative noise conversion processes in an oscillator. His assumptions are illustrated in Fig. I. 4 and are as follows:

- An additive far-from-carrier white noise floor, originating from thermal noise, governed by the amplifier's noise figure
- A multiplicative close-to-carrier flicker noise.

These two noise types are separated by a cutoff frequency $f_{c_{HF}}$. These assumptions are well explained in the thesis of G. Cibiel [3] where a detailed study has been made on microwave amplifiers' noise origins.

The illustration in Fig. I. 4 points out the fact that the flicker noise is mainly a conversion process noise and is related to the amplifier's low frequency noise. On the other hand, the white phase noise originates either from a conversion process or from an additive noise process. The phase fluctuations are converted into frequency fluctuations inside the resonator's 3 dB bandwidth:

$$f_{3dB} = \frac{f_{Osc}}{2Q_{RF}} \qquad \textit{(Eq. I. 10)}$$

From (Eq. I. 10), we can see that when Q_{RF} increases, the close-to-carrier phase noise decreases as the cutoff frequency of the loop filter, f_{3dB}, decreases (see the illustration in Fig. I. 5)

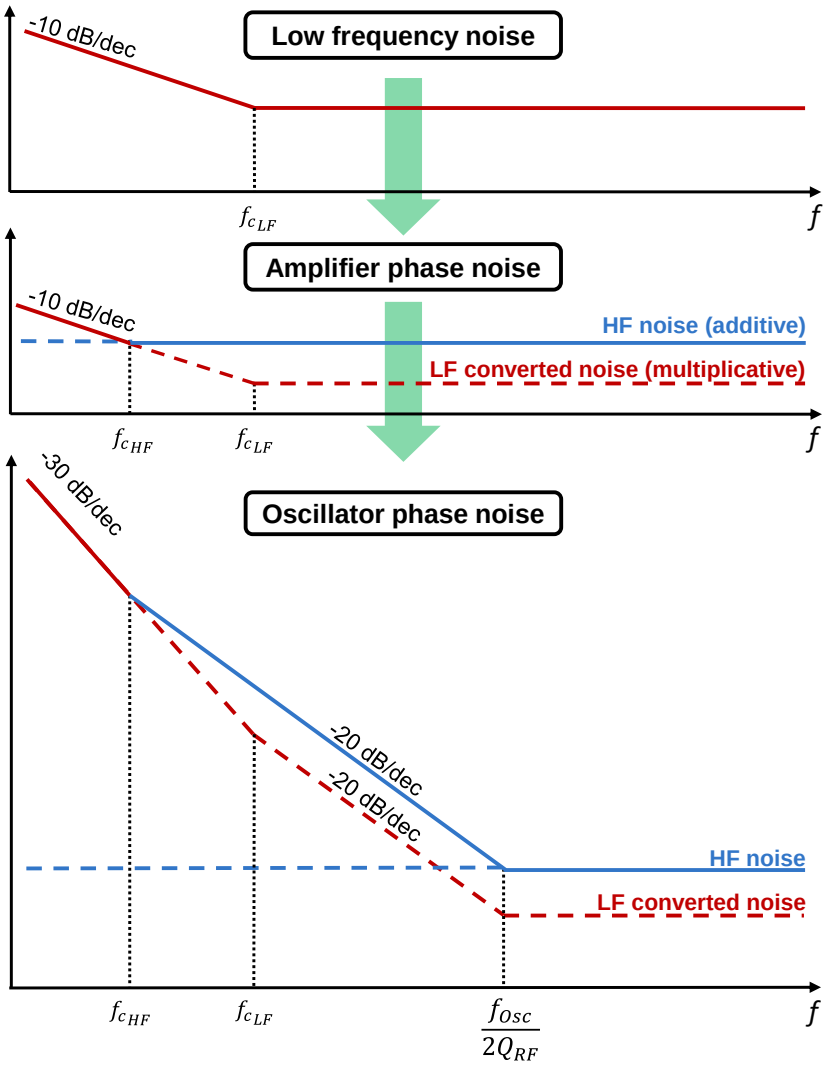

Fig. I. 4. Typical phase noise spectrum of an oscillator, following Leeson's assumptions. The oscillator phase noise originates from the amplifier phase noise, through different processes: conversion of the amplifier low-frequency noise (in red) and addition of the amplifier high-frequency noise (in blue)

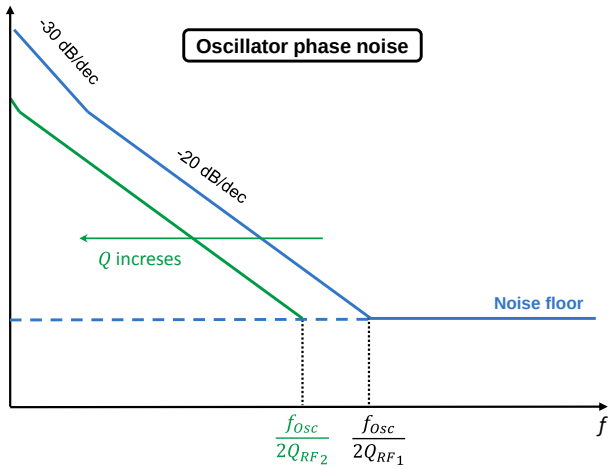

Fig. I. 5. Illustration of the theoretical evolution of the oscillator close-to-carrier phase noise as a function of Q

Until this day, Leeson's noise model still of great interest for scientists in the microwave oscillators field. Moreover, it held great interest for us in simulating the noise behavior of the optoelectronic oscillator (OEO). However, as we will see later, the OEO case is much more complex. Actually, the noise in these systems does not only originate from the microwave amplifier but also from different other optical, microwave and low-frequency active and even passive elements used inside the oscillation loop.

I.2.2.b *Noise characterization of microwave components*

To study the phase noise characteristics of microwave components in open-loop configuration, we have used the residual phase noise measurement method well described in [3] and [4]. The measurement bench is depicted in Fig. I. 6. The method is based on phase detection and it takes advantage of the cross-correlation technique to reach very low noise levels (a noise floor as low as −180 dBc/Hz at 10 kHz offset frequency can be obtained at 3.5 GHz). It allows residual phase noise characterization in the microwave range (1 to 18 GHz) of transistors and other devices such as amplifiers, mixers, frequency dividers and multipliers. Furthermore, this measurement bench has been also used to estimate the residual phase noise of an optical amplifier (as we will see later).

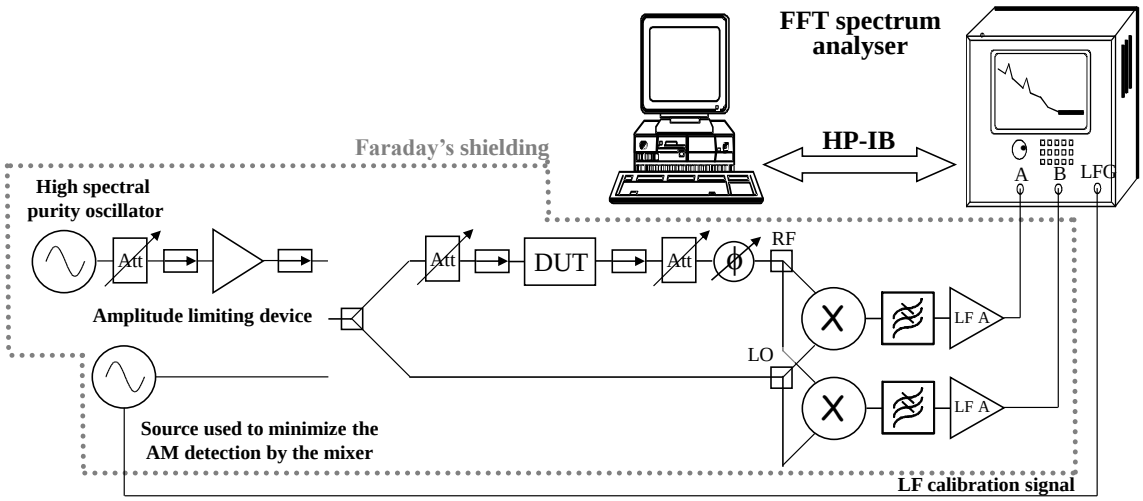

Fig. I. 6. From [4]: Residual phase noise measurement bench (phase detection from 1 to 18 GHz; low frequency observation band from 1 Hz to 100 kHz).

Finally, once in the oscillator loop, the measured components' residual phase noise can be introduced in the aforementioned oscillator model following Leeson's approach, taking into account the resonator's loaded quality factor at the oscillation frequency f_{Osc}.

I.2.3 State of the art microwave oscillators

From Leeson's relation given in (Eq. I. 9), it is very clear that the oscillator phase noise inside the resonator bandwidth is inversely proportional to the resonator's loaded quality factor. Therefore, the use of a resonator featuring a high quality factor is essential to get a low phase noise oscillator. On the other hand, it turned out not to be the only parameter that influences the oscillator phase noise because the insertion loss of the resonator has also to be considered. This has been already stated in [5] and, as we will see later, it is also the case in our OEOs.

In the microwave domain, different types of resonators can be found. The commonly used resonators are: LC resonators, micro strip based resonators, coaxial resonators, yttrium iron garnet (YIG) (tunable) resonators, surface acoustic wave (SAW) and bulk acoustic wave (BAW) resonators, metallic cavities resonators and ceramic or crystalline dielectric resonators… The schematic in Fig. I. 7 presents these different resonators with their loaded quality factors' values and the oscillators in which they are used, along with their phase noise performance scale.

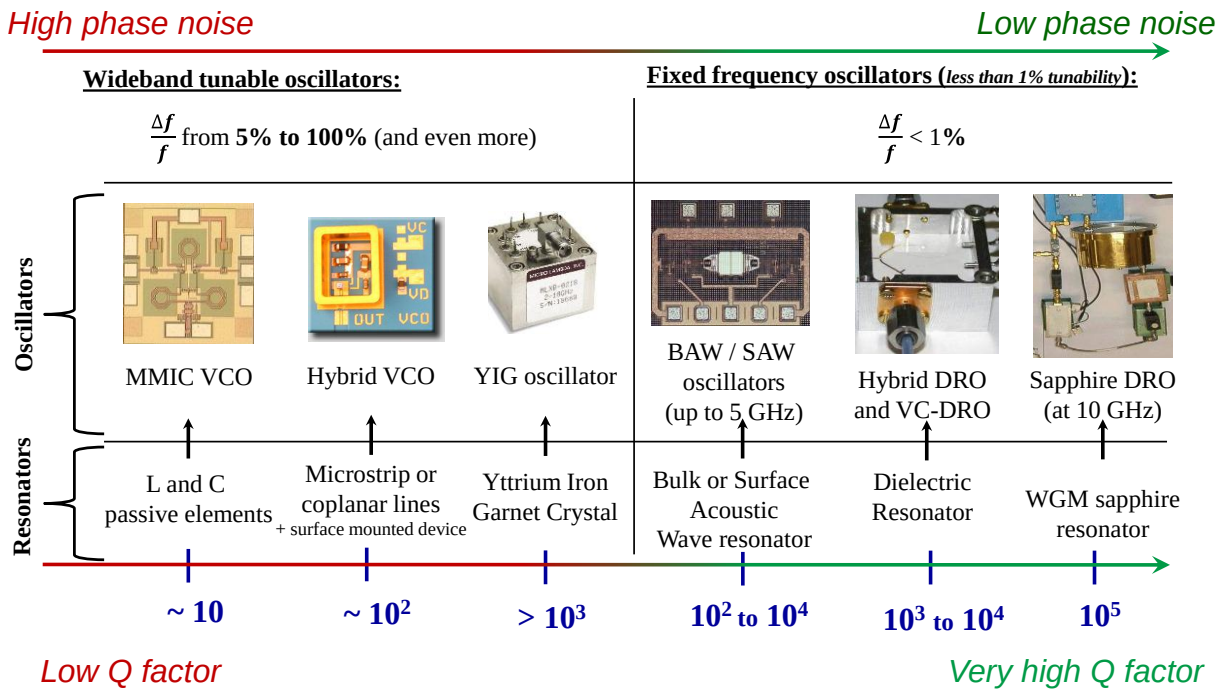

Fig. I. 7. Different microwave resonators with their loaded quality factors' values and the oscillators in which they are used. MMIC: monolithic microwave integrated circuit; VCO: voltage controlled oscillator; VC-DRO voltage controlled dielectric resonator oscillator; WGM: whispering gallery mode.

I.2.3.a *Dielectric resonator based oscillators (DROs)*

Among the resonators presented in the above section, we can notice that the most interesting results in terms of quality factor and oscillator phase noise are obtained when dielectric resonators are used. These resonators allow reaching a relatively high Q in a small volume, which makes them very efficient to design microwave filters and oscillators [6]. Nevertheless, the product of $Q_{RF}.f_0$ is almost always constant when using these resonators, which means that their quality factors degrade when the application frequency increases. These resonators are of two types: ceramic and sapphire resonators. In the last case, they are generally operated using a whispering gallery mode (WGM).

I.2.3.a.i *Ceramic resonators*

These resonators are fabricated from ceramic based materials that present large dielectric constants and low dissipation factors. Moreover, different materials can be mixed in the ceramic in order to reach a very low temperature coefficient for the resonator. Such resonators are often used to provide the frequency reference in microwave oscillators because of the high quality factor values that they can achieve (unloaded Q_{RF} above 1x10^4 at 10 GHz), adding the fact that they can be used in hybrid integrated circuits without giving too much care for the shielding.

However, the shielding is always necessary, even for ceramic resonators. A resonator in free space features a very low Q factor because of radiation losses. The circuit must be held in a metallic housing, with low loss metal above and under the resonator.

I.2.3.a.ii *Sapphire WGM resonators*

These structures are usually cylindrical in shape and are made of a single piece of sapphire crystal. Even not very stable in temperature, the sapphire features the lowest dielectric loss among all other materials in the microwave domain. It can therefore achieve very high quality factors (best unloaded Qs are close to $2x10^5$ in the X band).

The main drawback of sapphire lies in its relatively low dielectric constant, and also in the anisotropy of this constant, which limits the choice in resonator's modes and geometry. In order to achieve good energy storage in the resonator, high order modes must be used, such as whispering gallery modes, and a high quality metallic housing for the resonator must be designed.

All this makes the resonator quite bulky and the use of WGM modes often require a specific system to isolate one mode in the oscillator [3]. Finally, the quality factor of this resonator can be extremely increased if the resonator is used at cryogenic temperatures (Q_{RF} above $1x10^9$ at 10 GHz) [7].

I.2.4 State of the art microwave oscillators – noise results comparison

The sketch below gives some of the best (to our knowledge) phase noise results obtained, at 10 kHz offset frequency, using microwave oscillators when the above mentioned microwave resonators are used, particularly quartz piezoelectric resonators and ceramic and sapphire WGM dielectric resonators.

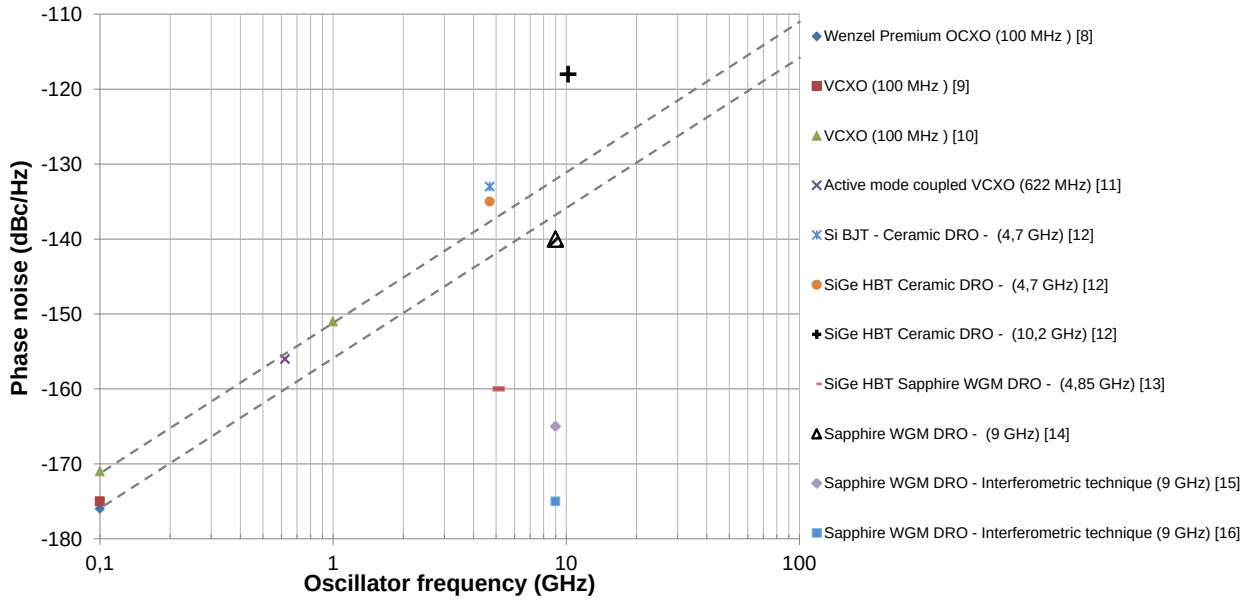

Fig. I. 8. Best (to our knowledge) phase noise results obtained, at 10 kHz offset frequency, using microwave oscillators. The RF quartz oscillators' results are shown for comparison and the performance that can be obtained at microwaves by multiplying these quartz sources is shown by the dashed lines (assuming that no additive multiplication noise is added). OCXO: oven controlled quartz oscillator; VCXO: voltage controlled quartz oscillator; SiGe HBT: silicon-germanium hetero-junction bipolar transistor; Si BJT: silicon bipolar junction transistor

The phase noise results presented in Fig. I. 8 initially show that quartz oscillators phase noise increases when the frequency is multiplied [8][9][10][11]. Moreover, Fig. I. 8 shows that the results

obtained in [12] for the same ceramic DRO are slightly different if different amplifiers were used in the oscillator loop (silicon-germanium hetero-junction bipolar transistor (SiGe HBT) or silicon bipolar junction transistor (Si BJT)).

Finally, in the X band, only the sapphire WGM based DRO's are capable of giving ultra-low phase noise levels [14], especially when the oscillator frequency is stabilized using a frequency discriminator with carrier rejection technique [15][16]. Of course, this kind of stabilization technique is very complex and needs a careful and precise control. Therefore it is mainly a laboratory frequency reference not suitable to be used in an embedded system.

I.3 Optoelectronic oscillators (OEOs)

As we have already seen, the quality factors of electronic resonators degrade when the application frequency increases. As a direct consequence, the spectral purity of the oscillators based on these resonators deteriorates. Therefore, achieving ultrahigh spectral purity in compact oscillators is linked to the investigations on new high quality factor resonators (or delay mediums) having the lowest dissipation factors.

The first demonstration of a microwave oscillator using optics was at the NASA's jet propulsion laboratory JPL, and it was published in 1991 by R. Logan et al. [17]. The system was simply based on a microwave oscillator with its frequency stabilized using a fiber-optic discriminator. It was called a fiber-optic stabilized oscillator (FOSO). The system performances were improved in a later version by employing a mode-locked laser diode in the oscillator scheme [18]. It is not until 1994 that the first architecture of the well-known OEO has been published by X. Yao et al. [19]. This architecture has been detailed later in many other communications, especially in [20] and [21].

I.3.1 Principle of delay line based OEO

The block diagram of a generic OEO is illustrated in Fig. I. 9. In this setup [22], light from a laser is modulated and passed through a long optical fiber before reaching the photodiode as in a classical optical link. Simultaneously, the output of the photodiode is amplified, filtered, adjusted for phase and then fed back to the modulator. This feedback loop can generate self-sustained oscillation if its overall gain is larger than the loss and the circulating waves can be combined in phase. This OEO architecture is quite flexible and can be configured in a variety of ways using different optical and electrical components, eventually different delay elements (e.g. optical resonators).

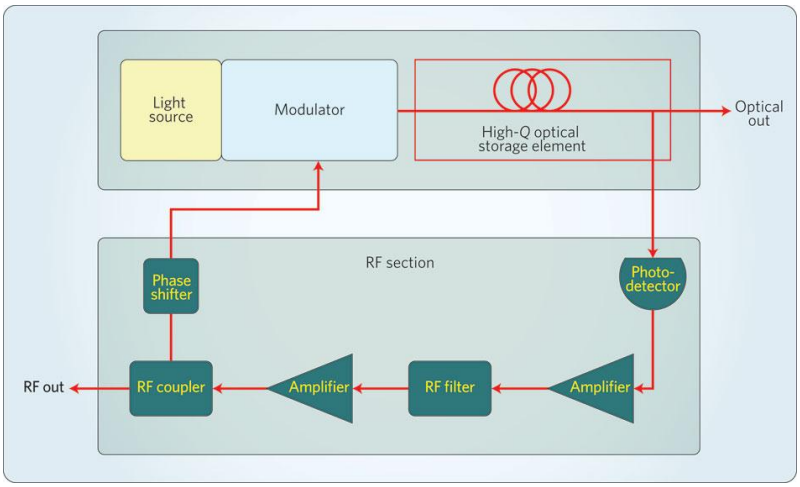

Fig. I. 9. From [22]: Block diagram of a generic OEO

The basic idea of this OEO is as follows: in a microwave oscillator, the microwave resonator can be simply replaced by a delay line (DL). Instead of using a microwave coaxial cable as a delay line, which is not a very efficient method, we can benefit from long optical fibers (few km-long) with extremely low transmission loss (0.2 dB/km in single mode fibers) to introduce a considerable delay (τ = several tens of microseconds) to the propagating microwaves carried by an optical wave. As a result, a very steep phase-to-frequency slope, proportional to this delay, can be obtained and is therefore equivalent to a high loaded quality factor (see (Eq. I. *7*)). This steep phase-to-frequency slope can considerably improve the oscillator stability.

In the delay line based OEO (DL-OEO), the relation between the delay of the propagating signal and the phase-to-frequency slope is given by:

$$\frac{d\emptyset}{df} = 2\pi\tau \qquad \textit{(Eq. I. 11)}$$

Using (Eq. I. 7) and (Eq. I. 11), the equivalent loaded quality factor can be written as follows:

$$Q_{RF} = \pi\tau f_{RF} \qquad \textit{(Eq. I. 12)}$$

From (Eq. I. 12), we can see that Q_{RF} is directly proportional to f_{RF}, which is not the case of microwave resonators. For example, if a 10 GHz frequency is used with an optical DL of 2 km (which adds about 10 microseconds delay to the travelling wave) the equivalent quality factor will be equal to 3.15×10^5. However, if f_{RF} is increased to 20 GHz, the equivalent quality factor will increase to 6.3×10^5.

Consequently, quality factors above 10^6 can be attained either by using a higher application frequency or by using a longer optical DL, and the spectral purity of the OEO can be therefore enhanced. Moreover, X. Yao et al. [23] have stated that, theoretically, a phase noise level below -140 dBc/Hz at 10 kHz offset frequency can be obtained for an OEO working at a 75 GHz frequency.

On the other hand, when the DL length increases, the system becomes bulky and dispersion effects appear with many other nonlinear optical effects generated in the fiber (as we will see later in chapters III and IV). Besides that, we have to add the difficulty in thermally stabilizing such a long fiber loop (knowing the negative effects of thermal instabilities on the phase noise of a transmitted signal over an optical fiber; [24]) and the spurious modes that appear in the oscillator's phase noise spectrum and that become very numerous as the DL length increases. One example of the phase noise spectrum obtained in a 4.4km-long DL-OEO is presented in Fig. I. 10 where we can see the numerous spurious modes that appear in the spectrum.

These spurious modes are highly undesirable for some applications (such as radars). They are caused by the propagation of the waves multiple times inside the OEO loop. The spacing between them, called free spectral range (FSR), is related to the loop trip time:

$$FSR = \frac{c}{n\,L} \qquad \textit{(Eq. I. 13)}$$

where c is the speed of light in free space (c ~ 3.10^8 m/s), n is the fiber refractive index and L is the fiber length.

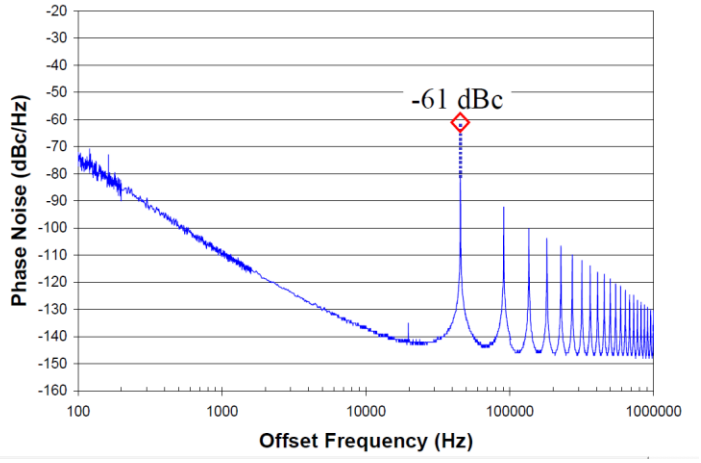

Fig. I. 10. From [27] : SSB phase noise of a single loop 4.4 km-long 10 GHz DL-OEO. The spurious modes clearly appears in the phase noise spectrum with a noise power level of -61 dBc for the first spur at 45 kHz offset

Therefore, from (Eq. I. 13), using a 10 km-long DL means that the first spurious mode will appear as close as 20 kHz to the carrier. In that case, the bandwidth of the RF filter used in the OEO loop will not be narrow enough to filter this undesirable noise peak. This could lead to mode hopping in the oscillation frequency of the OEO.

For these reasons, many other OEO architectures have been proposed to suppress or reduce the spurious modes. One elegant solution is to perform the filtering of these modes directly in the optical domain [25][26][27][28] using a system involving several DLs (two at least). In these schemes (see Fig. I. 11 (a)), detailed in [27], the longer DL sets the loaded quality factor of the oscillator and the shorter one

allows the recombination in phase of only one chosen mode of the longer DL, consequently the other modes are suppressed (see Fig. I. 11 (b)).

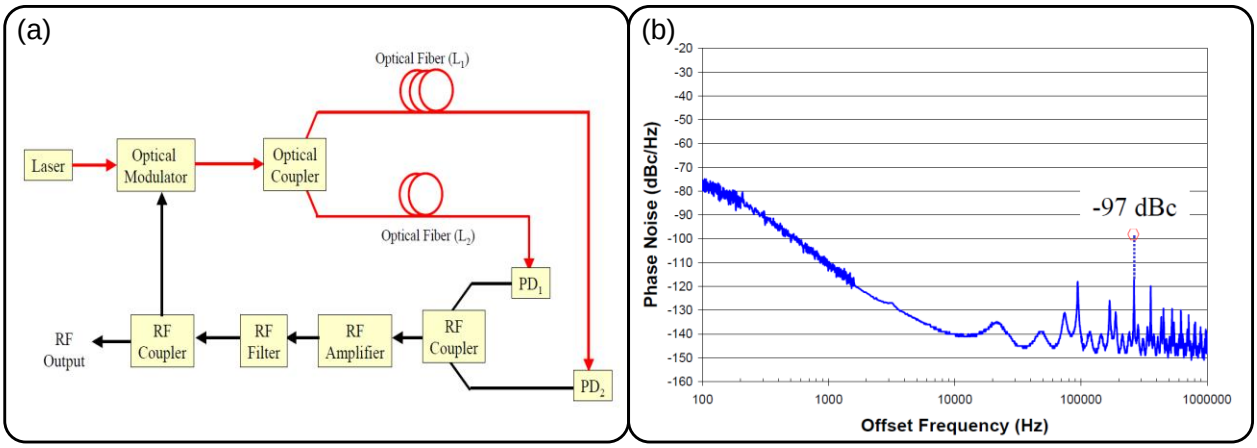

Fig. I. 11. From [27] : (a) Dual optical loop OEO configuration and (b) the SSB phase noise of 10 GHz signal generated by a dual optical loop OEO (8.4 + 2.2 km DLs) were spurious modes are clearly suppressed

Besides this method, another method based on dual injection-locked optoelectronic oscillators has demonstrated a good reduction in spurious modes in the phase noise spectrum [29]. After all, and despite their efficiency, both methods need bulky and complex configurations to be used.

On the other hand, and aside from their undesirable effects, spurious have appealing aspects. Because they are very close to each other, the simple use of a narrow-bandwidth tunable microwave filter in the RF loop of the OEO (such as a YIG filter) can result in a wideband tuning of the oscillation frequency (hopping from a mode to another) with a tuning step equal to the FSR of the DL we are using. This can be achieved without any change in the oscillator phase noise performance. Such a tunable OEO architecture has been demonstrated in [30].

Finally, it is noteworthy to point out that in contrast with microwave oscillators, where the phase noise mainly results from a conversion noise of the only active element in the loop (the microwave amplifier), the noise in the OEO depends (in addition to the microwave amplifier noise) on different other noise contributions from different passive and active elements in the OEO loop: the laser relative intensity noise (RIN), the laser frequency noise, the photon shot noise, the thermal noise, the interferometry noise, the noise generated by the nonlinear optical effects in the fiber, the fiber dispersion noise and many other noise contributions depending on the OEO architecture we are using.

If the microwave amplifier used in the OEO is carefully selected (having a low residual phase noise level), the far-from-carrier OEO phase noise level will be determined by the optical noise-to-carrier ratio (NCR). This NCR is mainly related to the laser RIN and to the photodiode shot noise. On the other hand, the close-to-carrier phase noise will be mainly linked to the loaded quality factor, and hence, to the DL length (as already illustrated in Fig. I. 5).

I.3.2 Principle of active cavity based coupled OEO (COEO)

In 1997, a novel and elegant architecture of the OEO has been demonstrated by the same team at the JPL [31], (see Fig. I. 12 (a)). In this architecture, the optical carrier is not provided by a laser independent from the rest of the system but it is generated by a fiber ring loop including a semiconductor optical amplifier (SAO), with its gain directly modulated (active ring resonator). Accordingly, the laser and the microwave oscillator were both benefiting from the same high optical quality factor (Q_{Opt}): the laser is no longer a single-mode laser but a multimode mode-locked fiber laser (MLL) and the beat-note of its optical modes is used for microwave oscillation in the RF loop. It is therefore a system including two coupled oscillators, an optical oscillator and a microwave oscillator. Because of this, it was called the COEO, which stands for “coupled optoelectronic oscillator”.

In addition to this, the COEO configuration acts like a double-loop OEO, therefore spurious modes are automatically suppressed, except that here the second loop is a pure optical cavity and an integral part of the fiber laser.

The generated frequency in the first version of this COEO was limited to a few hundreds of MHz because of the use of a direct modulated SOA [31]. The solution to this has been reported in another improved version of the COEO [32] (see Fig. I. 12 (b)), where a fast amplitude modulator has been used inside the optical loop instead of a direct modulation of the SOA gain. However, the phase noise results were not really improved until 2005, where a phase noise level of -140 dBc/Hz at 10 kHz offset frequency from the carrier has been obtained using a 330m-long active cavity based COEO [33] (currently commercialized by OEwaves) (see Fig. I. 13).

Finally, authors in [33] [34] have also predicted through a theoretical model of their system, an enhancement in the active cavity quality factor due to the positive feedback in the optical loop. Besides this important step in OEO design, the path towards integration has been opened with the introduction of optical resonators in the OEOs, especially optical micro-resonators.

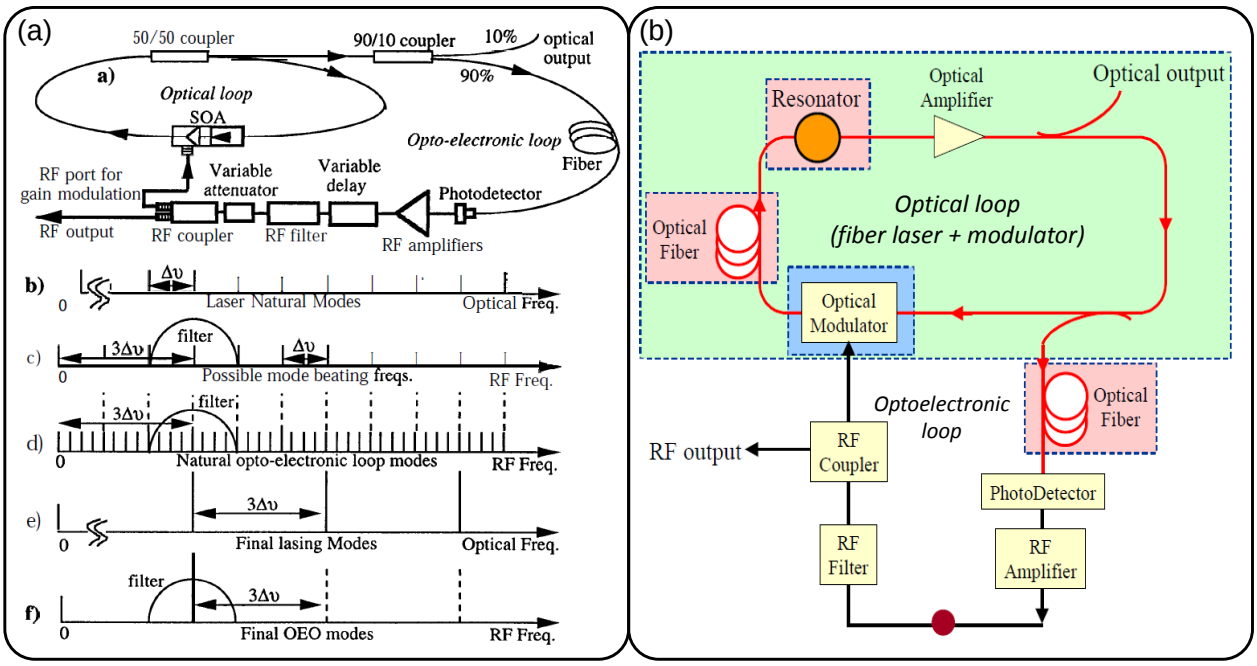

Fig. I. 12. (a) from [31]: first COEO architecture with the principle of operation and (b) From [33]: COEO improved architecture using a modulator inside the optical loop (eventually, a passive resonator can be used to increase optical modes selectivity)

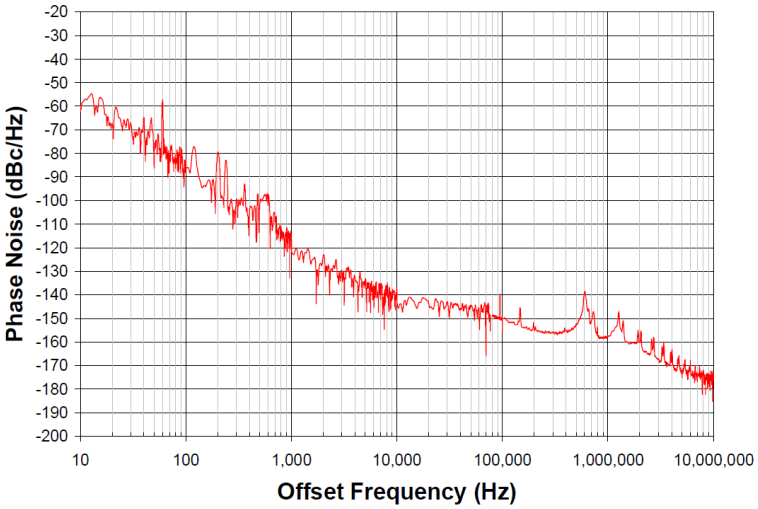

Fig. I. 13. From [33] : Phase noise of a 10GHz signal generated by a 330m-long active cavity based COEO

I.3.3 Principle of passive cavity based OEO

Despite the remarkable low phase noise results obtained with DL-OEOs, these systems remain bulky, their thermal stabilization is difficult and they produce spurious modes that need complex configurations to be reduced. Because of all these discouraging factors, an alternative solution is the use of optical resonators, featuring ultra-high optical quality factors (Q_{Opt} above 10^{10} or even 10^{11}). These ultra-high Q_{Opt} allows large optical delay values (ranging from nanosecond to tens of milliseconds) and relatively low dimensions due to the resonant effect.

Using these optical resonators, the equivalent microwave quality factor is linked to the optical quality factor by the following relation [35]:

$$Q_{RF} = Q_{Opt} \times \frac{f_{RF}}{f_{Opt}} \qquad \textit{(Eq. I. 14)}$$

where f_{Opt} is the optical frequency (f_{Opt}~193 THz).

We can see that as in the optical delay line case, the equivalent Q_{RF} of an optical resonator is directly proportional to f_{RF}. On the other hand, and in contrast with the optical delay line, which allows all optical frequencies in an open-loop configuration, an optical resonator act simultaneously as a delay element and an optical filter. It filters the microwave signals carried as modulation sidebands on an optical carrier (see the illustration in Fig. I. 14). The filtered microwave signals are then recovered in the microwave domain by means of a fast photodiode.

Indeed, the optical resonator generates an optical frequency comb with a mode spacing that depends on the resonator's size. This mode spacing or free spectral range (FSR) has the same definition as for the delay line. However, in the resonators' case, it has much higher values that range from a few tens of MHz (in few meters-long fibered resonators) to a few GHz (in micro-resonators; few millimeters in diameter). The beat-note of the optical signals passing through (and filtered by) this resonator can be therefore used in an OEO loop where the resonator is also considered as the frequency stability element due to the high optical delay it provides (high Q_{Opt}).

The OEO based on a passive resonator has the same principle of the DL-OEO. However, the difficulty here is the coupling of the laser light-wave into the resonator (especially when using micro-resonators). In addition, the laser wavelength must be stabilized onto one of the resonator's optical modes to be able to use the other modes of the resonator (see the illustration in Fig. I. 14). This can be achieved in several ways. We can particularly mention the laser optical injection lock technique and the Pound-Drever-Hall (PDH) laser stabilization technique [36]. The PDH technique has been chosen for our experiments made on the different types of optical resonators. It has been implemented during the thesis of P.H. Merrer [37] and we have tried to improve the experimental system since then. The PDH experimental setup we are using is briefly described in the next section.

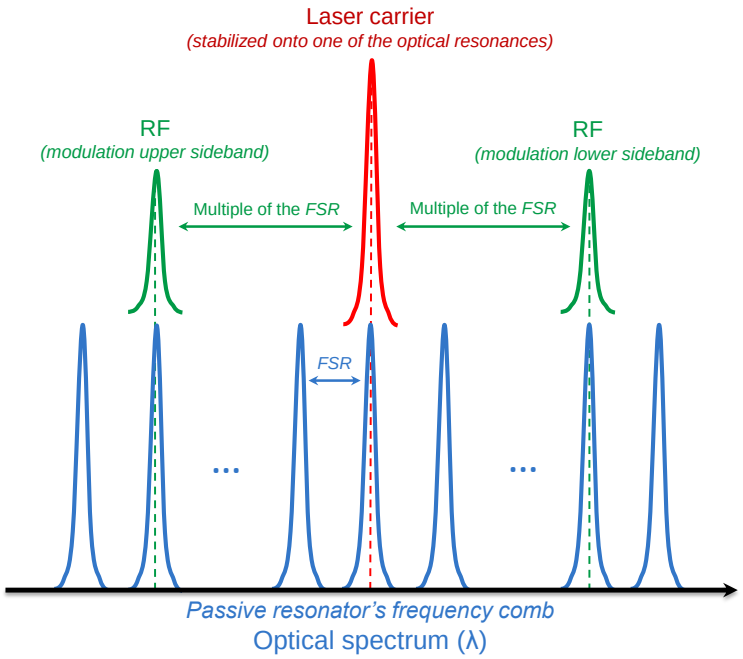

Fig. I. 14. Illustration of the microwave filtering using an optical frequency comb generated by an optical resonator

I.3.3.a *Pound-Drever-Hall (PDH) laser stabilization technique*

The Pound-Drever-Hall laser stabilization technique, invented by Ron Drever [36], was originally used to stabilize the frequency of a laser by locking it onto a Fabry-Perot reference cavity. It is based on using the phase information (instead of the amplitude information) of a laser signal passing through the resonator. In the following, a brief description of our experimental setup using the PDH technique is given (shown in Fig. I. 15). More details on this technique can be found in [38].

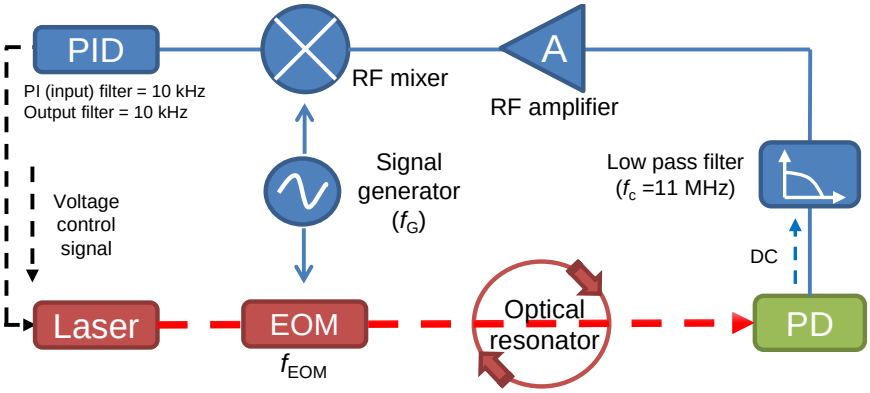

Fig. I. 15. PDH laser stabilization loop. EOM: electro-optic modulator; PID: proportional–integral–derivative controller.

In Fig. I. 15 setup, the laser carrier at 1.55 µm (from a tunable Koheras laser having a linewidth of 1 kHz) is phase modulated with a large modulation index at a RF frequency (f_G, from a signal generator) by means of an electro-optic modulator (EOM). The beam passes through the optical resonator, then the transmitted beam is sent to the same photodiode used in the oscillation loop (see the latter two sections). The amplitude of the photodiode's output voltage at f_G depends on the detuning between the

laser frequency and the optical resonance. This voltage signal passes through a low-pass filter to reduce its noise and eliminate unwanted higher modulation harmonics. It is then amplified and sent to an electrical mixer to be mixed with a fraction of the RF signal (f_G) used to drive the modulator. The mixer's output represents an error signal proportional to the frequency detuning between the laser and the optical resonance. This error signal is then sent to a proportional–integral–derivative controller (PID) in order to drive the laser's piezoelectric actuator (PZT) and adjust its wavelength. Finally, as soon as the laser is locked onto the optical resonance, it is possible to use the system for microwave applications.

A noteworthy remark, found through our experimental studies, points to the imperativeness of accurately adjusting the PDH loop parameters. This is due to the sensitivity of the OEO phase noise to the PDH loop settings because the OEO phase noise can be severely affected through laser noise conversion processes via the resonator (as we will see in chapter III).

Moreover, the PDH loop bandwidth seems to be a very critical parameter because if it is reduced (especially the PID input and output filters), it can considerably degrade the OEO phase noise performance (as we will see later in chapter IV).

I.3.3.b *OEO experimental setup*

The experimental setup of our 10 GHz OEO based on passive resonator is presented in Fig. I. 16. It includes the Koheras laser, a Mach-Zehnder modulator (MZM; 20 Gb/s EOspace) to modulate the laser carrier, an optical resonator, eventually an optical fibered EDFA amplifier and a fast photodiode (Discovery DCS30S).

The laser frequency is first stabilized onto one of the optical resonances using the aforementioned low frequency PDH feedback loop. The microwave oscillation is then maintained by another high frequency loop including two RF amplifiers, a phase shifter and (eventually) a RF filter in order to get a single mode oscillation (the RF filter is useless in case of micro-resonators because of the large $FSRs$ they can provide).

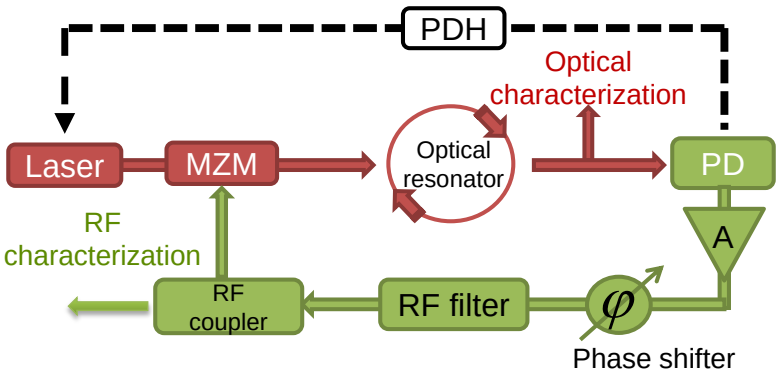

Fig. I. 16. Optical resonator based 10 GHz optoelectronic oscillator

Finally, like the DL-OEO, this OEO is capable of generating high spectral purity signals that can be locally used from the OEO's RF output, or directly distributed via long distance and low loss optical links, using the OEO's optical output.

I.3.3.c *OEO based on whispering gallery mode (WGM) resonator*

The first alternative approach using optical resonators is to replace the optical delay line in the OEO by a whispering gallery mode (WGM) optical resonator (WGMR) [39]. By definition, optical whispering gallery modes, similarly to microwave WGMs, are electromagnetic resonances that occur in circularly symmetric dielectrics that trap light in a circling orbit via total internal reflection inside the resonator. They can be produced in variety of shapes as well as encompassing small sizes (from few millimeters to few micrometers) because of the small wavelength of the optical signal. Consequently, a microwave signal carried by an optical carrier, like in generic OEO case, can be trapped into a resonator where its size is much smaller than the wavelength of the microwave signal. The basics of WGM resonators and their different applications have been thoroughly studied in [40] [41] [42].

The WGMRs can be fabricated from a variety of materials using different fabrication processes. These resonators can be especially fabricated using crystalline materials, such as calcium fluoride (CaF_2) to get high Qs [43], lithium niobate (LiNbO3) or lithium tantalate (LiTaO3) for tunable WGMRs [39], fused silica and many other materials.

These three-dimensional shape devices are spheres, torus or disks, in which the optical wave circulates close to the equator line. They present ultra-high Q_{Opt} with demonstrated values ranging from 10^8 to 10^{11} at 1.55 µm optical carrier [44]. In our experiments we used a disk-shaped WGMR based on calcium fluoride (CaF_2) with a diameter of about 5.5 mm (see Fig. I. 17 (a)).

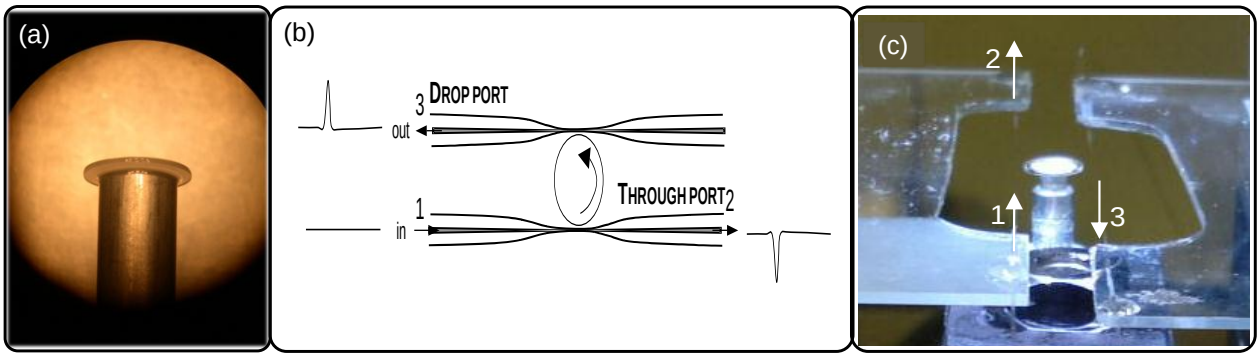

Fig. I. 17. (a) 5.5 mm whispering gallery mode CaF2 disk-shaped resonator fixed on a metallic rod; (b) illustration and (c) experimental setup of the symmetrical dual-coupling system with tapered fibers coupled to the CaF2 disk

As mentioned before, the main problem in using these resonators is the mechanical difficulty in setting up a reliable coupling with a light source. Moreover, and in addition to the generated fundamental frequency comb (equatorial mode), multiple optical frequency combs are generated by these resonators for both transverse electric (TE) and transverse magnetic (TM) modes. The use of an all-fiber polarization controller before the WGMR is therefore imperative so to be able to select TE or TM modes' frequency combs.

I.3.3.c.i *WGM resonator coupling technique*

Several coupling techniques have been investigated in our laboratory in order to obtain a selective and efficient coupling of the light into the WGMR. The oldest method and common technique

that is usually reported in the literature is the prism coupling configuration [45]. This approach can be simplified using an angle polished optical fiber [46]. In our case, we have chosen an alternative method that enables highly efficient optical power transfer to the WGMs in a symmetrical dual-coupling configuration with tapered optical fibers [47] [48].

Actually, tapered optical fibers meet the key requirements for a good performance and easy coupling: a complete phase-matching and a sufficient overlap between the evanescent electromagnetic fields. The first condition is satisfied by matching the fiber taper propagation constant to the WGM's propagation constant, while the overall coupling strength varies exponentially in function of the air gap between the resonator and the fiber taper.

In practice, these coupling conditions can be optimized by varying the position of the resonator along the bi-conical shape of the fiber taper (having a variable waist diameter all along its length) and by controlling the air gap distance (see Fig. I. 17 (b)). The minimum taper diameter in our work was typically less than 1 µm with less than 1 dB transmission loss. They were made by heating a single-mode silica fiber (typically SMF-28) with a torch and slowly pulling the fiber. Accordingly, phase-matching between the WGMR and the fiber taper is possible because CaF_2 and silica have each similar refractive index at 1.55 µm wavelength.

Finally, to be able to achieve the delicate adjustment of the fiber taper and the WGMR, and therefore get an efficient dual-coupling, a dedicated measurement bench has been used. It consists of two triple-axis piezoelectric nanometric holders to accurately place the two fiber tapers symmetrically with respect to the optical WGMR. The experimental setup of the coupling system is shown in (see Fig. I. 17 (c)). As a result, two nearly identical taper couplers were placed tangentially at the opposite sides of the disk-shaped WGMR, one serves as the input coupler and the other as the output coupler.

I.3.3.c.ii *OEO based on a CaF_2 WGM resonator*

As soon as the laser is locked onto an optical resonance (of the fundamental frequency comb) of the CaF_2 WGMR, using the PDH stabilization loop, the WGMR has been characterized in the microwave domain. We used an experimental setup comparable to the OEO configuration in Fig. I. 16 but in an open-loop configuration including an accurate vector network analyzer. This microwave domain characterization bench is fully described in the next chapter.

Using this experimental setup, we have been able to accurately measure the WGMR absorption and transmission transfer functions, and the different frequency combs are clearly visible in the results depicted in Fig. I. 18 (a) (absorption transfer function). These measurements give a 12.481 GHz FSR (for the fundamental frequency comb) and a Q_{Opt} of 8.4×10^7.

Once used in the OEO setup, the microwave oscillation frequency was defined by the FSR of the WGMR (FSR = 12.45 GHz for the fundamental frequency comb). We were able to measure a -94 dBc/Hz phase noise level at 10 kHz offset frequency from the carrier. The noise peaks above 10 kHz offset frequency are likely due to some mechanical perturbations in the optical coupling between the fiber taper and the WGMR.

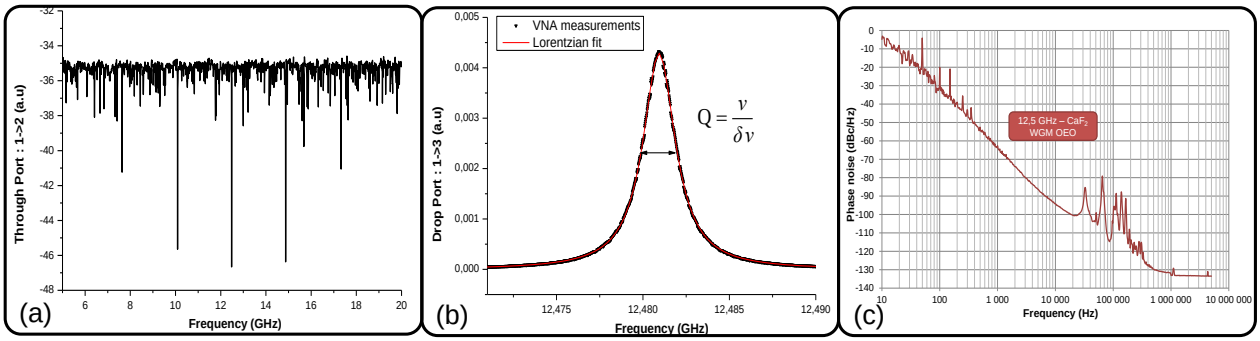

Fig. I. 18. CaF_2 disk WGMR: (a) absorption transfer function, (b) a focus on the fundamental comb's resonance in the transmission transfer function (which gives a Q_{Opt} f 8.4x10^7 at 1.55 µm optical carrier) and (c) phase noise results when the CaF_2 disk WGMR is used in an OEO setup (-94 dBc/Hz at 10 kHz offset frequency)

Aside from that, it is clear that this OEO phase noise spectrum includes an important $1/f$ noise contribution caused by the RF amplifier we were using the OEO loop. Further improvement of this WGMR based oscillator's stability can be obtained by understanding and reducing this noise contribution (use of an RF amplifier with a low residual phase noise) and especially by increasing the Q_{Opt} factor of the WGMR.

I.3.3.d *OEO based on fiber ring resonator*

The fiber ring resonator (FRR) is a simpler type of optical resonator than the WGMR. It is basically made of two low loss fibered 2x2 optical directional couplers, which are stable, easy to fabricate and to use, and are commercially available. These two couplers are linked together with a few meters-long single-mode optical fiber. The FRR has therefore a two-dimensional structure which can be easily integrated and in which only two similar optical frequency combs are generated (TE mode's frequency comb and TM mode's frequency comb). The selection of one of these two frequency combs can be made by using a polarization controller before the FRR. Therefore, it is easier to characterize and use a FRR than a WGMR. Of course better selection methods of mode's frequency comb are available and can be used, and they will be reported in the following chapters.

In our laboratory, the FRR has been used first in the aim of understanding WGMR's behavior because of the similarity in their resonance conditions. Nevertheless, we have rapidly realized that the FRR, in addition to its simplicity in fabrication, is able to reach relatively higher quality factors (Q_{Opt} > 10^9) than those obtained with WGMRs we were using.

For all these reasons, and because FRRs were not usually used for OEO purposes and they were not studied in the literature for such application, the work reported in this thesis is mostly concentrated on the study of these passive optical resonators and their use in an OEO setup in order to get a compact, stable and low phase noise oscillator.

I.3.4 State of the art optoelectronic oscillators – noise results comparison

The table below gives some of the best (to our knowledge) phase noise results obtained, at 10 kHz offset frequency, using optoelectronic oscillators based on the different delay elements we have mentioned above: optical delay line(s), active ring cavity and passive WGMR.

Oscillator type	Delay type	Length	Diameter	Q_{Opt}	FSR (Hz)	f_{Osc}	Phase noise at 10 kHz offset frequency	References
DL-OEO	SMF	4 km	-	-	50 kHz	10 GHz	**-132 dBc/Hz**	[50]
DL-OEO	SMF	4.4 km	-	-	45 kHz	10 GHz	**-135 dBc/Hz**	[27]
DL-OEO	Z-DSF	4 km	-	-	50 kHz	10 GHz	**-140 dBc/Hz**	[50]
DL-OEO	SMF	10 km	-	-	20 kHz	10 GHz	**-160dBc/Hz**	[51]
Multiple DL-OEO	SMF	8.4 km + 2.2 km	-	-	25 kHz	10 GHz	**-140 dBc/Hz**	[27]
Tunable multiple DL-OEO	SMF	4.4 km + 3 km + 1.2 km	-	-	45 kHz	10 GHz	**-128 dBc/Hz**	[30]
COEO	DSF+SMF	160 m	-	-	1.5 MHz	9.4 GHz	**-140 dBc/Hz**	[52]
COEO	SMF	330 m	-	-	650 kHz	10 GHz	**-140 dBc/Hz**	[33]
COEO	DSF+SMF	750 m	-	-	210 kHz	9.4 GHz	**-150 dBc/Hz**	[52]
WGMR-OEO	LiTaO3	-	2.54mm	$2x10^7$	35 GHz	35 GHz	**-70 dBc/Hz**	[39]
WGMR-OEO	LiTaO3	-	1.3mm	$1x10^8$	33 GHz	33 GHz	**-80 dBc/Hz**	[53]
WGMR-OEO	Disk-shaped CaF_2	-	5.5mm	$8.4x10^7$	12.45 GHz	12.45GHz	**-94 dBc/Hz**	[48]
WGMR Hyper-parametric oscillator (Four wave mixing)	CaF_2	-	-	$<3x10^9$	9.9 GHz	9.9 GHz	**-120 dBc/Hz**	[54]
WGMR Hyper-parametric Oscillator (Raman)	CaF_2	-	-	$<3x10^9$	35 GHz	35 GHz	**-105 dBc/Hz**	[54]
WGMR-OEO	Disk-shaped SiO_2 Fused silica	-	5mm	$1x10^8$	10.7 GHz	10.7 GHz	**-93 dBc/Hz**	[49]
Tunable WGMR-OEO	LiTaO3	-	1mm	$6.7x10^6$	48 GHz	9.8 GHz	**-100 dBc/Hz**	[55]

Table. I. 1. Best (to our knowledge) phase noise results obtained, at 10 kHz offset frequency, using different types of optoelectronic oscillators

It is clear from Table. I. 1 that the phase noise results obtained in the different OEOs demonstrate the efficiency of the OEO approach compared to classical microwave oscillators (e.g. sapphire WGM DRO in Fig. I. 8). The WGMR hyper-parametric oscillators can be considered as a special case because they use the nonlinear optical effects (Four wave mixing or Raman scattering; detailed in chapter IV) generated inside the WGM resonators, especially fluorite WGM resonators, to directly generate an optical frequency comb [54]. This comb acts like a multimode locked laser and a high spectral purity RF signal is therefore generated by demodulating the comb on a fast photodiode.

To be competitive with these different OEO's schemes, especially with WGMR-OEOs and COEOs (which are considered as compact OEOs), we have to search for an oscillator presenting a very high loaded quality factor (Q_{RF} > 10^5), a low phase noise close and far from the carrier as well as a possible tunability of its oscillation frequency. All this issues will principally depend on the oscillator's frequency stability element. The question is therefore: is the FRR capable of providing all these characteristics?

I.4 Conclusion

In this chapter, we have first briefly reviewed the definition of the oscillator frequency stability and the noise processes in a typical microwave oscillator. We have then listed the different microwave oscillators, used to generate spectrally pure signals, and the state of the art phase noise levels achieved with these systems. Among these, we can especially mention the microwave oscillator based on whispering gallery mode (WGM) sapphire resonator which can provide, in its classical configuration, a phase noise level of -140 dBc/Hz at 10 kHz offset frequency from a 9 GHz carrier. This phase noise can be radically decreased to a -175 dBc/Hz level if the oscillator is frequency stabilized using a frequency discriminator with carrier rejection technique. On the other hand, the system becomes very complex and bulky.

The elegant solution which uses optical delay line based optoelectronic oscillators (OEO) to generate microwave signals has been reviewed. This type of oscillators can provide very low phase noise levels and their noise performance, contrarily to microwave oscillators, is better when the RF application frequency increases. On the other hand, the oscillators remain bulky, their thermal stabilization still difficult and they produce spurious modes that need complex configurations to be reduced.

A novel OEO architecture joining between an optical oscillator (an active fibered cavity: a fiber laser) and a microwave oscillator and called coupled optoelectronic oscillator (COEO) seems to resolve almost all of the problems encountered in microwave oscillators (frequency limitations) and in classical optoelectronic oscillators (size, spurious modes suppression…). Interesting phase noise levels have been reported using this system; for example, a 330m-long active cavity based COEO can provide a -140 dBc/Hz phase noise level at 10 kHz offset frequency from a 10 GHz carrier.

Another possible solution for almost all the problems encountered in microwave oscillators and in classical OEOs, can be the use of passive optical resonators. The use of mm and sub-mm size WGM micro-resonators (WGMRs) sharply reduces the oscillator size and opens the path towards integration of such oscillators with a very satisfying phase noise levels in the generated microwave signals. Of course,

the use of such resonators is difficult because of the mechanical difficulty in setting up a reliable coupling with a light source and the numerous frequency combs that they generate.

A second and very interesting type of passive optical resonators is the fiber ring resonator (FRR): much simpler to use and fabricate than WGMRs (it can be simply made of optical directional couplers and single mode optical fibers). The FRR can provide ultra-high quality factors and therefore it is possible to get very low phase noise levels when using this passive optical resonator in an OEO setup. This is therefore the optical passive resonator that will be thoroughly studied in the rest of this manuscript.

I.5 References

[1] E.S. Ferre-Pikal, J.R. Vig, J.C. Camparo, L.S. Cutler, L. Maleki, W.J. Riley, S.R. Stein, C. Thomas, F.L. Walls, and J.D. White, "Draft revision of IEEE STD 1139-1988 standard definitions of physical quantities for fundamental, frequency and time metrology-random instabilities," Frequency Control Symposium, 1997., Proceedings of the 1997 IEEE International , vol., no., pp.338-357, 28-30 May (1997).

[2] D.B. Leeson, "A simple model of feedback oscillator noise spectrum," Proc. of the IEEE, vol. 54, no. 2, pp. 329-330, (1966).

[3] Gilles Cibiel, "Contribution à l'analyse d'amplificateurs microondes à très faible bruit de phase: application à la réalisation d'une source à très haute pureté spectrale en bande C.," Ph.D. thesis (Toulouse III - Paul Sabatier University, Toulouse, France, 2003).

[4] G. Cibiel, M. Regis, E. Tournier, and O. Llopis, "AM noise impact on low level phase noise measurements," Ultrasonics, Ferroelectrics and Frequency Control, IEEE Transactions on , vol.49, no.6, pp.784-788, June (2002).

[5] J.K.A. Everard, "Low noise oscillators," Microwave Symposium Digest, 1992., IEEE MTT-S International , vol., no., pp.1077-1080 vol.2, 1-5 Jun (1992).

[6] P. Guillon, "Dielectric resonators," Frequency Control Symposium, 1988., Proceedings of the 42nd Annual , vol., no., pp.259-262, 1-3 Jun (1988).

[7] J.G. Hartnett, N.R. Nand, and C. Lu, "Ultra-low-phase-noise cryocooled microwave dielectric-sapphire-resonator oscillators," Applied Physics Letters , vol.100, no.18, pp.183501-183501-4, Apr (2012).

[8] Wenzel Premium 100 MHz - SC Ultra low noise crystal oscillator datasheets, no. 501-04623.

[9] T. McClelland, C. Stone, and M. Bloch, "100 MHz crystal oscillator with extremely low phase noise," Frequency and Time Forum, 1999 and the IEEE International Frequency Control Symposium, 1999., Proceedings of the 1999 Joint Meeting of the European , vol.1, no., pp.331-334 vol.1, (1999).

[10] R. Boroditsky, and J. Gomez, "Ultra Low Phase Noise 1 GHz OCXO," Frequency Control Symposium, 2007 Joint with the 21st European Frequency and Time Forum. IEEE International , vol., no., pp.250-253, May 29 2007-June 1 (2007).

[11] U.L. Rohde, and A.K. Poddar, "A novel voltage controlled high frequency crystal oscillator circuits," Telecommunication in Modern Satellite, Cable, and Broadcasting Services, 2009. TELSIKS '09. 9th International Conference on , vol., no., pp.15-20, 7-9 Oct. (2009).

[12] M. Régis, O. Llopis, B. Van Haaren, R. Plana, A. Grhule, J. Rayssac, and J. Graffeuil, "Ultra low phase noise C and X band bipolar transistor dielectric resonator oscillators," in Proc. IEEE Int. Freq. Contr. Symp., pp. 507–511, May (1998).

[13] G. Cibiel, M. Regis, O. Llopis, A. Rennane, L. Bary, R. Plana, Y. Kersale, and V. Giordano, "Optimization of an ultra-low phase noise sapphire-SiGe HBT oscillator using nonlinear CAD," Ultrasonics, Ferroelectrics and Frequency Control, IEEE Transactions on , vol.51, no.1, pp.33-41, Jan. (2004).

[14] M.E. Tobar, E.N. Ivanov, R.A. Woode, J.H. Searls, and A.G. Mann, “Low noise 9-GHz sapphire resonator-oscillator with thermoelectric temperature stabilization at 300 Kelvin,” Microwave and Guided Wave Letters, IEEE , vol.5, no.4, pp.108-110, Apr (1995).

[15] E. N. Ivanov, M. E. Tobar, and R. A. Woode, “Ultra-low noise microwave oscillator with advanced phase noise suppression system,” IEEE Microwave Guided Wave Lett., vol. 6, no. 9, pp. 312–314, Sep. (1996).

[16] E.N. Ivanov, and M.E. Tobar, “Low phase-noise sapphire crystal microwave oscillators: current status,” Ultrasonics, Ferroelectrics and Frequency Control, IEEE Transactions on , vol.56, no.2, pp.263-269, February (2009).

[17] R.T. Logan, L. Maleki, and M. Shadaram, “Stabilization of oscillator phase using a fiber-optic delay-line ,” Frequency Control, 1991., Proceedings of the 45th Annual Symposium on , vol., no., pp.508-512, 29-31 May (1991).

[18] R.T. Logan, and L. Maleki, “Ultrastable microwave and millimeter wave photonic oscillators,” Frequency Control Symposium, 1992. 46th., Proceedings of the 1992 IEEE , vol., no., pp.420-424, 27-29 May (1992).

[19] X.S. Yao, and L. Maleki, “High frequency optical subcarrier generator,” Electronics Letters , vol.30, no.18, pp.1525-1526, 1 Sep (1994).

[20] X.S. Yao, and L. Maleki, “Optoelectronic oscillator for photonic systems,” Quantum Electronics, IEEE Journal of , vol.32, no.7, pp.1141-1149, Jul (1996).

[21] X. Yao, and L. Maleki, “Optoelectronic microwave oscillator,” J. Opt. Soc. Am. B 13, 1725-1735 (1996).

[22] L. Maleki, “Sources: The optoelectronic oscillator,” Nature Photonics, Vol. 5, pp.728–730, (2011).

[23] X. Yao, and L. Maleki, “Converting light into spectrally pure microwave oscillation,” Opt. Lett. 21, 483-485 (1996).

[24] T. Musha, J. Kamimura, and M. Nakazawa, “Optical phase fluctuations thermally induced in a single-mode optical fiber,” Appl. Opt. 21, 694-698 (1982).

[25] X. Yao, and L. Maleki, “Multiloop optoelectronic oscillator”, IEEE Journal of Quantum Electronics, vol 36, n° 1, pp. 79-84, January (2000).

[26] T. Banky, B. Horvath, and T. Berceli, “A new approach for ultra-low phase noise millimetre wave optoelectronic oscillators” Microwave Photonics MWP2003, sept. (2003).

[27] D. Eliyahu, and L. Maleki, “Low phase noise and spurious level in multi-loop optoelectronic oscillators”, Proc. of the 2003 IEEE Int. Freq Control Symp., P. 405-410, (2003).

[28] X. Yao, L. Maleki, and D. Eliyahu, “Progress in the optoelectronic oscillator – a ten year anniversary review”, 2004 IEEE Microwave Theory and Tech. Symp. Digest, pp. 287-290, (2004).

[29] O. Okusaga, E. J. Adles, E. C. Levy, W. Zhou, G. M. Carter, C. R. Menyuk, and M. Horowitz, “Spurious mode reduction in dual injection-locked optoelectronic oscillators,” Opt. Express 19, 5839-5854, (2011).

[30] D. Eliyahu, and L. Maleki, "Tunable, ultra-low phase noise YIG based opto-electronic oscillator," Microwave Symposium Digest, 2003 IEEE MTT-S International , vol.3, no., pp. 2185- 2187 vol.3, 8-13 June (2003).

[31] X. Yao and L. Maleki, "Dual microwave and optical oscillator," Opt. Lett. 22, 1867-1869 (1997).

[32] X.S. Yao, L. Davis, and L. Maleki, "Coupled optoelectronic oscillators for generating both RF signal and optical pulses," Lightwave Technology, Journal of , vol.18, no.1, pp.73-78, Jan. (2000).

[33] D. Eliyahu, and L. Maleki, "Modulation response (S21) of the coupled opto-electronic oscillator," Frequency Control Symposium and Exposition, 2005. Proceedings of the 2005 IEEE International , vol., no., pp.850-856, 29-31 Aug. (2005).

[34] A. Matsko, D. Eliyahu, P. Koonath, D. Seidel, and L. Maleki, "Theory of coupled optoelectronic microwave oscillator I: expectation values," J. Opt. Soc. Am. B 26, 1023-1031 (2009).

[35] P.H. Merrer, H. Brahimi, and O. Llopis, "Optical techniques for microwave frequency stabilization: Resonant versus delay line approaches and related modelling problems," Microwave photonics, 2008. jointly held with the 2008 asia-pacific microwave photonics conference. mwp/apmp 2008. international topical meeting on , vol., no., pp.146-149, Sept. 9 2008-Oct. 3 (2008).

[36] R. W. P. Drever, J. L. Hall, F. V. Kowalski, J. Hough, G. M. Ford, A. J. Munley, and H. Ward, "Laser phase and frequency stabilization using an optical resonator," Appl. Phys. B, vol. 31, pp. 97-105, (1983).

[37] Pierre-Henri Merrer, "Élaboration de sources hyperfréquences à haute pureté spectrale à base de résonateurs optiques," Ph.D. thesis (Toulouse III - Paul Sabatier University, Toulouse, France, 2009).

[38] E. Black, "An introduction to Pound-Drever-Hall laser frequency stabilization," Am. J. Phys. 69, 79-87 (2001).

[39] A. A. Savchenkov, V. S. Ilchenko, J. Byrd, W. Liang, D. Eliyahu, A. B. Matsko, D. Seidel, and L. Maleki, "Whispering-gallery mode based opto-electronic oscillators," in Proceedings of IEEE Conference Frequency Control Symposium, (IEEE, 2010), 554-557.

[40] A. B. Matsko and V. S. Ilchenko, "Optical resonators with whispering-gallery modes-part I: basics," IEEE Journal of Selected Topics in Quantum Electronics 12, 3- 14 (2006).

[41] V.S. Ilchenko, and A.B. Matsko, "Optical resonators with whispering-gallery modes-part II: applications," Selected Topics in Quantum Electronics, IEEE Journal of , vol.12, no.1, pp. 15- 32, Jan.-Feb. (2006).

[42] G. C. Righini, Y. Dumeige, P. Féron, M. Ferrari, G. Nunzi Conti, D. Ristic, and S. Soria, "Whispering gallery mode microresonators: Fundamentals and applications," Riv. Nuovo Cimento Soc. Ital. Fis. 34, 435 (2011).

[43] A. A. Savchenkov, A. B. Matsko, V. S. Ilchenko, and L. Maleki, "Optical resonators with ten million finesse," Opt. Express 15, 6768-6773 (2007).

[44] A. A. Savchenkov, V. S. Ilchenko, A. B. Matsko and L. Maleki, "Kilohertz optical resonances in dielectric crystal cavities," Phys. Rev. A 70, 05804, (2004).

[45] V. B. Braginsky, M. L. Gorodetsky, and V. S. Ilchenko, "Quality-factor and nonlinear properties of optical whispering-gallery modes," Physics Letters A 137, 393-397 (1989).

[46] V. S. Ilchenko, X. S. Yao, and L. Maleki, “Pigtailing the high-Q microsphere cavity: a simple fiber coupler for optical whispering-gallery modes,” Opt. Lett. 24, 723-725 (1999).

[47] M. Cai and K. Vahala, “Highly efficient optical power transfer to whispering-gallery modes by use of a symmetrical dual-coupling configuration,” Opt. Lett. 25, 260-262 (2000).

[48] P. Merrer, K. Saleh, O. Llopis, S. Berneschi, F. Cosi, and G. Nunzi Conti, “Characterization technique of optical whispering gallery mode resonators in the microwave frequency domain for optoelectronic oscillators,” Appl. Opt. 51, 4742-4748 (2012).

[49] K. Volyanskiy, P. Salzenstein, H. Tavernier, M. Pogurmirskiy, Y. K. Chembo, and L. Larger, “Compact optoelectronic microwave oscillators using ultra-high Q whispering gallery mode disk-resonators and phase modulation,” Opt. Express 18, 22358–22363 (2010).

[50] K. Volyanskiy, Y.K. Chembo, L. Larger, and E. Rubiola, “Contribution of Laser Frequency and Power Fluctuations to the Microwave Phase Noise of Optoelectronic Oscillators,” Lightwave Technology, Journal of , vol.28, no.18, pp.2730-2735, Sept.15, (2010).

[51] D. Eliyahu, D. Seidel, and L. Maleki, “RF Amplitude and Phase-Noise Reduction of an Optical Link and an Opto-Electronic Oscillator,” Microwave Theory and Techniques, IEEE Transactions on , vol.56, no.2, pp.449-456, Feb. (2008).

[52] E. Salik, N. Yu, and L. Maleki, “An Ultralow Phase Noise Coupled Optoelectronic Oscillator,” Photonics Technology Letters, IEEE , vol.19, no.6, pp.444-446, March15, (2007).

[53] V.S. Ilchenko, J. Byrd, A.A. Savchenkov, A.B. Matsko, D. Seidel, and L. Maleki, “Miniature oscillators based on optical whispering gallery mode resonators,” Frequency Control Symposium, 2008 IEEE International , vol., no., pp.305-308, 19-21 May (2008).

[54] L. Maleki, V.S. Ilchenko, A.A. Savchenkov, W. Liang, D. Seidel, and A.B. Matsko, “High performance, miniature hyper-parametric microwave photonic oscillator,” Frequency Control Symposium (FCS), 2010 IEEE International , vol., no., pp.558-563, 1-4 June (2010).

[55] A. Savchenkov, V. Ilchenko, W. Liang, D. Eliyahu, A. Matsko, D. Seidel, and L. Maleki, “Voltage-controlled photonic oscillator,” Opt. Lett. 35, 1572-1574 (2010).

Chapter II Modeling and characterization of the fiber ring resonator and the optoelectronic oscillator

II.1 Introduction

Among different optical resonators, the ring resonator represents the simplest form. Its architecture was first proposed by E. A. J. Marcatili in 1969 in an integrated double-coupled ring structure [1]. Since then, the ring resonator has been extensively studied and used, especially the ring resonators fabricated using low loss optical fibers and optical directional couplers.

Due to its simplicity and the very high quality factor that could be obtained using it, the fibered ring resonator has been chosen in most of our work as the frequency stability element in our optoelectronic oscillator setup. However, despite its simple architecture, the ring resonator must be studied and modeled when used in an optoelectronic oscillator because in this case it is not only its quality factor that counts. Furthermore, the overall system must be modeled to investigate the different noise contributions, especially those related to the resonator itself, in order to improve the oscillator stability and reduce its phase noise.

In this chapter we first present the different ring resonator architectures and the one we have chosen to be used in the oscillator setup that we have previously presented in chapter one. This resonator has been modeled by different means, mainly using a microwave modeling software, also used to model the overall optoelectronic oscillator system.

II.2 Fiber ring resonator (FRR)

In 1982, Stokes et al. have presented a fibered structure of the ring resonator, fabricated using a cross-coupled single-mode optical fiber [2], (see Fig. II. 1 (a)). The resonator finesse (F) was not very high as it reached only 80, but it has been greatly improved to 500 by using a low loss optical coupler [3]. Still, this cross-coupling ring structure requires a fibered directional coupler whose coupling coefficient (κ) is close to unity. This may result in relatively large losses and asymmetric optical output, which can lead to serious problems [4].

A different and more successful resonator architecture is the direct-coupled ring resonator (see Fig. II. 1 (b)). This architecture has been widely used in different applications: optical filters [5], fiber gyroscopes [6], fiber ring lasers, temperature and pressure sensors etc... The difference is that this resonator is easier to fabricate, it has higher finesse and more symmetrical output than the cross-coupled ring resonator. This structure has been thoroughly studied in [4] and [7].

The add-drop ring resonator architecture is similar to the direct-coupled fiber ring resonator but it has two directional couplers instead of only one, (see Fig. II. 1 (c)). This ring resonator type behaves as a narrow-band filter that adds or drops a frequency band from an incoming signal. This resonator is the one we have used in our optoelectronic oscillator and we call it the fiber ring resonator (FRR) in this manuscript.

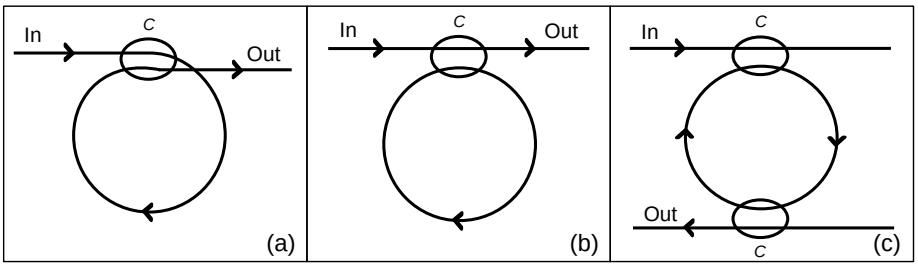

Fig. II. 1. Ring resonator different architectures: (a) cross-coupling, (b) direct coupling and (c) double coupler add-drop ring resonators; c: optical directional coupler

II.2.1 FRR principle and characteristics

The FRR, shown in Fig. II. 2, is made of two low loss fibered 2x2 optical directional couplers (C_1 and C_2), linked with a single-mode polarization-maintaining (P-M) fiber. This resonator is analogous to a microwave travelling-wave resonator, consisting of a resonant ring circuit and a directional coupler [8], [9].

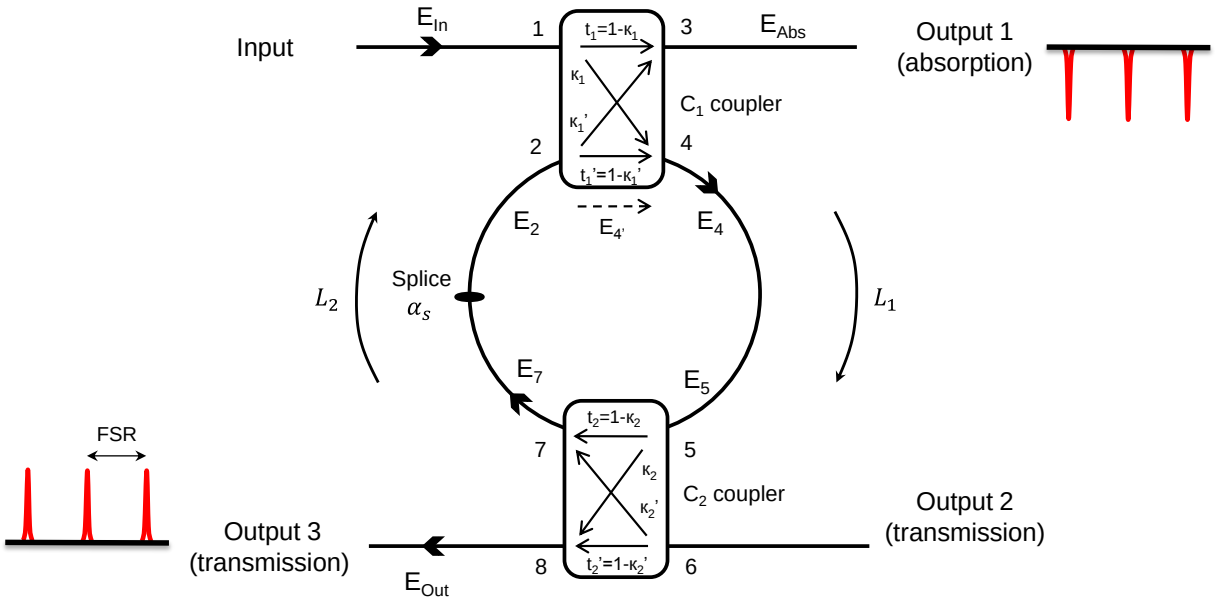

Fig. II. 2. Double directional coupler fiber ring resonator

In this structure, resonance occurs if the total integrated phase shift of the incident light wave (λ_l ~ 1.55 µm) around the resonator ring is an integer multiple of 2π (rad). In this case, the incident light wave constructively interferes with its replica (the circulating wave) coming from the second port of C_1 after a turn inside the resonator. As a result, the circulating light wave build-up to a higher power value than that of the initially injected wave and a transmission line results at the resonator's third output, (see Fig. II. 3 for illustration). Conversely, this interference is destructive at the third port of C_1 and an absorption line results at the resonator's first output.

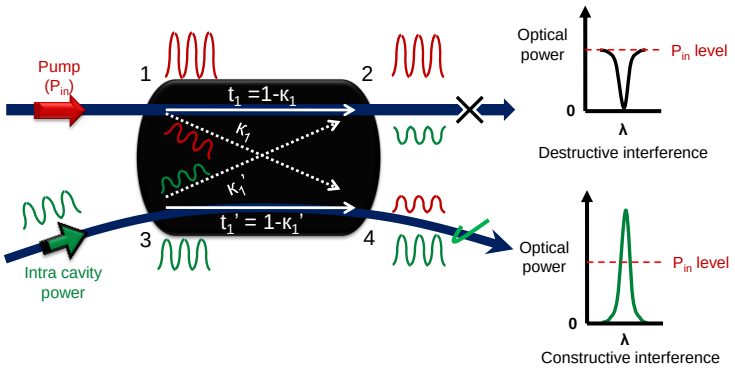

Fig. II. 3. Illustration of the constructive and destructive interferences at the input coupler C_1, when the laser frequency is resonant inside the resonator

As already stated in chapter I, this FRR generates a transverse single frequency comb with microwave spacing, the free spectral range. The FSR of this resonator is directly linked to the fiber length ($L = L_1 + L_2$) and to its refractive index (n) by the relation below:

$$FSR = \frac{c}{n \cdot (L_1 + L_2)} \qquad \textit{(Eq.II. 1)}$$

The resonator finesse F is defined as the ratio of the FSR to the full-width at half-maximum ($FWHM$) of the resonance transmission intensity:

$$F = \frac{FSR}{FWHM} \qquad \textit{(Eq.II. 2)}$$

It is therefore directly linked to the resonator quality factor. This quality factor is usually defined as the ratio of the energy (E) stored in a resonant mode to the energy dissipated (DE) in the same mode during a 2π cycle. Another mathematical definition can be also used. It defines the quality factor as the ratio of the resonant frequency (f_{Res}) to the resonant mode $FWHM$, (see Fig. II. 4). The quality factor is thus given by:

$$Q = 2\pi \cdot \frac{E}{DE} \qquad or \qquad Q = \frac{f_{Res}}{FWHM} \qquad \textit{(Eq.II. 3)}$$

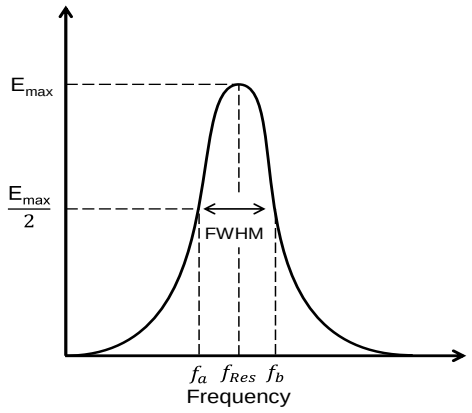

Fig. II. 4. Resonant mode at f_{Res} and its full-width at half maximum

In the FRR, the optical quality factor (Q_{Opt}) depends on the resonator length L, the couplers coupling coefficients (κ_1 for C_1 and κ_2 for C_2) and the resonator intrinsic loss (couplers excess loss γ_1 and γ_2, splices loss α_s and fiber linear loss α_f).

The fiber linear loss is given by:

$$\alpha_f(m^{-1}) = \frac{A_f\ (dB/m)}{4.34} \qquad \textit{(Eq.II. 4)}$$

where A_f is the fiber attenuation in (dB/m); typically, A_f= 0.5 dB/km in a P-M fiber and 0.2 dB/km in SMF.

One of the advantages of this resonator is that the 3dB bandwidth of the optical resonances is maintained when the resonance is used for microwave domain applications, such as the OEO. As we have seen in chapter I, the resonator equivalent microwave quality factor Q_{RF} is linked to Q_{Opt} and it is directly proportional to the microwave application frequency [10]; therefore Q_{RF} increases with the RF application frequency for a fixed optical frequency, which is not the case of microwave resonators.

For this reason, to reach equivalent RF quality factors higher than those obtained in microwave resonators, Q_{Opt} should be higher than 10^9 because of the frequency ratio between f_{RF} and f_{Opt}. This ratio is about 10^{-4} for a laser carrier at 1.55 µm wavelength (~ 193 THz) and a microwave signal around 20 GHz.

Usually, if the coupling coefficients κ_1 and κ_2 are chosen small enough (transmission coefficients t_1 and t_2, t_1 = 1- κ_1 and t_2 = 1- κ_2, are near unity) and if the residual losses of all resonator elements are sufficiently low, a significant circulating intra-cavity power (P_{Cavity}) could result. This could lead, if an optimal coupling is established, to an absorption line with a resulting power equal to null, (see illustration in Fig. II. 3). Accordingly, the optical resonator will possibly feature a high Q_{Opt} factor and photons inside the resonator will encounter an optical delay (τ) as if they were travelling into an equivalent optical delay line in single-pass geometry [10]. This equivalent length is given by:

$$L_{eq} = \frac{Q_{Opt} \cdot c}{n \cdot \pi \cdot f_{Opt}} \qquad \textit{(Eq.II. 5)}$$

The aim of using such a resonator as the frequency stability element, with the highest Q_{Opt} possible in the smallest resonator size and structure, is to reduce the OEO close-to-carrier phase noise. On the other hand, a high Q_{Opt} does not necessarily mean that a lower oscillator phase noise could be always obtained because the resonator transmission loss (IL) plays also an important role in the oscillator stability, as we will see later in chapter III. Furthermore, a high Q_{Opt} may lead to significant circulating power inside the cavity, which in turn reduces the thresholds of many nonlinear optical effects. Unfortunately, these effects were found to be the principal cause of the OEO phase noise degradation as we will see later in chapter IV.

Consequently, in order to optimize the resonator characteristics, while always taking into account their contributions to the oscillator stability, we had to model the resonator separately and then inside a global model of the OEO system.

II.2.2 Modeling of the FRR

To model the FRR separately, we have first used a resonator model that has been developed and implemented in MATLAB during the thesis of P.H. Merrer [11]. This model was based on A. Yariv's modeling studies using coupled-mode theory [12], [13]. This model was able to predict the resonator Q_{Opt}, FSR, and transmission loss, (see Fig. II. 5 for the simulation results of a 20m-long FRR). As well, the study [11] has reported simulation results showing how the FSR decreases and the Q_{Opt} increases when the FRR length increases (see Fig. II. 6).

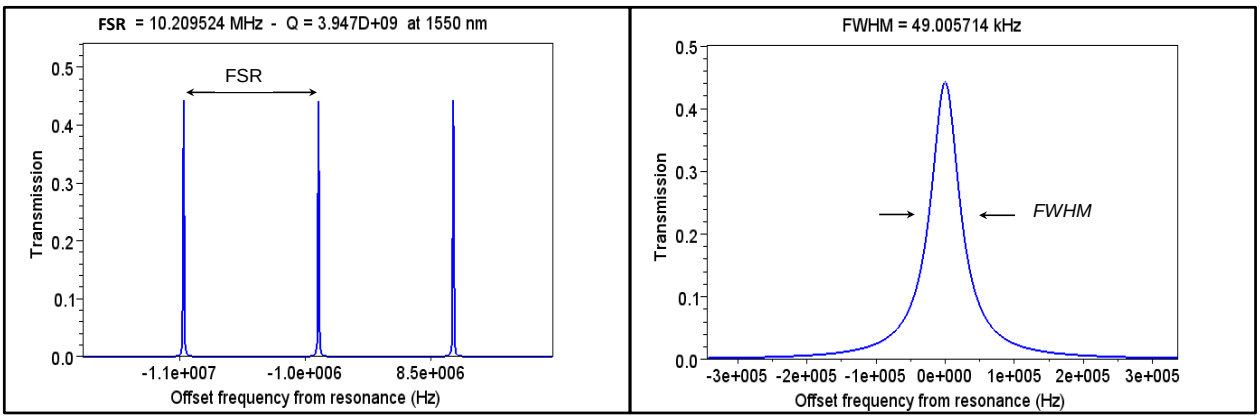

Fig. II. 5. MATLAB simulation results of a 20m-long FRR with the following resonator parameters: $\kappa_1 = \kappa_2 = 1\%$; $\gamma_1 = \gamma_2 = 0.03$ dB; $\alpha_s = 0.01$ dB and $\alpha_f = 0.5$ dB/km

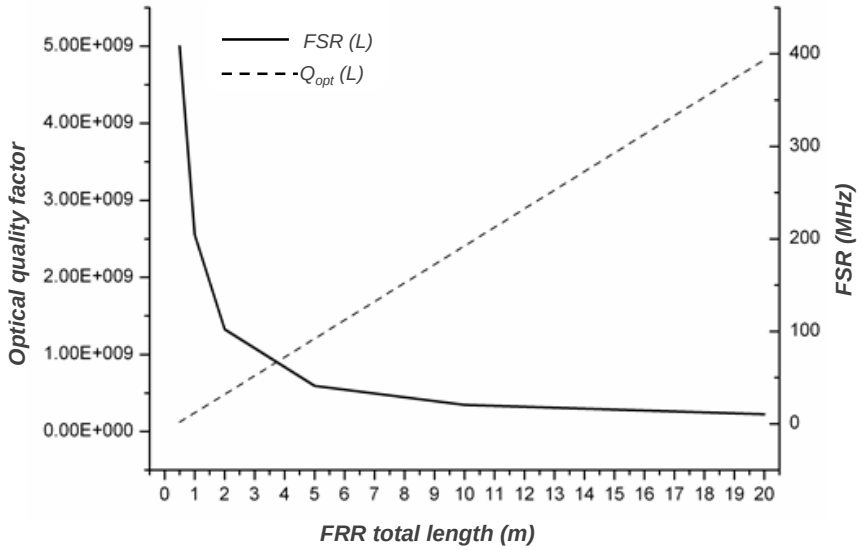

Fig. II. 6. From [11]: MATLAB simulation results for Q_{Opt} and FSR versus the FRR length

Despite the utility of this model, and to get more accurate results about another important characteristic of the FRR, which is the intra-cavity power enhancement factor ($IPEF$), we had to extend F. Zhang et al. [4] study made on a single-coupler direct-coupling ring resonator. As a result, analytical expressions for the different characteristics of our FRR have been developed; especially the resonator $IPEF$ and transmission loss (see Appendix A for the detailed extended analytical study).

These analytical expressions describe the complex electric field (E) behavior inside the resonator (see Fig. II. 2), where couplers C_1 and C_2 are assumed to be reciprocal.

At resonance, the circulating optical wave is in phase with the input light wave and the resonance phase condition is therefore as follows:

$$\beta \cdot L = p\ 2\pi \qquad \textit{(Eq.II. 6)}$$

where β is the optical propagation constant ($\beta = \frac{n \cdot 2\pi}{\lambda}$) and *p* is an integer ($p = 1,2,3 \dots$).

The expression of the intensity ratio at the first output of the FRR (absorption output) is written as:

$$\left|\frac{E_{Abs}}{E_{In}}\right|^2 = (1-\gamma_1)\left[1 - \left(\frac{\frac{\kappa_1 \cdot (1-\kappa_1-A)}{(1-\kappa_1)}}{1+A-2\sqrt{A}\cdot\cos\beta L}\right)\right] \qquad \textit{(Eq.II. 7)}$$

where $A = t_1 \cdot (1-\gamma_1) \cdot t_2 \cdot (1-\gamma_2) \cdot (1-\alpha_s) \cdot e^{-2\alpha_f L}$ for simplicity.

The expression of the circulating intensity ratio inside the FRR:

$$\left|\frac{E_4}{E_{In}}\right|^2 = \frac{\kappa_1 \cdot (1-\gamma_1)}{1+A-2\sqrt{A}\cdot\cos\beta L} = IPEF \qquad \textit{(Eq.II. 8)}$$

The expression of the intensity ratio at the third output of the FRR (transmission output) is written as:

$$\left|\frac{E_{Out}}{E_{In}}\right|^2 = \frac{\kappa_1 \cdot (1-\gamma_1) \cdot \kappa_2 \cdot (1-\gamma_2) \cdot e^{-\alpha_f L_1}}{1+A-2\sqrt{A}\cdot\cos\beta L} \qquad \textit{(Eq.II. 9)}$$

II.2.2.a *FRR simulation using Maple13*

The numerical results of the above three analytical expressions were calculated for a 20m-long FRR using Maple13. This software allows 3D simulations that give us the possibility to easily calculate the resonator's different transfer functions while changing more than one parameter at the same time. We have therefore simulated the 20m-long FRR absorption and transmission transfer functions using respectively *(Eq.II. 7)* and *(Eq.II. 9)*. Moreover, we were able to simulate the $IPEF$ behavior versus different FRR's parameters using *(Eq.II. 8)*, but especially versus the FRR's coupling coefficients. In all the following simulation results presented in this section, when unchanged, the different FRR's parameters were set as follows: (κ_1 = κ_2 = 1%; γ_1 = γ_2 = 0.03 dB; α_s = 0.01 dB and α_f = 0.5dB/km).

II.2.2.a.i *Absorption transfer function*

The 20-m-long FRR absorption transfer function at the first output has been simulated using *(Eq.II. 7)*, while changing the coupling coefficients κ_1 and κ_1, first separately then jointly. The results in Fig. II. 7 show that, when only κ_1 is changed (Fig. II. 7 (a)) and at resonance ($\beta L = p\ 2\pi$; Fig. II. 7 (c)), the power at the FRR first output is null when κ_1 is equal to 1.9 %. This means that this is the optimal (critical) coupling at these conditions (see the previous paragraph for the other parameters' values).

Now if only κ_2 is changed (see Fig. II. 7 (b)), we can see that the weaker κ_2 is, the closer to null the FRR's absorption response is, (see also Fig. II. 7 (d) when *(Eq.II. 6)* is satisfied).

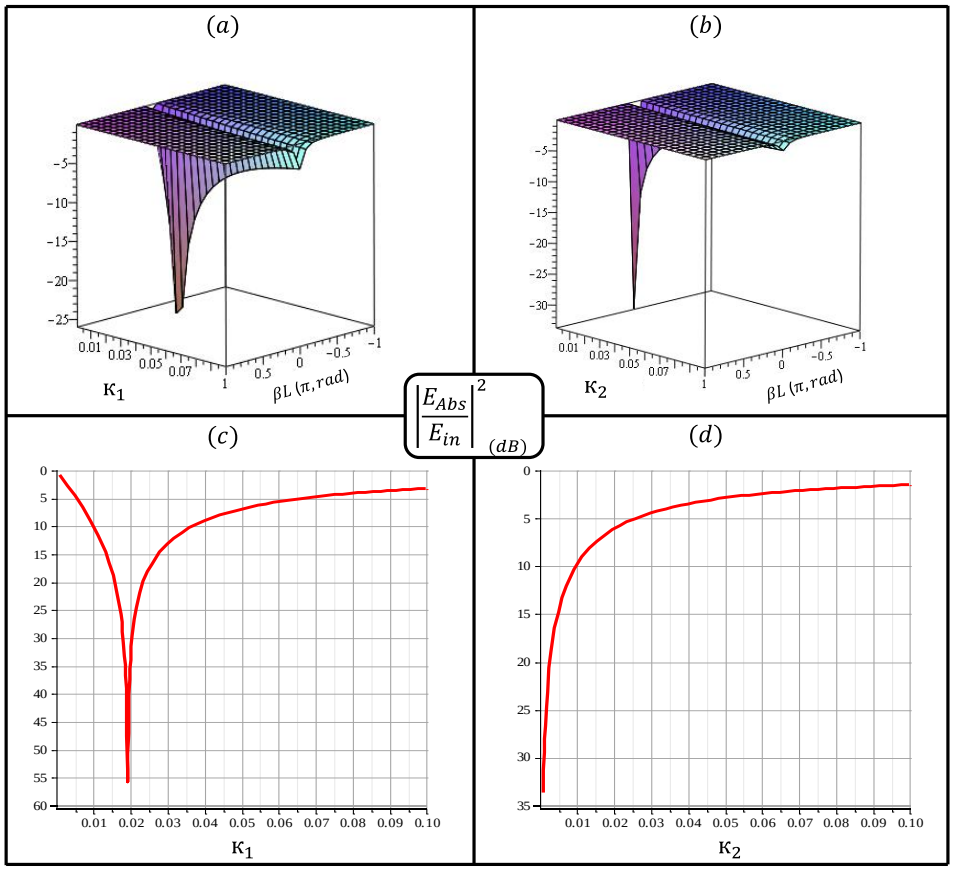

Fig. II. 7. FRR absorption transfer function (in decibels) at the resonator first output, while changing the coupling coefficients κ_1 (a) and κ_2 (b) separately (from 0.1 to 10 %) (and changing βL as well); then by changing κ_1 (c) and κ_2 (d) separately when (Eq.II. 6) is satisfied

Finally, when κ_1 and κ_2 are changed at the same time, while considering *(Eq.II. 6)* satisfied, it seems that κ_2 has to be always a little less than κ_2 to establish an optimal coupling in the FRR regarding the absorption output, (see Fig. II. 8).

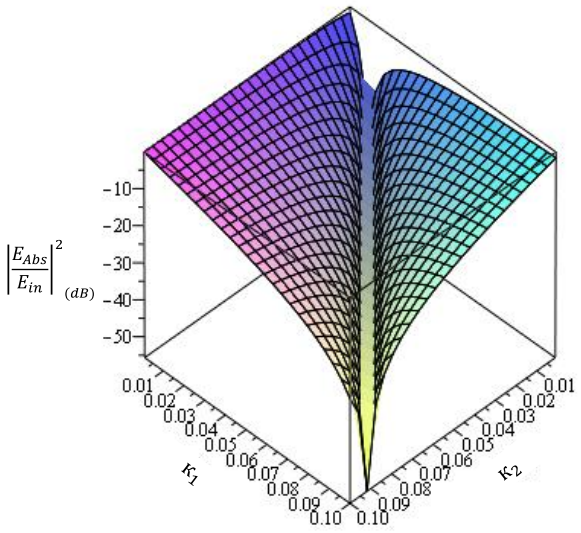

Fig. II. 8. FRR absorption transfer function at the resonator first output, while changing the coupling coefficients κ_1 and κ_2 jointly (from 0.1 to 10 %) and considering that (Eq.II. 6) is satisfied

II.2.2.a.ii *Intra-cavity power enhancement factor*

Similarly, the 20 m-long FRR $IPEF$ has been simulated using *(Eq.II. 8)*. Again, the results depicted in Fig. II. 9 and Fig. II. 10 show that κ_1 has an optimal value equal to 1.9 % when κ_2 is fixed to 1%, and an $IPEF$ around 52 (~17 dB) is obtained. On the other hand, the results in Fig. II. 9 (a) show that the weaker κ_2 is, the higher Q_{Opt} is (the resonance width becomes narrower).

Moreover, Fig. II. 10 shows that the weaker κ_2 is, the higher the $IPEF$ is, and we can see that the $IPEF$ could reach more than 90 when κ_2 is much lower than 1%.

All in all, we can conclude that κ_1 is the key element in finding an optimal coupling, taking both $IPEF$ and Q_{Opt} into consideration. Till here, κ_2 can be considered as an additional loss factor in the FRR (the lower κ_2 is, the better it is for both $IPEF$ and Q_{Opt}).

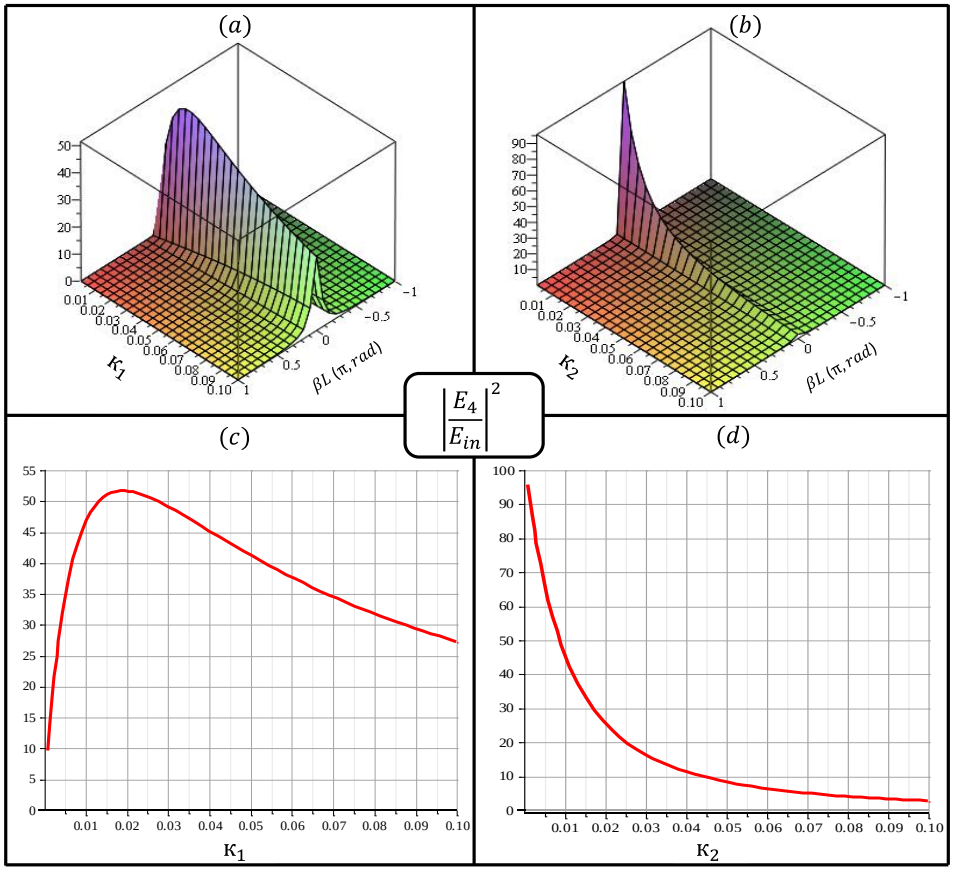

Fig. II. 9. FRR $IPEF$ level, while changing the coupling coefficients κ_1 (a) and κ_2 (b) separately (from 0.1 to 10 %) (and changing βL as well); then by changing κ_1 (c) and κ_2 (d) separately when (Eq.II. 6) is satisfied

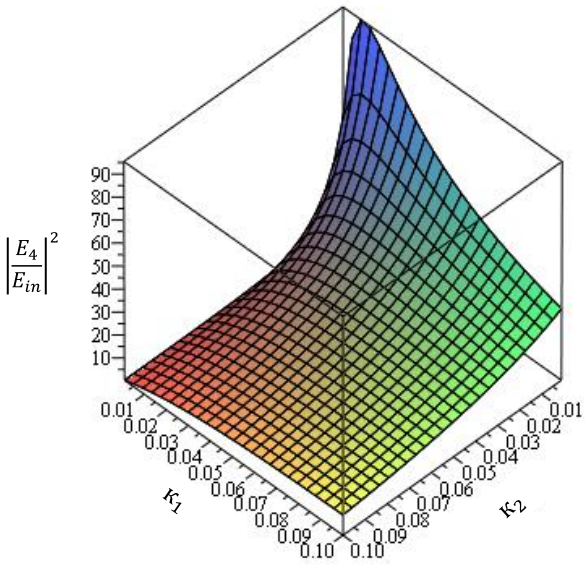

Fig. II. 10. FRR $IPEF$ level, while changing the coupling coefficients κ_1 and κ_2 jointly (from 0.1 to 10 %) and considering that (Eq.II. 6) is satisfied

II.2.2.a.iii *Transmission transfer function*

The 20m-long FRR transmission transfer function at the third output has been simulated using *(Eq.II. 9)*. This is the most important response to scale, especially if the resonator is meant to be used in an OEO setup.

The simulation results in Fig. II. 11 are interesting because they indicate that when κ_1 and κ_2 are changed separately, the optimal transmission response is only obtained when the couplers' coupling coefficients are the same (symmetrical couplers must be used). This is also confirmed in Fig. II. 12 results where both κ_1 and κ_2 were changed at the same time while considering that (Eq.II. 6) is satisfied.

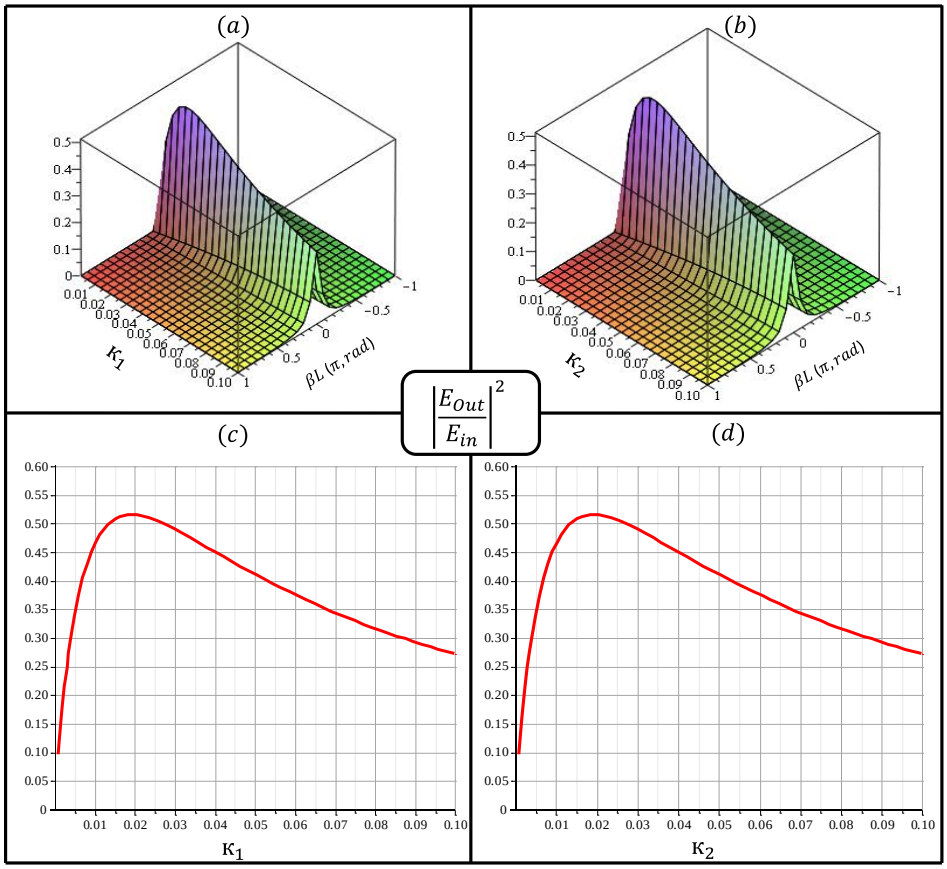

Fig. II. 11. FRR transmission transfer function at the resonator third output, while changing the coupling coefficients κ_1 (a) and κ_2 (b) separately (from 0.1 to 10 %) (and changing βL as well); then by changing κ_1 (c) and κ_2 (d) separately when (Eq.II. 6) is satisfied

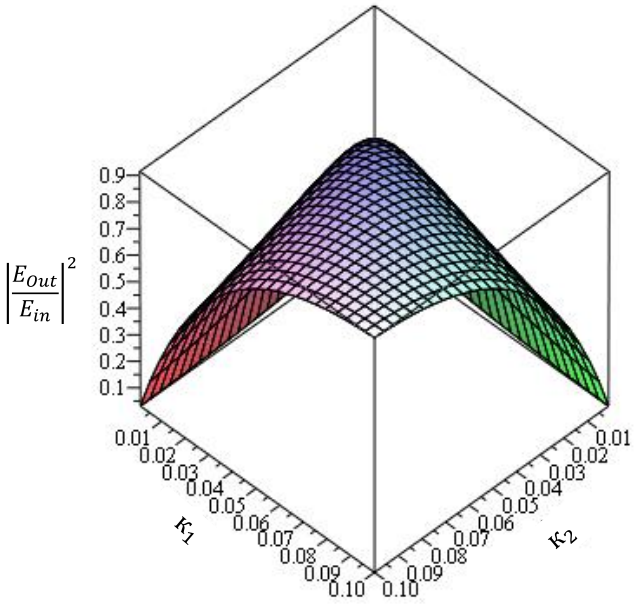

Fig. II. 12. FRR transmission transfer function at the resonator third output, while changing the coupling coefficients κ_1 and κ_2 jointly (from 0.1 to 10 %) and considering that (Eq.II. 6) is satisfied

Finally, all the resonator parameters were fixed and only βL was changed. By doing this we can compute the FRR FSR and the resonance peak's characteristics (IL, $FWHM$, F, Q_{Opt} etc…); (see Fig. II. 13).

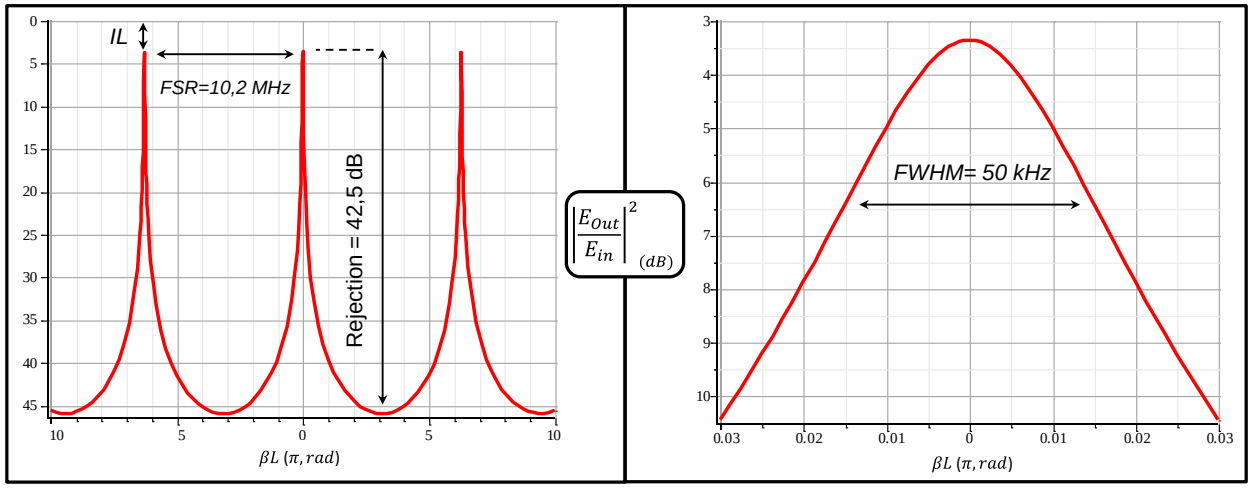

Fig. II. 13. FRR transmission transfer function (in decibels) at the resonator third output while changing βL. The other parameters were fixed as follow: $\kappa_1 = \kappa_2 = 1\%$; $\gamma_1 = \gamma_2 = 0.03$ dB; $\alpha_s = 0.01$ dB and $\alpha_f = 0.5$dB/km

The results presented in Fig. II. 13 were completely in agreement with MATLAB simulation results regarding the resonator characteristics. Furthermore, both models were experimentally validated.

II.2.2.a.iv *Effects of γ_1, γ_2, α_s and α_f on the FRR's transmission response*

In the same perspective, we have simulated the effects of the splices loss (α_s was changed from 0.01 to 0.05 dB), the fiber linear loss (α_f was changed from 0.2 to 0.5 dB/km) and the couplers' loss (both γ_1 and γ_2 were changed from 0.02 to 0.1 dB) on the FRR transmission response. From all the simulation results presented in Fig. II. 14., it seems that couplers excess loss (Fig. II. 14. (c)) is the leading factor after the couplers' coupling coefficients in shaping the FRR resonance.

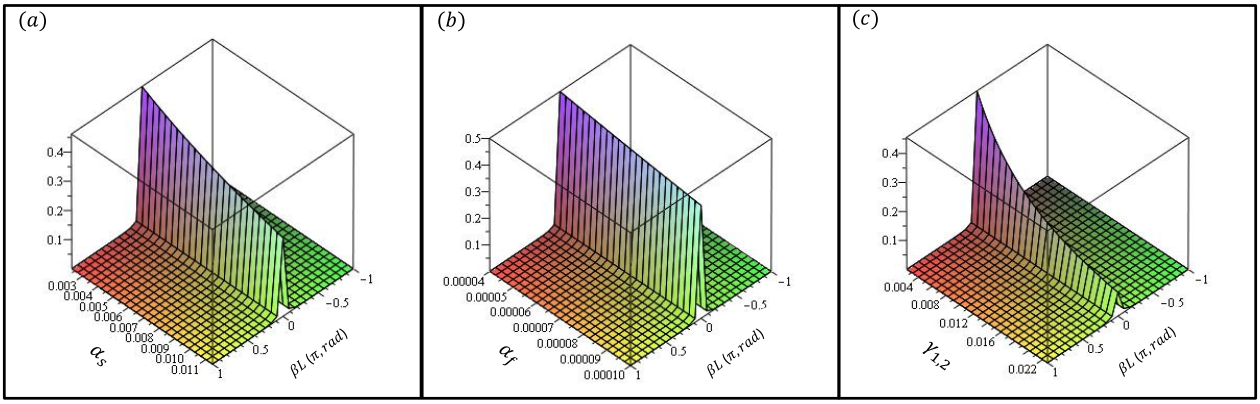

Fig. II. 14. Effects of couplers loss, fiber linear loss and splices loss on the FRR transmission response when: (a) α_s was changed from 0.01 to 0.05 dB; (b): α_f was changed from 0.2 to 0.5 dB/km; (c) both γ_1 and γ_2 were changed from 0.02 to 0.1 dB

All things considered, we can see that unfortunately, having the highest Q_{Opt} and the highest $IPEF$ at the same time will not be possible if the FRR third transmission output is used. Therefore, there is a trade-off to be made regarding the FRR's coupling coefficients: couplers must be symmetrical and their coupling coefficients must guarantee the highest $IPEF$ possible. Besides that, all resonator intrinsic losses have to be the lowest possible in order to improve the resonator characteristics ($IPEF$, IL, $FWHM$, F, Q_{Opt} etc…).

II.3 A CAD approach of the fiber ring resonator based OEO using a microwave software

As we have already mentioned at the end of section II.2.1, to optimize the FRR characteristics while taking into account its contributions to the oscillator stability, we have to model the resonator separately and then inside a global model of OEO system. Thus, the modeling study must be made using the same simulation software.

The OEO system we need to model can be quite complex with electrical and optical parts, and various loops and nonlinear elements. It may be possible to obtain an analytical model of such a system, but there is a little chance that such a model will be able to describe the complex nonlinear noise conversions between the different carriers (the DC, the RF oscillation frequency and the laser carrier ~193 THz). Moreover, the analytical model would be valid only for a given system topology, but we need a system model that will be able to help us in choosing among different OEO topologies. Furthermore, this model is expected to help us in optimizing the oscillator or, at least, to allow us to understand the

different noise sources, their conversion processes and which impact each of these noise sources has on the overall phase noise performance of the OEO.

Consequently, we think that only a computer based approach is able to perform such a work. However, no commercial CAD software is able today to describe this kind of optoelectronic systems. We have thus chosen a software dedicated to model microwave circuits and systems: Agilent™ ADS. The choice of this software has been mainly based on the ability of ADS to compute the noise conversions in nonlinear devices.

In a conventional microwave oscillator, one of the key points of phase noise simulation lies in the ability of computing the interactions between very low frequency fluctuations ($1/f$ noise sources) and a high frequency signal. Time domain approaches cannot be used directly for this purpose because it would require too much simulation data. In the microwave community, this problem has been solved using the harmonic balance approach and various perturbations techniques such as the modulation technique or the conversion matrices technique [14]. The conversion matrices technique allows the computation of correlation between the fluctuations around every frequency involved in the circuit. This is the technique which is implemented in ADS and which we have chosen to use in modeling the noise behavior in the OEO.

Indeed, in the case of optoelectronic systems, we are facing a similar problem. However, in addition to the electronic case, there is one more carrier which must be taken into account in the circuit: the optical carrier at 193 THz. Fig. II. 15 illustrates this problem: the noise lateral sidebands at DC, at the RF main frequency and its harmonics, and at the optical carrier, are correlated through the system nonlinearities.

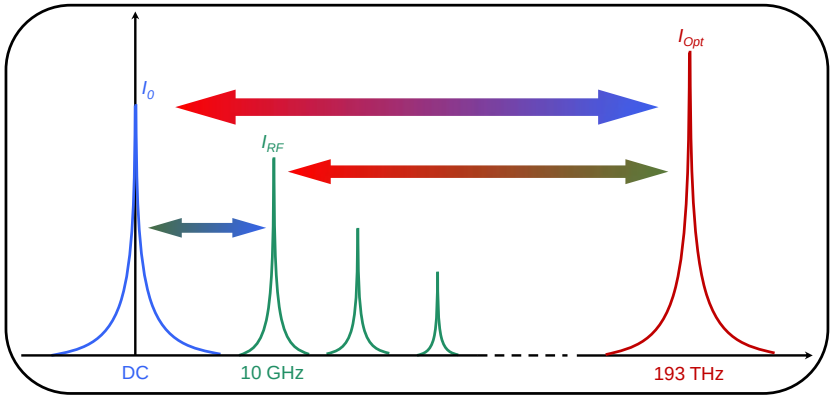

Fig. II. 15. DC, microwave and optical noise sidebands conversions that have to be taken into account in OEO system noise modeling

In our approach, the optical carrier is considered just like an RF carrier, but at an extremely higher frequency. This will not be a problem if ideal elements are used in the circuit model. On the other hand, the main problem using ADS is that this software does not include models of optical components; however, it is possible to create these models using either electrical equivalent circuits or mathematical black boxes, or a mix between these two approaches. That is how we were finally able to create a global

OEO model including the FRR, the laser, the Mach-Zhender modulator, the photodiode, the amplifiers, the RF resonator and many other optical and RF elements.

II.3.1 Modeling of the FRR using ADS

To be able to simulate the global OEO system, the first element we have to add to our microwave-optical models is the optical resonator. For this purpose, we have developed an equivalent model of the FRR using ADS.

II.3.1.a *FRR ADS model*

As already mentioned in section II.2.1, the FRR is made of two low loss fibered 2x2 optical directional couplers, linked with a P-M optical fiber. Consequently, to be able to create a FRR model using ADS, we had to create ADS models describing exactly the real behavior of the optical fiber and the optical couplers operating at the optical frequency f_{Opt}.

II.3.1.a.i *Optical fiber model*

Optical fibers have several characteristics that differ from those of HF transmission lines, especially their very low transmission loss (~ 0.2dB/km in SMF fibers and ~ 0.5 dB/km in P-M fibers compared to ~ 1dB/m in HF transmission cables). Therefore, it was necessary to use a HF transmission line model that ADS offers. In this model, we can define the loss parameters, but also a dielectric constant (k_d) which is equivalent to optical fiber's refractive index n ($k_d = n^2$). The geometric length L of the line and the optical frequency f_{Opt} can be also defined (in all the following simulations using ADS, f_{Opt} is defined to be equal to 200 THz). Finally, the transmission line's ADS model we have created copies almost the real behavior of an optical fiber.

II.3.1.a.ii *Optical coupler model*

At the beginning, we have searched for an ADS coupler model which describes the real behavior of the optical coupler. ADS offers a coupler model that includes two micro strip lines on a substrate. In this model, it has been necessary to fit the substrate parameters and those of the two micro strip lines, including their length (L_m), spacing (S_m) and widths (W_m). This is in order to get a complete impedance match at the input and the output of the coupler, and a valid coupling in a frequency range above 50 GHz around the central operating optical frequency of 200 THz. Furthermore, an option has been added to this coupler model, which is the coupler's excess loss, in order to be able to control this parameter.

To push the simulation capabilities a bit further, we have realized that we must look for a "tunable" optical coupler model, where the coupling coefficient could be changed independently without changing the other parameters of the coupler. For this purpose, we have chosen to use an ADS lossy coupled transmission lines model with the possibility of changing its different parameters. As for the aforementioned coupler, this coupler model has been modified to make it describe the real behavior of the optical coupler. In addition, a coupling coefficient tunability ranging from 0 to 100% has been achieved using this model. The tunability in the coupling coefficient is accomplished by changing the coupler's even-mode effective dielectric constant (K_e) from 1.8051 to 1.801 as depicted in Fig. II. 16. Moreover, the coupler's excess loss is easily controlled by varying the even-mode (A_e) and odd-mode (A_o) coupler's attenuation parameters.

Finally, the optical splices loss α_s has been modeled by adding an ADS attenuator model inside the FRR loop. The FRR model has been finally created (see Fig. II. 17) and the resonator's characteristics can be therefore accurately simulated. These characteristics can be simulated using the scattering-parameters simulation mode that ADS offers, even at 200 THz operating frequency, with a step resolution that can be even less than 1 mHz. As an example, the simulation results of a 20m-long FRR ADS model are presented in Fig. II. 18. These ADS simulation results are perfectly in agreement with MATLAB, Maple13 simulation results, and they are in good agreement as well with our experimental results. This clearly proves the efficiency of our approach using ADS. Moreover, it is a real progress because, already at the resonator level, it is much easier to simulate the FRR behavior using ADS than using a specific model developed using Maple13 or MATLAB (described both in section II.2.2).

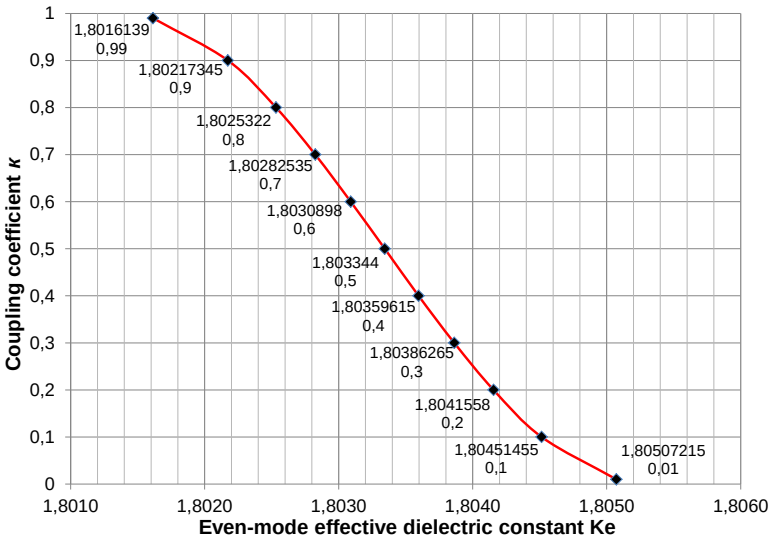

Fig. II. 16. Tunability in the coupling coefficient κ of the optical coupler's ADS model, achieved by changing the coupler's even-mode effective dielectric constant K_e

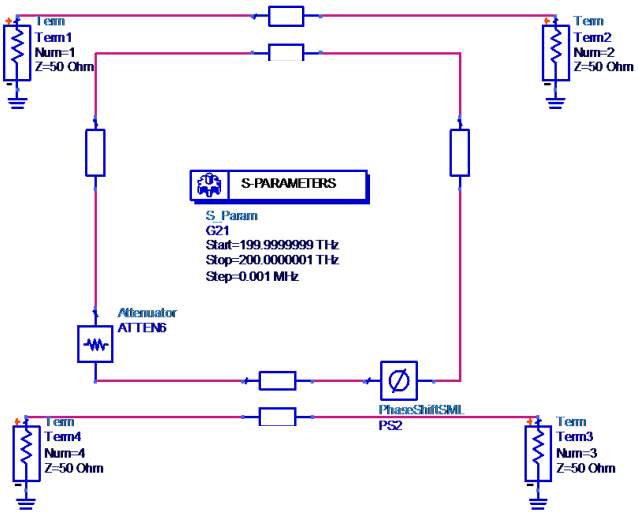

Fig. II. 17. ADS modelof the FRR

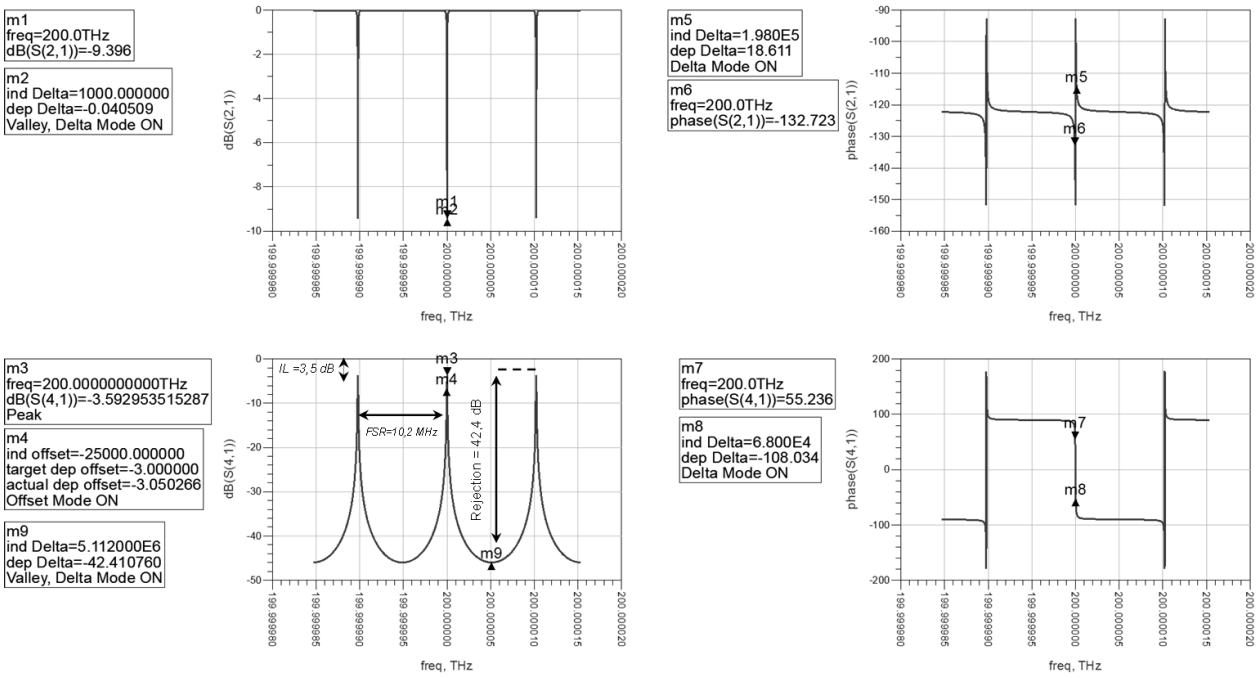

Fig. II. 18. 20m-long FRR ADS model: Scattering-parameters' amplitude and phase simulation results

II.3.1.b *Modeling of compound and complex architectures based on multiple FRRs*

Besides its usefulness in modeling the global OEO behavior, one other important advantage of the FRR ADS model is the ease in simulating very complex schemes based on multiple optical FRRs. These schemes are usually hard to analytically describe and then to simulate using Maple13 or MATLAB or any other calculation software.

In Fig. II. 19 we present an example of an ADS model and the simulation results of a high rejection optical filter based on three compound FRRs with different parameters each and a total length of less than one meter. This model can be created and simulated in a few minutes only, using the basic FRR model described in the section above. Such a structure would need of course much more time to be analytically described, then coded and simulated using a calculation software like Maple13 or MATLAB.

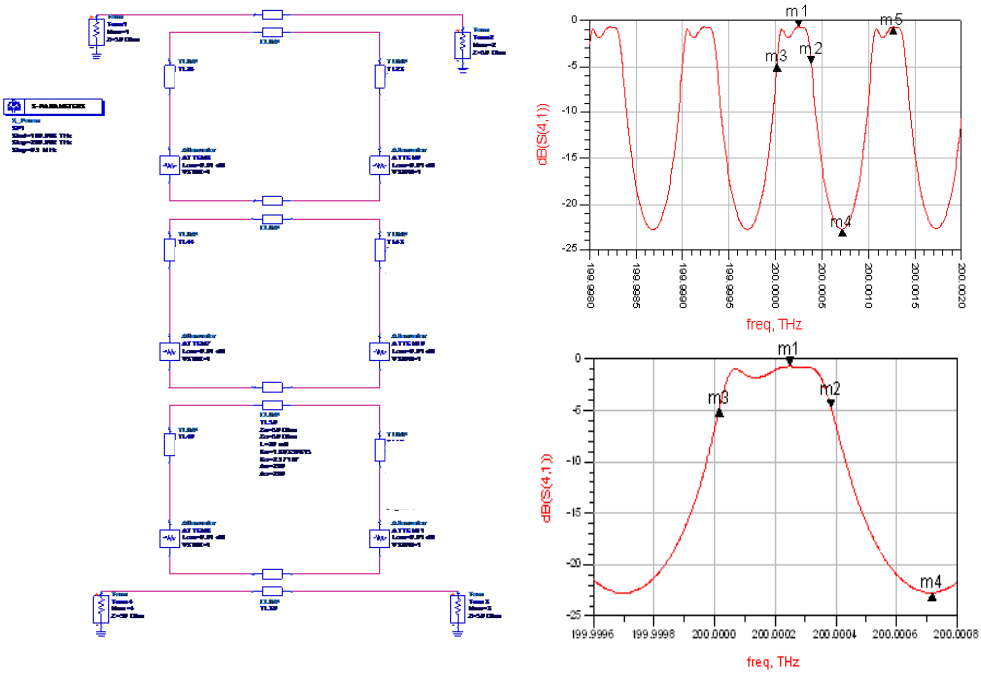

Fig. II. 19. ADS model and S parameters simulation results of a high rejection optical filter based on three compound FRRs with a total length of less than 1 meter

II.3.2 Resonator experimental characterization techniques

Once fabricated, the FRR needs to be experimentally characterized in order to extract its real characteristics, especially its Q_{Opt}, IL, FSR, *rejection*, $IPEF$ etc… This has been done through many characterization techniques: optical domain and microwave domain techniques. Of course, the measurement accuracy differs from one technique to another because of the extremely small resonance bandwidth we are characterizing. As an example, a Q_{Opt} factor in the order of 10^9 at λ_l = 1,55 µm will result in a 3 dB bandwidth in the order of 200 kHz, which is lower than the spectral width of a semiconductor laser. One solution is the use of high spectral purity laser (such as a fiber laser) to scan the optical resonance. Still, when the laser light is injected in the resonator, it heats the resonator (due to the high $IPEF$) and leads to a frequency shift in the optical resonance. Consequently, the laser carrier is shifted far away from the resonance.

Considering these problems, three characterization techniques have been considered and compared one to another in order to investigate the resonator's characteristics. The first one is the optical scan method, which uses the slow tuning of a high spectral purity laser to scan the resonant modes. The second one is the cavity ring down method, a time domain approach which has been set up at FOTON-ENSSAT Lannion (France). The third one is a spectral domain measurement bench based on a microwave network analyzer, which features an extremely high spectral resolution.

II.3.2.a *Optical domain characterization techniques*

II.3.2.a.i *Narrow linewidth laser wavelength scanning method*

This method consists in a frequency fine-tuning of a narrow linewidth (~1 kHz) Koheras fiber laser to explore the FRR optical frequency comb by recording the FRR response on a Photodiode followed by an oscilloscope, (see Fig. II. 20). The Koheras laser is tunable thanks to a thermal control (on a 120 GHz range). In addition, a more accurate piezoelectric control can be also used (on a 2 GHz range). This method allows a good measurement of the FSR. Moreover, thanks to the Koheras laser narrow linewidth, a good estimation of the Q_{Opt} can be obtained by observing precisely one optical resonant mode. Nonetheless, because of the resonator's thermal heat and the resulting resonance frequency shift, it is difficult to be sure of the accuracy in the observed resonance response, even if the laser frequency tuning speed is carefully adjusted. Therefore, more accurate characterization techniques must be explored.

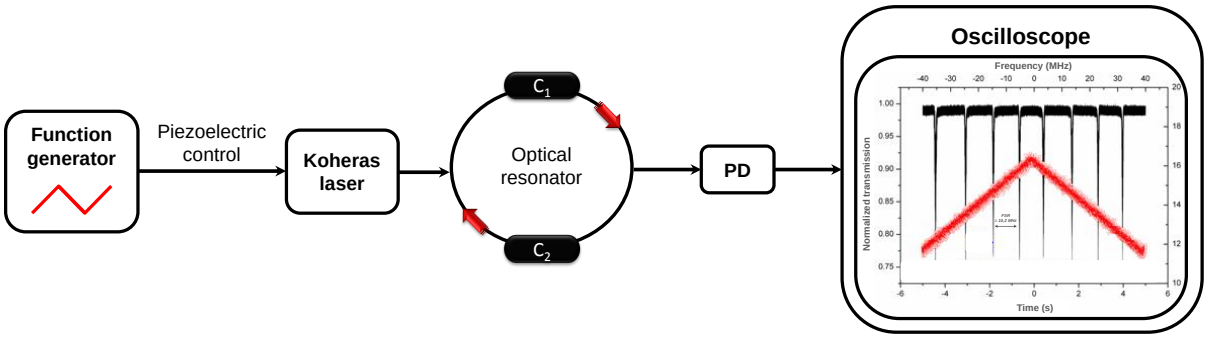

Fig. II. 20. Narrow linewidth laser wavelength scanning method; PD: photodiode

II.3.2.a.ii *Cavity ring down method*

The cavity ring down (CRD) technique avoids the difficulty in comparing between the laser linewidth and the resonant mode because measurements are directly performed in the time domain. The principle is the same as for the laser wavelength scanning method, but the laser frequency is rapidly tuned in this case. Therefore, thermal effects will not have time to appear resulting with less measurement perturbations. The CRD technique consists of measuring the photon lifetime inside the resonant cavity by studying its relaxation regime. This technique has been already modeled and tested by Y. Dumeige et al. in [15]. It has been indicated that through this technique it is possible to determine the different contributions of the resonator parameters to its global optical quality factor Q_{Opt}: the intrinsic factor Q_{Opt_i} which is linked to the internal losses of the cavity and the coupling factor Q_{Opt_c} which is linked to the couplers characteristics. Furthermore, CRD technique provides unambiguously the state of the resonator coupling regime: critical, under-coupled or over-coupled. It also provides the coupling coefficient between the resonators and the access line. Fig. II. 21 shows an example of the result that can be obtained using the CRD technique to characterize a 20m-long FRR. This measurement has been performed at FOTON-ENSSAT Lannion (France).

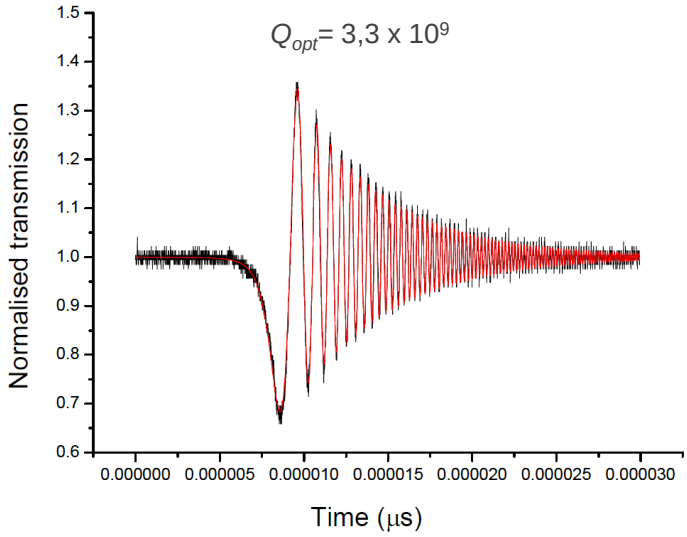

Fig. II. 21. CRD measurement of a 20m-long FRR; (FOTON-ENSSAT, Lannion)

II.3.2.b *Microwave domain characterization technique using a vector network analyzer*

As already stated, the FRR we are studying here is meant to be used in the microwave domain and for microwave applications. It is therefore essential to test the resonator's behavior in a configuration which is as close as possible to the final system. The microwave domain characterization bench we have developed is very similar to the OEO system in open-loop configuration, but it uses a vector network analyzer (VNA) in addition. This bench, depicted in Fig. II. 22 (a), is very efficient to measure the optical properties of an optical resonator with a very high frequency precision. It was used to characterize either WGM resonators or FRRs in our laboratory [16].

To be able to use this characterization bench, the laser has been stabilized onto one of the resonator's resonant frequencies. This has been realized using the Pound-Drever-Hall feedback loop (detailed in section I.3.3.a in chapter I). As soon as the laser is locked to the optical resonance, a sweeping RF signal coming out from the microwave network analyzer drives the MZM and the resulting modulation optical sidebands goes through the optical resonator. Their response is finally recovered on a fast photodiode and then analyzed on the network analyzer input port. This response transcribes accurately the resonator frequency comb and, when focusing on one of the resonant modes, we can obtain the different resonator characteristics, especially its $FWHM$ and thus its Q_{Opt}, with the precision of the microwave network analyzer that can be as good as 0.1 Hz.

Using this technique, any problem in the resonance shape is immediately detected (such as two states of polarization behavior of the optical carrier, leading to two optical modes competition inside the resonator [17]). The only limit in precision will be the ability of locking the laser well onto the center of one of the optical resonances and controlling the MZM linearity by a correct setting of its DC bias voltage ($V_{DC} = V\pi_{/2}$). Fig. II. 22 (b) shows an example of measurements performed on a 20m-long FRR, where we have measured a Q_{Opt} equal to the one obtained using the aforementioned CRD technique.

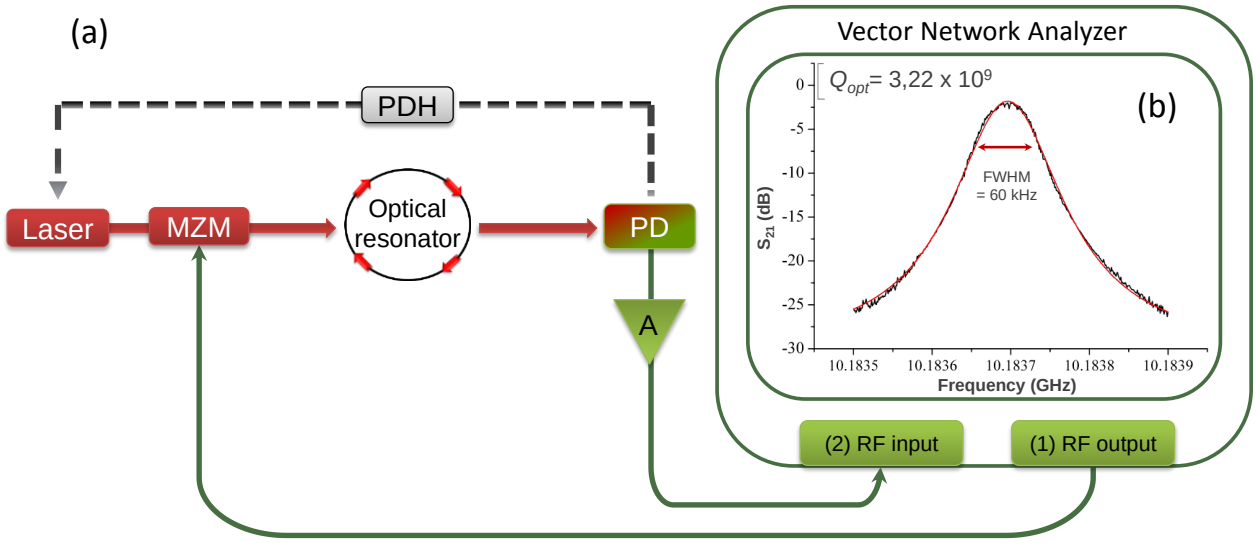

Fig. II. 22. (a) Microwave domain characterization technique using a vector network analyzer and (b) S_{21} measurement of a 20m-long fiber ring resonator

II.3.3 Modeling of the FRR based OEO using ADS

During the thesis of H. Brahimi [18], a first ADS model of an optical link has been created. It included ADS models of a laser source, a MZM and a photodiode. In order to simulate our OEO behavior, especially its phase noise, the FRR ADS model has been included into this optical link model and we have added another element modeling an ideal RF filter and an ideal RF amplifier at the same time (see Fig. II. 23).

Actually, ADS gives access to two noise variables when performing noise simulations in the nonlinear regime: the "pnmx" and the "anmx". "pnmx" means phase noise from mixing analysis, which is based on frequency mixing or on the conversion matrices method described previously. The "anmx" means amplitude noise from mixing analysis. The conversion matrices method (harmonic balance ADS simulations) can describe the noise conversion of $1/f$ noise of the DC spectrum component (see Fig. II. 15). Besides, it can calculate the noise conversions between the different white frequency noise levels around the harmonics of the different spectral components.

Using the OEO ADS model and the harmonic balance simulation technique, we have performed some open-loop simulations (from node A to node B, through the FRR model; Fig. II. 23), and we have then tried to simulate the OEO behavior in a closed-loop configuration. In the following two sections, we describe the different optical and RF components' ADS models that we used in our OEO ADS model.

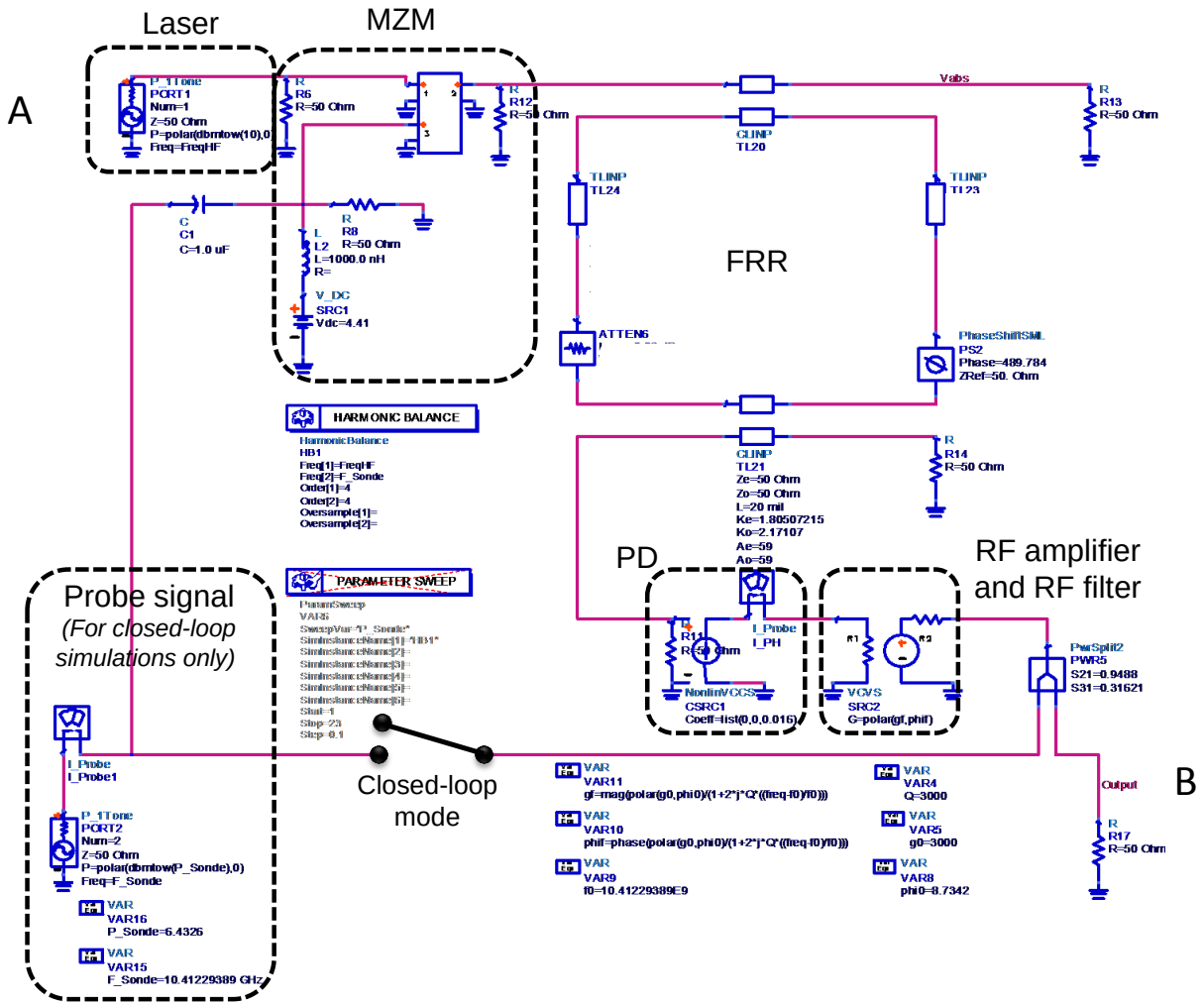

Fig. II. 23. ADS model of the FRR based OEO

II.3.3.a *Optical components modeling*

To create ADS models of the optical components, regarding the fact that the ADS library does not include this type of models, we have created our own models using either electrical equivalent circuits or mathematical black boxes, or a mix between these two approaches.

II.3.3.a.i *Laser model with its amplitude and phase noise*

Actually, the laser noise is known to contribute to different noise conversion phenomena that usually occur in nonlinear systems, especially in the optoelectronic oscillators (as we will also see later in chapter III): these conversions are either AM to AM/PM, or PM to AM/PM noise conversions. Therefore, the laser AM and PM noise characteristics should be taken into account in any noise simulations.

Consequently, the optical carrier was represented in the OEO ADS model by a frequency source with its noise components: AM and PM. The AM noise data were extracted from the laser low frequency relative intensity noise (RIN) measurements which characterize the laser relative power fluctuations and it is given by:

$$RIN = 10\log\left(\frac{\Delta\overline{P^2}_{Opt}}{{P_{Opt}}^2}\right) \qquad dBc/Hz \qquad \textit{(Eq.II. 10)}$$

where P_{Opt} is the laser optical power and $\Delta\overline{P^2}_{Opt}$ is the optical power fluctuations average.

The RIN of the Koheras laser we are using in our OEO setup has been measured at different laser power levels using the method reported in [18] and detailed in [19]. The RIN experimental results are represented in Fig. II. 24. These results show a decrease in the RIN level when the optical power increases. This is a usual behavior of laser's RIN, but the unusual RIN shape observed close to the carrier is likely due to a control circuit inside the Koheras fiber laser system.

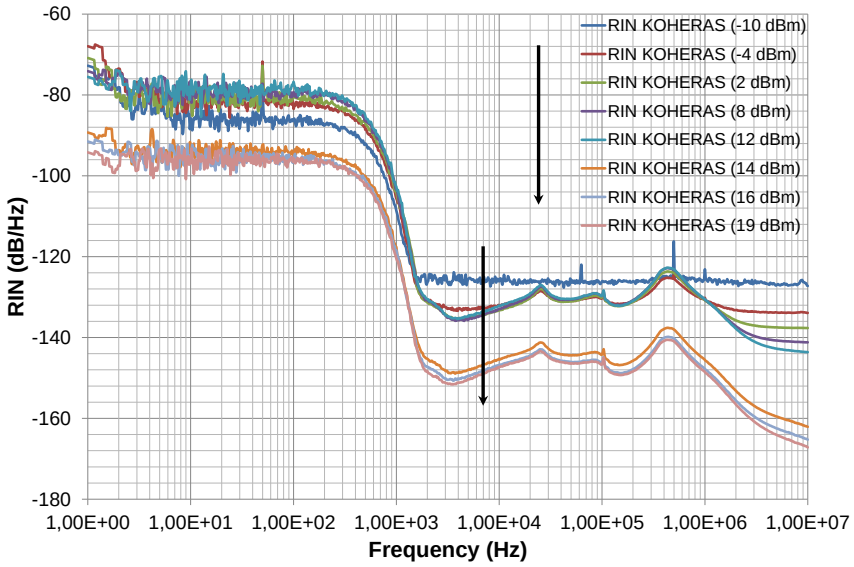

Fig. II. 24. Koheras laser RIN measurements at different power levels using the technique described in [19]. These measurements show a decrease in the RIN level when the optical power level increases which is a usual behavior of laser's RIN. The unusual shape in the close-to-carrier RIN is likely due to a control circuit inside the Koheras fiber laser

The laser FM noise is defined by the frequency noise power spectral density $S_{\nu_l}(f_m)$, expressed in (Hz²/Hz), and the laser PM noise $S_{\emptyset_l}(f_m)$ in (rad²/Hz) can be calculated from its frequency noise by:

$$S_{\emptyset_l}(f_m) = \frac{S_{\nu_l}(f_m)}{{f_m}^2} \qquad rad^2/Hz \qquad \textit{(Eq.II. 11)}$$

Therefore, the single-sideband laser phase noise can be written as follows:

$$L_{\emptyset_l}(f_m) = 10log\left(\frac{S_{\nu_l}(f_m)}{2{f_m}^2}\right) \qquad dBc/Hz \qquad \textit{(Eq.II. 12)}$$

where $f_m$is the offset frequency.

The Koheras laser phase noise has been measured using two different techniques based on a frequency discriminator: the homodyne technique and the self-heterodyne technique. Both techniques are well described in [20]. These techniques have given the same experimental results when measuring the laser PM noise, (see Fig. II. 25).

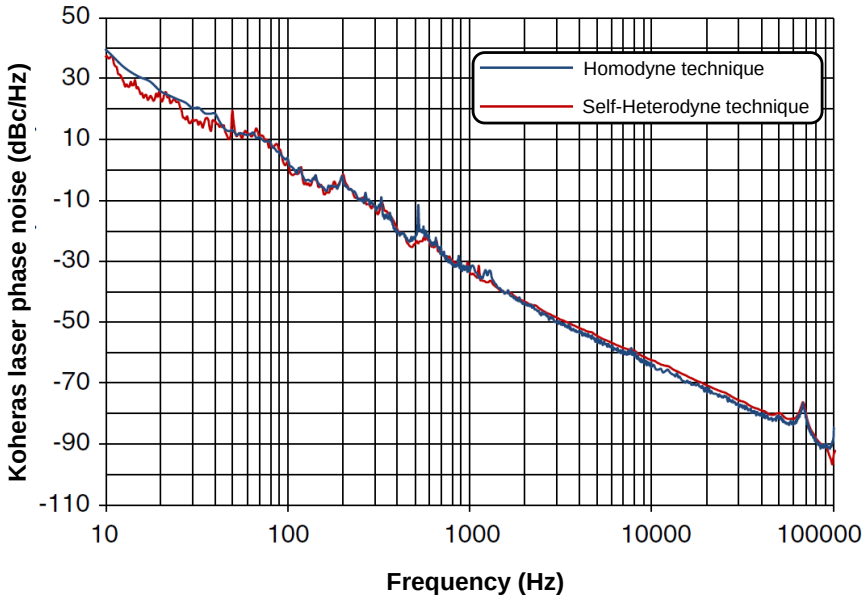

Fig. II. 25. Phase noise measurement of the Koheras laser at 15 dBm optical power, using two techniques: homodyne technique (in blue) and self-heterodyne technique (in red)

Finally, the laser RIN data have been implemented in ADS using a block that consists of a voltage noise source (V_Noise) feeding an amplitude modulator that we added at the laser output. Likewise, the laser phase noise measurement data were directly entered into the laser ADS model. The simulations of laser AM and PM noise components are presented with the laser ADS model in Fig. II. 26.

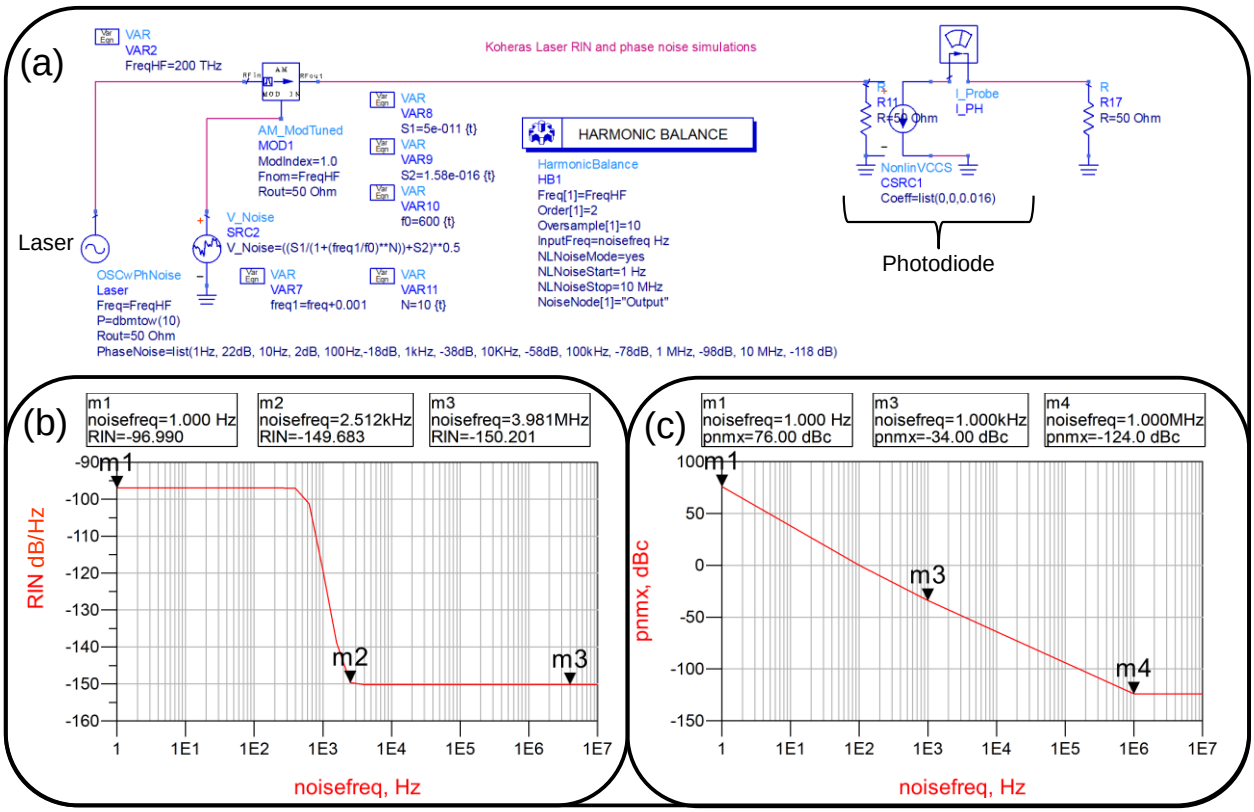

Fig. II. 26. (a) Laser ADS model and the simulations of its (b) AM noise and (c) PM noise.

II.3.3.a.ii *Mach-Zhender modulator model*

The MZM ADS model, detailed in [19], [21] and [22], has been created using a symbolically defined device (SDD), ADS's black box, to include the MZM optical interference equation:

$$P_{Out_{MZM}} = \frac{P_{Opt} \cdot IL_{MZM}}{2}(1 + \cos\varphi_{MZM}(t)) \qquad \textit{(Eq.II. 13)}$$

$P_{Out_{MZM}}$ being the optical power detected by the Photodiode at the MZM output, IL_{MZM} is the MZM insertion loss and $\varphi_{MZM}(t)$ is the phase difference between the waves propagating through the MZM two arms (see Fig. II. 27).

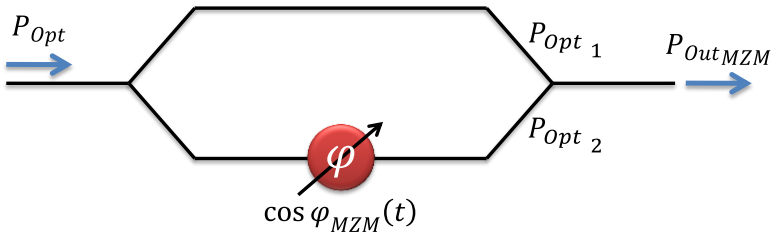

Fig. II. 27. MZM principle

This phase difference is given by:

$$\varphi_{MZM}(t) = \pi \frac{(V_{DC} - V_0) + V_{RF}(t)}{V_\pi - V_0} \qquad \textit{(Eq.II. 14)}$$

where V_{DC} is the MZM DC bias voltage, V_0 is the MZM maximum power voltage, V_π is the MZM extinction voltage and $V_{RF}(t)$ is the RF modulation signal voltage.

Finally, a capacitive network has been added at the MZM RF port to model its response attenuation when the RF modulation frequency increases. The MZM ADS model is presented in Fig. II. 23. The ADS simulation results of the MZM resulting optical spectrum and the transfer function when the MZM is derived with a 10 GHz RF signal, are presented in Fig. II. 28 (a) and Fig. II. 28 (b) respectively. Moreover, the measured transfer function of the EOSPACE MZM we are using in our OEO setup is presented in Fig. II. 28 (c). We can see that the ADS model transcribes exactly this transfer function.

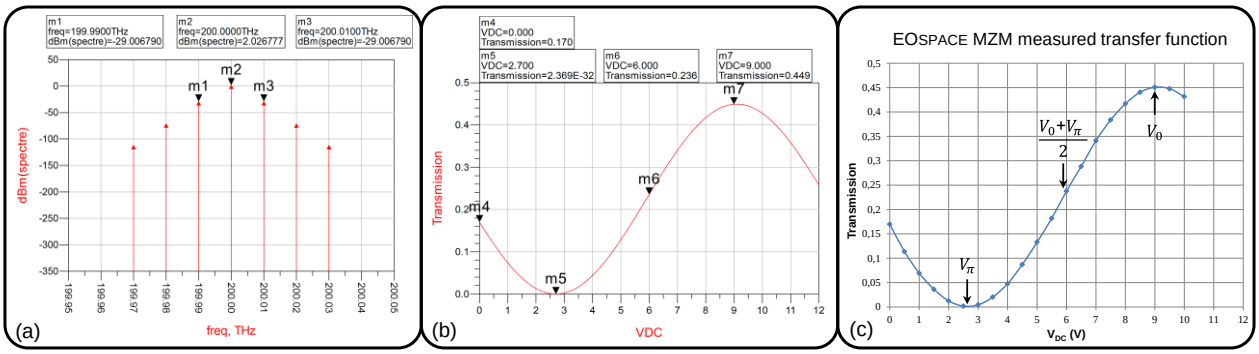

Fig. II. 28. MZM ADS model simulation results: (a) MZM output spectrum when the MZM is derived with a 10 GHz RF signal and (b) MZM transfer function. (c) Measured transfer function of the EOSPACE MZM we are using in our OEO experimental setup.

II.3.3.a.iii *The PDH loop*

During our different simulations, and due to the difficulty in modeling the low frequency PDH loop behavior using ADS, we have chosen to manually stabilize the laser carrier frequency onto the center of one of the optical resonances of the FRR model (or inversely by fixing the laser frequency and then controlling the FRR resonance using a phase shifter inside the FRR model; the resonance tunability will be detailed in chapter V).

II.3.3.a.iv *Photodiode model*

The photodiode is the component that is capable of converting light into electrical current; it performs optical to electrical signal conversion with a given efficiency. The generated current i_{PD} at the photodiode output is proportional to the optical power of the received signal, and not to its amplitude. That is why the photodiode response is called quadratic. This current is given in a function of the received optical power by the following relation:

$$i_{PD} = S_{PD} \cdot P_{Opt} \qquad \textit{(Eq.II. 15)}$$

where S_{PD} is the Photodiode responsivity in A/W.

Using ADS, we have chosen a nonlinear voltage-controlled current source to model the behavior of the Discovery DSC30S photodiode (the photodiode we are using in our OEO experimental setup). The model response is governed, following (Eq.II. 15), by the relation below:

$$i_{PD} = \frac{S_{PD}}{R} \cdot {V_{Out}}_{MZM}^{\,2} \qquad \textit{(Eq.II. 16)}$$

where R is the resistance load at the MZM output (50 ohms in our ADS model) and ${V_{Out}}_{MZM}$ is the MZM output voltage.

Finally, the photodiode was followed by a nonlinear capacitive network to describe its frequency response; however, we have first tried to simulate the OEO noise behavior considering that our photodiode's ADS model is noise-free.

The photodiode's ADS model is presented in Fig. II. 23. Fig. II. 29 (a) and Fig. II. 29 (b) present respectively the RF frequency spectrum and power simulation results of a linear modulation (with a 10 GHz RF modulation frequency) using the ADS models of the laser, the MZM and the photodiode. Moreover, the same ADS optical link model has been used to simulate the different RF output harmonics resulting from a 10 GHz linear modulation (using a slightly modified MZM ADS model to describe another MZM we are using in our laboratory; [23]). These simulation results are presented in Fig. II. 29 (c) with the experimental measurements validating our ADS simulation approach (at least for the open-loop power and frequency simulations part).

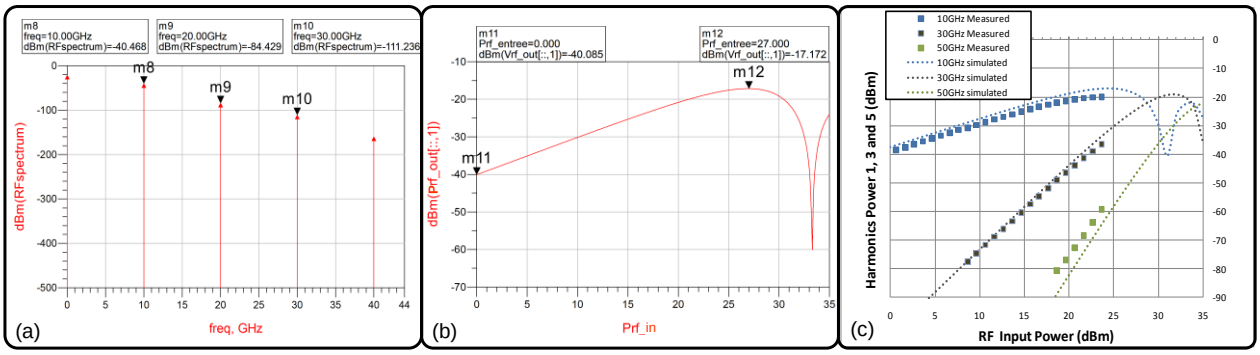

Fig. II. 29. Simulation results of a linear modulation (with a 10 GHz RF modulation frequency) using the ADS models of the laser, the MZM and the Photodiode: (a) RF output spectrum (b) RF output power versus the RF modulation signal's input power. (c) From [23]: Simulation and experimental results of the different RF output harmonics resulting from a 10 GHz linear modulation.

II.3.3.b *Microwave components modeling*

Contrarily to the optical components case, simulating RF components using ADS is much easier because ADS library includes many RF components models. Nevertheless, we have changed some of these models to create our own RF models that we used in the OEO ADS model.

II.3.3.b.i *Modeling the RF filter, the RF phase shifter and the RF amplifier*

Using ADS, we have chosen a voltage-controlled voltage source to describe the response of three RF components at the same time: the filter, the amplifier and the phase shifter, (see Fig. II. 23). In this (ideal and noise-free) model we have modified the complex gain definition to take into account the RF resonator resonant frequency, its Q factor, the amplifier gain and the phase shift of the phase shifter. The oscillator loop has been thus closed by this element which allows the control of the phase, the gain and which also filters the signal with the same Q factor as the dielectric resonator we are using in the real OEO experimental setup ($Q = 2000$).

II.3.3.c *Simulation of the FRR response*

All ADS optical and RF models considered, the response of the 20m-long FRR ADS model has been simulated by sweeping the frequency of the RF signal feeding the MZM modulator. In this way, we are exactly transcribing the microwave characterization bench explained in section II.3.2.b (an ideal ADS RF amplifier model has been added after the Photodiode model to calibrate the power of the open-loop link). The ADS simulation results are presented in Fig. II. 30 and they demonstrate a complete agreement with our experimental results. Furthermore, the simulation results, like the experimental results, show the effect of the photodiode quadratic detection, where the FRR *IL* (IL_{Opt} ~ 3.5 dB) is doubled (in dB) in the RF domain (IL_{RF} ~ 7 dB) (all other FRR characteristics remain unchanged, especially its 3dB bandwidth).

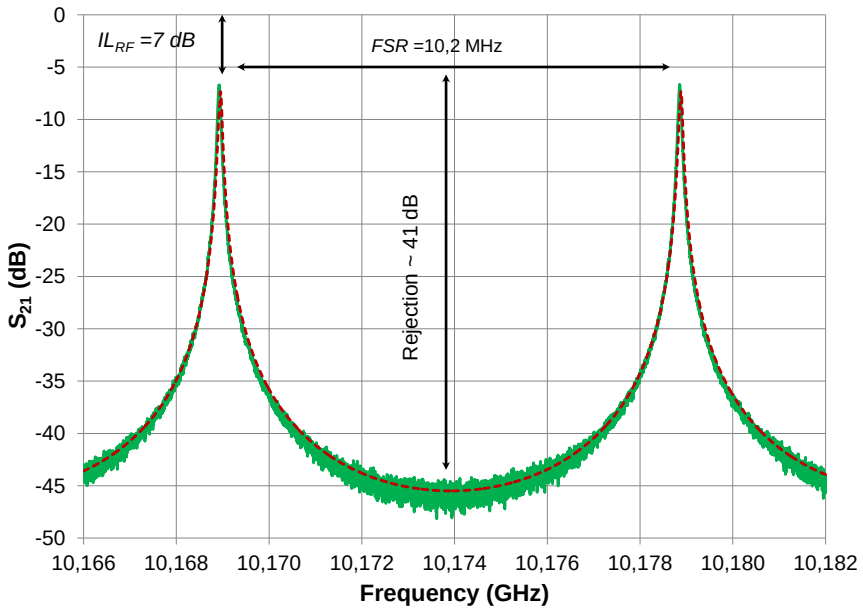

Fig. II. 30. Transmission response of a 20m-long FRR: (in dashed red) simulated using the ADS open-loop model and (in green) measured using the characterization bench described in section II.3.2.b

II.3.3.d *OEO phase noise modeling using ADS*

Following the modeling strategy using Agilent ADS software, we have finally tried to simulate a complete OEO system. This is of course more difficult than in the open-loop case using amplitude modulated optical link.

The difficulty in simulating the OEO in a closed-loop configuration lies in the fact that it is an autonomous system, and that the oscillation frequency must be found prior to any noise analysis. While for open-loop simulations, this frequency is chosen manually by a desired external signal. Therefore, we have first tried to simulate the OEO noise behavior in open-loop configuration, and then we have tried to push our simulations a bit further to be able to describe the OEO closed-loop noise behavior.

II.3.3.d.i *Open-loop phase noise simulations*

The OEO ADS noise simulations have been first performed in an open-loop configuration, using the harmonic balance technique and the "pnmx" noise variable to display the OEO phase noise results. For these simulations, we have used two different laser's PM noise data: real laser PM noise data (from Fig. II. 25) and theoretical laser PM noise data, (see Fig. II. 31).

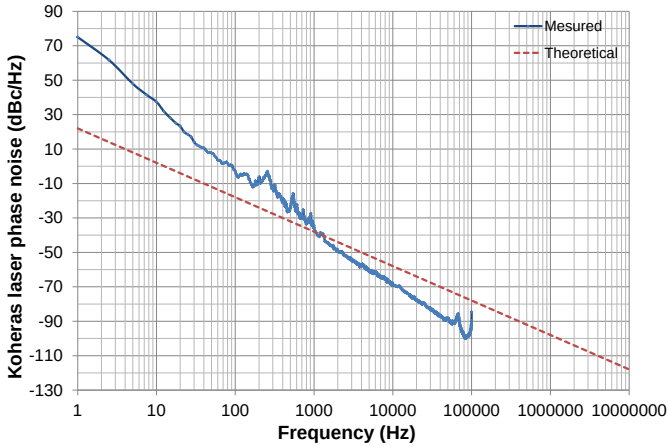

Fig. II. 31. Measured and theoretical phase noise data of the Koheras laser, used to simulate the OEO phase noise

The laser theoretical PM noise data were estimated by considering that the laser spectrum has a lorentzian shape. We therefore used the relation that links its spectral linewidth $\Delta\nu_l$ to its frequency noise power spectral density $S_{\nu_l}(f_m)$ by:

$$S_{\nu_l}(f_m) = \frac{\Delta\nu_l}{\pi} \qquad Hz^2/Hz \qquad \textit{(Eq.II. 17)}$$

Hence, form (Eq.II. 12), the laser PM noise is given by:

$$L_{\phi_l}(f_m) = 10log\left(\frac{\Delta\nu_l}{2\pi {f_m}^2}\right) \qquad dBc/Hz \qquad \textit{(Eq.II. 18)}$$

According to the datasheet, our Koheras laser has approximately a 1 kHz linewidth, therefore $S_{\nu_l}(f_m) = 318.3\ Hz^2/Hz$.

Finally, using both experimental and theoretical laser phase noise data, we have simulated the OEO phase noise in open-loop configuration. The phase noise we have obtained in both cases seems to

have a very high level (Fig. II. 32 (b)), which could not be realistic regarding the high Q_{Opt} of the FRR model we are using (Q_{Opt} = 3.9x10^9 which means a Q_{RF} = 2x10^5 at 10 GHz application frequency). Moreover, the open-loop phase noise results seem to be very dependent on the laser phase noise level, which could be real. However, we cannot rely on these simulations to calculate this dependency factor.

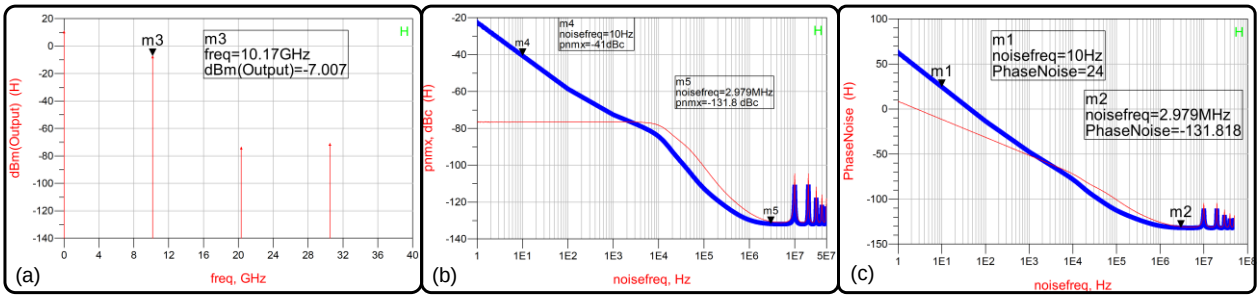

Fig. II. 32. Phase noise simulations using the ADS model of Fig. II. 23, including the 20m-long FRR's model. (a) Oscillation frequency, (b) open-loop OEO phase noise simulations and (c) closed-loop OEO phase noise simulations. Using the laser model with the measured (in thick-blue) or theoretical (in red) laser phase noise data

II.3.3.d.ii *Closed-loop phase noise simulations*

Of course, the OEO phase noise simulations using ADS are so far not realistic, and the whole ADS model needs further improvement regarding the noise simulations.

Despite that, if the open-loop noise simulations problem could be resolved, we can easily obtain the OEO phase noise results in closed-loop configuration. This could be achieved by using Lesson's model, [24] (detailed in chapter I), to convert the simulated open-loop phase noise to a closed-loop phase noise following the relation below:

$$L_{OEO}(fm) = 10\,Log\left(\left(\frac{{f_{Osc}}^2}{8\,{Q_{RF}}^2 {f_m}^2}+1\right)\overline{\Delta\emptyset_{OEO}{}^2}\right) \qquad \textit{(Eq.II. 19)}$$

where $L_{OEO}(fm)$ is the oscillator single sideband phase noise in dBc/Hz, f_{Osc} is the oscillation frequency, and $\overline{\Delta\emptyset_{OEO}{}^2}$ represents the OEO open-loop simulated phase noise in rad²/Hz (represented in Fig. II. 32 (b) in our noise simulation example).

Using *(Eq.II. 19)*, we can convert the simulated open-loop phase noise (Fig. II. 32 (b)) to closed-loop phase noise (Fig. II. 32 (c)). Also, and as for the open-loop noise simulations, the same conclusions apply.

Finally, we have tried to simulate directly the OEO phase noise in closed-loop configuration using ADS. Nevertheless, as already pointed out, the closed-loop OEO simulation is not easy because the oscillating signal has to autonomously start in the loop. For this purpose, ADS uses a specific element called "osc_port" to simulate classical RF oscillators. However, the "osc_port" is useless in our case because there is already a laser frequency at 200 THz in the system, and "osc_port" simulation works only when there is no other frequency in the system.

In fact, if a frequency generator is included in the oscillating circuit model, the harmonic balance simulation will use this frequency as the main generator and calculate the circuit equations at this frequency and at its different harmonics. Therefore, we have tried to create our specific “osc_port” to find the oscillation’s conditions manually.

We have first tried to use the “probe method”. This method has been reported in [25] and it has been used to simulate an analog frequency divider having already a frequency source in the circuit, like the laser source in our OEO case. The method consists of imposing the oscillation frequency to the simulator by adding a second frequency generator in the OEO model, generating a signal at the oscilator’s oscillation frequency. Of course, this generator does not exist in the real OEO circuit (because the oscillation usually takes place due to the noise amplified by the feedback loop). It is thus necessary to insert this generator without disturbing the OEO circuit. To do this, we have placed a probe current in the branch relating this generator to the OEO circuit, (see Fig. II. 23), and the oscillator’s own noise behavior will be obtained when the current supplied by this generator through the probe is null. The research of such a null-current state can be tedious, and it has to be made by adjusting the amplitude and the phase of the frequency generator, in addition to the gain of the OEO loop.

Despite all that, and even when the null-current state has been found in our case, the noise simulations have not revealed any logic conversion of the OEO open-loop phase noise to a closed-loop phase noise.

We have then tried the “infinite loops method”, also reported in [25]. This method consists of describing the closed-loop OEO circuit as a multiple cascaded open-loop OEO circuits. After that we search for the convergence condition where the input power becomes equal to the input power of two successive stages at the end of the chain. Unfortunately, no open-loop to closed-loop clear logic noise behavior has been obtained using this method neither.

II.4 Conclusion

In this chapter we have reported different modeling studies that have been made to simulate the FRR characteristics in function of its different parameters, especially its couplers coupling coefficients. Different analytical expressions have been developed then implemented in different simulation software to serve this purpose. The obtained simulation results have been validated experimentally using optical domain and microwave domain characterization benches, also described in this chapter.

To model the FRR based OEO behavior, and especially its phase noise, we have created a FRR model using a microwave CAD software (ADS from Agilent). This FRR model has been implemented in a global OEO model which has been created using the same software and open-loop power and frequency simulations have been performed and experimentally validated. Still, the phase noise simulations using this OEO ADS model are so far not realistic and noise modeling needs further investigations to make it possible.

However, as we will see later in the following chapters, these modeling studies have been of great interest in optimizing the different FRRs we have designed and fabricated during this thesis, and

also for our investigations on the tunability of the FRR (as we will see in chapter V). Moreover, even if a direct computation of the phase noise still difficult, the OEO ADS model has helped us to understand the different noise conversion phenomenon occurring inside the OEO we have build-up using the FRR, and which will be detailed in the next two chapters.

II.5 References

[1] E. Marcatili, “Bends in optical dielectric guides,” The Bell System Technical Journal, 48, 2103–2132, (1969).

[2] L. Stokes, M. Chodorow, and H. Shaw, “All-single-mode fiber resonator,” Opt. Lett. 7, 288-290 (1982).

[3] M. H. Yu and D. B. Hall, “Low Loss Fiber Ring Resonator,” Proc. Soc. Photo-Opt. Instrum. Eng. 478, 104 (1984).

[4] F. Zhang and J. Lit, “Direct-coupling single-mode fiber ring resonator,” J. Opt. Soc. Am. A 5, 1347-1355 (1988).

[5] P.H. Merrer, O. Llopis, and G. Cibiel, “Laser stabilization on a fiber ring resonator and application of RF filtering,” IEEE Photon. Technol. Lett. 20, 1399–1401, (2008).

[6] D. Ying, H. Ma, and Z. Jin, “Dynamic resonance characteristic analysis of fiber ring resonator,” Optical Fiber Technology, Volume 15, Issue 1, Pages 15-20, January (2009).

[7] J.E. Heebner, V. Wong, A. Schweinsberg, R.W. Boyd, and D.J. Jackson, “Optical transmission characteristics of fiber ring resonators,” Quantum Electronics, IEEE Journal of , vol.40, no.6, pp. 726-730, June (2004).

[8] H. Golde, “Theory and Measurement of Q in Resonant Ring Circuits,” Microwave Theory and Techniques, IRE Transactions on , vol.8, no.5, pp.560-564, (1960).

[9] J.E. Page, J. Esteban, and C. Camacho-Penalosa, “Microwave circuit theory-based models for predicting the resonant frequencies of a class of ring resonators,” Electrotechnical Conference, 2006. MELECON 2006. IEEE Mediterranean , vol., no., pp.272-275, 16-19 (2006).

[10] P.H. Merrer, H. Brahimi, and O. Llopis, “Optical techniques for microwave frequency stabilization: Resonant versus delay line approaches and related modelling problems,” Microwave photonics, 2008. jointly held with the 2008 asia-pacific microwave photonics conference. mwp/apmp 2008. international topical meeting on , vol., no., pp.146-149, Sept. 9 2008-Oct. 3 (2008).

[11] Pierre-Henri Merrer, “Élaboration de sources hyperfréquences à haute pureté spectrale à base de résonateurs optiques,” Ph.D. thesis (Toulouse III - Paul Sabatier University, Toulouse, France, 2009).

[12] A. Yariv, “Critical coupling and its control in optical waveguide-ring resonator systems,” Photonics Technology Letters, IEEE , vol.14, no.4, pp.483-485, April (2002).

[13] A. Yariv, “Universal relations for coupling of optical power between microresonators and dielectric waveguides,” Electronics Letters , vol.36, no.4, pp.321-322, 17 Feb (2000).

[14] V. Rizzoli et al., “General noise analysis of nonlinear microwave circuits by the piecewise harmonic-balance technique,” IEEE trans. on MTT, 42(5), pp. 807-19, (1994).

[15] Y. Dumeige, S. Trebaol, L. Ghisa, T.K.N. Nguyen, H. Tavernier, and P. Feron, “Determination of coupling regime of high-Q resonators and optical gain of highly selective amplifiers,” Journal of the Optical Society of America B 25(12), pp. 2073–2080, (2008).

[16] P. Merrer, K. Saleh, O. Llopis, S. Berneschi, F. Cosi, and G. Nunzi Conti, “Characterization technique of optical whispering gallery mode resonators in the microwave frequency domain for optoelectronic oscillators,” Appl. Opt. 51, 4742-4748, (2012).

[17] P.H. Merrer, O. Llopis, and G. Cibiel, “Laser Stabilization on a Fiber Ring Resonator and Application to RF Filtering,” Photonics Technology Letters, IEEE , vol.20, no.16, pp.1399-1401, Aug.15, (2008).

[18] Houda Brahimi, “Étude en bruit de systèmes optiques hyperfréquences. Modélisation, caractérisation et application à la métrologie en bruit de phase et à la generation de fréquence,” Ph.D. thesis (Toulouse III - Paul Sabatier University, Toulouse, France, 2010).

[19] H. Brahimi, P. Lacroix and O. Llopis, “Mesure du bruit relatif d’intensité (RIN) de composants laser,” LAAS report N° 07606, 37p., October (2007).

[20] O. Llopis, P. Merrer, H. Brahimi, K. Saleh, and P. Lacroix, “Phase noise measurement of a narrow linewidth CW laser using delay line approaches,” Opt. Lett. 36, 2713-2715, (2011).

[21] H. Brahimi, P.H. Merrer, and O. Llopis, “CAD of microwave optical systems for time & frequency applications” Proc. of the European Frequency and Time and Forum (EFTF), Toulouse, April (2008).

[22] H. Brahimi, H. L. Martinez-Reyes, P. H. Merrer, A. Bouchier, and O. Llopis, “A CAD approach of microwave optical systems including noise performance,” Microwave Conference, 2009. EuMC 2009. European , vol., no., pp.1642-1645, (2009).

[23] O. Llopis , P. Martinet, P. H. Merrer, and K. Saleh, “50–60 GHz local oscillator transmission over fiber using optical frequency multiplication,” Microw. Opt. Technol. Lett., vol. 54, issu 5, pp. 1313–1316, May (2012).

[24] D.B. Leeson, “A simple model of feedback oscillator noise spectrum,” Proceedings of the IEEE, vol.54, no.2, pp. 329- 330, Feb. (1966).

[25] S. Desgrez, “Conception de diviseurs de fréquence analogiques réalisés en technologie monolithique à base de transistors pseudomorphiques à haute mobilité électronique,” Ph.D. thesis (Toulouse III - Paul Sabatier University, Toulouse, France, 1997).

Chapter III Optoelectronic oscillator based on fiber ring resonator: optimization studies

III.1 Introduction

Optical resonators allow the achievement of really high quality factors in the microwave frequency range while ensuring low dimensions. Fiber ring resonators are easy to integrate and to use as the stability element in an optoelectronic oscillator (OEO) setup. Nevertheless, the OEO is a complex system in which the resonator Q_{Opt} factor is not the only parameter to optimize in order to get a good phase noise performance. Furthermore, the OEO setup may involve many noise conversion processes that have to be evaluated and understood.

In this chapter, we present a FRR optimization study based on the evaluation of the white frequency noise contribution to the OEO phase noise, which is directly linked to the noise to carrier ratio and to the resonator quality factor. Through this study, an optimized 20m-long FRR has been fabricated and used in an OEO setup, and a low OEO phase noise has been measured.

Moreover, the different noise conversion processes that are likely to occur inside the FRR based OEO have been studied, especially the laser noise conversion into RF amplitude and phase noise through the optical fiber chromatic dispersion, through the FRR itself (via the PDH stabilization loop) and finally through the photodiode nonlinearity.

III.2 OEO first realization based on a 10m-long polarization maintaining FRR

III.2.1 The 10m-long FRR architecture

The first FRR we have used in our study was considered as a test-resonator and its structure was not fully optimized. It was a 10m-long FRR fabricated using two optical couplers with coupling coefficients κ_1 and κ_2 close to 10 % and a P-M optical fiber to join between them. P-M Fibers were used in order to prevent two polarization states behavior of the optical carrier inside the resonator [1].

III.2.2 The 10m-long FRR experimental characteristics

The 10m-long FRR has been characterized using the microwave domain measurement bench described in chapter II. We have measured a 20 MHz FSR, a 1 MHz $FWHM$ and thus a Q_{Opt} of 2x10^8 at 1.55 µm optical carrier (see Fig.III. 1).

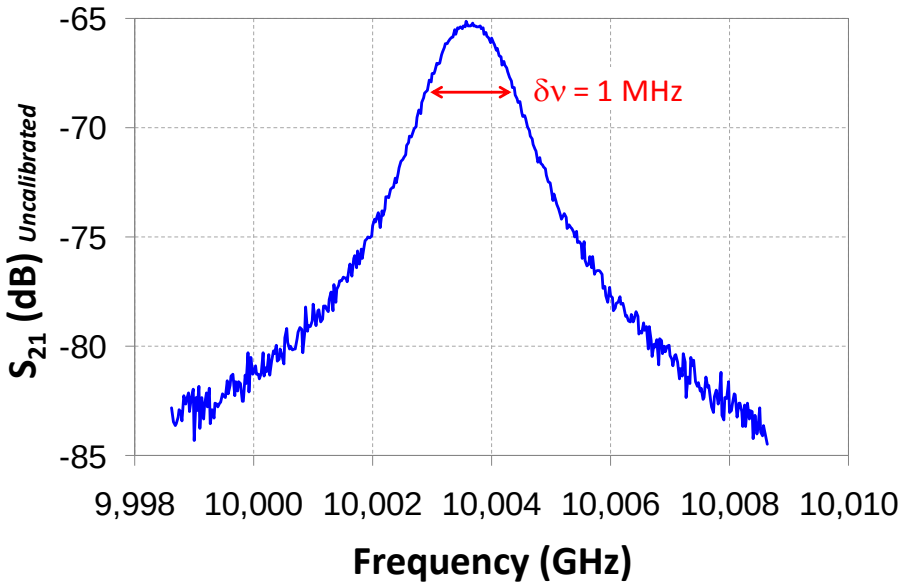

Fig.III. 1 S_{21} amplitude response of the 10m-long FRR characterized using the microwave domain technique described in chapter II

III.2.3 The 10m-long FRR based OEO experimental phase noise results

The 10m-long FRR has been included in the OEO setup, which has been fully described in chapter I. The OEO phase noise spectrum, shown in Fig.III. 2, has been measured using the Agilent E5052B signal source analyzer (SSA). In this spectrum, we can distinguish the three classical phase noise spectrum parts: the $1/f$ frequency noise (or flicker noise) part that occupies the 10 Hz to 1 kHz offset frequency band (characterized by a noise slope of -30 dB/dec), the white frequency noise (WFN) part that occupies the noise spectrum between 1 and 400 kHz offset frequencies (characterized by its -20 dB/dec noise slope) and finally the phase noise floor that appears after 400 kHz offset frequency, with a -120 dBc/Hz noise level. The decrease in the noise level above 3 MHz offset frequency is linked to the filtering effect of the dielectric resonator used in the OEO setup to prevent oscillation mode-hopping. The noise peaks between 0.1 and 1 kHz offset frequencies are most likely due to thermal or mechanical fluctuations in the OEO different optical and RF components, especially in the FRR.

Finally, the knee frequency f_c between the WFN and the noise floor was at 400 kHz, which means a loaded microwave quality factor Q_{RF} of 1.2x10^4 at 10 GHz oscillation frequency, according to [2]. This Q_{RF} value lands in a good agreement with the optical quality factor that we have already measured for the 10m-long FRR.

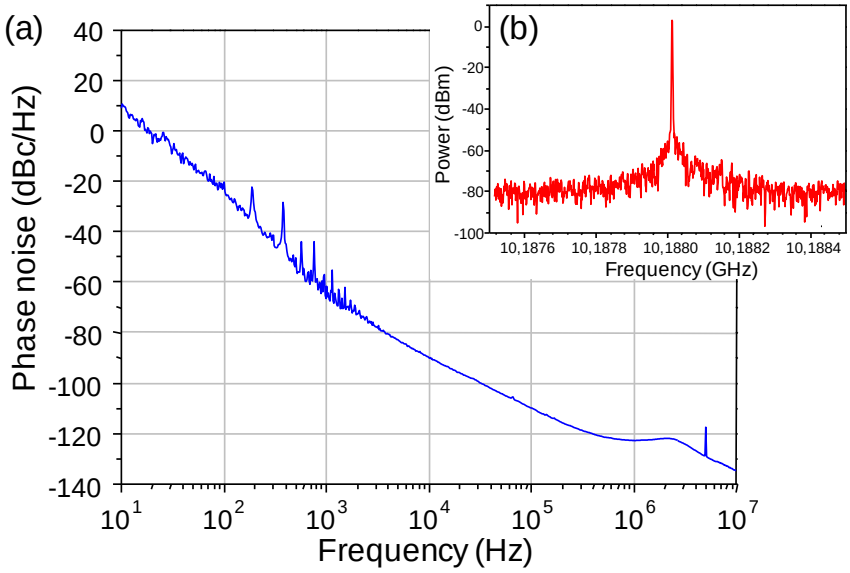

Fig.III. 2 (a) Phase noise spectrum and (b) oscillating frequency spectrum of the 10m-long FRR based 10 GHz OEO

III.2.4 Results discussions

In spite of the relatively good loaded quality factor of the FRR, the OEO phase noise level was very high. This is due to the fact that the resonator's noise to carrier ratio (NCR) has not been optimized and the FRR transmission loss was significant: the coupling ratios were very high and also the couplers' excess loss. As a result, the oscillator phase noise is degraded, especially the WFN part.

Besides, the noise induced by the optical and electrical amplifiers can have an impact on the *1/f* noise part of the OEO phase noise. We have therefore measured their residual phase noise and then introduced the measurements data into a simplified model following Leeson's approach [2]. This model calculates the noise conversion from an open-loop configuration into a closed-loop configuration, while taking into account the resonator's loaded quality factor Q_{RF} as already explained in chapter I. The calculation results are shown in Fig.III. 3 and compared to the OEO measured phase noise. We can clearly see that the amplifiers' noise contribution is about 15 to 30 dB lower than the measured OEO phase noise, and it is therefore not high enough to influence the oscillator phase noise.

In addition to what we have mentioned above, the excess phase noise may be caused by the laser amplitude (AM) and frequency (FM) noise folded onto the OEO oscillation frequency (f_{Osc}) through the oscillator's nonlinearity, or even through other complex phenomena (as we will see later in section III.4).

The WFN contribution to the OEO phase noise can be easily calculated as it is directly related to the NCR. Therefore, a theoretical study has been performed on this noise contribution in order to optimize the FRR, its Q_{Opt} and the NCR, and therefore to reduce the OEO phase noise.

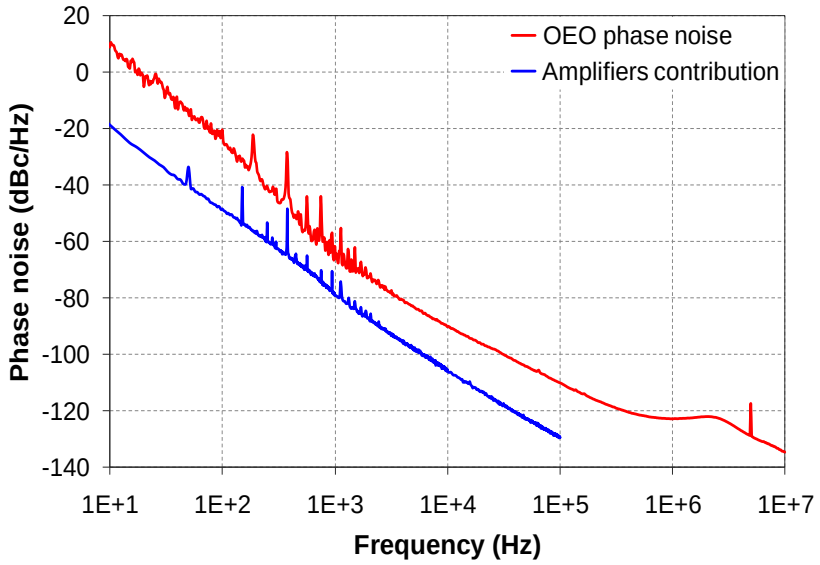

Fig.III. 3.Contribution of the amplifiers noise to the OEO phase noise and comparison with the measured OEO phase noise spectrum at 10 GHz

III.3 OEO optimization study

Our optimization study has been made in two steps: first we have modeled the resonator (using the FRR Matlab model described in chapter I and in [3]; *the other resonator Models using Maple13 and ADS have not been created yet at the time we have made this study*), then we have calculated the influence of the resonator's parameters on its Q_{Opt}, the NCR and finally on the oscillator phase noise at a given offset frequency.

III.3.1 White frequency noise modeling following Leeson's approach

In [4], J. Everard reports on the presence of a resonator's optimal coupling in microwave resonator based oscillators, for which a low oscillator phase noise could be obtained. This approach is only valid for the additive white noise, but as the white frequency noise was the main contribution to the OEO phase noise above 1 kHz offset frequency, it was interesting to use Everard's approach for the OEO case. We have therefore extended this concept to our FRR based OEO in order to optimize the WFN contribution to the OEO phase noise.

Following Leeson's approach [2], we have computed the WFN contribution inside the OEO loop bandwidth; this noise contribution depends on the offset frequency (f_m), the FRR's Q_{Opt} and the in-loop NCR as shown in the relation below:

$$WFN(f_m) = 20.\log\left(\frac{f_{Opt}}{2.\sqrt{2}.Q_{Opt}.f_m}\right) + 10.\log(NCR) \qquad dBc/Hz \qquad \textit{(Eq.III. 1)}$$

The in-loop NCR depends on the measured optical power (P_m) at the resonator's output, the photodiode sensitivity (S_{PD} ~ 0.8 A/W), the modulation index (m ~ 0.8) and on other different noise contributions: the thermal noise, the shot noise and the laser noise. The NCR is given as follows:

$$NCR = \frac{2(S_{Laser} + S_{th} + S_{shot})}{P_m^2 . {S_{PD}}^2 . m^2} \qquad \textit{(Eq.III. 2)}$$

The thermal noise S_{Th} is given by:

$$S_{Th} = \frac{4. k_B . T}{R} \qquad A^2/Hz \qquad \textit{(Eq.III. 3)}$$

where *T* is the room temperature (*T* = 293 K), k_B is Boltzmann's constant (k_B = 1,381×10^{-23} J .K^{-1}) and *R* is the photodiode's load resistance (R = 50 ohm)

The shot noise S_{Shot} is given by:

$$S_{Shot} = 2. q . S_{PD} . P_m \qquad A^2/Hz \qquad \textit{(Eq.III. 4)}$$

with *q* is the electron charge (q= 1.6×10^{-19} coulombs).

The laser noise S_{Laser} detected at the photodiode, taking into account the laser's *RIN* (*RIN* ~ -150 dBc/Hz), is given by:

$$S_{Laser} = P_m^2 . {S_{PD}}^2 . RIN \qquad A^2/Hz \qquad \textit{(Eq.III. 5)}$$

Using all these relations, we can finally estimate the WFN contribution to the OEO phase noise in function of the resonator's two characteristics: its quality factor and its transmission loss.

III.3.1.a *White frequency noise model: validation and use*

Using the above equations, we can easily determine the FRR real couplers' characteristics and the FRR real intrinsic loss (the splices loss and the fiber linear loss). This could be achieved by comparing the OEO measured and simulated phase noise data. Actually, by adjusting the theoretical values of the coupling coefficients and the ring intrinsic loss, we can fit of the simulated data to the experimental data with a unique solution regarding the optical quality factor. As a result, the resonator different parameters could be accurately obtained.

For example, the comparison between the measured and the simulated phase noise data of the 10m-long FRR based OEO is shown in Fig.III. 4. Of course, (Eq.III. 1) only takes into account the frequency range on which the phase noise is dominated by the WFN contribution and the noise floor. Finally, with a good fit of the simulation data to the experimental data, for both phase noise spectrum and Q_{Opt}, we were able to determine the couplers' coupling coefficients (κ_1 and κ_2 = 14% ± 0.4 %) and the couplers' excess losses (γ_1 and γ_2 = 0.59 dB). The splices loss was determined to be close to 0.005 dB.

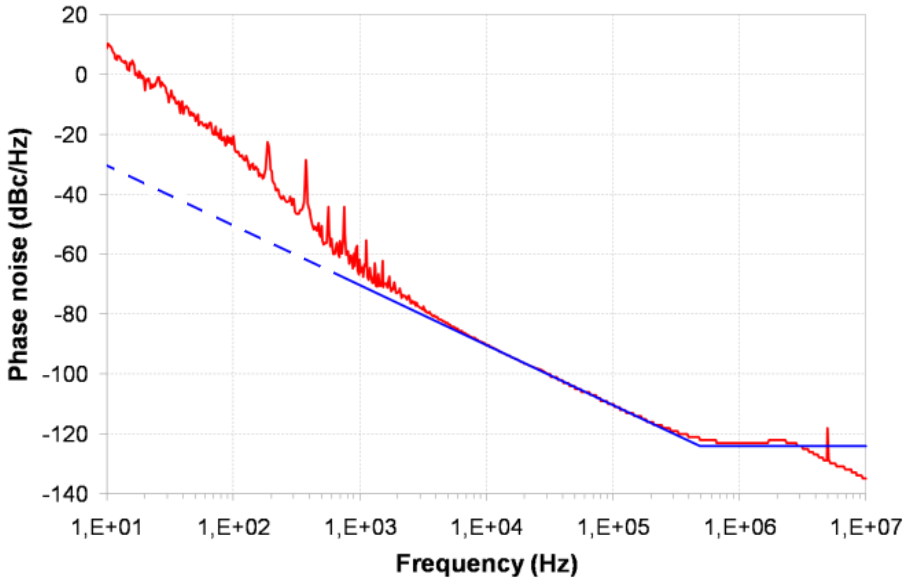

Fig.III. 4 Simulated (in blue) and experimental (in red) phase noise data; Simulations are only valid in the frequency range on which the phase noise is dominated by the white frequency noise contribution and the noise floor

III.3.1.b *Influence of the fiber ring length*

As it has been already mentioned in chapter II, the FRR Q_{Opt} increases when the fiber length increases. For example, a 1m-long FRR can feature a Q_{Opt} of 2x10^8 at 1.55 µm if it is fabricated using symmetrical couplers with coupling coefficients of 1%. However, this Q_{Opt} can increase to 5x10^9 if the resonator length is increased to 20 meter. In our optimization study, we have fixed the total length of the FRR to 20 meter and we have studied the influence of the other FRR parameters on the WFN contribution.

III.3.1.c *Influence of coupling coefficients, couplers' excess loss and the FRR loss*

To study the influence of couplers' excess losses and the FRR's loss, we have calculated (Eq.III. 1) while considering that the FRR intrinsic loss is only due to splices loss (optical fibers are considered lossless). Moreover, we have fixed the offset frequency at 10 kHz in our calculations.

In Fig.III. 5 are presented the simulation results of the WFN contribution to the OEO phase noise and the Q_{Opt} for different values of α_S, γ_1 and γ_2, versus the couplers' coupling coefficients (κ_1 *and* κ_2). In our study, we consider that the two couplers are symmetrical ($\kappa_1 = \kappa_2$ and $\gamma_1 = \gamma_2$).

The results in Fig.III. 5 show that when couplers and fibers are considered lossless, the optimal coupling will only depend on the coupling coefficient, which has to be the lowest possible (κ_1 and κ_2 near zero). On the other hand, for real values of the couplers' and fibers' losses, we can notice the presence of an optimal value regarding the couplers' coupling coefficient for each set of values of α_S, γ_1 and γ_2.

For example, when α_S is equal to 0.01 dB (a splices loss value that can be achieved when splicing two fibers) and γ_1 and γ_2 are equal to 0.1 dB each (commercially available), the optimal coupling

coefficient that gives the lowest WFN will be equal to 1.3 % (-19 dB). On the other hand, and in the same loss conditions, the optimal coupling coefficient that gives the highest Q_{Opt} will be the lowest possible (lower than -30 dB). This reveals the fact that a trade-off has to be made regarding the coupling coefficient in order to get the lowest WFN contribution while maintaining a sufficiently high Q_{Opt} of the FRR.

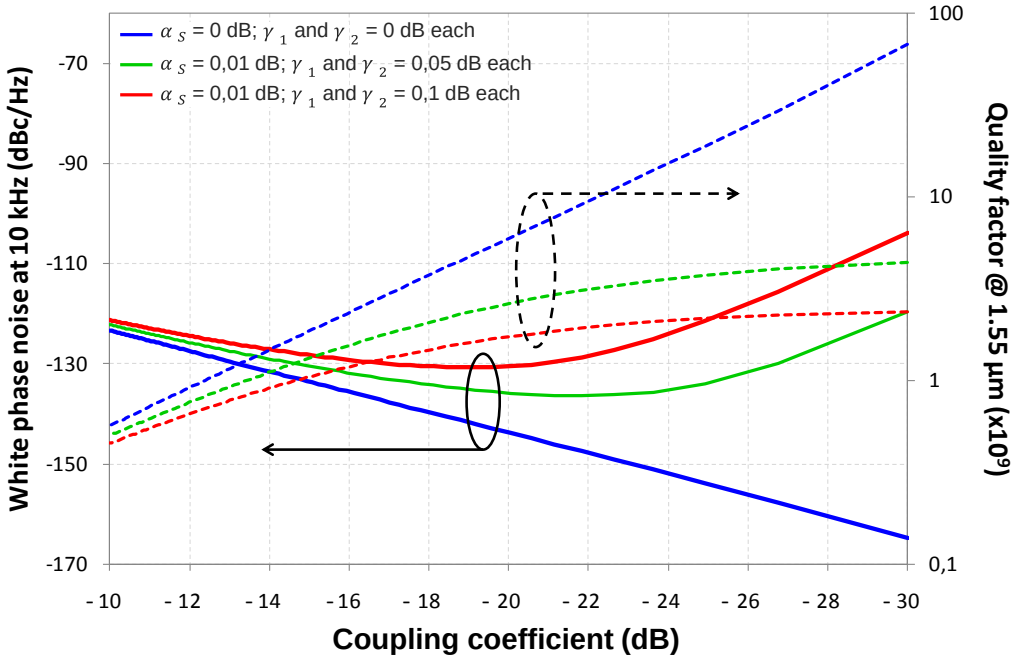

Fig.III. 5. Simulation results of the white frequency noise contribution and the optical quality factor, calculated versus the couplers' coupling coefficient, while changing the splices loss and the couplers' losses values

Finally, we have performed some simulations on the WFN contribution with α_S fixed to 0.02 dB, while changing the coupling coefficient and the couplers' excess losses (see Fig.III. 6 (a)). In Fig.III. 6 (a) results, we can also notice the presence of an optimal value regarding the coupling coefficient for each set of values of γ_1 and γ_2.

Likewise, Fig.III. 6 (b) presents some simulations that were made while considering the couplers to be ideal (γ_1 and γ_2 = 0 dB) and changing the coupling coefficient and the splices losses. Comparable to the previous case, there was also an optimal value regarding the coupling coefficient for each value of α_S. Moreover, Fig.III. 6 results show that the lower the couplers' and splices' losses are, the better it is to get a low WFN contribution to the OEO phase noise.

Of course, in what concerns the Q_{Opt}, it strongly depends on the FRR intrinsic loss and the couplers loss. For example, if a 1% (-20 dB) coupling coefficient is used and α_S is fixed to 0.02 dB, Q_{Opt} can decrease from 5.5x10^9, when the couplers are lossless, to 0.1x10^9, when γ_1 and γ_2 are equal to 1 dB each (see Fig.III. 6 (a) and (b)).

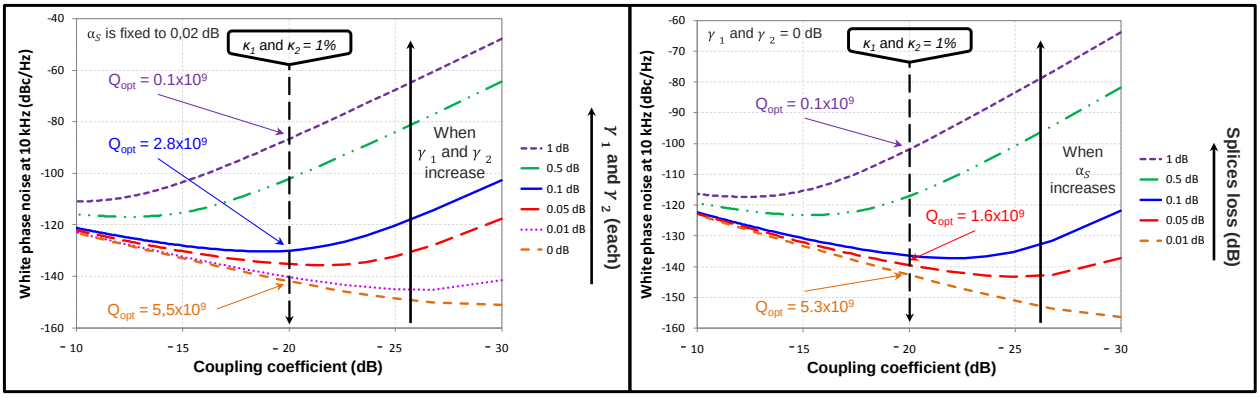

Fig.III. 6. Simulation results of the white frequency noise contribution versus the couplers' coupling coefficient while changing: (a) the couplers' excess losses (the splices loss was fixed to 0.02 dB), (b) the splices loss (the couplers are considered lossless)

III.3.2 OEO based on the optimized 20m-long FRR

III.3.2.a *The optimized 20m-long FRR*

Thanks to our theoretical study, evaluating the WFN contribution, and all simulation results considered, we have designed and fabricated a new 20m-long FRR with a 1 % coupling coefficient and with α_S less than 0.01 dB, and γ_1 and γ_2 less than 0.05 dB each.

We have then characterized this FRR using the microwave domain measurement bench. A resonance linewidth of 38 kHz has been measured, which means an optical quality factor of 5.1x10^9 at 1.55 µm (see Fig.III. 7), and thus an L_{eq} of 1720 m (see chapter II).

Moreover, we have measured a 3.7 dB optical transmission loss. Using this transmission loss value, and taking into account an output coupler coupling coefficient of 1 %, we can estimate an $IPEF$ of ~ 54 (17 dB). This $IPEF$ value has been also confirmed via ADS and Maple13 simulations.

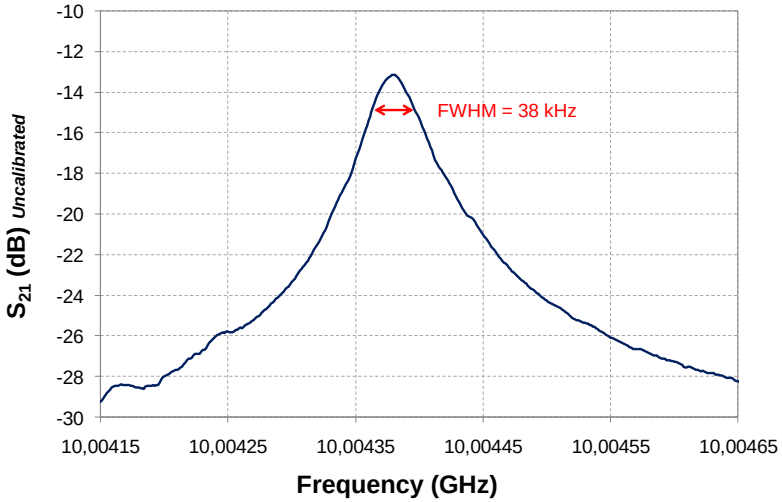

Fig.III. 7. S_{21} transmission response of the 20m-long FRR, characterized using the microwave domain technique described in chapter II

Finally, with these interesting characteristics of the 20m-long FRR, a WFN contribution to the OEO phase noise is expected to be less than -130 dBc/Hz at 10 kHz offset frequency (see the green dashed curve in Fig.III. 8). This should lead to an important reduction in the OEO phase noise.

III.3.2.b *The 20m-long FRR based OEO phase noise results*

The 20m-long FRR has been used as the frequency stability element in the 10 GHz OEO. The OEO phase noise has been measured and the results are presented in Fig.III. 8 (blue curve), and then compared to the 10m-long FRR based OEO phase noise results (red curve). We can clearly witness the OEO significant phase noise reduction. A phase noise level of -115 dBc/Hz can be measured at 10 kHz offset frequency and about -40 dBc/Hz at 10 Hz offset frequency. The Leeson frequency confirms a Q_{RF} of 2.5x10^5 at 10 GHz for our 20m-long FRR based OEO (Theoretically: f_{Leeson} ~ 20 kHz; Experimentally: f_{Leeson}~ 25 kHz).

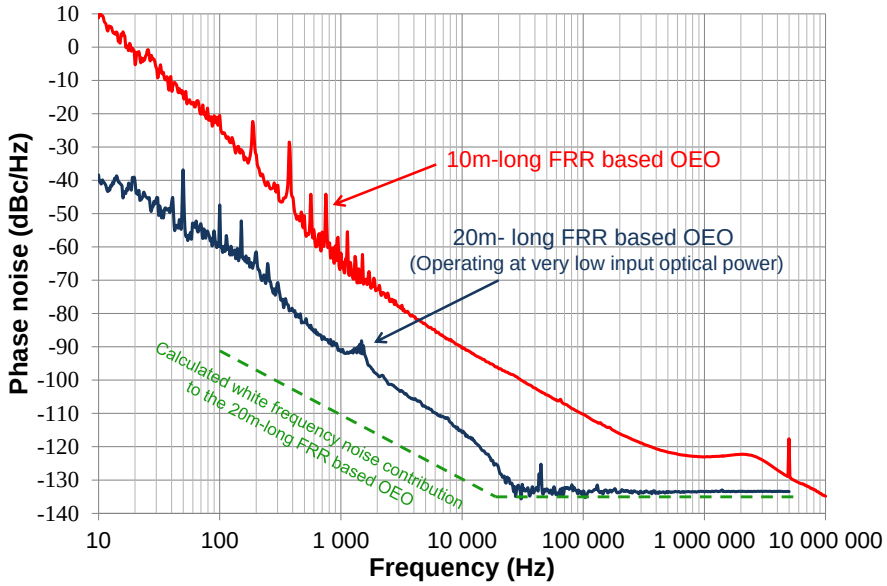

Fig.III. 8. Phase noise spectra of the 10m-long FRR based OEO (in red) and the optimized 20m-long FRR based OEO (in blue). The green dashed curve shows the contribution of the white frequency noise of the 20m-long ring on the OEO phase noise calculated using (Eq.III. 1)

III.3.3 Results discussions

The coupling optimization study of the FRR has revealed that in order to obtain a low phase noise when using the FRR in an OEO setup, we have to make a trade-off in the couplers' coupling coefficient regarding the resonator transmission loss and its optical quality factor. The objective is to finally get a low WFN contribution to the OEO phase noise with a sufficiently high Q_{Opt}. The efficiency of such an optimization has been validated through the fabrication and the use of the 20m-long FRR in an OEO setup, where a phase noise level of -115 dBc/Hz at 10 kHz offset frequency has been measured. Still, this phase noise result was far from our theoretical expectations.

Actually, there is a very important issue that we have to mention here in what concerns the OEO phase noise spectrum we have measured using the 20m-long FRR. The phase noise data presented in

Fig.III. 8 were the best results that we have been able to obtain using this FRR. The 20m-long FRR based OEO phase noise measurements have been performed while using a very low optical power at the FRR input (less than -10 dBm) in the OEO loop (the NCR was obviously degraded in this case). This is because we have noticed that, in this oscillator, when the optical power increases the OEO phase noise increases as well.

In fact, we have found that the very high Q_{Opt} of the 20m-long FRR and its high $IPEF$ lead to the generation of many nonlinear optical effects inside the resonator, especially the stimulated Brillouin scattering. These effects were found to be the main contributors to the OEO phase noise degradation. Moreover, the resonator Q_{Opt} has degraded a few months later to around $3.5x10^9$. This was likely due to the extremely high intra-cavity power that was building up inside the resonator (e.g. a 10 mW of optical power at the resonator input means approximately a 540 mW inside the resonator at resonance, which is much higher than what optical fiber couplers can handle (the optical couplers power limit is around 300 mW)). Consequently, the nonlinear optical effects generated inside this FRR have been the field of many studies, which are detailed in the next chapter.

Aside from these nonlinear optical phenomena, there were many other noise conversion processes which needed further investigations. We can especially mention the laser AM and FM noise conversions to RF phase noise by different means inside the OEO setup. These noise conversions have been studied and are detailed in the next section.

III.4 Laser amplitude and frequency noise conversions inside the OEO setup

The laser noise seems to be a very important parameter to scale in RF over fiber (ROF) links and optoelectronic systems like OEOs, particularly the laser noise conversion processes into RF phase noise. The importance of such processes is attested by the numerous studies we can find in the literature on this subject [5]-[10]. These studies have investigated the different means by which the laser AM and FM noise conversion processes could take place, and their effect on the phase noise of a transmitted (or generated) RF signal. For this reason, we have investigated the different noise conversion processes that can occur in the special type of OEOs we are using, the FRR based OEO.

Actually, even if the FRR is used in the OEO setup as the frequency stability element, it may also degrade the OEO phase noise if all the different elements in the OEO setup are not properly adjusted.

III.4.1.a *Laser noise conversions through fiber chromatic dispersion*

Recently, it has been reported by Volyanskiy et al. [9] that laser's wavelength fluctuations conversion into RF phase noise, in delay line based OEOs, could be further increased by the chromatic dispersion(D_λ) of the optical fiber used as the delay element. Actually, in these OEOs, the laser optical frequency fluctuations (Δf_{Opt}) are converted into delay fluctuations ($\Delta\tau_{Opt}$) via the fiber dispersion, and therefore into RF phase fluctuations ($\Delta\emptyset_{RF}$). In addition, this contribution to the OEO phase noise has been found to be proportional to the product $D_\lambda . L$. From [9], this noise conversion relation is given by:

$$\Delta\emptyset_{RF} = -2\pi . f_{Osc} . \Delta\tau_{Opt} = 2\pi \cdot f_{Osc} \cdot \lambda_l \cdot D_\lambda \cdot \frac{L}{c} \cdot \Delta f_{Opt} \qquad \textit{(Eq.III. 6)}$$

In (Eq.III. 6), it is clear that one efficient solution to reduce this noise contribution is the use of zero-dispersion fibers or the use of a laser wavelength near the zero-dispersion point of single mode optical fibers (~1.33 µm). When using a zero-dispersion fiber instead of SMF, Volyanskiy et al. [9] have observed a 10 dB reduction in the phase noise of a 4 km delay line based OEO. On the other hand, they have reported that the laser RIN has only a minor influence on the RF phase noise.

Of course, this noise conversion process may similarly occur in our FRR based OEO because the resonator cavity is also a delay element and the optical fibers we use to fabricate the FRR have a dispersion D_λ=17 ps/nm.km. Unfortunately, and particularly in the FRR case, using a zero-dispersion fiber (or working near the zero-dispersion point) will intensify the nonlinear optical phenomena. These phenomena have been found to be the main cause of the FRR based OEO phase noise degradation, as we will see later in the next chapter. Therefore, no current action has been taken to reduce the optical fiber's chromatic dispersion in our FRR based OEO.

III.4.1.b *Laser noise conversions through the FRR*

Because the FRR based OEO is a more complex system than conventional delay line OEOs, and in order to evaluate the laser FM noise conversion through the resonator, we have used a dedicated simulation approach: the OEO ADS model which has been detailed in chapter II.

To simulate the effect of the PDH loop on the laser frequency stability when the laser is stabilized to the FRR, and therefore the effect of the PDH loop on the output RF signal stability, the OEO open-loop response has been simulated. Like in the real case, a MZM linear modulation has been used. As a result, the modulated laser carrier features two optical sidebands which simultaneously go through two lateral modes of the resonator. This process gives birth to a unique microwave mode at the photodiode output, which results from the two optical modulation sidebands and the laser carrier folded one onto the other.

During the simulations, we have first stabilized the laser carrier onto the center of the optical resonance, and then we have shifted the carrier onto one of the optical resonance edges (the right edge or the left edge). The stabilization to the resonance edges results in a complete deformation of the resonance RF amplitude response (a splitted resonance) and therefore a Q_{RF} factor degradation. Moreover, the RF phase transition response at the resonance becomes less sharp, with two phase transitions corresponding to the two "resonances" of the splitted resonance (see Fig.III. 9).

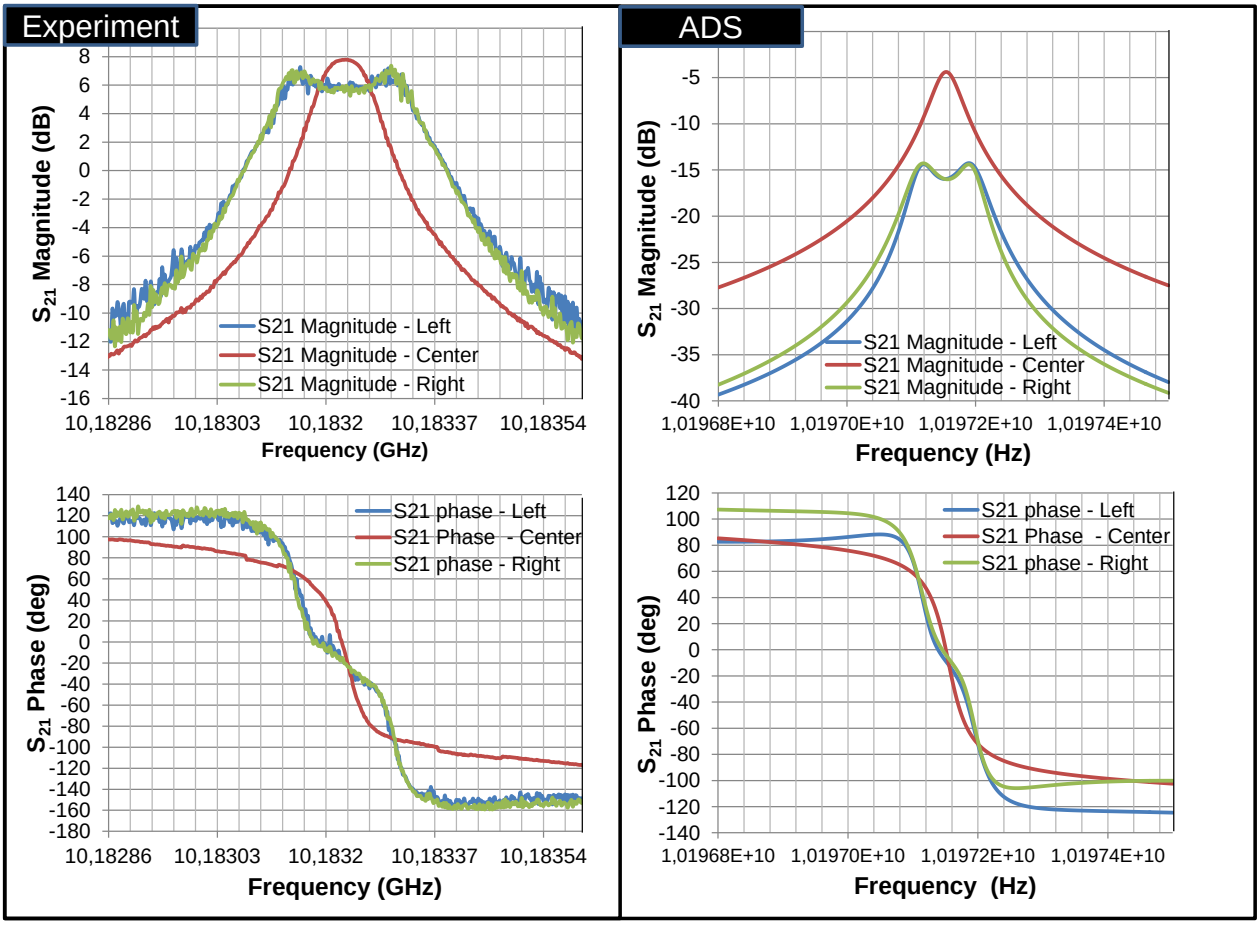

Fig.III. 9. Experimental and simulated RF amplitude and phase responses of the resonance. Quantitatively, ADS simulation results and experimental results both show that the resonance RF amplitude and phase responses are deformed when the laser is stabilized onto one of the edges of the optical resonance. See also Image 8 in appendix C

These results have been also validated experimentally by changing the PDH loop's stabilization set-point in order to stabilize the laser frequency onto one of the optical resonance edges and then recording the photodiode's amplitude and phase responses using the microwave domain characterization bench. The experimental results are depicted in Fig.III. 9.

Quantitatively speaking, the contribution impact is not the same between the simulation results and the experimental results (due to the improvement work that has to be made on the OEO ADS model). Despite that, these simulations have confirmed that the laser FM noise could be converted into RF AM and PM noise inside our OEO setup, through the FRR. Indeed, a shift in the laser frequency results in a deformation in the RF amplitude and phase responses. Furthermore, the experimental results have confirmed that the PDH loop is a critical parameter that must be carefully adjusted to prevent this type of noise conversion in the OEO oscillation loop (the best condition being the laser stabilized onto the center of the optical resonance).

The conversion factor of the laser frequency noise into RF phase noise can be thus denoted by $\kappa_{\varphi-FM-FRR}$. However, due to the fact that currently we cannot rely on ADS simulation results regarding this conversion factor, we have either to estimate it through our experimental results, or we can simply

rely on the fact that our PDH loop is well adjusted in such a way that the laser frequency is stabilized onto the center of the optical resonance and therefore $\kappa_{\varphi-FM-FRR}$ could be neglected in our noise calculations.

Finally, the same simulations have been repeated by fluctuating the laser power and not its frequency (the laser was stabilized onto the center of the optical resonance) in order to simulate the laser AM noise (RIN) conversion into RF phase noise inside the OEO loop. Our simulation results have not shown any significant change in the RF response. However, it is important to mention that in our OEO ADS model the photodiode model was simplified. It was only based on a quadratic detector followed by a linear circuit to describe its frequency response. The nonlinear behavior of the photodiode capacitance, for example, has not been taken into account.

III.4.1.c *Laser noise conversions through the photodiode nonlinearity*

It is well known that the laser RIN is one of the limiting factors of signals transmission over optical fibers. It could play a role in both additive and multiplicative noise conversion processes. On one hand, this power fluctuations noise increases the link noise and mainly degrades its NCR. On the other hand, the baseband RIN can be up-converted into RF AM and PM noise via optical link nonlinearities, especially via the photodiode nonlinearity as it has been reported in delay line based OEOs in [10].

Therefore, we have experimentally studied the nonlinear behavior of our photodiode (Discovery DCS30S) versus the received optical power. The experimental bench is illustrated in Fig.III. 10. It uses a VNA to accurately characterize the photodiode's S_{21} amplitude and phase responses (an averaging factor of 1000 has been used during the measurements).

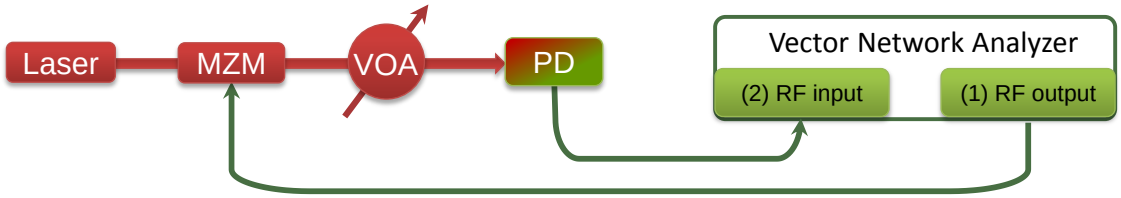

Fig.III. 10. Characterization bench of the photodiode's amplitude and phase responses; VOA: variable optical attenuator

First of all, the laser power has been set at its highest value, then the laser carrier has been externally modulated at 10 GHz by means of the MZM (the same frequency of the OEO oscillation frequency has been chosen because the photodiode nonlinear behaviour is also frequency dependent [11] and even bias voltage dependent). The driving 10 GHz RF signal comes from a calibrated vector network analyzer working in a CW mode. The amplitude and phase responses of the S_{21} parameter were accurately measured while changing the received optical power at the photodiode input. For this purpose, an optical variable attenuator has been used just before the photodiode and the MZM nonlinearity can be therefore discarded. The experimental results are presented in Fig.III. 11.

The results of Fig.III. 11 show that at low optical input power, the RF power increases rapidly versus the received optical power following the well-known square low: $P_{RF} = {P_{Opt}}^2$. However, near photodiode saturation, we can clearly observe the presence of a reduced slope in the RF amplitude

response versus the received optical power. This photodiode behavior is due to the fact that below saturation, the number of electron–hole carriers in the photodiode PIN increases when the optical power increases. On the other hand, when the photodiode saturates, the generated electron–hole carriers screen the external electric field of the reversed DC bias at the photodiode junction [12], so that an increase in the optical power does not result in the generation of additional RF power.

Consequently, the RIN-to-RF AM noise conversion factor, denoted $\kappa_{\varphi-AM-PD}$, could be reduced if we push the photodiode to saturation. However, a 25 mW optical power level is difficult to be achieved at the end of the OEO open-loop optical link. Moreover, at this optical power level, another conversion factor may appear.

Actually, in addition to this RIN-to-RF AM noise conversion factor, the results in Fig.III. 11 show a more interesting nonlinear behavior of the photodiode, where two zero slopes in the photodiode's S_{21} phase response can be observed.

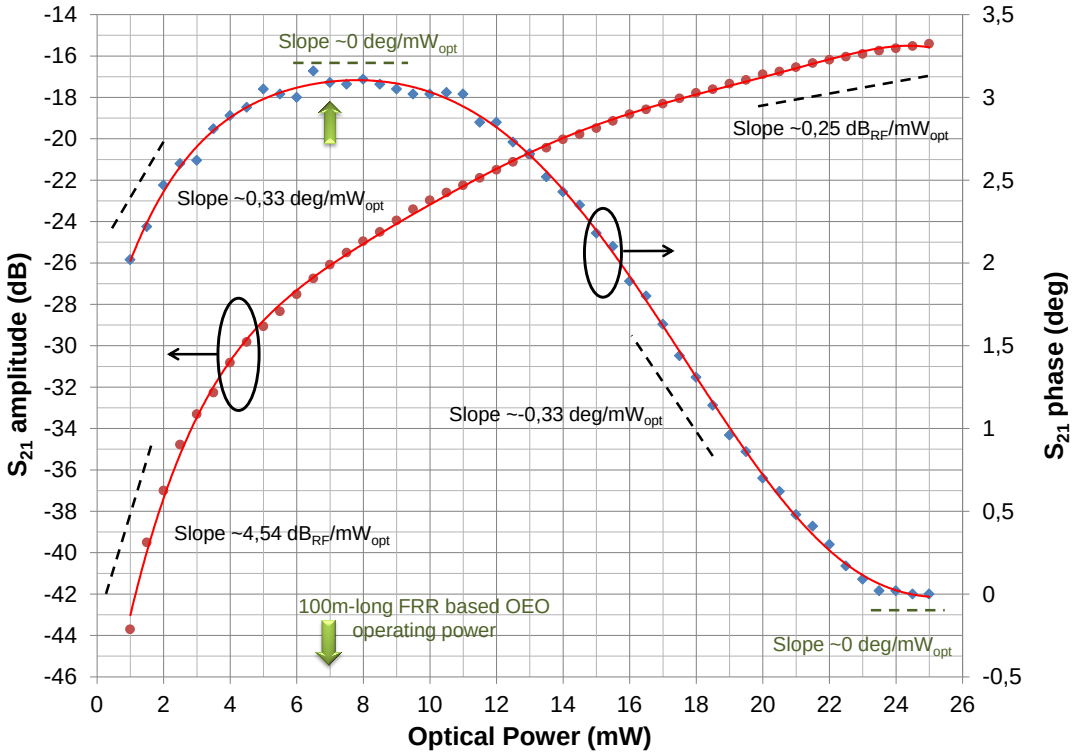

Fig.III. 11. S_{21} RF amplitude and phase responses of the Discovery DCS30S photodiode, versus the received optical power; sixth order polynomial fit is used for both curves

A quite similar behavior has been reported in [10], and it has been analytically described by considering the laser RIN conversion into RF phase noise. The open-loop RIN-to-RF phase noise conversion via the photodiode nonlinearity is given by:

$$L_{\phi_{RF-PD}}(f_m) = \kappa_{\varphi-PM-PD} + RIN(f_m) \qquad (\text{dBc/Hz}) \qquad \textit{(Eq.III. 7)}$$

where $L_{\emptyset_{RF-PD}}(f_m)$ is the RF signal's single-sideband phase noise at the offset frequency f_m from the RF carrier, resulting from the laser RIN conversion through the photodiode nonlinearity. $\kappa_{\varphi-PM-PD}$ being the RIN-to-RF phase noise conversion factor in decibels:

$$\kappa_{\varphi-PM-PD} = \frac{{P_{Opt}}^2}{2} \cdot \left(\frac{d\varphi_{RF}}{dP_{Opt}}\right)^2 \qquad \textit{(Eq.III. 8)}$$

where $\frac{d\varphi_{RF}}{dP_{Opt}}$ is the RF phase-to-optical power slope (in rad/mW).

The polynomial fit of the photodiode S_{21} phase response has been used to calculate (Eq.III. 8) (in decibels) versus the received optical power (in mW). The results of this calculation are illustrated in Fig.III. 12. They show that $\kappa_{\varphi-PM-PD}$ could be reduced by 38 dB if a 7 mW optical power is received by the photodiode (a $\kappa_{\varphi-PM-PD}$ of -62 dB can be obtained; logically, this value should tend to minus infinite because we have a zero conversion slope at 7mW, but we have used here a large sampling step to do the calculation). This being said, our laser high frequency RIN level, which is around -150 dB/Hz, will be converted to a RF phase noise level that is below -210 dBc/Hz.

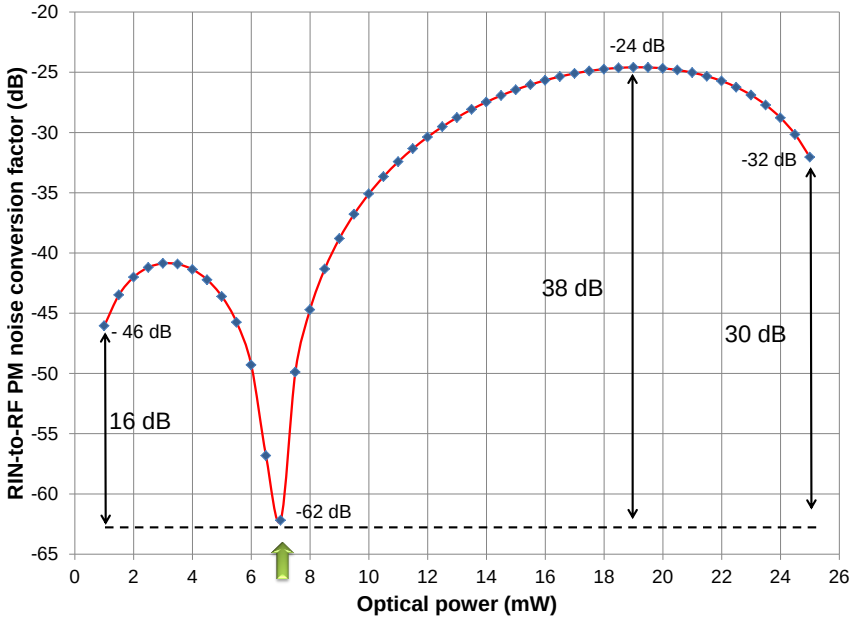

Fig.III. 12. RIN-to-RF phase noise conversion factor of the Discovery photodiode DCS30S, versus the received optical power; sixth order polynomial fit is used

Such a RIN-to-RF phase noise conversion level is far below the other noise contributions (Shot, thermal and laser noise contributions) generated at the photodiode in this power conditions (at an optical power level of 7 mW, (Eq.III. 2) gives a NCR level of -148 dBc/Hz), at least for the high frequency part in the RIN spectrum.

However, the RIN-to-RF noise contribution to the close-in RF phase noise spectrum could be much higher. Fig.III. 13 shows the calculation results of (Eq.III. 7) for different received optical power levels at the photodiode, taking into account the laser RIN measurements reported in chapter II (see the

blue dashed curve in Fig.III. 13). These results are compared to the laser RIN level and to the different NCR levels calculated using (Eq.III. 2) in the same power conditions.

We can see from Fig.III. 13 results that among the aforementioned photodiode's noise contributions (thermal, shot and laser noise contributions), the contribution of the laser RIN converted into RF phase noise through the photodiode nonlinearity is usually dominant in the close-in RF phase noise spectrum, unless if the received optical power is around 7 mW. At offset frequencies above 1 kHz, the other noise contributions are dominant. Finally, it is clear that the lowest RIN-to-RF phase noise conversion can be obtained if a 7 mW optical power level is received at the photodiode.

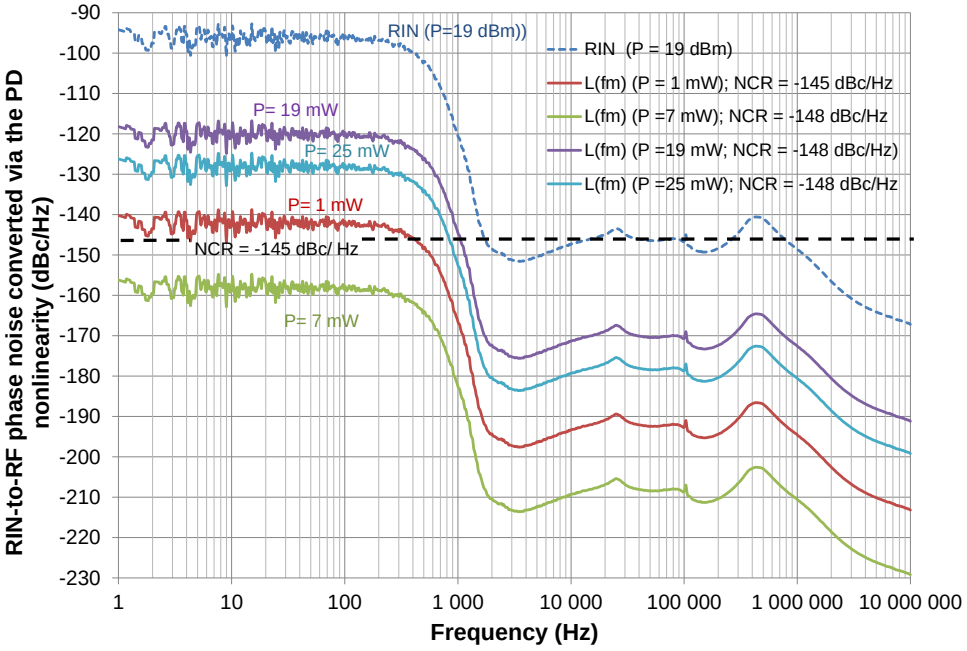

Fig.III. 13. Calculation results of (Eq.III. 7) for different received optical power at the photodiode, taking into account the laser RIN measurements reported in chapter II. The noise to carrier ratio is also calculated for each case.

Furthermore, knowing that the RIN-to-RF phase noise conversion affects much more our OEO phase noise than the RIN-to-RF amplitude noise conversion, and that a 7 mW optical power at the end of the OEO optical link is possible, we have chosen to work at this optical power in our new OEO based on a 100m-long FRR. This 100m-long FRR based OEO will be detailed and discussed in the next chapter.

Unfortunately, in the case of the 20m-long FRR based OEO, a 7 mW optical power is far from being achieved. In fact, the laser carrier saturates when passing through this FRR because of the generation of different nonlinear optical effects inside the resonator at very low power thresholds, (as low as -10 dBm for the stimulated Brillouin scattering). In these conditions, only 0.7 mW optical power can be obtained at the photodiode input (a -13.5 dBm optical power can be obtained at the FRR output, it will be then amplified to 1.5 dBm by the EDFA amplifier (G_{EDFA} = 15 dB), then splitted equally by the optical coupler at the EDFA output where finally one part is sent to the photodiode input and the other part is sent through the out-of-loop optical link to perform the phase noise measurements; see the OEO schematic in chapter I).

Therefore, from Fig.III. 12, the RIN-to-RF PM noise conversion factor will be equal to -46 dB and our laser RIN level will be converted to a higher RF phase noise level than the one obtained in the case of a 7 mW received optical power (see Fig.III. 13).

Finally, one has to take into account that the RIN-to-RF phase noise conversion via the photodiode nonlinearity, calculated from (Eq.III. 7), is in an open-loop configuration. Once the OEO loop is closed, this equation must be included in Leeson's model to take into account the FRR loaded quality factor Q_{RF} as already explained in chapter I, and used in section III.2.4 for the RF amplifiers case, to finally get an estimation of the open-loop to closed-loop phase noise conversion.

III.5 Conclusion

In this chapter, we have evaluated the white frequency noise contribution to the FRR based OEO phase noise. We have shown that there is a trade-off to be made regarding the resonator coupling coefficients in order to get a satisfying Q_{Opt} and a low noise to carrier ratio at the same time, which should lead to a low white frequency noise contribution. Thanks to this study, an important reduction of the OEO phase noise has been demonstrated using an optimized 20m-long FRR.

Despite this result, the obtained OEO phase noise was still far from our theoretical expectations. We have therefore investigated the different noise conversion processes that can take place in the OEO setup. We have mainly studied the conversions of the laser noise into RF amplitude and phase noise through optical fiber chromatic dispersion, the FRR itself (via the PDH laser stabilization loop) and the photodiode nonlinearity.

Our noise studies have revealed that the laser frequency noise can be converted into OEO phase noise via the FRR when the laser is not properly stabilized onto the center of the optical resonance via the PDH loop. Furthermore, we have found that the laser relative intensity noise (RIN) can be up-converted into microwave amplitude and phase noise via the photodiode nonlinearity. A photodiode optimal optical power working point, at which the photodiode RIN-to-RF phase noise conversion could approximately vanish, has been identified.

Still, and despite all these studies, another important noise contribution to the OEO phase noise has to be studied: the nonlinear optical effects generated inside the FRR because of its very high Q_{Opt} and intra-cavity power enhancement factor.

III.6 References

[1] P.H. Merrer, O. Llopis, S. Bonnefont, L. Ghisa, Y. Dumeige, P. Feron, and G. Cibiel, "Microwave Filtering Using High Q Optical Resonators," Microwave Conference, 2008. EuMC 2008. 38th European , vol., no., pp.381-384, 27-31 Oct. (2008).

[2] D.B. Leeson, "A simple model of feedback oscillator noise spectrum," Proc. of the IEEE, vol. 54, no. 2, pp. 329-330, (1966).

[3] Pierre-Henri Merrer, "Élaboration de sources hyperfréquences à haute pureté spectrale à base de résonateurs optiques," Ph.D. thesis (Toulouse III - Paul Sabatier University, Toulouse, France, 2009).

[4] J.K.A. Everard, "Low noise oscillators," Microwave Symposium Digest, 1992., IEEE MTT-S International , vol., no., pp.1077-1080 vol.2, 1-5 Jun (1992).

[5] W. Shieh, and L. Maleki, "Phase noise of optical interference in photonic RF systems," Photonics Technology Letters, IEEE , vol.10, no.11, pp.1617-1619, Nov. (1998).

[6] O. Okusaga, J. Cahill, W. Zhou, A. Docherty, G. M. Carter, and C. R. Menyuk, "Optical scattering induced noise in RF-photonic systems," Frequency Control and the European Frequency and Time Forum (FCS), 2011 Joint Conference of the IEEE International , vol., no., pp.1-6, 2-5 May (2011).

[7] A. Docherty, C.R. Menyuk, O. Okusaga, and W. Zhou, "Stimulated Rayleigh scattering and amplitude-to-phase conversion as a source of length-dependent phase noise in OEOs," Frequency Control Symposium (FCS), 2012 IEEE International , vol., no., pp.1-5, 21-24 May (2012).

[8] O. Okusaga, W. Zhou, J. Cahill, A. Docherty, and C.R. Menyuk, "Fiber-induced degradation in RF-over-fiber links," Frequency Control Symposium (FCS), 2012 IEEE International , vol., no., pp.1-5, 21-24 May (2012).

[9] K. Volyanskiy, Y.K. Chembo, L. Larger, and E. Rubiola, "Contribution of Laser Frequency and Power Fluctuations to the Microwave Phase Noise of Optoelectronic Oscillators," Lightwave Technology, Journal of , vol.28, no.18, pp.2730-2735, September (2010).

[10] D. Eliyahu, D. Seidel, and L. Maleki, "RF Amplitude and Phase-Noise Reduction of an Optical Link and an Opto-Electronic Oscillator," Microwave Theory and Techniques, IEEE Transactions on , vol.56, no.2, pp.449-456, February (2008).

[11] W. Zhang, T. Li, M. Lours, S. Seidelin, G. Santarelli, Y. Le Coq, "Amplitude to phase conversion of InGaAs pin photo-diodes for femtosecond lasers microwave signal generation," Applied Physics B 106, Issue 2, Page 301-308 (2012).

[12] D. A. Tulchinsky, K. J. Williams, X. Li, N. Li, and J. C. Campbell, "High power photodetectors," IEEE LEOS Newslett., vol. 19, no. 2, pp. 16–17, (2005).

Chapter IV Nonlinear optical effects generated in the 20m-long FRR and OEO phase noise degradation

IV.1 Introduction

In optical fibers, many nonlinear optical phenomena can occur, especially when high optical power levels are used [1]. Compared to bulk mediums, optical fibers are ideal for the outbreak of nonlinear optical mechanisms; this is due to two important factors: they feature ultra-low attenuation coefficients and they have small core diameters. Among these nonlinear optical mechanisms we can especially mention the Rayleigh, Brillouin and Raman scatterings, which have two scattering modes each: spontaneous and stimulated scatterings. These mechanisms depend on molecular or density variations of silica in optical fibers. Furthermore, another nonlinear optical effect could be generated in optical fibers: the four-wave mixing. These scattering mechanisms are almost all power dependent and they are capable of inducing noise in the spectra of optical signals travelling through the optical fiber. This fiber-induced noise limits the Q_{Opt} factors of fibered resonators and degrades low-noise signals transmitted via optical fibers [2]. To these nonlinear mechanisms we can also add the Fresnel back-reflection at the fiber end faces. Even not considered to be a nonlinear effect, the Fresnel back-reflection can also induce interferometry noise in fibered optical links.

RF-over-fiber links usually requires relatively high laser carrier power in order to increase the spur-free dynamic range and reduce the noise figure. On the other hand, this high power level leads to nonlinear scattering mechanisms and induces additional noise on the optical signal traveling through the fiber. This additional optical noise is then converted into RF noise after being detected by the photodiode.

In the previous chapter, we have found that many noise conversion processes could degrade the OEO phase noise. In spite of that, nonlinear optical scattering mechanisms generated inside the high Q_{Opt} FRR, seemed to be the main reason behind most of the $1/f$ excess noise observed in our OEO. This has led us to deeply investigate the nonlinear optical effects generated inside the 20m-long FRR, especially on the stimulated Brillouin scattering and the stimulated Rayleigh scattering. The aim was to understand these processes, then to find the optimal solution that leads to an optimized FRR featuring a very high Q_{Opt} and which will be immunized against the nonlinear optical phenomena.

In this chapter, we first give a description of each of the nonlinear optical phenomena and on their possible contributions to the noise induced in our FRR based OEO. After the descriptions, we demonstrate how these nonlinear optical effects, especially the stimulated Brillouin scattering, could be useful to generate high power and high spectral purity millimeter wave signals. Then we present the different methods used in the literature to suppress these nonlinear optical effects in optical fibers, and we describe the suppression method we have used in our FRR. Finally, an optimized and immunized FRR is fabricated and a significantly reduced FRR-OEO phase noise level is measured.

IV.2 The Brillouin scattering in the FRR based OEO

The stimulated Brillouin scattering (SBS) results from a stimulated inelastic scattering in which an optical field transfers a part of its energy to the nonlinear medium and thus creates, then interacts with, medium density variations that changes its frequency and its traveling direction. SBS is one of the first nonlinear optical effects studied in optical fibers. It has been first used in many remarkable applications such as Brillouin lasers, Brillouin amplifiers… Nevertheless, more recently, it has been found that SBS could be an important source of optical fiber induced noise. Therefore, a large number of scientists in the optoelectronics field were interested by the SBS noise aspect. Since then, many studies were reported on SBS noise in single-path-geometry (SPG) optical fibers and low noise RF-over-fiber links. However, we can barely find some studies on SBS behavior and SBS noise in FRRs in the literature. We have thus tried to theoretically and experimentally describe the SBS behavior in the FRR in order to find a way that leads to a complete suppression of the SBS and its noise induced in the FRR, while maintaining a high Q_{Opt}.

IV.2.1 Brillouin scattering in optical fibers and FRRs

Theoretically predicted by L. Brillouin in 1922 [3], SBS was firstly observed in quartz and sapphire crystals in 1964 [4], and has been extensively studied in optical fibers since then [2] [5] [6]. This scattering phenomenon is recognized to be the dominant nonlinearity in optical fibers.

IV.2.1.a *Brillouin scattering theory*

The Brillouin scattering is caused by the interaction between a light wave (laser carrier) and an acoustic wave existing already at the optical medium thermal equilibrium. This acoustic wave travels at the sound speed in the optical fiber (c_{ac} ~ 6 km/s) and produces a periodic modulation of its refractive index. The index periodic modulation acts like a moving fiber Brag grating (FBG), also known as propagating density waves or acoustic phonons, and it refracts a part of the incident light wave. This interaction creates a scattered wave and in this case we are in the spontaneous regime. Still, this regime refers to the process where the optical material properties are not affected by the presence of the incident light wave.

In optical fiber, Fig. IV. 1, the acoustic wave frequency (ν_{ac}) depends on its speed in the fiber (c_{ac}), the fiber effective refractive index (n), the laser carrier wavelength (λ_l) and the scattering angle (θ) between the wave vectors of the carrier and the scattered wave. It is given by the relation below:

$$\nu_{ac} = 2 \cdot c_{ac} \cdot \frac{n}{\lambda_l} \cdot sin\left(\frac{\theta}{2}\right) \qquad \textit{(Eq.IV. 1)}$$

From this relation we can see that in optical fiber, the backscattered Stokes wave is privileged and is frequency downshifted from that of the incident light wave by an amount ν_B set by the nonlinear medium characteristics (ν_B ~ ν_{ac}). From (Eq.II. 1), this frequency shift is about 11 GHz in silica fibers [1]. This negative frequency shift (Stokes wave) is caused by the Doppler effect of the interaction between the light wave and the acoustic wave part (the moving Brag mirror) travelling in the same direction of the light [7]. However, a very weak scattered wave travelling in the same direction of the Stokes wave, called

anti-Stokes, but up-shifted in frequency by ν_B, can be also generated. Its positive frequency shift is due to the interaction between the light wave and the acoustic wave part travelling in the opposite direction.

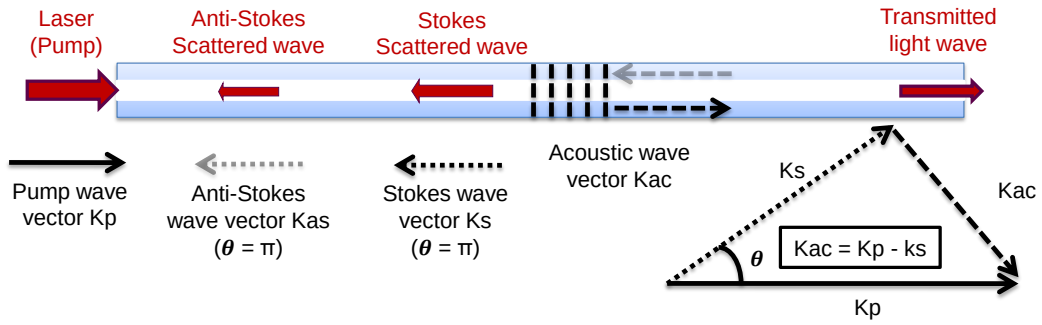

Fig. IV. 1. Wave vector diagram illustrating SBS efficiency in the backward direction in the optical fiber

At a critical incident light wave power, called SBS threshold ($SBST$), the nature of the scattering process grossly modifies the optical properties of the medium where the interference between the Stokes wave and the incident light wave amplifies the acoustic wave through electrostriction. The electrostriction is the tendency of materials to become denser in regions of high optical intensity [8]. Consequently, the scattered wave becomes more intense and reinforces the interference and so on; we are thus in the stimulated regime.

One of the SBS penalties in optical links is the carrier depletion. This optical carrier depletion occurs at power levels above the $SBST$ because a large part of the additional optical power injected in the fiber is converted to the Stokes wave via the electrostriction process (the anti-Stokes wave contribution to the scattering process is very weak as we have mentioned above). Furthermore, when the Stokes wave power exceeds the medium's $SBST$, it creates a second order Stokes wave downshifted in frequency from the first Stokes wave by ν_B, and thus by $2\nu_B$ from the incident light wave. The theoretical spectral representation of the first and second order SBS waves (Stokes and anti-Stokes waves) is illustrated in Fig. IV. 2. This illustration also includes the SBS own Rayleigh-scattered waves with their small frequency shift (few kHz). Moreover, the travelling directions of all these scattered waves are the same as in a FRR, and are represented in Fig. IV. 3. The Rayleigh scattering will be discussed in section IV.3.

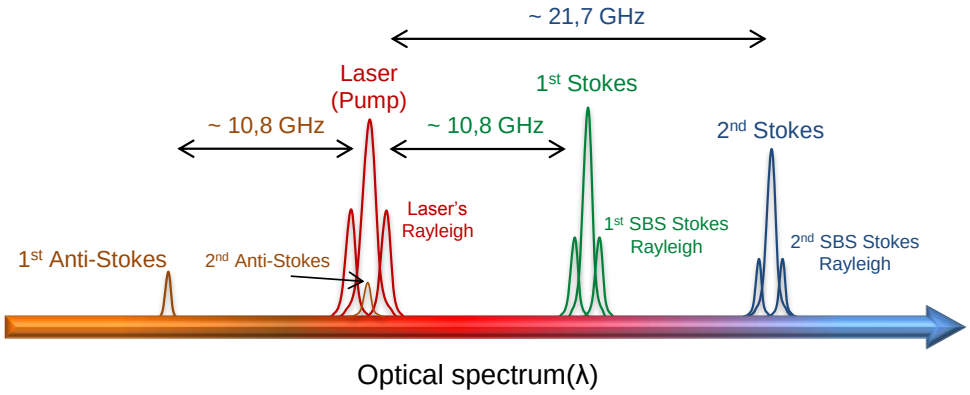

Fig. IV. 2. Optical spectrum representation of the first and second order SBS waves and their own Rayleigh-scattered waves generated in an optical fiber. Stokes and anti-Stokes terms in this scheme refer to SBS waves only

In the FRR, due to its architecture and the scattered waves travelling directions, the different spectral components represented in Fig. IV. 2 will get out from the FRR through different outputs, (see Fig. IV. 3 and Fig. IV. 4). The SBS odd orders gets out from the resonator's second output and SBS even orders gets out from the resonator's third output. This fact will help us in easily distinguishing and characterizing them in the FRR, as we will see later in section IV.2.3.

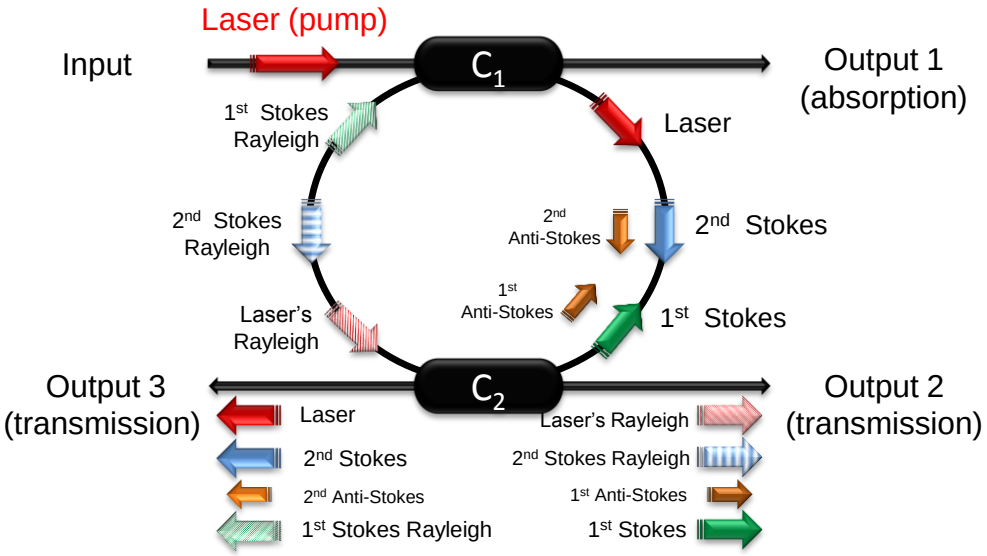

Fig. IV. 3. Double directional coupler fiber ring resonator and the generation of nonlinear optical effects inside. The travelling directions of these waves are illustrated. Stokes and anti-Stokes terms refer to SBS waves only

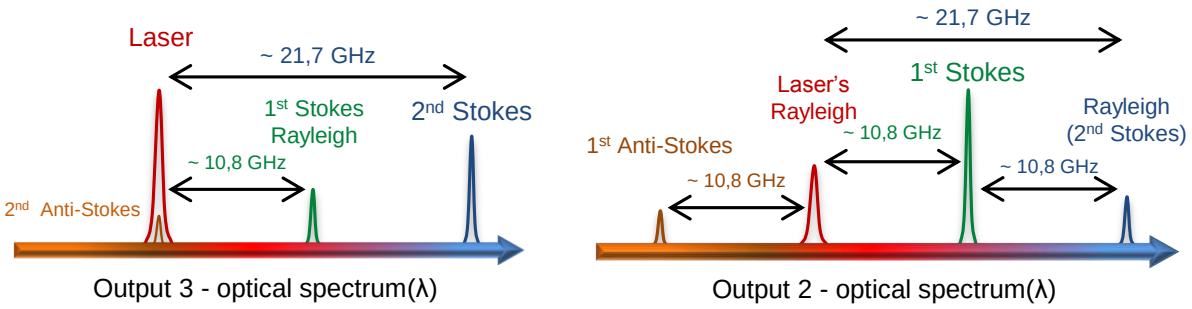

Fig. IV. 4. Optical spectrum representation of the FRR's second and third outputs when the second order SBS is generated. Stokes and anti-Stokes terms refer to SBS waves only

IV.2.1.b *Stimulated Brillouin scattering (SBS) threshold definition*

Many theoretical studies have been made to describe the Brillouin scattering behavior in optical fibers [1], [5] - [8]. Still, these studies were always based on approximations. We can find that they were not in agreement with each other most of the time, especially in what concerns the Brillouin scattering threshold definition [9], its theoretical evaluation [10] and its experimental evaluation methods [11].

Even though, we can find an old common $SBST$ definition that used to be accepted by the scientists in the field. It defines the $SBST$ in optical fiber as the power input at which the scattered power measured at the fiber input becomes equal to the transmitted power measured at the fiber output, [1]. Although based on approximations, leading to less accuracy, this definition seems to be adequate for our aims. Actually, in our FRR based OEO setup, all what we need to know is the optical power at which the first SBS wave is generated. From [1], this $SBST$ definition is given for a SPG fiber by:

$$P_{th-SBS-SPG} = 21 \cdot \frac{A_{eff} \cdot K}{g_0 \cdot L_{eff}} \qquad \textit{(Eq.IV. 2)}$$

where 21 is an approximation factor [10], and A_{eff} (m²) is the fiber effective core area, it is given by:

$$A_{eff} = \pi \cdot \omega^2 \qquad \textit{(Eq.IV. 3)}$$

where ω (m²) is the mode radius (or light spot size radius), that equals to the half of the mode field diameter.

In (Eq.IV. 2), g_0 is the maximum Brillouin gain value for silica fibers (g_0~ 4.10^{-11} m/W), K is the polarization factor {K = 1 in P-M fibers, where the laser carrier and Stokes wave interaction is maximum (due to the polarization state match between the two travelling waves), and K = 1.5 in single mode SMF fibers} and L_{eff} is the fiber effective length.

The nonlinear interactions in the optical fiber depend on the fiber effective length. The longer the effective length is, the more the interactions are efficient and the worse the effects of nonlinearity

are on the transmission link. This effective length depends on the fiber physical length (L) and its linear loss (α_f). It is given by:

$$L_{eff} = \frac{1 - e^{-\alpha_f \cdot L}}{\alpha_f} \qquad \textit{(Eq.IV. 4)}$$

Using (Eq.IV. 2), (Eq.IV. 3), and (Eq.IV. 4), with L = 20 m, α_f = 1.15 10^{-4} m^{-1} and A_{eff} = 86 µm², we get a $SBST$ of $P_{th-SBS-SPG}$ = 2.27 W (33.5 dBm).

The $SBST$ in SPG optical fiber is drastically reduced if the same fiber length is used in FRR geometry and the $SBST$ reduction factor is directly linked to the resonator Q_{Opt}. Actually, if we consider the FRR equivalent length defined in (chapter II), we can extend equation (Eq.IV. 2) to estimate the SBS intra-cavity power threshold ($P_{th-SBS-IC}$) in a FRR. L_{eff} in (Eq.IV. 2) can be thus replaced by the resonator equivalent length L_{eq} given in function of its quality factor in (chapter II). The FRR intra-cavity $SBST$ will be then as follows:

$$P_{th-SBS-IC} = 21 \cdot \frac{A_{eff} \cdot K}{g_0 \cdot L_{eq}} \qquad \textit{(Eq.IV. 5)}$$

Using (Eq.IV. 5) for the 20m-long FRR case with Q_{Opt} = 3.5x10^9, and thus an equivalent length L_{eq} =1180m, $P_{th-SBS-IC}$ will be around 38 mW (15.8 dBm), instead of 2.27 W (33.5 dBm) for the same fiber length in SPG.

However, (Eq.IV. 5) gives only the intra-cavity $SBST$ and not the SBS input threshold. In order to get the resonator input power $SBST$, ($P_{th-SBS-R}$), we have to use the relation given in [12] which gives an approximation of the power enhancement factor between the input power and the circulating power inside the resonator:

$$\frac{P_{th-SBS-IC}}{P_{th-SBS-R}} = \frac{1 - \gamma_1}{1 - t_1} \qquad \textit{(Eq.IV. 6)}$$

In our 20m-long FRR, the C_1 coupler fractional power loss (γ_1) was around 0.7% (0.03 dB) and its transmission coefficient (t_1) was around 98.1%. $P_{th-SBS-R}$ will be then 52 times (17.1 dB) lower than $P_{th-SBS-IC}$, (a power enhancement factor of ~54 was also simulated using ADS) with a value of 0.73 mW (-1.4 dBm).

If we compare $P_{th-SBS-R}$ and $P_{th-SBS-SPG}$, we will find a $SBST$ reduction factor of 3109 (34.9 dB) between the 20m-long fiber length in SPG and the same fiber length in FRR geometry, (of course, the FRR geometry must be optimized in order to get a very high Q_{Opt}, thus a very long L_{eq}). Such a significant $SBST$ reduction in a FRR will make it unfortunately very harmful to our OEO at 10 GHz frequency because this means the presence of high order Brillouin lines in the optical spectrum, thus in the RF spectrum of the OEO (~11GHz, 22 GHz…), see Fig. IV. 2.

IV.2.2 SBS frequency shift and gain spectrum characterization in the 20m-long FRR

In order to inspect the SBS generated inside the FRR, we had to firstly know its frequency shift and gain spectrum. In fact, many Brillouin gain spectrum (BGS) full width at half maximum values have been reported in the literature for silica fibers: $\Delta\boldsymbol{\nu}_B$ = 20 MHz in [5] for SMF28 fibers and 33 MHz in [13] for P-M panda fibers, but less than 10 MHz in [14] also for a P-M fiber. Due to these different reported values, we have chosen an accurate method, well described and explained in [7] and [15], to measure the BGS in our 20m-long resonator under test (RUT).

Of course, in [15], the method is used to describe the BGS in SPG fibers. However, the FRR frequencies are discrete, so the resolution of the BGS characterization method will depend on the resonator FSR. In the 20m-long FRR, the FSR is around 10 MHz, therefore the use of this method can give us a measurement point each 10 MHz frequency step. Despite that, these measurement points are enough to predict the Brillouin gain characteristics in our FRR. The experimental measurement bench is presented in Fig. IV. 5.

The only difference with [15] is that the SPG optical fiber is replaced by the FRR geometry and that we have to use a very low carrier power at the resonator direct input in order to generate only the spontaneous Brillouin scattering at the beginning and not the SBS. This is because of the FRR intra-cavity power enhancement factor (~54).

Furthermore, the laser carrier is stabilized onto the resonator using the PDH loop, and the carrier is phase-modulated at 10 MHz frequency via the EOM used for this purpose. Interestingly, it seems that this phase modulation has no suppressing effect on the SBS (neither on the Rayleigh scattering) in our FRR, contrarily to what it is usually observed in SPG fibers, [2].

The MZM DC bias voltage is set in order to get a double sideband suppressed carrier modulation; this prevents the interference between the laser carrier's two parts circulating inside the resonator in opposite directions. The BGS is then measured by sweeping the RF driving frequency of the MZM. We also use a low RF driving power to get low optical power modulation sidebands, henceforward to be sure that the resulting RF signals visualized at the electrical spectrum analyzer (ESA) are the result of the BGS amplification.

When the wavelength of the modulation upper sideband (USB) falls within the BGS, it takes benefit of its gain and it is thus amplified by the process called Brillouin selective sideband amplification (BSSA) [16]. In this architecture, many optical interactions occur as follows: the direct propagating laser carrier (DPC) generates the spontaneous BGS inside the resonator, then the (counter-propagating) modulation USB interacts with the DPC and grows exponentially via the BSSA and the electrostriction processes, (the DPC is thus depleted), depending on the modulation frequency position regarding the BGS frequency shift.

Similarly, the LSB of the modulation can feed the DPC by the same processes, but this case is insignificant because the LSB power is very low. Finally, the beat note of the DPC and the SBS waves from the resonator's both outputs on a fast PD provides an accurate scan of the BGS using the ESA.

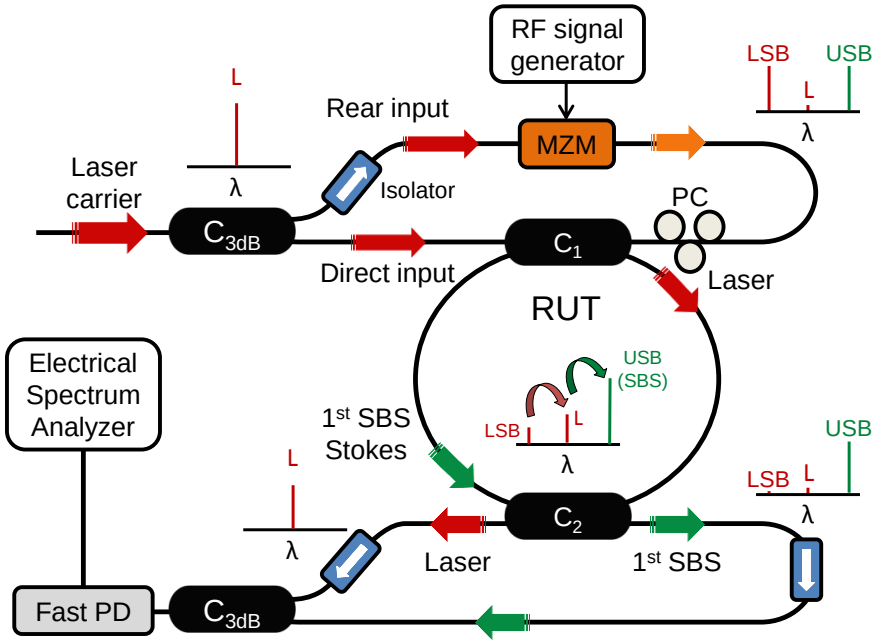

Fig. IV. 5. FRR Brillouin gain spectrum characterization bench. PC: polarization controller; C_{3dB}: 3dB coupler; RUT: resonator under test; LSB: lower sideband; USB: upper sideband

The characterization of the BGS in the FRR has led us to the same conclusion reported in [15] about the polarization dependence of the BGS. We have thus set the polarization of the MZM output and the laser carrier at the FRR inputs in order to get the maximum BGS. The results of the 20m-long FRR BGS characterization are depicted in Fig. IV. 6.

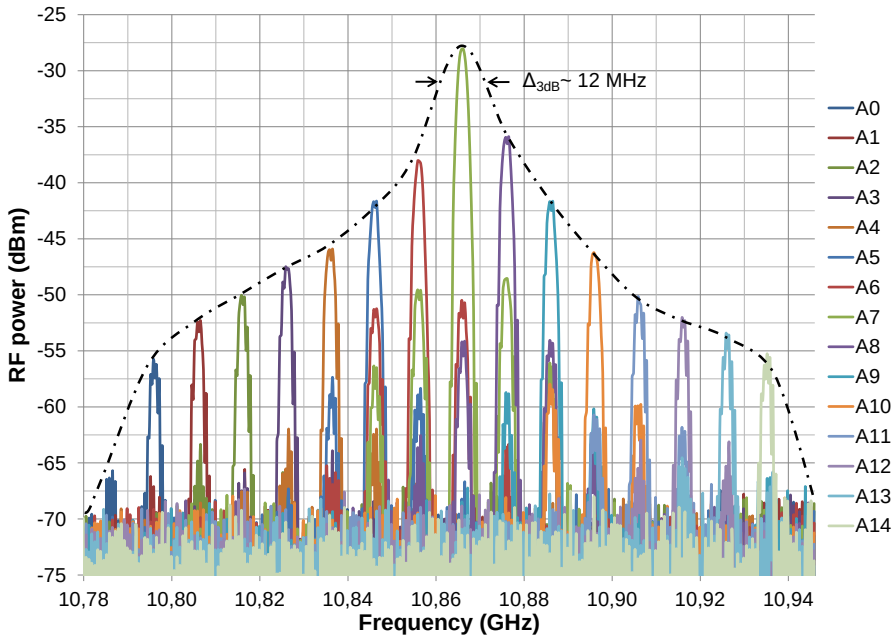

Fig. IV. 6. 20m-long FRR Brillouin gain spectrum characterized using the experimental setup of Fig. IV. 5. We sweep the RF modulation frequency and we take an acquisition on the ESA at each resonator resonance. We manage the polarization of the laser carrier in order to get the maximum BGS.

Fig. IV. 6 results give a Brillouin frequency shift of 10.868 GHz and a gain $FWHM$ of about 12 MHz. Thus, we are sure to get a quasi-single mode Stokes wave operation inside the resonator with a good rejection of the Brillouin superior sidebands (at least 20 dB rejection of the first sidebands; see the A7 acquisition in Fig. IV. 6).

IV.2.3 SBS power characterization in the 20m-long FRR

The power of the different SBS Stokes waves generated inside the resonator were measured, until the fourth order, in function of the laser input power in the optical domain. We used the experimental setup depicted in Fig. IV. 7. Also, the same setup is used to characterize both optical and RF spectrums at the resonator's combined outputs.

First, the laser (pump) beam is split equally by means of a 3dB optical coupler. The first part is sent to the resonator input and the second part is sent to an optical power meter in order to know exactly the power level we are injecting in the resonator. The different measurements are then performed at the resonator's outputs. The optical measurements and spectrum characterization were performed using an Agilent HP 86142A optical spectrum analyzer (OSA) with 0.06 nm resolution and ±1 dB amplitude precision. The RF spectrum characterization was performed using a Rohde & Schwarz 67 GHz ESA.

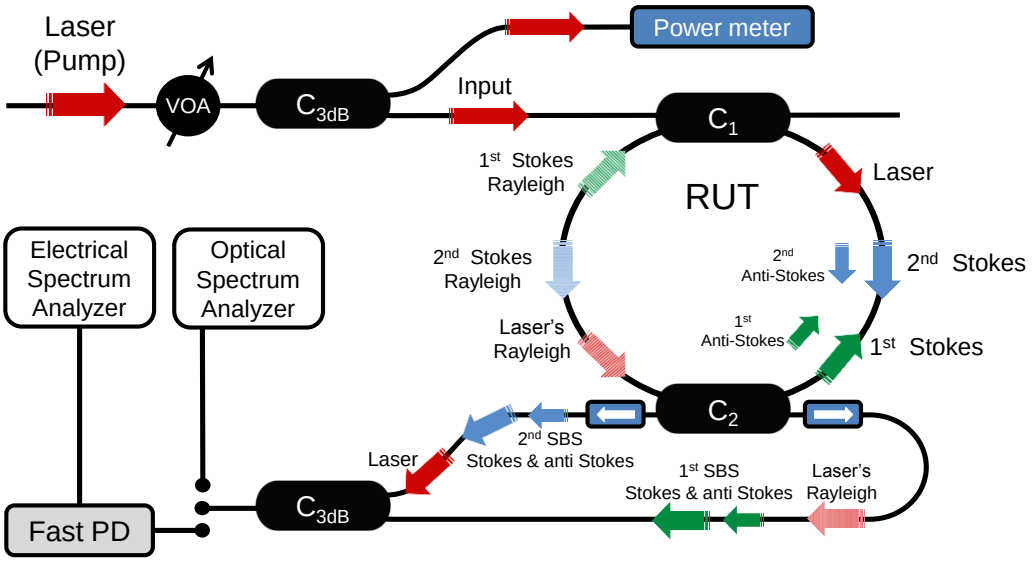

Fig. IV. 7. Experimental setup for power and spectrum characterizations of nonlinear optical effects in the FRR. VOA: variable optical attenuator; PD: photodiode; C_{3dB}: 3dB coupler; •••: optical switch (or coupler). Stokes and anti-Stokes terms refer to SBS waves only

Fig. IV. 8 shows the measured power levels of the first four SBS Stokes waves, the laser carrier and the laser's Rayleigh scattered wave. Certainly, it will be impossible to distinguish each spectrum of these different optical components if we rely only on the OSA resolution. But the resonator geometry helps to easily distinguish between them because of their different travelling directions (see Fig. IV. 3).

At very low input power (-12 dBm), when there is almost no additional nonlinear loss, the ring loss between the input port and the third output port was around 3.7 dB. From Fig. IV. 8, the

experimental first $SBST$ is around -3.5 dBm according to the definition in [1] for SPG optical fibers ($SBST$ *= the power input at which the scattered power measured at the fiber input becomes equal to the transmitted power measured at the fiber output*). This seems to fit with our theoretical approximation on the FRR $SBST$ in (Eq.IV. 5) and (Eq.IV. 6), with 2.1 dB error. This error could be due to the OSA power measurements accuracy or to the $SBST$ definition in [1], which is still an approximation. Indeed, even with 5 dB under the -3.5 dBm input power value, we can always notice that the first Stokes wave is already in a stimulated regime and that the laser output starts to saturate at -8 dBm of input laser power because of the SBS, which starts to convert the laser additional input power via electrostriction. It is obvious that this carrier depletion causes the degradation of the optical link's noise to carrier ratio.

The first Stokes wave also starts to saturate, at -3 dBm of laser input power, when the second Stokes wave starts to be in a stimulated regime and converts the first Stokes wave power. The little increment in the laser output power between -3 dBm and -1 dBm input power levels is due to the second SBS anti-Stokes wave that overlaps with the laser carrier and increases its power (see Fig. IV. 4).

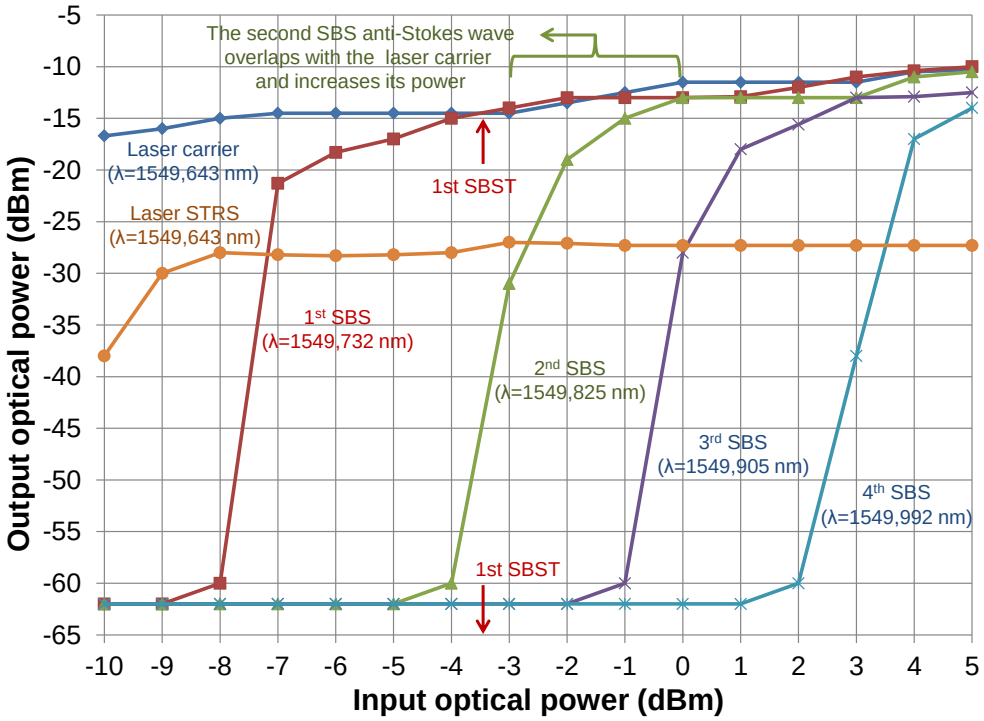

Fig. IV. 8. Experimental power measurements results in the 20m-long FRR of the laser output, laser's Rayleigh scattering and SBS waves, versus the laser input optical power

IV.2.4 SBS spectrum characterization in the 20m-long FRR

The optical spectrum of the resonator's combined outputs has been also measured on the OSA for different laser input power levels using Fig. IV. 7 experimental setup. Optical spectrum results are presented in Fig. IV. 9. The SBS odd orders gets out from the resonator's second output and SBS even orders gets out from the resonator's third output, as already illustrated in Fig. IV. 3. These different SBS orders were spaced by 0.088 nm (10.86 GHz) from each other. Interestingly, the seventh SBS order can be generated with less than 10 mW (10 dBm) laser input power. This seventh mode features less than

8 dB power gap with the laser output power, and is frequency spaced by ~ 76 GHz from the optical carrier(0.616 nm).

Finally, the beat note of this optical spectrum, at 10 dBm input power, has been also measured on the 67 GHz ESA using a fast photodiode (U²t PD, with 70 GHz bandwidth). Results are presented in Fig. IV. 10.

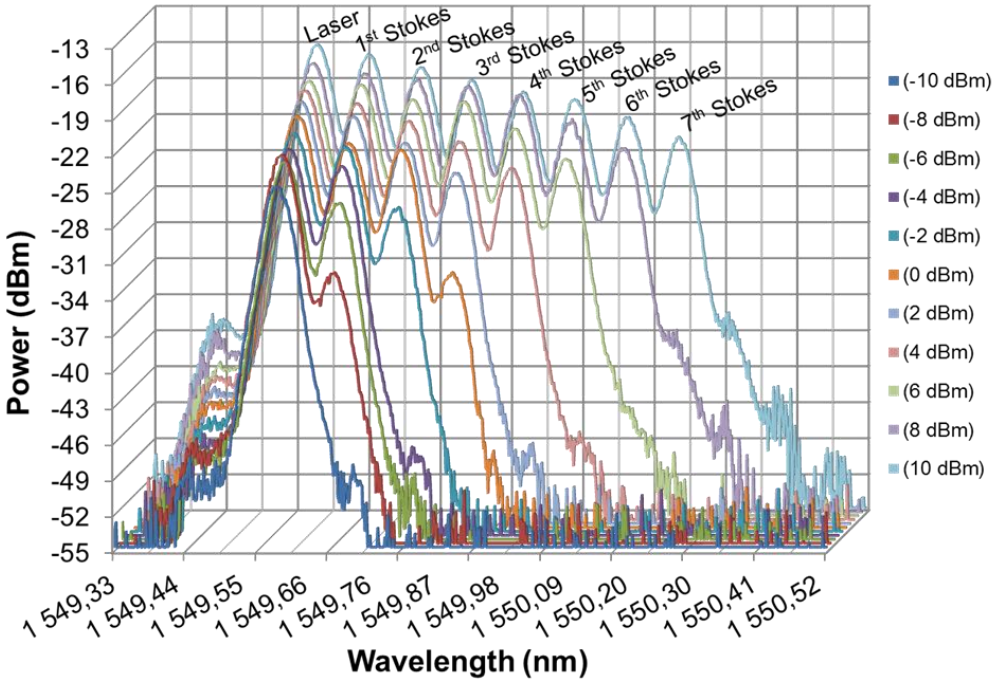

Fig. IV. 9. Multiple acquisitions for the optical spectrum at the 20m-long FRR's combined second and third outputs, for different laser input power levels

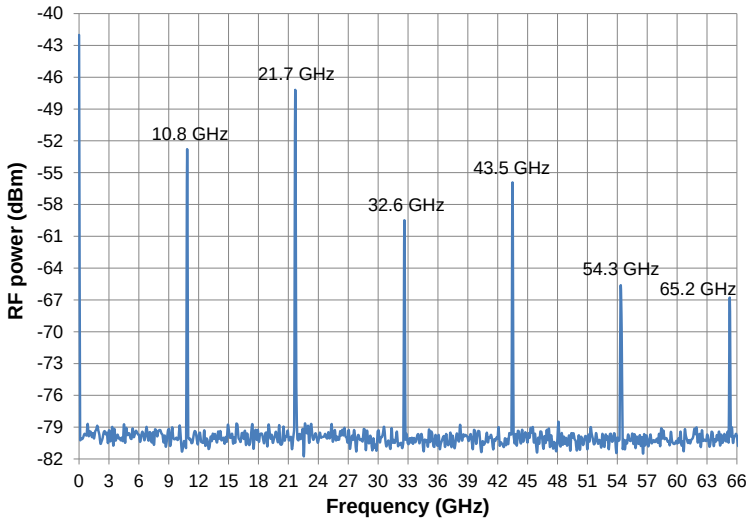

Fig. IV. 10. SBS RF spectrum at the 20m-long FRR's combined second and third outputs, for a 10 dBm laser input power. Span =67 GHz; RBW = 300 kHz; VBW = 20 kHz

The stability of the whole RF spectrum shown in Fig. IV. 10 and each of the Stokes waves depends on the resonator thermal stability, and especially on the laser stabilization to the resonance center by means of the PDH loop. The use of such nonlinear optical effect to generate high spectral purity millimeter wave signals at 76 GHz and above could be very appealing. Furthermore, it is interesting to see that the spectral linewidth of these Stokes waves seems to be in the range of few kHz. This is due to the resonator's narrow bandwidth filtering effect, as a result of its very high Q_{Opt}.

Fig. IV. 11 shows the RF spectrum resulting from the beat note of the first SBS Stokes wave and the laser carrier at the resonator's combined outputs. It has a $FWHM$ of only few tens of kHz (~ 25 kHz). Indeed, it has been reported in [17] - [20] that the laser phase noise is transferred to the emitted SBS Stoke wave after being strongly reduced and smoothed and that the linewidth of the Stokes wave becomes narrower than that of the pump laser. Thus, we have used the Brillouin effect and the BSSA process to generate high power and high spectral purity millimeter wave signals. This study is well detailed in section IV.5 and published in [21].

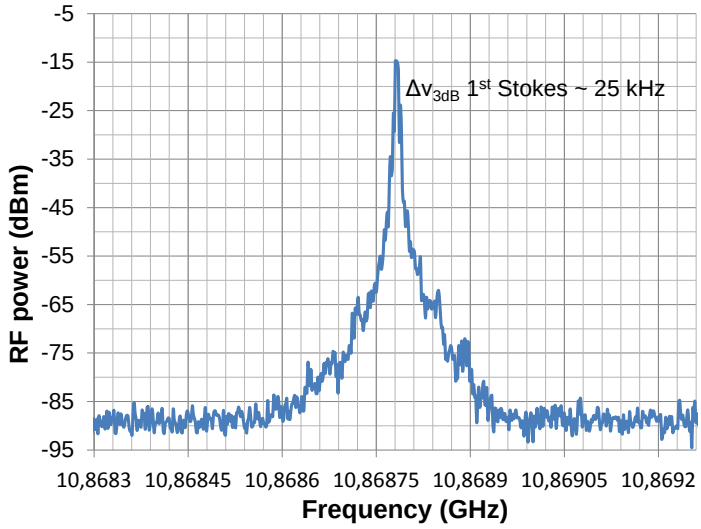

Fig. IV. 11. RF spectrum resulting from the beat note of the first SBS Stokes wave and the laser carrier at the resonator's combined second and third outputs. Span =1 MHz; RBW = 1 kHz; VBW = 200 Hz

IV.2.5 Laser RIN degradation caused by the SBS

Other than the optical link NCR degradation, resulting from the SBS generation, leading to carrier depletion, we have found that the SBS can also affect the laser relative intensity noise (RIN). To do so, we have measured the laser RIN at the FRR third output while injecting a laser power higher than the first $SBST$ at the resonator input (we put a slow PD at the FRR third output and we measure the RIN on the Agilent E5052B SSA using the baseband noise measurement option (BNA)),(see Fig. IV. 12).

The RIN measurements are presented in Fig. IV. 13 where they show a high degradation in the laser RIN between the input and the output of the ring resonator.

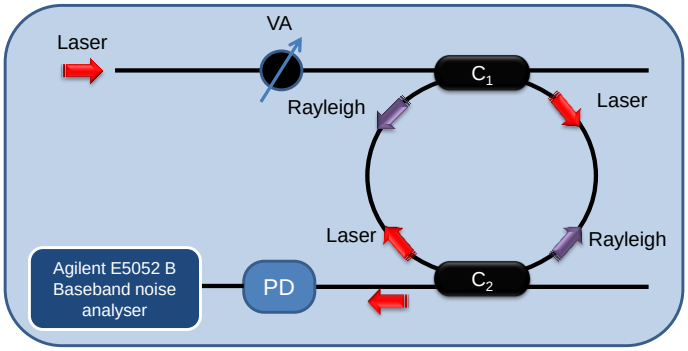

Fig. IV. 12. Measurement bench used to evaluate the laser RIN degradation. See also Image 1 in appendix C

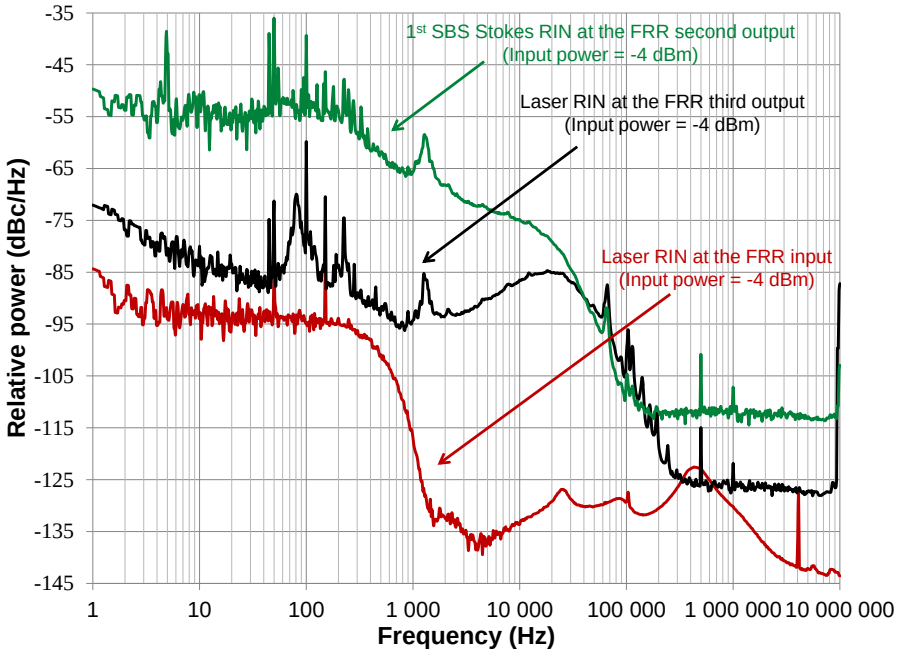

Fig. IV. 13. Laser RIN degradation caused by the SBS generation inside the 20m-long FRR. The first Brillouin Stokes wave's RIN was also measured at the FRR's second output

We have also measured the Brillouin first Stokes wave RIN (in the same way but at the FRR second output). We can see that its low frequency RIN is higher than the laser RIN. However, a lower Brillouin RIN than the laser pump has been reported in [18] and [19]. On the other hand, it has been reported in [20] that the Brillouin RIN becomes better than the laser pump's RIN at higher offset frequencies.

IV.2.6 OEO phase noise degradation caused by the SBS and the Rayleigh scattering

With all these SBS Stokes waves generated around the optical carrier, adding the weak (frequency up-shifted) anti-Stokes waves (Fig. IV. 2), the carrier depletion, the NCR degradation and the laser RIN degradation, we can expect that our OEO RF signal at ~ 10 GHz will be severely affected by the presence of the SBS in the FRR. More precisely, it will be affected by the nonlinear noise conversion processes between all these optical carriers. One of these processes is the DC noise detection by the photodiode of all these waves, which are again folded onto the RF carrier either by the photodiode

nonlinearity or inside the resonator through interference processes. Therefore, the phase noise of a 10 GHz RF carrier of the 20m-long FRR based OEO has been carefully measured with an Agilent E5052 B signal source analyzer at different laser input power levels. The experimental results are depicted in Fig. IV. 14. The study is published in [22].

Fig. IV. 14 shows that the 1/f phase noise observed near the carrier is strongly related to the laser power. Indeed, we can clearly notice a significant reduction in the close-to-carrier OEO phase noise at low optical input power. This phase noise reduction can be about 30 dB at 10 Hz offset frequency between two input optical power levels: 2 dBm (above the second $SBST$) and -10 dBm (under the first $SBST$). The increment in the noise floor is a consequence directly linked to the NCR which degrades when the carrier power decreases.

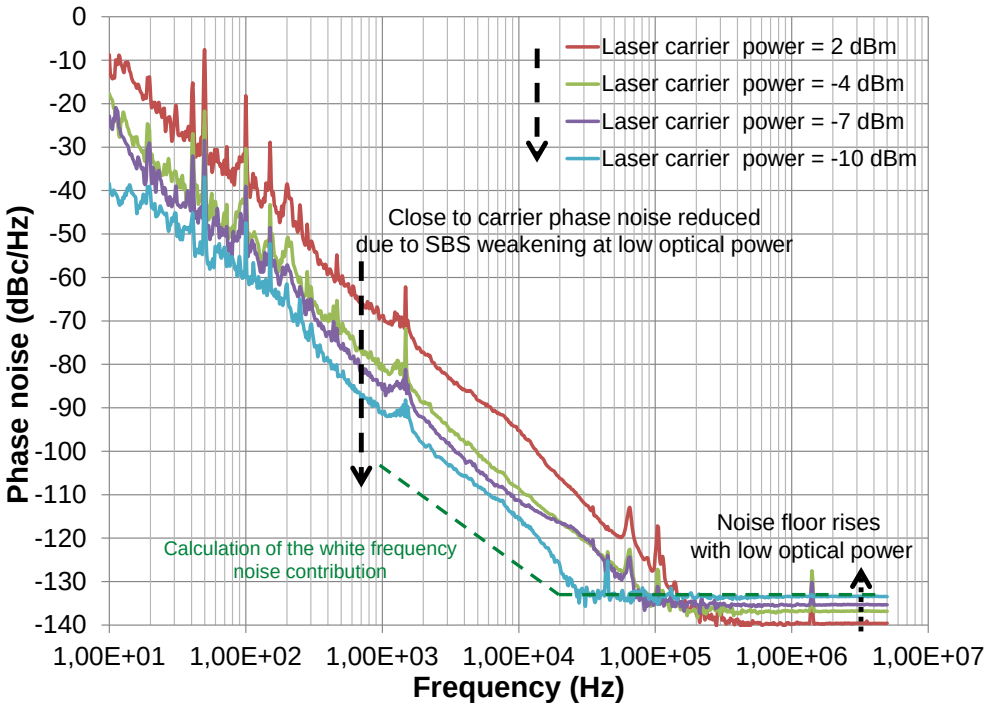

Fig. IV. 14. Phase noise reduction of a 20 meter-long fiber ring resonator based 10 GHz OEO, due to SBS weakening at low optical carrier power. However, the phase noise level remains far from theoretical expectations (dashed curve)

Finally, Fig. IV. 15 shows that the SBS effect on the OEO phase noise can be also easily detected by just monitoring the OEO microwave spectrum behavior when operating at power levels above and under the $SBST$. The signal spectrum becomes clearly smoother at low input laser carrier power.

These results clearly demonstrate that the optical power at the resonator input must be maintained below the first $SBST$ to get an adequately low phase noise in a FRR-OEO. Our computations reveal that, even in this case, this measured phase noise level is not limited by RF amplifier's noise (in the 20m-long FRR OEO case). However, the obtained OEO phase noise shape is still unusual and higher than our theoretical expectations (for example, see the green dashed curve in Fig. IV. 14 related to the white frequency noise contribution), (see chapter III, and [23]). Some of the possible causes of this phase noise

shape and level are the stimulated Rayleigh scattering (STRS), the spontaneous Brillouin scattering and the other laser and PD noise conversion phenomena (as we have already explained in chapter III).

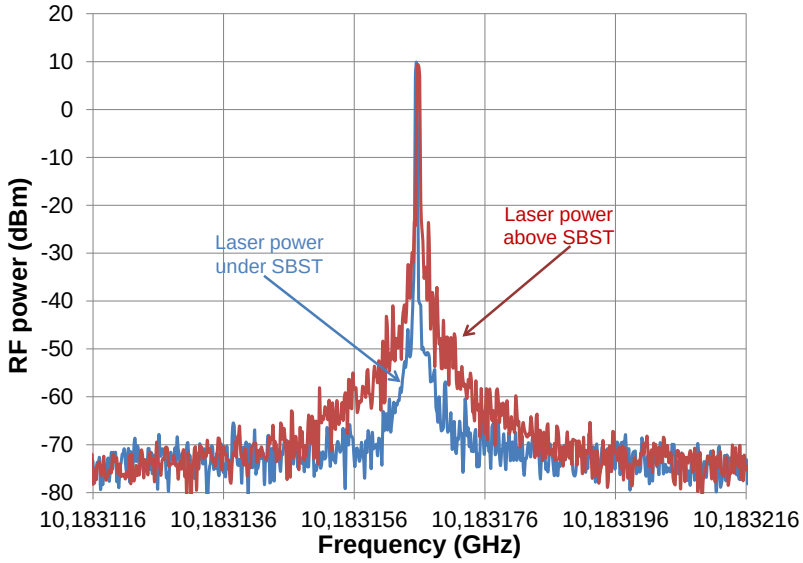

Fig. IV. 15. OEO spectrum at 10 GHz: when operating above the first SBST, and the visible smoothing effect on the spectrum when the laser power is under the SBST. Span = 100 kHz; RBW = 100 Hz; VBW = 200 Hz

In fact, when operating at low optical power, the SBS is reduced, but the spontaneous Brillouin scattering noise contributions still exist and the photodiode nonlinearity may increase because it could not be working at its optimal input optical power (see chapter III). This may lead to many AM and PM noise conversion processes. Moreover, as it has been reported in [2], the Rayleigh noise spectrum becomes broader at low optical input power. Therefore, it can affect the phase noise of the RF signal at higher offset frequencies. This last assumption can explain a main part in the OEO phase noise shape deformation.

IV.3 The Rayleigh scattering in the FRR based OEO

Named in honor of Lord Rayleigh, who has first described the phenomenon in 1871, stimulated Rayleigh scattering was theoretically predicted [24] then observed [25] in liquids in 1967, then in gases in 1968 [26]. It has been extensively studied in bulk materials since then [8]. Yet, the Rayleigh scattering and its applications and noise contribution have not been well studied in optical fibers until recently [27] - [30]. STRS is the elastic scattering of light in a medium composed of particles whose sizes are much smaller than the wavelength of the incident light photons (see illustration in Fig. IV. 16). Elastic scattering means that the light frequency is preserved after being scattered but its travelling direction changes.

As we have previously seen in section IV.2.6, the STRS is suspected to play a role in the OEO phase noise degradation when the SBS is reduced. It could also have an impact on the phase noise shape deformation. Consequently, we have tried to describe its behavior in the FRR, based on the few studies that have been done on the subject in SPG fibers in the literature, in order to reduce its harmful effect on the OEO phase noise.

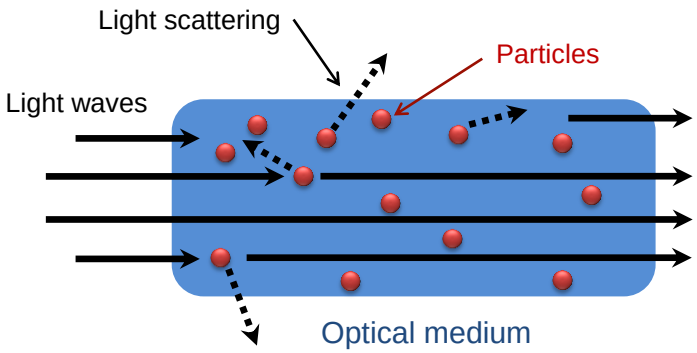

Fig. IV. 16. Rayleigh scattering in an optical medium

IV.3.1 Rayleigh scattering in optical fibers and FRRs

The Rayleigh scattering occurs from random and non-propagating density fluctuations (that is why no significant frequency shift follows). This scattering effect is the key element that defines the linear loss α_f in optical fibers (about 96%) and the ultimate limitation in the Q_{Opt} factor of optical ring and WGM resonators [31]. The spontaneous Rayleigh scattering is associated to density fluctuations, partly caused by local thermal instabilities in the optical medium [27]. These density fluctuations scatter the laser light wave travelling in the optical fiber or in bulk materials [8]. The electrostriction is the dominant effect that generates STRS in optical fibers, which has the potential to degrade the performance of low noise optoelectronic systems [28], [29], such as OEOs.

On the other hand, STRS is not the dominant nonlinear optical effect. In fact, STRS is rapidly buried by the SBS because the SBS gain coefficient is two orders of magnitude higher than that of STRS in long fiber lengths. However, there is an exception for P-M fibers where only one order of magnitude gain difference exists between STRS and SBS (g ~ $1x10^{-12}$ m/W in P-M fibers; [27]). This is because STRS gain is polarization dependent like the SBS. In spite of this, STRS linewidth in optical fibers is much narrower than that of the SBS (~12 MHz) and it is in the order of tens of kilohertz. Therefore, it has been used to build single-longitudinal-mode lasers with very narrow linewidth [30], which are of considerable interest for many applications: optical precision metrology, high-resolution spectroscopy, sensors, and communication systems. Moreover, it has been reported in [2] and [30] that STRS linewidth decreases when the optical power increases.

IV.3.2 STRS power characterization in the 20m-long FRR

In order to describe the STRS behavior in a FRR, we have first measured its power at the 20m-long FRR second output versus the laser input power (see Fig. IV. 8). The STRS power increases with the laser input power but it saturates after the Brillouin scattering process starts to be stimulated. Such a Rayleigh-Brillouin scattering behavior has been already reported and thoroughly studied in SPG optical fibers [2], [27]. It has been noticed in [2] that at power levels above $SBST$, the SBS draws power away from the scattering process, thereby clamping the STRS gain. Besides this, it has been stated that both mechanisms can contribute to the noise induced in RF photonic systems, including delay line OEOs.

IV.3.3 STRS spectrum characterization in the 20m-long FRR

The STRS gain spectrum can experience anti-Stokes frequency shift due to a coupling between the spontaneous thermal fluctuations and the incident light wave. On the other hand, the STRS can experience Stokes shift due to electrostriction; these frequency shifts are of few kHz in P-M fibers and increase at high input optical power, as already observed in [27], [28], and through our experimental results using the FRR. It has been established that our FRRs are made of P-M fibers to prevent two polarization states behavior of the optical carrier inside the resonator. The high intra-cavity power inside the FRR will thus make the frequency shift of the Rayleigh scattering more visible.

In order to describe the STRS spectrum behavior in the FRR, and since the STRS frequency shift is very weak, we have measured the STRS baseband noise at the resonator's second output. The measurements were performed on the Agilent E5052B BNA. We have used almost the same measurement bench and principle as in [2] and [28] to investigate the STRS spectra in SPG optical fibers. It consists of a cross-correlation RIN measurement system with homodyne detection scheme, (see Fig. IV. 17). The coherent detection scheme is used to increase the sensitivity of electrical domain measurements.

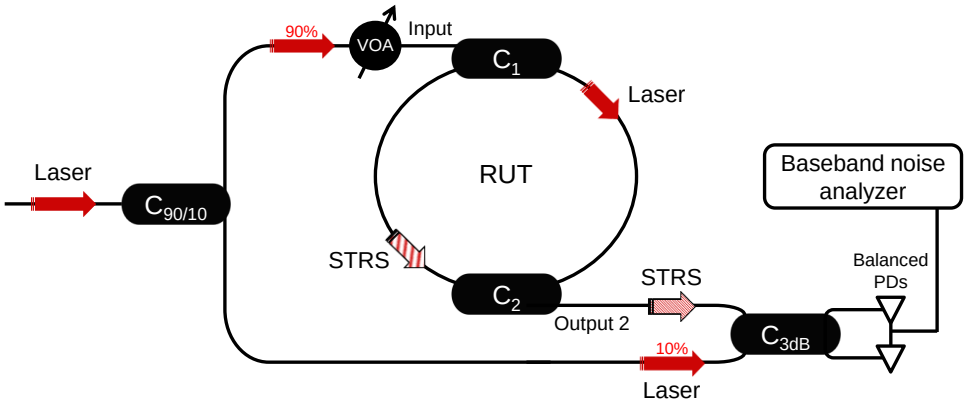

Fig. IV. 17. Backscattered STRS spectrum measurement bench. VOA: variable optical attenuator; PDs: photodiodes; C_{3dB}: 3dB coupler. See also Image 2 in appendix C

We split off 10% of the laser carrier power, used as local oscillator (LO), and we send them directly to one of the inputs of a 2x2 optical coupler. The remaining 90% of the carrier power are sent to the resonator input. The input level is controlled using a calibrated variable optical attenuator (VOA). The carrier is then stabilized onto the resonator using the PDH loop. The backscattered STRS gets out naturally from the resonator at its second output and is sent to the other input of the 2x2 optical coupler. The two outputs of the coupler are then sent to a pair of balanced slow photodiodes. The output current from the balanced photodiodes is then proportional to the product of the STRS and the laser carrier amplitudes. The baseband noise is then measured using the BNA and the results are depicted in Fig. IV. 18.

From these results, we can notice that the close-to-carrier noise (from 10Hz to 200 kHz offset frequencies) increases when increasing the input power. Also, two noise peaks clearly arise around

1.5 kHz and 60 kHz. Those two peaks testify the presence of the Rayleigh scattering in the noise spectrum; we therefore termed them the Rayleigh signature. Moreover, it has been found in [27] that the Rayleigh induced frequency shift is around 1 kHz in P-M fiber, and that it increases at high optical power. However, a 50 kHz Rayleigh induced frequency shift has been reported in [28] for single mode fibers. Both studies confirm the reading of experimental results we have obtained on the Rayleigh induced noise in the FRR.

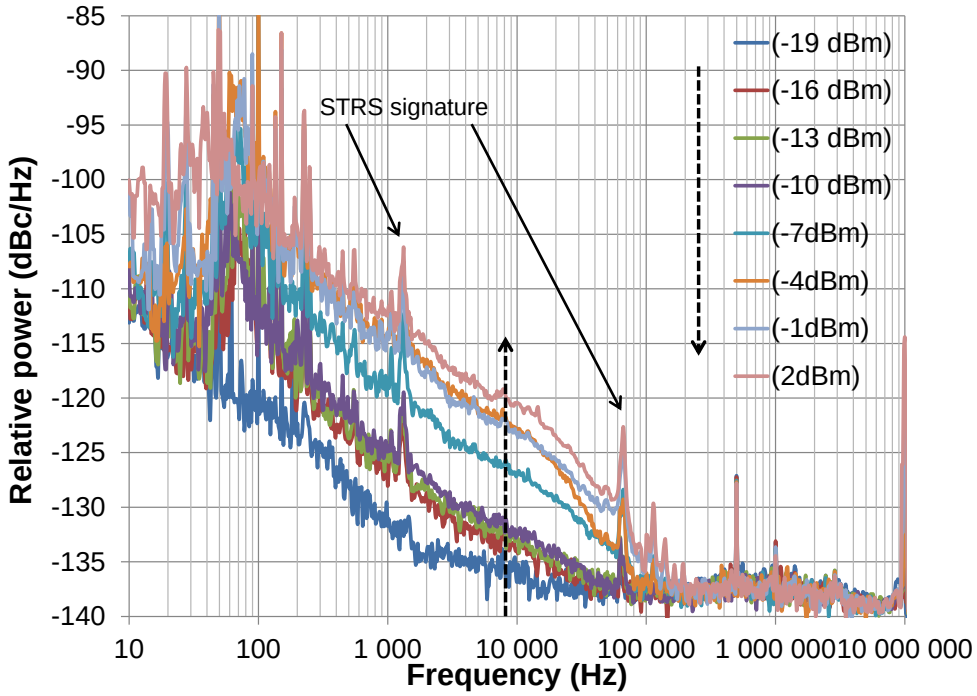

Fig. IV. 18. Baseband noise power spectra at the second output of the 20m-long FRR, measured in the electrical domain using Fig. IV. 17 setup

IV.3.4 Laser RIN degradation caused by the STRS

Of course, the laser's Rayleigh scattered wave is back-reflected and it naturally gets out from the resonator at its second output. However, as intended for our low noise applications using the FRR in an OEO setup, the most important parameter to scale is the STRS effect on the laser carrier directly transmitted through the resonator and getting out from its third output, especially on the laser RIN. We have therefore measured the laser RIN level and behavior at the resonator's third output versus the optical input power (same scheme as in Fig. IV. 12). The laser carrier RIN results are depicted in Fig. IV. 19 (for input power levels ranging from -20 dBm to -6 dBm) and in Fig. IV. 20 (for input power levels ranging from -6 dBm to 7 dBm).

First of all, to witness the noise induced by the Rayleigh scattering inside the FRR, the FRR was replaced with a 3.7 dB optical attenuator (simulating the same optical loss of the 20m-long FRR). We have then measured the laser RIN using a very low input power level (-20 dBm; far below the $SBST$ to be able to discard the SBS effect on the laser carrier) (see Fig. IV. 19).

Now, when the FRR is used, at the same input power level, the RIN spectrum was higher with a different noise shape and the Rayleigh signature clearly appears. We have then measured an almost uniform behavior of the RIN spectrum until -6 dBm input power. This excess in the RIN is generated inside the resonator bandwidth almost because of the Rayleigh scattering and thus it could directly affect our OEO phase noise. Yet, because of the resonator's high Q_{Opt}, this noise is filtered outside of the resonance bandwidth.

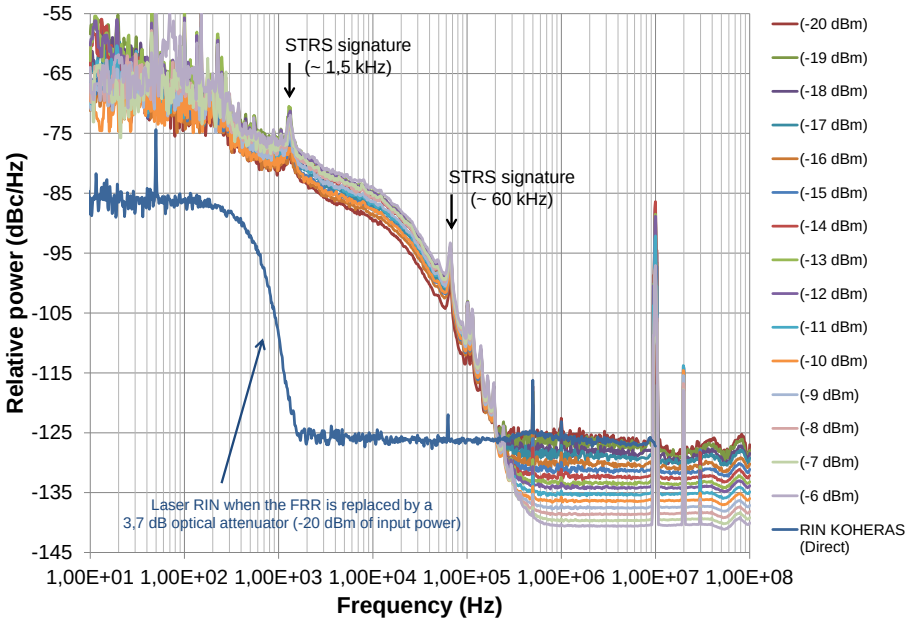

Fig. IV. 19. Laser RIN power spectra at the 20m-long FRR third output, versus the input optical power (from -20 dBm to -6 dBm)

Above -6 dBm input optical power, the RIN level and shape change dramatically (see Fig. IV. 20). These experimental results were repetitive. Also, we can see that the STRS signature is more present around 60 kHz offset frequency at high optical power levels. The peaks at 10 MHz frequency and its multiples correspond to the noise filtered by the 20m-long FRR resonances.

The RIN behavior above -6 dBm input power is likely due to the SBS generation inside the resonator. Indeed, the second SBS Stokes wave appears at -5 dBm input power, (see Fig. IV. 8), and it gets out from the FRR at its third output. Therefore, its baseband noise is detected by the photodiode and mixes with the RIN of the direct transmitted laser wave (also affected by the laser's Rayleigh scattered wave). To this process, we have to add the Rayleigh-scattered waves of the different even SBS Stokes waves. Consequently, the measurements of the STRS effect on the laser RIN are inaccurate above -10 dBm input power (the first $SBST$). In order to be able to only measure the STRS contribution to the baseband noise, it is essential to use a narrow bandpass optical filter at the resonator outputs. This will filter all additional optical components, (eventually SBS Stokes and anti-Stokes waves), around the laser carrier and its own Rayleigh-scattered wave.

To sum up, if this laser carrier RIN degradation is combined with the photodiode's RIN-to-RF AM and PM noise conversion coefficients (see chapter III), an increase in the OEO phase noise can be obviously expected.

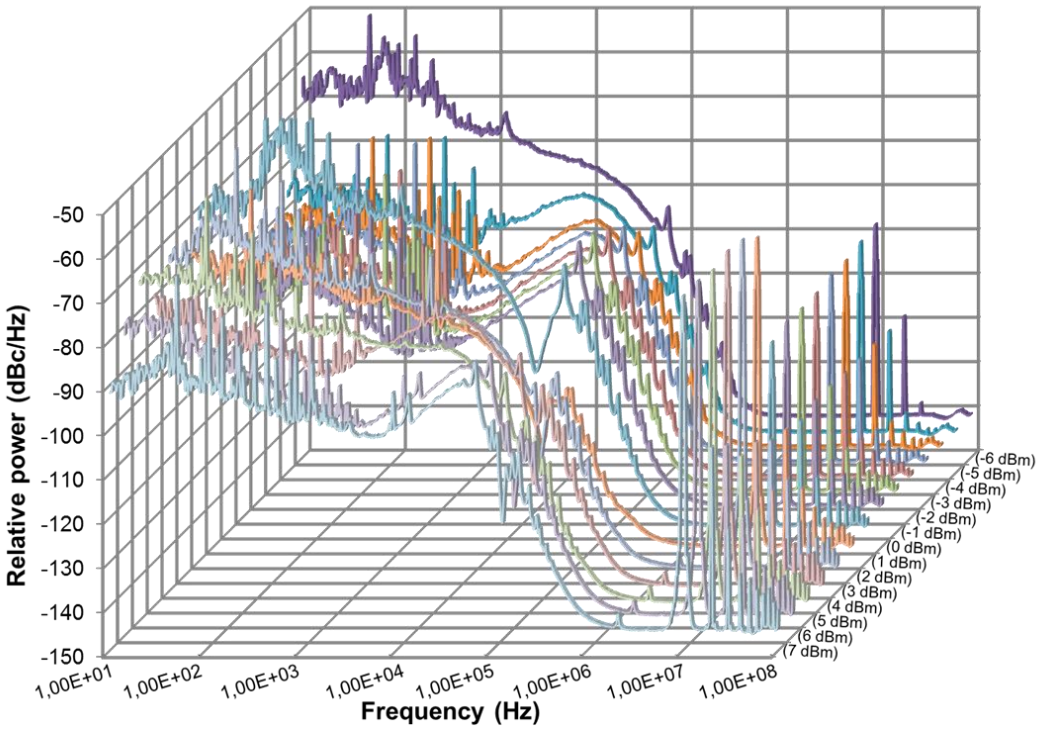

Fig. IV. 20. Laser RIN power spectra at the 20m-long FRR third output, versus the input optical power (from -6 dBm to 7 dBm). Frequencies are represented in logarithmic scale

IV.4 Other nonlinear optical effects and scattering mechanisms inside the FRR

As we have already mentioned, optical fibers have many important parameters that make them an ideal medium to generate nonlinear optical mechanisms. Two of the well-known nonlinear optical effects, other than SBS and STRS, are the Raman scattering and the four-wave-mixing. Finally, we can mention the Fresnel back-reflection at the fiber end faces as a scattering mechanism.

IV.4.1 Fresnel back-reflection

Fresnel back-reflection causes light to change direction in an optical fiber and to return to the source and then to the photodiode. This results in the well-known interferometry noise in optical links. The Fresnel back-reflection occurs most often at the connectors interfaces where the glass-air interface causes the reflection of the light; also it can occur at optical splices in the fiber. It can be avoided by using optical fibers with cleaved connectors (cleaving angle ~ 8°) [32]. In addition, it can be avoided by using index matching gel between the fibers' connectors.

In our FRR architecture, and in all the optical part of the OEO setup, we use angled-polished connectors (FC/APC). Hence, we think that this kind of reflection in our system is thus considerably minimized.

IV.4.2 Raman scattering

Stimulated Raman scattering (SRS), discovered by C. V. Raman in 1928, is an important nonlinear process that can turn optical fibers into broadband Raman amplifiers and tunable Raman lasers [1], but it can also severely limit the performance of multichannel optical links by transferring energy from one channel to the neighboring channels.

SRS, like SBS, falls in the stimulated inelastic scattering category. However, the main difference between them is that optical phonons participate in SRS while acoustic phonons participate in SBS. SRS is capable of transferring a fraction of power from one optical field into another, whose frequency is downshifted (Stokes) by an amount determined by the vibrational modes of the medium. The Raman gain in silica fibers extends over a large frequency range (up to 40 THz) with a broad peak located near 13 THz [1].

Fortunately, the SRS threshold (SRST) is very high compared to other nonlinear optical effects. It is thus not likely to occur in isolated channels of an optical communication system because their power levels are typically below 10 mW. However, it becomes a limiting factor for multichannel systems because of the Raman-induced power transfer process among the different channels. The SRS threshold in SPG optical fibers is given from [1] by:

$$P_{th-SRS-SPG} = 16 \cdot \frac{A_{eff} \cdot K_R}{g_R \cdot L_{eff}} \qquad \textit{(Eq.IV. 7)}$$

where g_R is the Raman gain (g_R ~ 0.65x10^{-13} m/W; [33]) and K_R is the Raman polarization factor (SRS gain is also polarization dependent and K_R ranges from 1 in P-M fibers to 2 for a scrambled polarization). A_{eff} and L_{eff} have the same definitions as for SBS.

In the FRR case, even with the high power enhancement factor due to the resonance effect, we are far from the outbreak of the SRS inside the resonator. In fact, if we take the FRR equivalent length approximation mentioned in (chapter II), (L_{eq}= 1180m for the 20m-long FRR), and the Raman threshold definition in (Eq.IV. 7), we will find that the total intra-cavity power needed to generate the SRS inside the 20m-long FRR is about 18W. This means, considering (Eq.IV. 6), a laser input power of at least 350 mW (25.5 dBm) at the resonator input.

Of course, the generated, equally spaced, SBS waves may act in the FRR as a multichannel system. Thus a Raman-induced power transfer among these different channels may occur. However, SRS has not been observed experimentally in the 20m-long FRR, even in the presence of the seventh SBS Stokes wave.

IV.4.3 Two and four wave mixing

Four-wave mixing (FWM), a third-order nonlinear optical effect, is a type of optical Kerr effect. It occurs when light of two or more different wavelengths are launched into an optical fiber with sufficient optical power, giving rise to a new wave known as an idler [1]. Generally speaking, FWM is a kind of optical parametric oscillation and behaves like intermodulation phenomenon in optical systems, similar

to the third-order intermodulation in microwave systems. Through a classical FWM process, three optical waves at frequencies f_i, f_j and f_k ($i \neq j \neq k$) generate a fourth optical wave at a frequency f_{jik} given by:

$$f_{ijk} = f_i + f_j - f_k \qquad \textit{(Eq.IV. 8)}$$

FWM can also arise if f_i and f_j are of equal frequencies, i.e. in the presence of only two optical signals. In this case, the more specific term "degenerate four-wave mixing" (DFWM) is used (also called two wave mixing), and a less efficient f_{jik} may be written as:

$$f_{ijk} = 2f_i - f_k \qquad \textit{(Eq.IV. 9)}$$

The result of FWM and DFWM between three different frequencies can lead to the generation of twelve new waves (three of these new waves overlap), as it has been mentioned in [34]. The number of interfering products increases rapidly with the number of signals (see Fig. IV. 21 (a)). A critical case occurs, when the spacing between the three input frequencies is the same: $\Delta f = f_j - f_i = f_k - f_j$. In this case, the three input signals overlap with three of the twelve newly generated waves, (see Fig. IV. 21 (b)).

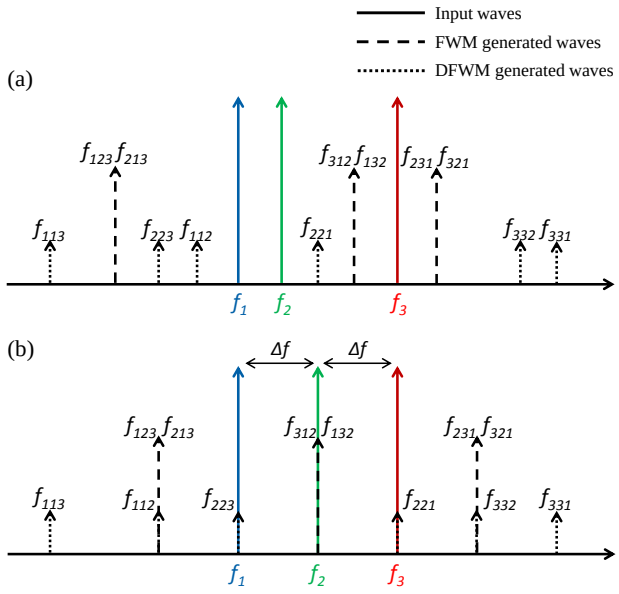

Fig. IV. 21. Illustration of the frequencies of the three input waves and the twelve generated waves via four-wave mixing and degenerate four-wave mixing processes (two-wave mixing), for unequally (a) and equally (b) spaced input waves. According to relations (Eq.IV. 8) and (Eq.IV. 9)

FWM (and DFWM) is a polarization-dependent process and inversely proportional to the fiber dispersion (more dispersion means less efficiency). It requires phase-matching and high optical power to build up efficiently along the optical fiber. In optical fibers, it can be both harmful and beneficial, depending on the application.

In our FRR, the critical case mentioned above may occur. The generated SBS waves inside the FRR are equally spaced (10.86 GHz) and the phase-matching condition is automatically satisfied because they are all resonant in the FRR. They create each other and they have enough intra-cavity power due to the resonance effect (see Fig. IV. 9). The only thing that may prevent an efficient FWM process in our FRR is the dispersion in the optical fiber we used to fabricate the resonator (D_λ ~17 ps/nm.km). Fortunately, we have not found any trace of the FWM in the optical spectrum at the resonator's different outputs, even in the presence of the seventh SBS wave while using the OSA with high amplitude sensitivity (~ -60 dBm). This is probably due to the high dispersion in the fiber used to build the resonator.

IV.5 High power and high spectral purity millimeter-wave (MMW) signals generation using the Brillouin selective sideband amplification inside the 20m-long FRR

Extremely high frequency signals generation and distribution using optical techniques represents an interesting challenge. These techniques can be used in many applications, from telecommunications to radio-astronomy, and at distances ranging from few meters (e.g inside a plane or a satellite) to few kilometers (e.g. antenna networks) and even several tens of kilometers (e.g inter-laboratories clock comparison). Many millimeter-wave (MMW) sources, carried using optics, have been demonstrated [35]. Among these, two methods have become quite popular because they do not require an ultra-high frequency optical modulator: the one using the beat note of a dual frequency (or mode locked) laser where two modes are sharing the same cavity and the same gain [36], and the one based on heterodyning of two independent lasers [37]. Using a dual frequency laser is particularly interesting to get high output power and good NCR in the MMW range. Furthermore, we benefit from the fact that noise in the system affects each of the laser's two modes equally. This leads to a noise reduction in the RF domain. On the other hand, either in the case of dual mode laser or heterodyning of two independent lasers, it is difficult to get a strong correlation between the two optical modes, thus an efficient rejection of the laser phase noise. Accordingly, the beat note is degraded, and therefore the resulting RF signal.

Contrarily to the above mentioned methods, frequency multiplication technique is quite easy to set up and only requires a Mach-Zehnder modulator [38]. With this approach, the optical harmonics generated by the MZM nonlinearity are strongly correlated so that the noise is equally distributed in the optical domain and thus cancelled in the RF domain. The only problem using this method is low power levels of the harmonics [38], particularly in case of high order harmonics, which thus degrades the NCR. It is therefore motivating to find a way to amplify the different optical harmonics while preventing a gain competition between them. Fortunately, optical harmonics can be independently amplified thanks to the Brillouin selective sideband amplification concept (BSSA) [16].

In this section, we present a millimeter-wave signal generation setup based on the frequency multiplication approach, using a MZM to generate high optical modulation harmonics, combined with the high Q_{Opt} 20m-long FRR in order to generate a selective Brillouin gain spectrum at each of these optical harmonics. This will independently amplify the optical harmonics, while maintaining a low close to the carrier phase noise of the generated MMW signals. The 20m-long FRR used in the BSSA MMW signals generation (BSSA-SG) system is depicted in Fig. IV. 3.

The BGS in the 20m-long was less than 12 MHz, as we have already seen in section IV.2.2. Therefore, with a resonator FSR of 10 MHz, the generated Brillouin (amplifying) lines inside the resonator feature a single mode operation and automatically resonate, thus taking benefit of the resonator's power enhancement factor. Now even if the generation of the Brillouin scattering is known to be very harmful to optical links [2] and optical systems like optoelectronic oscillators [22], it can be on the contrary useful in many other applications: such as low noise and ultra-narrow linewidth Brillouin lasers [18] or in modulation depth enhancement of optically carried RF signals [14]. Our aim here is to use the Brillouin effect, generated at very low threshold inside the resonator, to selectively amplify the different optical modulation harmonics generated in the MMW range, and thus generate high power and high spectral purity MMW signals.

IV.5.1 Millimeter-wave signals generation setup

The BSSA-SG setup is illustrated in Fig. IV. 22. We use the Koheras laser at 1.55µm wavelength (with its 1 kHz linewidth). The optical carrier is stabilized to the FRR via the PDH loop, then modulated via a 20Gbits/s EOspace MZM DC biased at $V_{\pi/2}$ in order to get a linear modulation and thus high order upper and lower sidebands around the laser carrier, while keeping a high carrier power to be able to generate SBS in the FRR. Around $V_{\pi/2}$ DC bias, the MZM transfer function is odd, and only odd harmonics are generated: 1st, 3rd, 5th… [38]. At that moment, we use the Brillouin gain generated by the FRR every 10.87 GHz multiple in the optical spectrum to amplify these optical harmonics.

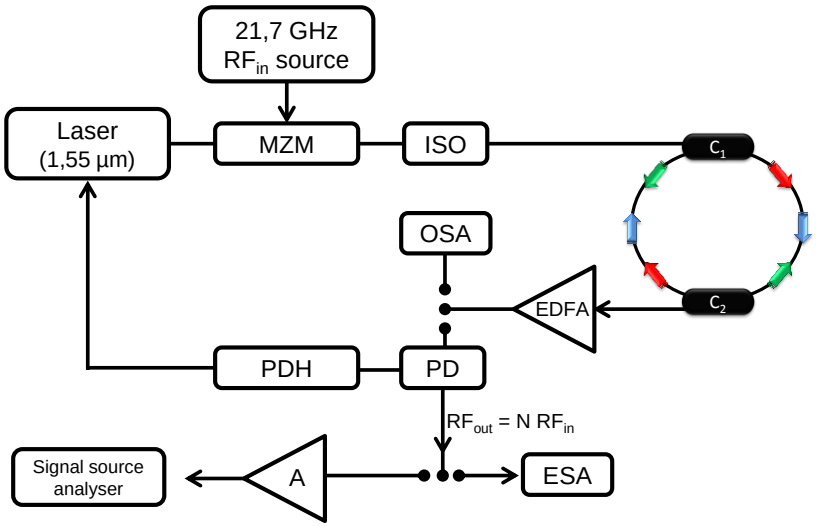

Fig. IV. 22. BSSA-SG setup using a 20m-long FRR; ISO: isolator; EDFA: erbium doped fiber amplifier; OSA: optical spectrum analyzer; PD: photodiode; PDH: Pound-Drever-Hall laser stabilization system; ESA: electrical spectrum analyzer; A: MMW amplifier; •••: optical and RF switches (or couplers). See also Image 3 in appendix C

On the receiver side, we visualize the optical spectrum at the FRR third output on the Agilent HP 86142A OSA, and then we send it to a 75 GHz U^2T photodiode. At the photodiode output, we visualize the RF spectrum on the 67 GHz Rohde & Schwarz ESA and then we analyze the signal phase noise using the Agilent E5052B SSA, which uses two equilibrated Agilent 50-85 GHz external mixers, preceded by a Spacek-Labs MMW amplifier.

IV.5.2 Optical characterization

In order to optically characterize the efficiency of the BSSA-SG technique, the spectrum of the laser carrier at the resonator input and the spectrum at the resonator third output were visualized on the OSA. Results are depicted in Fig. IV. 23.

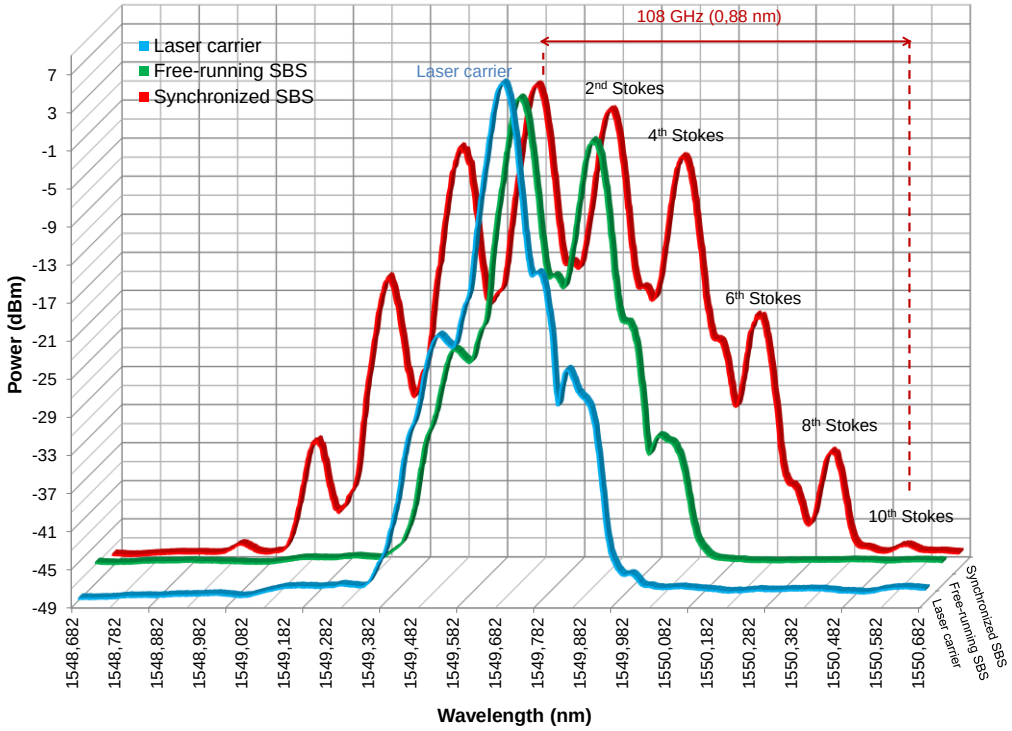

Fig. IV. 23. Optical spectrum of the laser carrier at the resonator input, and optical spectrum at the resonator third output when the SBS is in a free-running behavior and when modulating the laser carrier at 21.7 GHz with a 20 dBm RF seed signal

From Fig. IV. 23, we can see that with an input laser carrier power around 2 dBm, at least the second order SBS Stokes wave is generated (see the green curve in Fig. IV. 23), spaced by 21.742 GHz (0.176 nm) from the laser carrier. We call it here the free-running SBS.

Now if a RF seed signal, called seed signal and having the same frequency of the second SBS line, is injected to the MZM with a high RF power level (20 dBm), the modulator will produce odd upper and lower sidebands (±21.742 GHz, ±65.226 GHz…) around the laser carrier. It is well known that the higher the order of these harmonics is, the lower is their power [38]. However, due to the Brillouin selective gain spectrum created by the carrier inside the resonator, especially Stokes lines gain, these harmonics will be amplified by the BSSA process, and we will be able to measure even the tenth modulation harmonic, spaced by 108 GHz (0.88 nm) from the carrier (see the red curve in Fig. IV. 23). Additionally, the Brillouin scattering generation can also help to increase the optical modulation depth [14].

IV.5.3 RF characterization

The resulting beat note of the third output on the 75 GHz photodiode has been observed on the ESA and results are presented in Fig. IV. 24. The 2 dBm input carrier leads to a high RF power free-running SBS wave at 21.74 GHz and a weaker one at 43.4 GHz frequency. In addition, we can find a 10.87 GHz component in the RF spectrum. This RF component is created as a result of the beat note of the laser carrier wave, the second SBS Stokes wave and the first SBS Stokes Rayleigh-scattered wave as already mentioned in Fig. IV. 4.

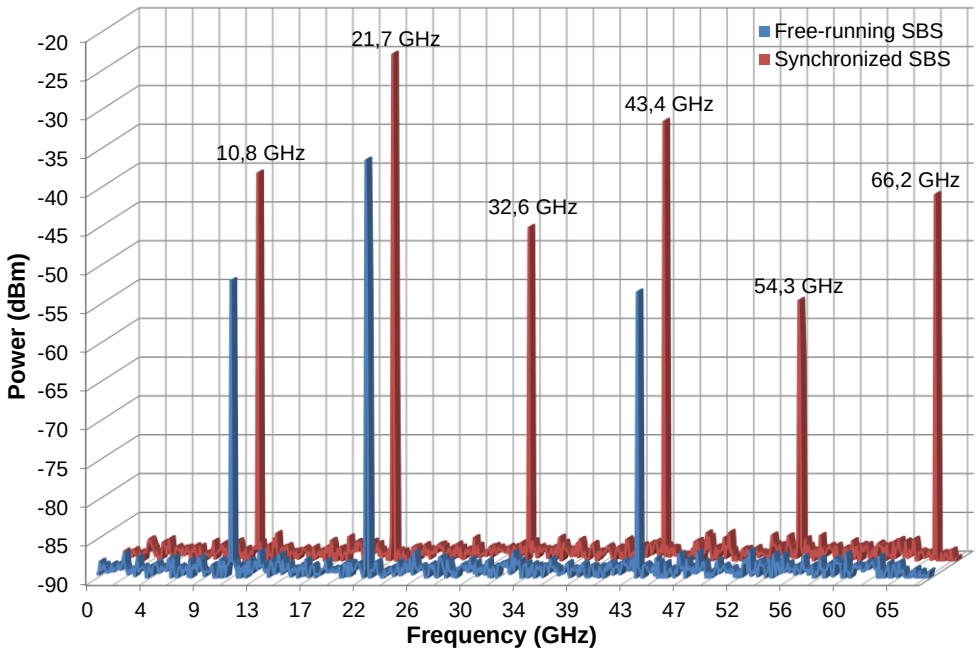

Fig. IV. 24. RF spectrum of the resonator third output when the SBS is in a free-running behavior and when modulating the laser carrier at 21.7 GHz with a 20 dBm RF seed signal. A 6dB attenuator was used at the ESA input

When the laser carrier is modulated by the 21.74 GHz RF seed signal with a 20 dBm power level, the RF components at the resonator third output will be considerably amplified (odd harmonics) and we can especially notice the creation of a 65.2 GHz component with a -36 dBm power level (a 6 dB attenuator was used at the ESA input). The 10.8 GHz, 32.6 GHz and 54.32 GHz even harmonics exist because of the same reason mentioned in the paragraph above as well as a non-perfect linear modulation response of the MZM.

In order to evaluate the power gain difference between the BSSA-SG method and the classical frequency multiplication method [38], the first and third harmonics power levels were measured versus the 21.7 GHz RF seed signal power. For the classical method, the resonator was replaced by a 3.7 dB optical attenuator to simulate its intrinsic and nonlinear losses to be in the same conditions as for the BSSA-SG method. Results are presented in Fig. IV. 25.

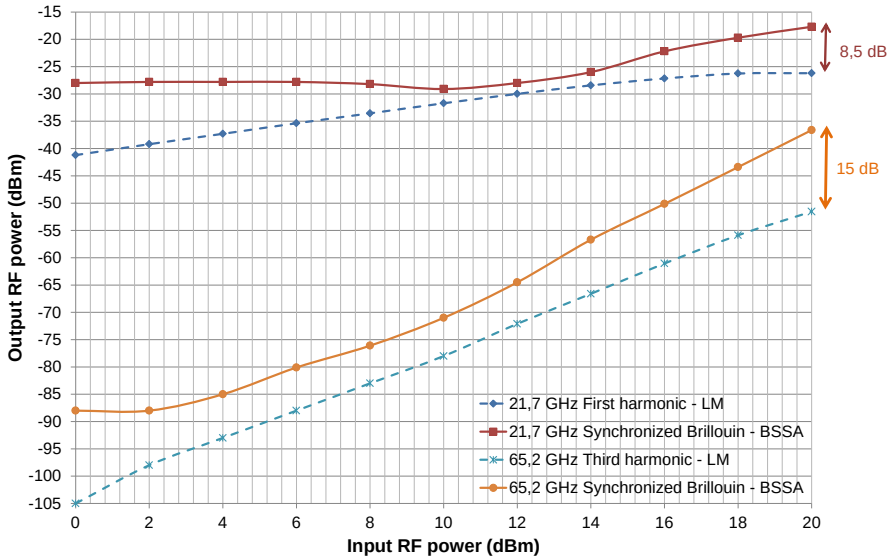

Fig. IV. 25. RF output power of the first and third harmonics versus the RF 21.7 GHz seed signal power: when using the classical frequency multiplication method and when BSSA-SG technique is used

The results in Fig. IV. 25 clearly show a real power gap between the two methods. Moreover, this power gap seems to increase with higher harmonic orders. For example, an 8.5 dB power gap is obtained for the first harmonic signal, while a 15 dB power gap is obtained for the third harmonic signal. This demonstrates the increasing behavior of the BSSA-SG power gain efficiency.

IV.5.4 Noise characterization

Besides the measurements performed in the RF domain in the above section, an important parameter to be characterized is the phase noise of the MMW generated signals via the BSSA-SG method. For this purpose, the phase noise spectrum of the Brillouin waves at 21.7 GHz and 65.2 GHz has been measured using the SSA. Fig. IV. 26 shows the phase noise of the free-running SBS at 21.7 GHz, the synthesizer RF seed signal at the same frequency, and finally the phase noise of synchronized SBS wave at 21.7 GHz via the BSSA-SG method.

Moreover, the impact of BSSA-SG on the spectral purity of the different free-running SBS components can be easily noticed even when using the ESA only, (see Fig. IV. 26 – up-right corner). Fig. IV. 26 results clearly demonstrate that the BSSA-SG method seems to not only amplify the desired harmonics, but it also significantly reduces the Brillouin gain spectrum noise. As a result, the Brillouin gain will get almost the spectral shape and purity of the seed signal through synchronization, so then a more stable amplification process is obtained.

Finally, the phase noise of the generated 65.2 GHz signal has been measured and compared to the original 21.7 GHz RF seed signal phase noise and to its theoretical phase noise after being multiplied by 3, (+20log(M) where M is the frequency multiplication factor), see Fig. IV. 27.

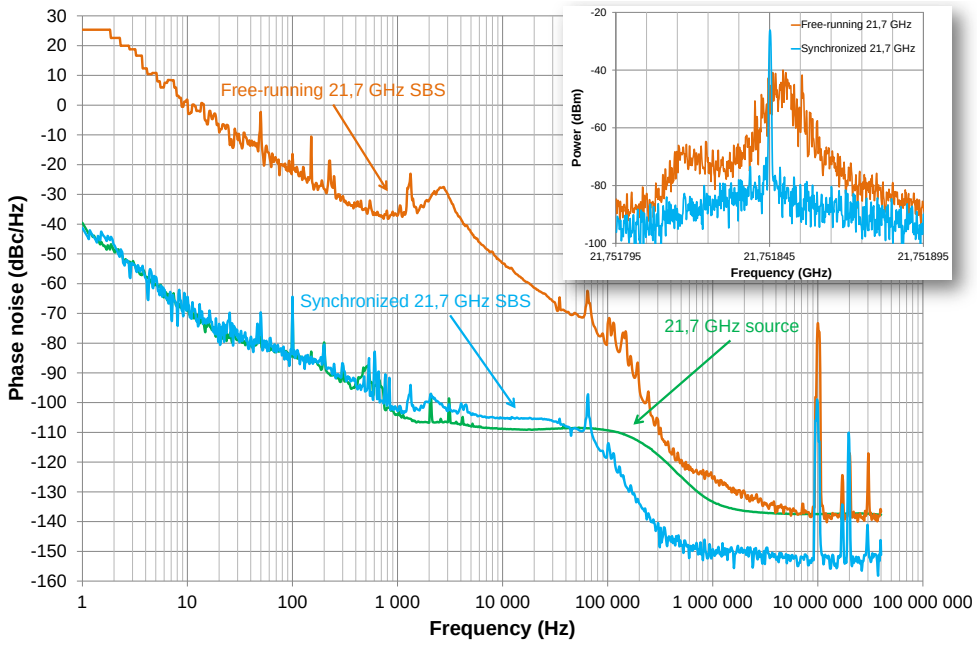

Fig. IV. 26. Phase noise of the free running SBS wave at 21.7 GHz, the synthesizer RF seed signal at the same frequency, and the synchronized SBS wave via the BSSA-SG method. In the up-right corner, the free-running SBS wave spectral purity enhancement was visible on the ESA after being synchronized by the RF seed signal (ESA: 100 kHz span, 30 Hz RBW and VBW)

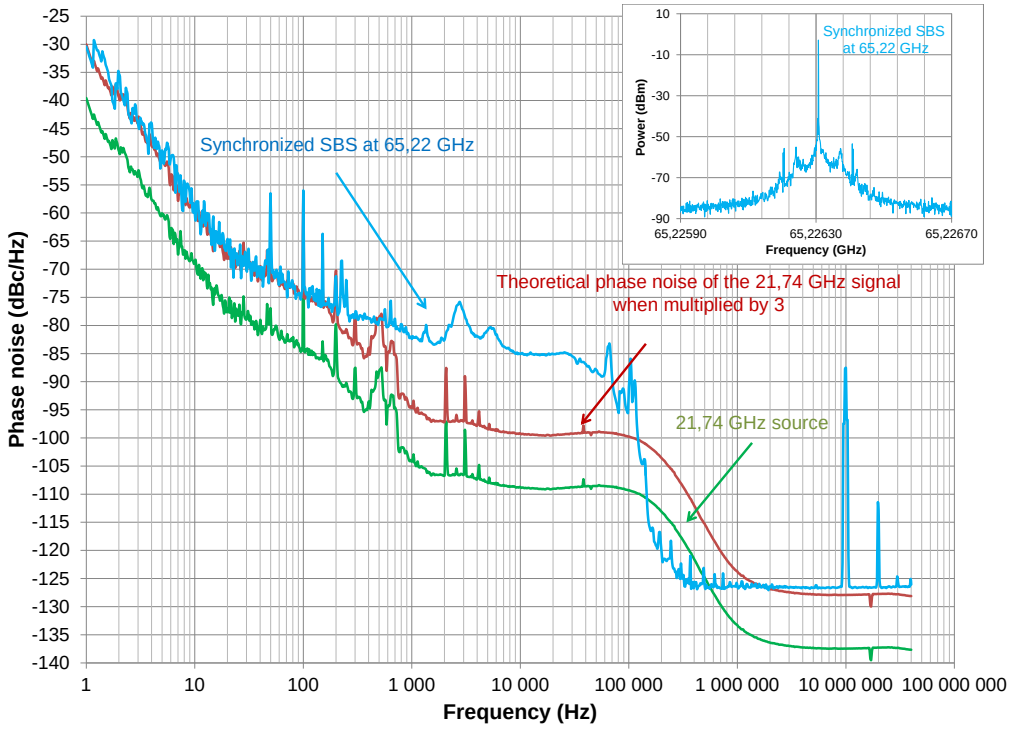

Fig. IV. 27. Phase noise of the synthesizer seed signal at 21.7 GHz, of the synthesizer phase noise multiplied to 65.2 GHz and of the generated 65.2 GHz signal via BSSA-SG method. In the up-right corner, the spectrum of the 65.2 GHz generated signal was visualized on the ESA after being synchronized by the RF seed signal (ESA: 100 kHz span, 100 Hz RBW and VBW)

Form these results, we can notice that the synchronized signal at 65.2 GHz features the same phase noise spectrum as if it was generated by the classical multiplication method, at least in the close to carrier noise range from 1 Hz till 200 Hz offset frequencies. The excess noise in the 200 Hz to 80 kHz frequency band seems to be generated either by the different Rayleigh-scattered waves of the different optical spectrum components or by the noise of the Brillouin gain. Even the PDH laser stabilization loop could have a part in this excess noise. The rapid decrease in the phase noise after the 40 kHz offset frequency is due to the FRR filtering effect. The PDH noise part could be reduced if a double PDH stabilization technique, controlling the laser and the resonator at the same time, is used. This has been already reported in [39], were interesting MMW signals generation system stability and accurate tunability were demonstrated.

Finally, using our BSSA-SG method, higher order and low phase noise MMW signals generation is possible because there is theoretically no limit in the generation of higher order Brillouin lines in such resonators; The only limit will be at the receiver side, especially the photodiode bandwidth.

IV.6 New passive 100m-long FRR, optimized and immunized against nonlinear optical effects

Among all nonlinear optical effects mentioned in sections IV.2, IV.3 and IV.4, we have seen that the Brillouin and Rayleigh scatterings can both have the most harmful effects on our FRR characteristics (Q_{Opt}, NCR…) and therefore on the FRR-OEO phase noise.

Of course, by reducing the optical power, we can limit the SBS effect and reduce the OEO phase noise [22]; yet, we will still have the spontaneous Brillouin scattering and the STRS effects. In addition, we will have a laser carrier RIN degradation, the NCR degradation and the PD increased nonlinearity when a low optical power is used etc... Therefore, high spectral purity signal generation using the FRR based OEO will not be achieved unless we find a solution to suppress all these nonlinear optical effects. It is thus crucial to find a way to mainly suppress the SBS and to reduce the STRS effect, while keeping a high Q_{Opt} and a low transmission loss through the resonator.

IV.6.1 SBS and STRS suppression methods

While frequency or phase modulation of the laser carrier is the most reported method in the literature to suppress the STRS (also the SBS) in optical fibers [2], [40], many studies on SBS and on related suppression methods have been reported [13], [15], [41] - [44]. Actually, the frequency or phase modulation technique is based on spreading the signal spectrum of the laser carrier. This method can efficiently reduce the SBS and STRS in optical fibers by more than 50 dB, [2]. On the other hand, spreading the signal spectrum may interfere with low phase noise coherent detection schemes similar to those proposed in [5]. Likewise, as we have previously mentioned in chapter III, the PDH loop we use to stabilize the laser carrier to the resonator, already carries out a 10 MHz phase modulation of the carrier for stabilization purpose. Conversely, it seems to have no visible effect on the SBS or on the STRS in the FRR case. Moreover, even when the modulation frequency has been reduced to be between 10 kHz and 100 kHz, which corresponds to the polarization fluctuations frequencies in glass fibers [40] (amplified by the incident optical carrier), the same negative results have been obtained. This is probably because of the discrete resonant frequencies of the FRR.

It is well-known that BGS characteristics depend on different parameters: they depend strongly on the fiber temperature (when the temperature increases, the SBS frequency shift and gain increase, and the BGS bandwidth decreases), and on the fiber strain (when the strain increases, the SBS frequency shift and BGS bandwidth increase, and the SBS gain decreases), (see Fig. IV. 28 (a) and (b); [43]). Furthermore, the SBS depends also on the pressure (when the pressure increases, the SBS frequency shift decrease, but the BGS bandwidth remains constant; [44]), on the fiber core doping concentration etc...For these different reasons, all the SBS suppression studies were thus concentrated on these parameters, like applying temperature or strain distribution to the fiber coil to reduce the SBS [45] - [47]…

Unfortunately, these methods increase the $SBST$ only by a few decibels. Thus, they are still not efficient, especially for low noise applications and low noise systems such as our OEO. One other interesting method can be used to suppress the SBS, while keeping a low noise in an optical link. It has been proven in [48] that concatenating multiple fibers, having different BGS frequency shifts each, can lead to an increase in the $SBST$ of about 6 dB. However, this is still inefficient for our applications.

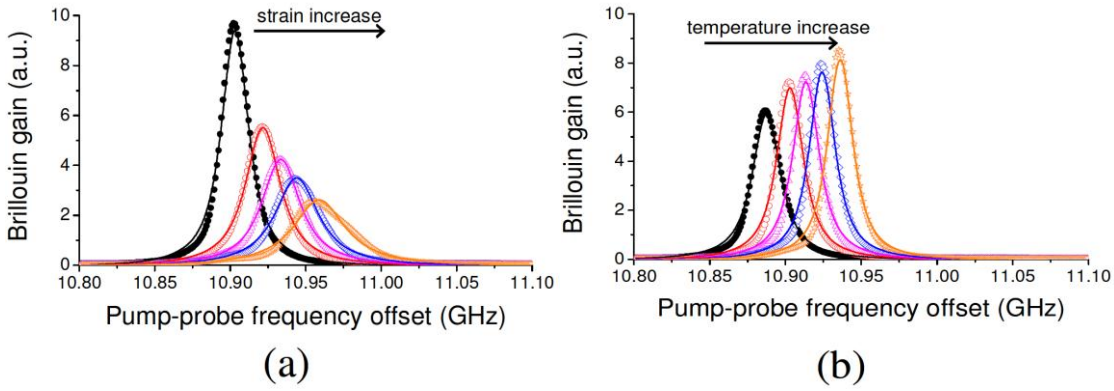

Fig. IV. 28. From [43]: Dependence of the BGS on strain and temperature. Measured BGS when applied strain (a), (or temperature (b)), is increased. Points represent experimental data and solid curves denote Lorentzian fitting.

IV.6.2 SBS suppression using optical isolators

Yet not very efficient, an elegant method used in SPG optical fibers to suppress the SBS, can be very appealing if used in the FRR case. It is based on inserting optical isolators at different distances in a SPG optical link [49]. The isolation of the different isolators will thus prevent the SBS from intensifying in the backwards direction in the optical fiber.

Essentially, in SPG optical fibers, the generated SBS Stokes wave travels backwards and it is amplified by the Brillouin gain as it has been already explained in section IV.2.1.a. Now, when an optical isolator is inserted in a fiber of a total length (L_T), and its own effective length L_{eff} and $SBST$, the isolator virtually cuts the fiber into two new lengths (L_1 and L_2) regarding the Brillouin gain. Consequently, the SBS interaction between the fiber's two sections is absent and the fiber $SBST$ is increased because it is replaced by two other $SBST$s related to the new fiber sections, L_1 and L_2. The SBS Stokes wave will be thus completely cut off by the isolator in the fiber link. However, to prevent the SBS from being generated in long optical links, the length of each fiber section (sections are separated by

isolators) must respect the launched power into each fiber section input in order not to exceed the section $SBST$.

Of course, this method has its drawbacks because it depends on the isolator insertion loss and isolation. In addition, it depends on the optimal position of the isolators in the optical link: the spacing between isolators should be shorter near the fiber input because the Brillouin gain is higher there. For example [49], in a 55 km optical fiber with nine isolators inserted in their optimal locations in the fiber, the best result we can get is a 6 dB increment in the $SBST$.

Fortunately, this method could be of great interest in the FRR case because it could be much more efficient in a FRR geometry. Like in SPG fibers, $SBST$ in the FRR basically depends on the FRR equivalent length L_{eq}, while the FRR physical length L is much shorter than L_{eq}. The SBS power in the optical fiber depends on the effective interaction length between the optical and the acoustic waves [1]. Photons circulate many times inside the FRR, due to its high Q_{Opt} (high optical delay τ), as if it was a long optical fiber. This increases the virtual interaction length (~1180m in the 20m-long FRR) between the spontaneous Brillouin scattered wave, the optical carrier and the acoustic wave. Thus, the spontaneous Brillouin scattered wave will be intensified all along this virtual length and will become stimulated. It could also create other higher order SBS waves with their own Rayleigh-scattered waves, as we have already seen in section IV.2. One of the severe consequences of this is optical carrier depletion and noise added to the optical link (or system) due to all these waves considered as parasitic signals.

If one ideal isolator (with zero insertion loss and infinite isolation) is inserted inside the FRR, it will completely prevent the SBS from building-up inside the resonator. This is due to the fact that, virtually, we will have a number (N) of isolators. N will be equal to the photons total laps inside the resonator ($N=L_{eq}/L$). The virtual isolators will be spaced by the FRR physical length L. Thus, the SBS Stokes wave will be completely cut off by these virtual isolators, and the $SBST$ inside the resonator will be increased to be the one of the physical resonator length L, not the $SBST$ of the FRR equivalent length L_{eq}, (see Fig. IV. 29 for the method illustration if applied to the 20m-long FRR case).

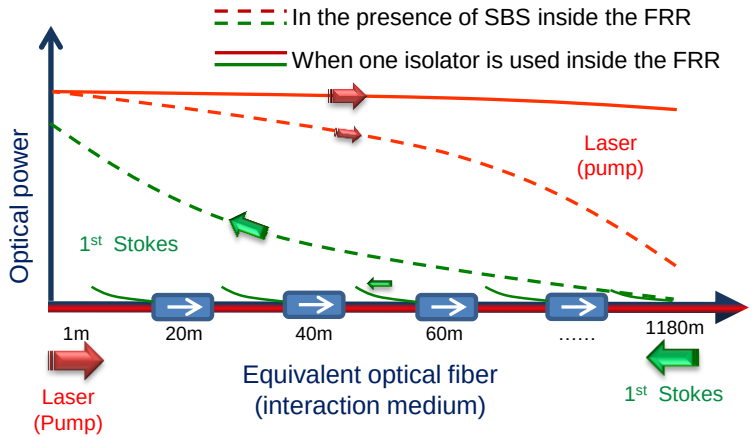

Fig. IV. 29. Illustration of the laser (pump) and first SBS Stokes wave behavior inside the 20m-long FRR, with and without one (ideal) isolator inserted inside the FRR

For example, the $SBST$ of the 20m-long FRR will be increased from -1.4 dBm (for a ~1180m virtual length) to 33.5 dBm (for a 20m physical length), thereupon by approximately 35 dB. The presence of the isolator in the FRR will also efficiently reduce the Rayleigh scattering.

Unfortunately, and despite the fact that the SBS will be suppressed and the STRS will be reduced, the optical isolator is not ideal, and it does not have zero insertion loss and infinite isolation. Thus, in the FRR case, the isolator insertion loss will be also multiplied by the photons laps *N*. Therefore, the FRR Q_{Opt} will be reduced unless if we optimize the resonator's different parameters: length, coupling factor, architecture, loss etc... This optimization study has to be done in order to compensate the isolator loss and get a SBS suppression, a STRS reduction, a satisfying quality factor, low transmission loss and finally a good phase noise result once the device is included in an OEO setup.

IV.6.3 Optimized and immunized FRR (IFRR)

IV.6.3.a *IFRR optimization using ADS*

The FRR optimization study has been performed on the FRR model we have developed using a microwave simulation software, ADS (Agilent). The modeling of the resonator using ADS has been already detailed in chapter II.

In Fig. IV. 30 and Fig. IV. 31, we present quality factor, intra-cavity power and transmission loss ADS simulation results obtained for a 100m-long FRR. We have found that an optimized coupling factor of 8%, while mainly taking the resonator's transmission loss and Q_{Opt} into account, must lead to a 92 kHz $FWHM$ (consequently a Q_{Opt} of 2.1x10^9 (Q_{RF} of 1.1x10^5 at f_{RF} = 10 GHz)) with a 2 MHz FSR, a 4 dB optical transmission loss, a 7 dB power enhancement factor and a 22.7 dB rejection.

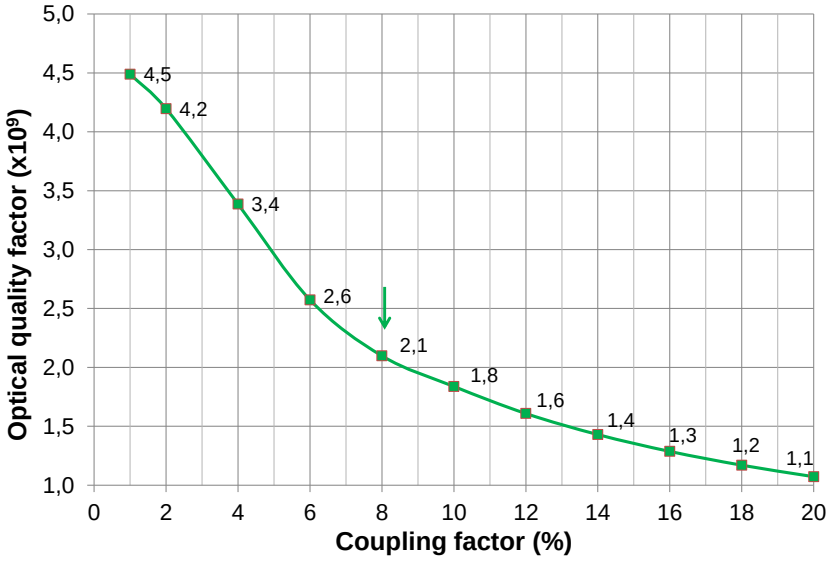

Fig. IV. 30. 100m-long FRR optical quality factor versus the coupling factor (for both couplers), simulated using FRR ADS model

A Q_{Opt} of 2.1x10^9 means an equivalent length L_{eq} of 708m, consequently an intra-cavity $SBST$ of 64 mW (18 dBm) according to (Eq.IV. 5). Furthermore, with a 7 dB intra-cavity power enhancement factor, the resonator input power $SBST$ will be about 12.7 mW (11 dBm), always according to the $SBST$ definition in [1]. Thus, if the SBS is generated inside the resonator, it will be detected far below this $SBST$ value (at least 5 dB below this $SBST$ theoretical value and definition, see the 20m-long FRR $SBST$ power measurements in Fig. IV. 8).

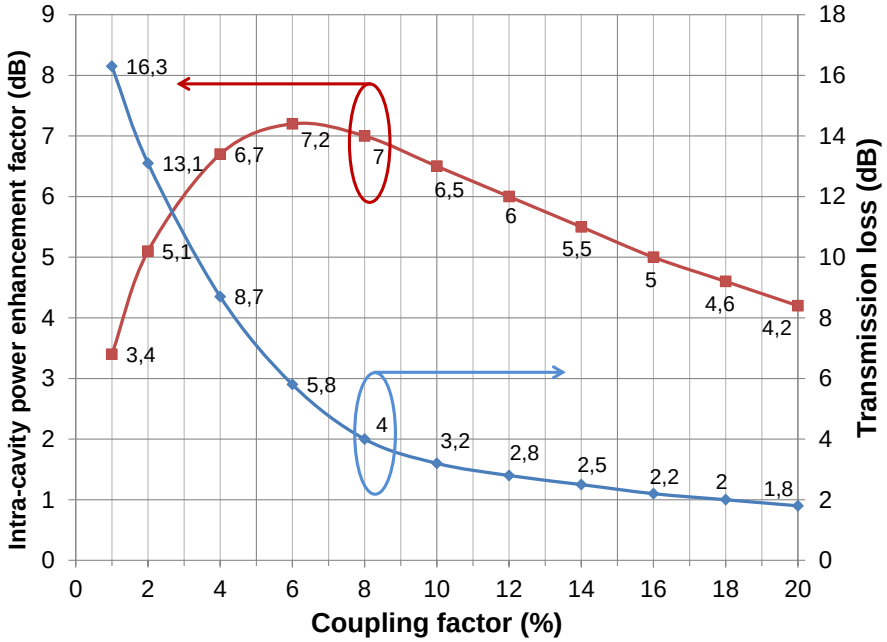

Fig. IV. 31. 100m-long FRR intra-cavity power enhancement factor and transmission loss, versus the coupling factor (for both couplers), simulated using FRR ADS model

In the 100m-long P-M FRR structure, we have added an optical inline polarizer at the resonator input. This polarizer will completely eliminate the possibility of two polarization states behavior of the optical carrier at the FRR input. Essentially, P-M fibers in the resonator assembly will only maintain the carrier's states of polarization and do not ensure only one polarization state behavior. The 100m-long immunized FRR (IFRR) architecture is depicted in Fig. IV. 32.

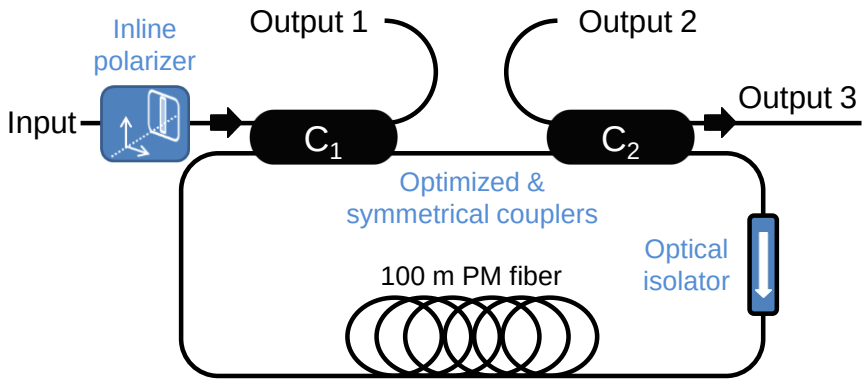

Fig. IV. 32. 100m-long immunized FRR architecture. See also Image 4 in appendix C

IV.6.3.b *IFRR optical characterization*

Once the 100m-long IFRR has been fabricated, all experimental results were at expectations. First, the IFRR has been optically characterized using the same setup of Fig. IV. 7. The optical power measurements are depicted in Fig. IV. 33.

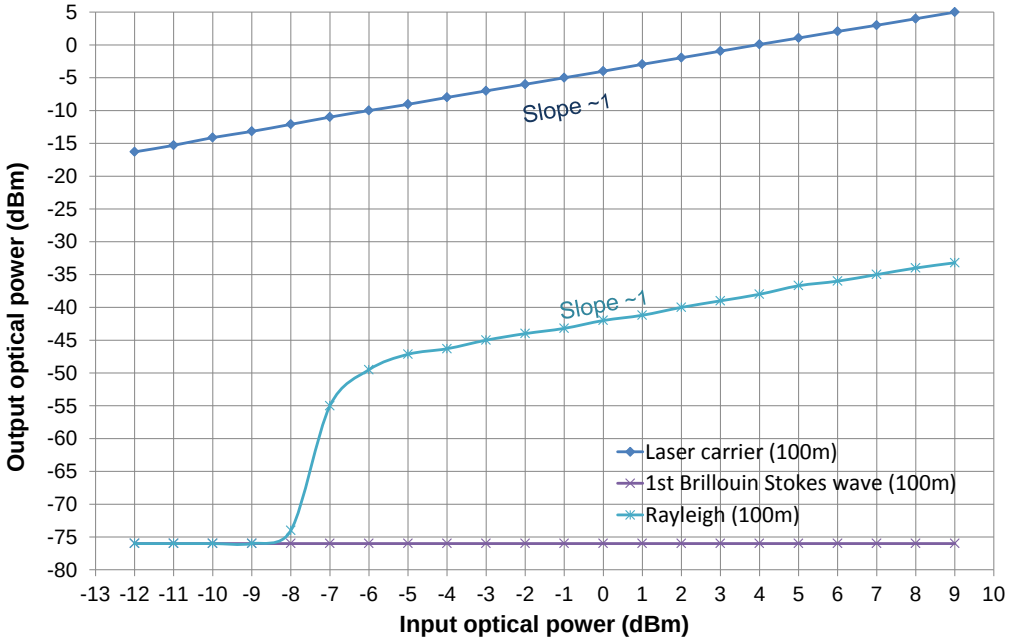

Fig. IV. 33. Experimental power measurements results in the 100m-long IFRR of the laser output, laser's Rayleigh scattering and the first SBS Stokes wave, versus the laser input optical power

We can clearly see from these results that the SBS has been completely suppressed. Indeed, no carrier saturation has been observed (the carrier power at the resonator output linearly increases with a slope equal to 1; about 4 dB optical loss and 7 dB power enhancement factor have been obtained). Besides, the STRS intensity has been efficiently reduced (more than 40 dB rejection). The optical 4 dB power loss and 7 dB power enhancement factor have been also accurately measured using an optical power meter. In addition, the DC detection of the photodiode at the 100m-long IFRR third output has been measured, using the laser scanning method (described in chapter II), when the laser power injected at the resonator input exceeds 9 dBm. The result is presented in Fig. IV. 34 and we can clearly notice that no saturation is visible on the detected signal; on the contrary of what we have observed when the same measurement was done using the 20m-long FRR with a laser carrier power that exceeded only the first experimental $SBST$ (experimental $SBST$ ~-8 dBm; see Fig. IV. 8).

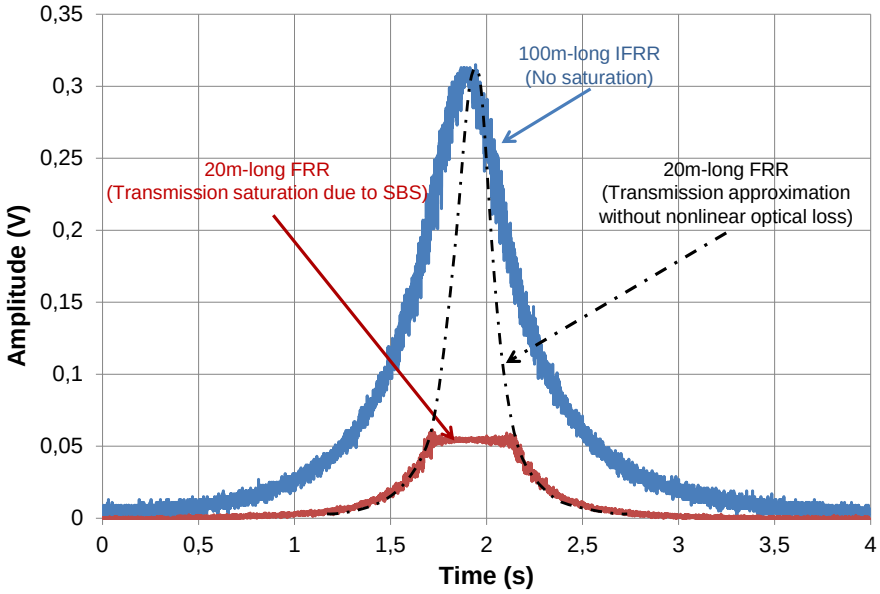

Fig. IV. 34. Photodiode DC voltage measured using an oscilloscope at the FRR third output while the laser frequency is scanning a resonance line: visible laser carrier saturation due to SBS generation inside the 20m-long FRR, on the other hand no carrier saturation is observed for the 100m-long IFRR even with a laser carrier power above 9 dBm

IV.6.3.c *STRS behavior in the IFRR*

In order to describe the STRS spectrum behavior in the 100m-long IFRR, the STRS baseband noise power spectrum has been measured at the resonator second output using Fig. IV. 17 setup; results are depicted in Fig. IV. 35. These results show that the STRS noise level has been considerably reduced by more than 50 dB all over the baseband noise spectra compared to the results obtained in Fig. IV. 18 for the 20m-long FRR.

However, we can also notice that only the 1.5 kHz Rayleigh signature increases gradually with the optical input power. This is because the STRS is no longer dominated by the SBS in the IFRR. Also, the 1.5 kHz signature is more present than the one observed at 60 kHz in the 20m-long FRR case. This means that it is the only pure STRS shift, while the one detected in the 20m-long FRR at 60 kHz and reported in [28] could be the result of a mixed STRS with spontaneous Brillouin scattering or even with forward SBS, called guided acoustic wave Brillouin scattering (GAWBS).

This type of Brillouin scattering generally occurs in photonic crystal fibers or hole-assisted fibers because of their interesting acoustic properties [50], with frequency shifts above tens to hundreds of MHz. GAWBS is less efficient in single mode fibers and it is caused by transverse acoustic resonant modes of the cladding in the fiber structure [51]. GAWBS appear as peaks in the baseband noise from few kHz till around 400 MHz in these fibers.

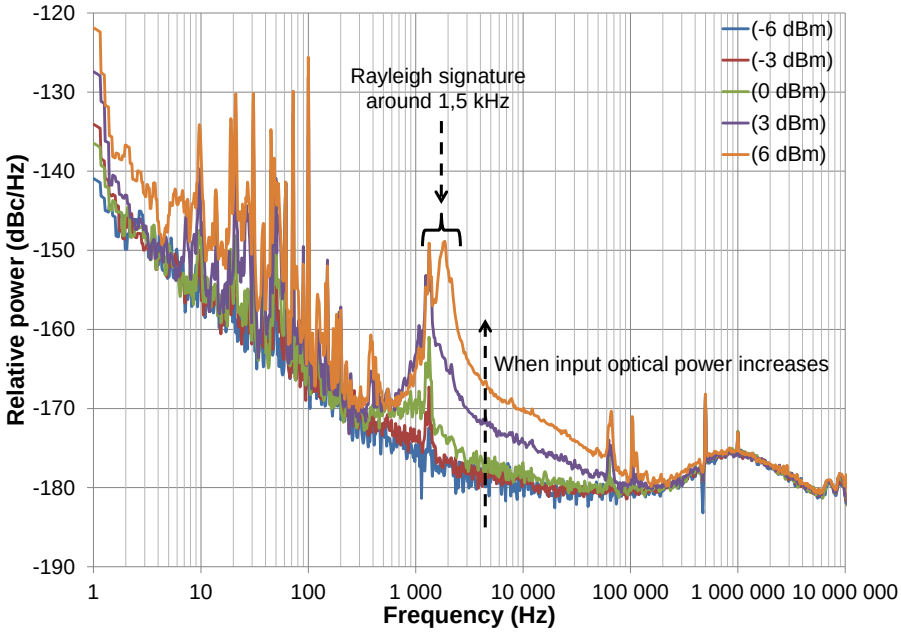

Fig. IV. 35. Baseband noise power spectra at the second output of the 100m-long IFRR, measured in the electrical domain using Fig. IV. 17 setup

IV.6.3.d *Laser RIN behavior in the IFRR*

Even not severely degraded by the nonlinear optical effects as in the 20m-long FRR case, the laser RIN measurements at the IFRR input and output respectively, using Fig. IV. 12 setup, have shown a degradation in the laser RIN in the frequency band ranging from 200 Hz to 200 kHz when an optical carrier power of 0 dBm is used. The results are depicted in Fig. IV. 36.

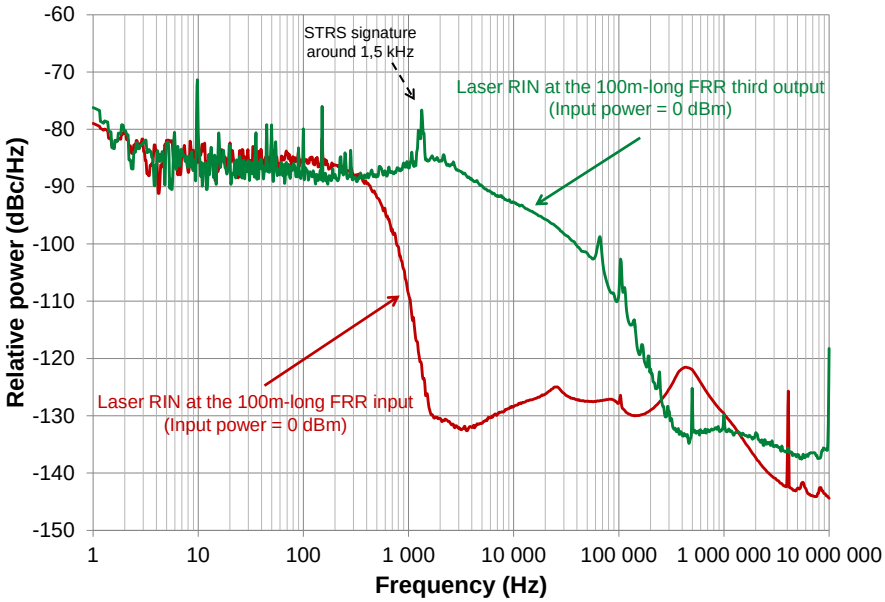

Fig. IV. 36. Laser RIN degradation in the 100m-long IFRR, probably caused of the residual STRS noise generated inside the resonator and by the PDH laser stabilization loop

This RIN degradation is probably caused by the residual STRS noise in this frequency band because we can clearly notice the STRS signature at 1.5 kHz. On the other hand, the RIN degradation is rapidly reduced and filtered by the FRR above 40 kHz offset frequency. Finally, this RIN degradation could be also caused by the PDH laser stabilization loop because a bad setting of the PDH loop parameters could increase the laser AM and FM noise conversions via the resonator, as we have stated in chapter III and also as we will see in section IV.7.4 in this chapter.

IV.6.3.e *IFRR RF characterization*

The IFRR characterization results in the RF domain also met our expectations: Q_{Opt} (*because the resonance 3dB bandwidth is maintained in the RF domain*), rejection, FSR, RF transmission loss (doubled in the RF domain because of the PD quadratic detection), (see Fig. IV. 37). These RF characteristics were accurately measured using the high resolution vector network analyzer method described in chapter II.

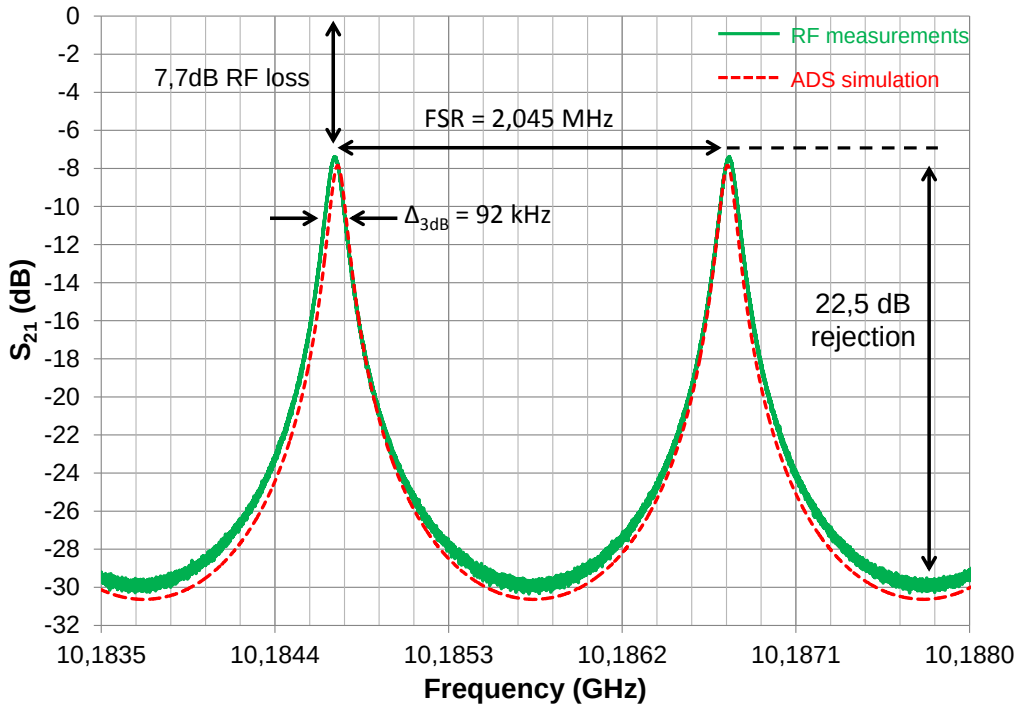

Fig. IV. 37. RF transmission characteristics of the 100m-long IFRR

IV.6.3.f*Signal phase noise behavior through the IFRR*

In the same perspective, characterizing the new IFRR, we have measured the phase noise of a 10 GHz RF synthesizer signal transmitted through a classical optical link using a MZM. The same OEO architecture and components were used in this link but in open loop configuration, with and without the 100m-long IFRR. The phase noise measurements are depicted in Fig. IV. 38. Results show a slight degradation in the phase noise when the 100m-long-FRR is used. Interestingly, this phase noise degradation occurs in the same offset frequency range as for the laser RIN aforementioned case. We assume that, like for the RIN case, the same degradation reasons apply.

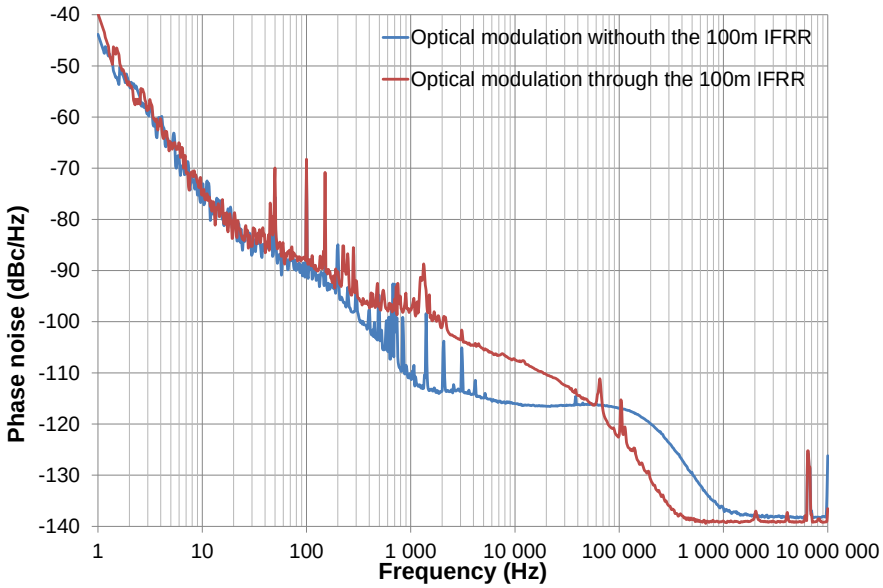

Fig. IV. 38. Phase noise of a 10 GHZ RF synthesizer signal, transmitted through an optical link (the OEO setup in open loop configuration), with and without the 100m-long IFRR included

IV.7 OEO based on the new passive 100m-long IFRR

All things considered, the new IFRR experimental results prove that we have an optimized resonator with a high Q_{Opt} and low transmission loss. Moreover, the resonator is completely immunized against the SBS, and the STRS is efficiently reduced (even with the STRS slight possible contribution to the signal RIN and phase noise degradation). Therefore, using this resonator as a frequency stability element in an OEO setup should now considerably reduce its phase noise.

IV.7.1 OEO phase noise: theoretical expectations

If the new 100m-long IFRR is used in the OEO setup, the OEO noise modeling approach, detailed in (chapter III), it expects a white frequency noise contribution of -134 dBc/Hz at 10 kHz offset frequency to the OEO phase noise, (see the dashed curve in Fig. IV. 42). However, the phase noise contribution of the optical amplifier and RF amplifiers, which are intended to be use in the OEO setup, must be estimated and added in order to get an accurate theoretical expectation of the OEO phase noise. To do so, we have first measured the optical and RF amplifiers' residual phase noise using the method we have already mentioned in chapter I.

First, the residual phase noise of the two RF amplifiers (an AML 812PNA2401 low noise amplifier (f= 2-12 GHz; G=24 dB) and a Pseudomorphic High Electron Mobility Transistor (PHEMT) LP7612 (f= -18 GHz; G=10 dB)) has been measured. Both amplifiers were used after the PD in the OEO RF loop. We have also measured the phase noise of the RF amplifier (Watkins Johnson – VERSA 6885-815(f=5-19 GHz; G=31 dB)) used outside of the OEO loop and placed before the PD employed at the SSA to measure the OEO phase noise. Furthermore, the residual phase noise of the EDFA optical amplifier, used before the PD in the OEO optical loop, has been also evaluated. This has been done first by adding a classical optical link as a DUT in the measurement bench and measuring the link residual phase noise, then by adding the optical amplifier in the optical link and repeating the same measurement. We can then get an estimation

of the phase noise added by the EDFA to the optical link. Residual phase noise results of the optical and RF amplifiers are presented in Fig. IV. 39.

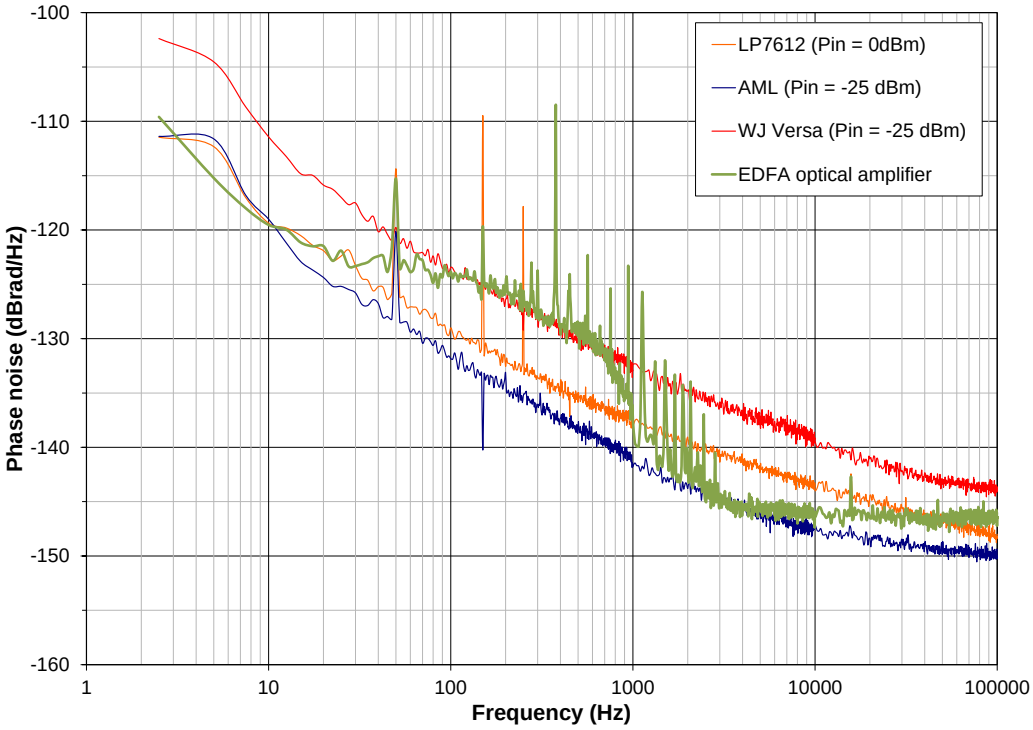

Fig. IV. 39. Residual phase noise of the optical and RF amplifiers intended to be used in both optical and RF loops in the OEO, and of the RF amplifier to be used in the OEO phase noise measurement link. Measurements were performed using residual phase noise measurement bench described in chapter I

Once in the OEO loop, the measured amplifiers residual phase noise can be then introduced in the simplified OEO model, following Leeson's approach [52](detailed in chapter I), taking into account the resonator equivalent Q_{RF} factor at the OEO oscillation frequency (f_0 = 10.2 GHz).

Using Leeson's approach and Fig. IV. 39 measurement data, we can compute the different in-loop amplifiers phase noise contributions to the OEO phase noise. The results are represented in Fig. IV. 40.

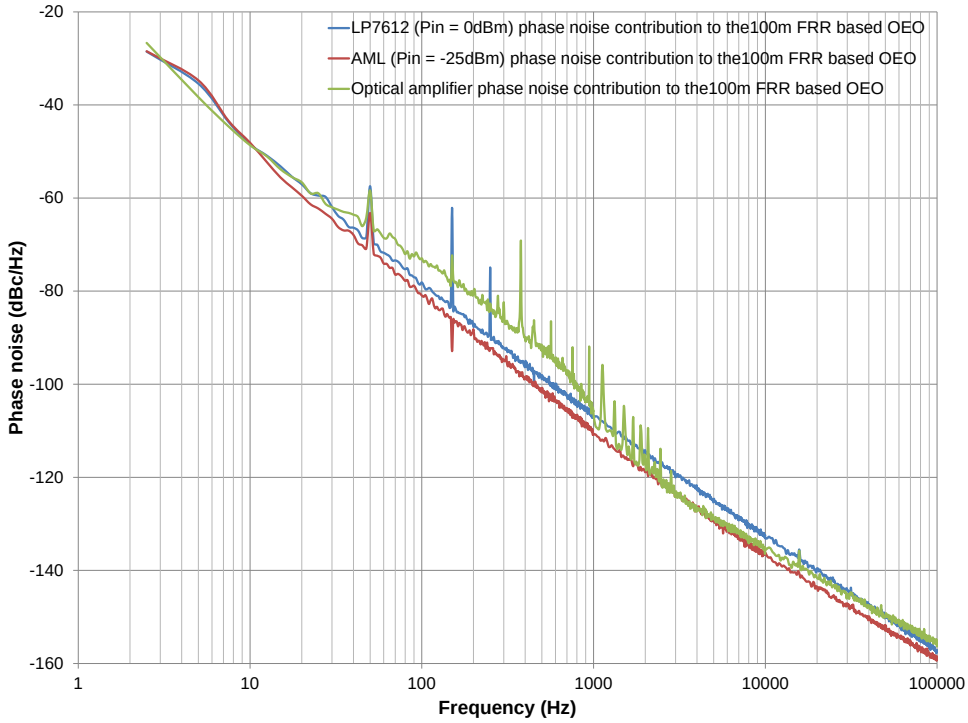

Fig. IV. 40. Phase noise contributions, of the optical amplifier and the two RF amplifiers inside the OEO loop, to the OEO phase noise. Calculated using Leeson's relation (detailed in chapter I) including Fig. IV. 39 measurement data

Actually, in the OEO experimental setup and in order to measure the OEO phase noise, we have used a 3 dB optical coupler at the end of the OEO optical loop after the optical amplifier. One part of the splitted optical signal feeds the oscillation loop and the other part is sent via a 20m-long optical link ended by a photodiode and the WJ Versa RF amplifier. The amplifier output is then sent to the SSA, (see Fig. IV. 41).

In that case, the OEO signal we are characterizing gets out from the FRR , followed by the EDFA, and then by the out-of-loop photodiode and WJ versa RF amplifier. Lesson's model can be thus extended to take into account this situation and a more detailed relation can be then developed. This relation is given by:

$$L_{Osc-2}(f_m) = 10.\log\left\{\left(\left(\frac{{f_0}^2}{8.{Q_{RF}}^2.{f_m}^2}\right) * \left(S_{\varphi-OA}(f_m) + S_{\varphi-A1}(f_m) + S_{\varphi-A2}(f_m) + NCR_1\right)\right) + \left(\frac{S_{\varphi-A3}(f_m) + NCR_2}{2}\right)\right\} \quad \textit{(Eq.IV. 10)}$$

where $L_{Osc-2}(f_m)$ in (dBc/Hz) is the oscillator single sideband phase noise at an offset frequency f_m, following the extended OEO noise model, and $S_\varphi(f_m)$ in (rad²/Hz) is the different amplifiers' residual phase noise power spectral density in one Hz bandwidth at an offset frequency f_m, ($S_\varphi(f_m)$ measured values are represented in Fig. IV. 39). NCR_1 and NCR_2 are respectively the in-loop and the out-of-loop noise to carrier ratios.

Hence, this relation takes into account the amplifiers' noise contributions in the OEO closed loop, adding the in-loop NCR_1 and the FRR quality factor effect on the close-to-carrier phase noise (first term in the relation). Furthermore, the out-of-loop NCR_2 and RF amplifier noise, used to measure the OEO phase noise, are taken into account (second term in the relation).

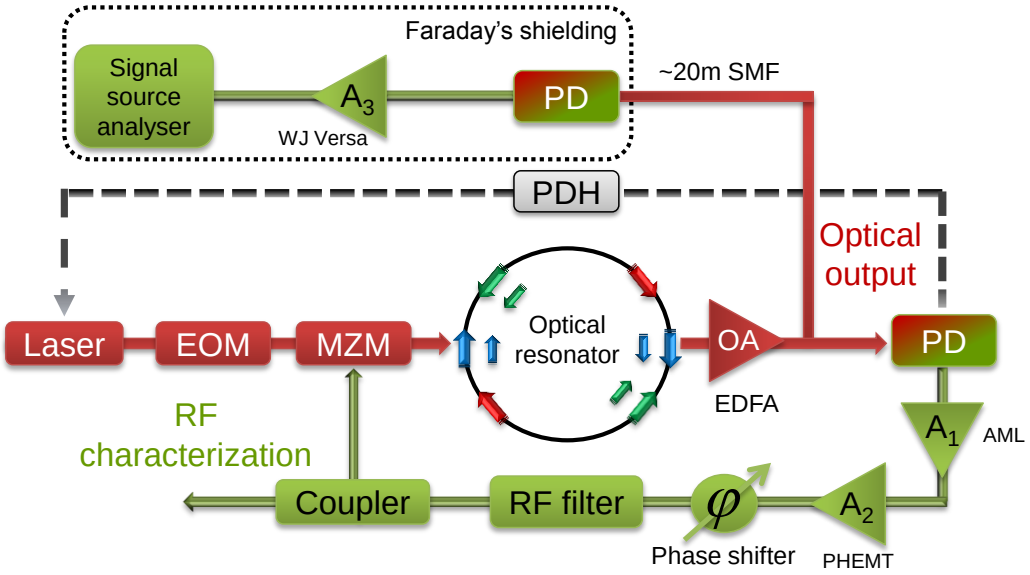

Fig. IV. 41. OEO detailed architecture, including the output characterization link. See also Image 5, Image 6, Image 7 and Image 9 in appendix C

Finally, as a result of managing the in-loop optical power to get 7 mW at photodiode$_1$ input to vanish its RIN-to-RF PM noise conversion coefficient (chapter III), of considering the IFRR's measured parameters and by adding the different amplifiers residual phase noise measurement results and the calculation of both $NCRs$ following the relation we have detailed in chapter III, relation (Eq.IV. 10) expects a -128 dBc/Hz phase noise level at 10 kHz offset frequency, (see the blue curve in Fig. IV. 42).

IV.7.2 OEO phase noise: experimental results

After all these studies, the 100m-long IFRR resonator has been included in the OEO experimental setup and a considerably reduced OEO phase noise has been measured, with a -128 dBc/Hz noise level at 10 kHz offset frequency and a -150 dBc/Hz noise floor as theoretically predicted using relation (Eq.IV. 10), (see the green curve in Fig. IV. 42). The slight close-to-carrier noise difference with the theory is due to amplifiers' noise measurements used when calculating relation (Eq.IV. 10) because their close-to-carrier phase noise is power-sensitive and we did not have the same input power on each of the amplifiers in the OEO experimental setup like when characterizing their noise.

The rapid increase in the OEO close-to-carrier phase noise is likely due to thermal effects because this OEO is a laboratory setup and all its parts were exposed in free space where they were not thermally isolated, including the optical resonator.

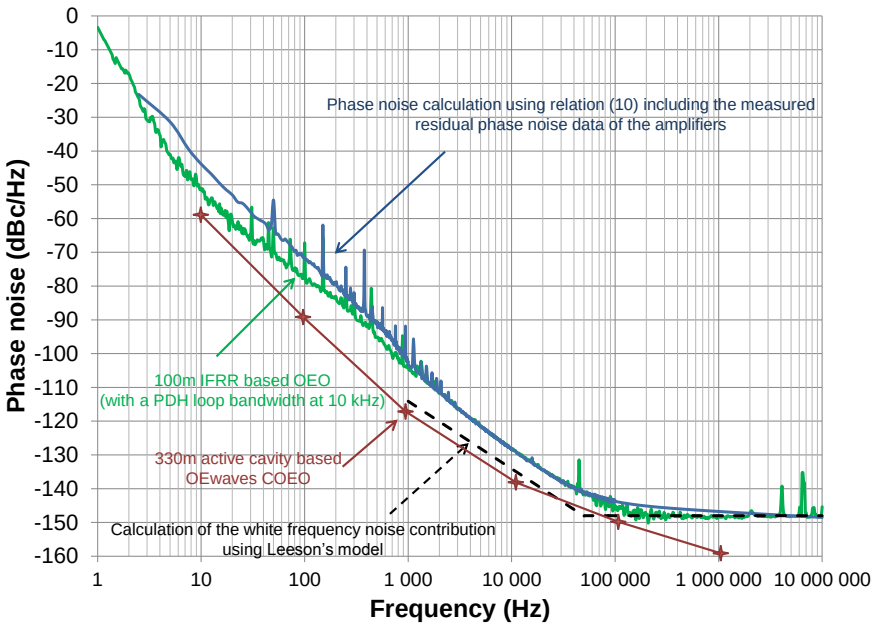

Fig. IV. 42. 100m-long passive IFRR based OEO: phase noise calculation, measurement and comparison with OEwaves 330m-long active-cavity based COEO

The 100m-long IFRR based OEO phase noise result is very encouraging if compared to the 330m-long active-cavity based OEO, also known as coupled optoelectronic oscillator (COEO) and currently commercialized by OEwaves [53], (see the red-stars curve in Fig. IV. 42). That being said when taking into account the fact that our IFRR is a passive resonator and it has more than three times shorter length. We can expect even better results if only the optical and RF amplifiers contribution is lowered (at least 7 dB reduction in the phase noise at 10 kHz offset frequency are possible in this OEO).

IV.7.3 Comparison to a 756m delay line based OEO

Compared to a classical 756m-long delay line based OEO (*see the ARAMOS second interim report – internal report*), our 100m-long IFRR based OEO features the same phase noise level down to 1 kHz offset frequency. However, our OEO has the advantage of being spurs-free below 2 MHz offset frequency, and spurs are very low above this offset frequency. In addition, below 1 kHz offset frequency, the IFRR based OEO seems to feature a lower flicker noise (at least 16 dB lower) than the delay line based oscillator. This also demonstrates the efficiency of such oscillator architecture.

IV.7.4 Effects of the PDH stabilization loop bandwidth

The PDH loop bandwidth appears to be a very critical parameter in our OEO setup. In fact, in the new 100m-long IFRR based OEO, we have found that when the PDH loop bandwidth is reduced to a few hundreds of Hz (especially the PID input and output filters – see chapter I), it can considerably degrade the OEO phase noise. On the other side, when its bandwidth is highly increased, the PDH stabilization loop starts to be unstable and the stability is achieved only for a short time. The optimal bandwidth setting that has been found was around 10 kHz, (see the green and orange curves in Fig. IV. 43).

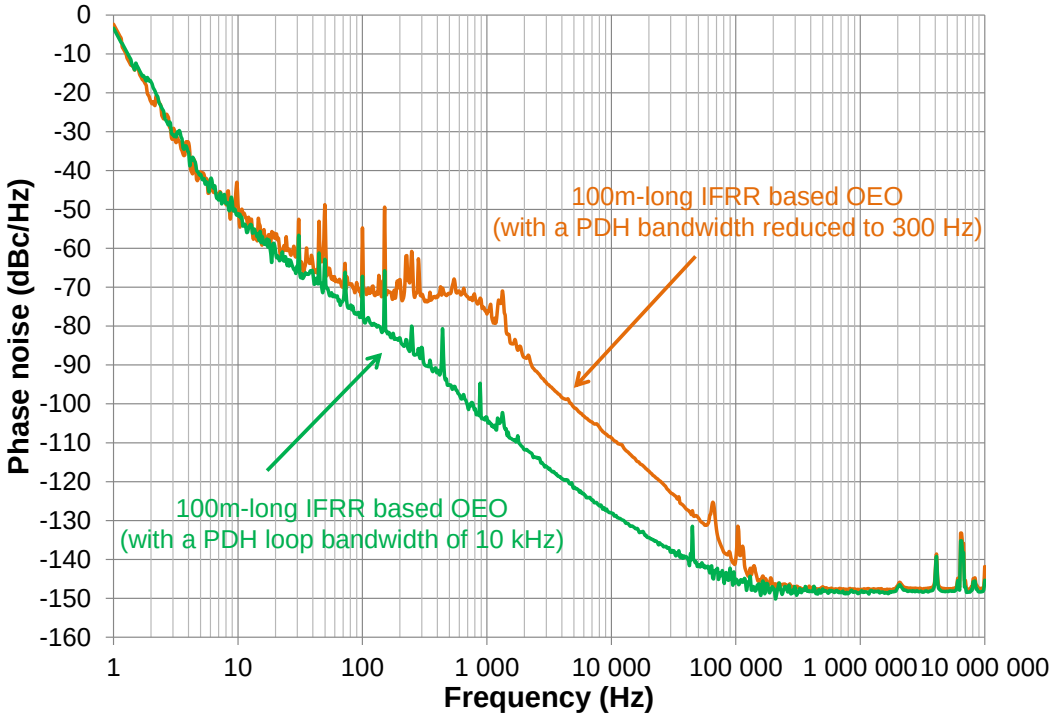

Fig. IV. 43. The effect of the PDH bandwidth reduction on the 100m-long IFRR based OEO phase noise.

This PDH effect is due to the fact that when the PDH loop bandwidth is reduced, it will only control the slow frequency fluctuations of the laser carrier inside the FRR. In this case, the laser high frequency fluctuations will not be efficiently corrected and they will be converted to RF phase noise in the OEO loop via the different processes that we have already stated in chapter III.

IV.8 Conclusion

In this chapter, we have studied the influence of nonlinear optical phenomena, generated inside a 20m-long fiber ring resonator (FRR), on the OEO phase noise. These nonlinear effects have been found to be the main reason behind the excess phase noise in a FRR based OEO setup. Hence, they have been deeply studied in the resonator case, especially the Brillouin scattering and the Rayleigh scattering. Through these studies, we have found a way to completely suppress the Brillouin scattering and to reduce the Rayleigh scattering in a new design of an immunized 100m-long fiber ring resonator (IFRR). Once this IFRR has been used in an OEO setup, we have been able to measure a considerably reduced phase noise, with a -128 dBc/Hz noise level at 10 kHz offset frequency and a -150 dBc/Hz noise floor.

The 100m-long IFRR based OEO phase noise results were also compared to those of a 330m-long active-cavity based OEO, also known as coupled optoelectronic oscillator (COEO) that is currently commercialized. The comparison between these two OEOs shows a slight noise gap between both OEOs which is in favor of the COEO. However, taking into account the fact that our IFRR is a passive resonator that has more than three times shorter fiber length, this makes our OEO results very encouraging compared to the COEO. Moreover, we can expect to get an even better result than the one presented in Fig. IV. 42 if lower loss isolator is used inside the resonator (thus much better resonator characteristics could be obtained), if RF amplifiers contribution to the OEO phase noise could be reduced (the OEO

phase noise spectrum was clearly limited by amplifiers noise in its white frequency noise part) and if low noise optoelectronic components (laser, PD…) are used. Indeed, a 7 dB reduction in the OEO phase noise at 10 kHz offset frequency could be theoretically obtained if only the RF amplifiers noise contribution is reduced.

Aside from its negative effects on the FRR based OEO phase noise, and in parallel with our OEO optimization studies, investigations have been performed on the generation of millimeter-wave signals using the Brillouin selective sideband amplification process in a 20m-long high Q_{Opt} FRR. The synchronization of the Brillouin amplification lines with a 21.7 GHz RF seed signal has resulted in high power and high spectral purity millimeter-wave signals generation up to 65 GHz, which is of great interest for many applications. The proposed technique allows us to easily get high signal to noise ratio and low close-to-carrier phase noise for the generated millimeter-wave signals.

IV.9 References

[1] G.P.Agrawal, “Nonlinear Fiber Optics,” 4th ed. (Academic Press 2007), chapters (8, 9,10).

[2] O. Okusaga, J. Cahill, W. Zhou, A. Docherty, G. M. Carter, and C. R. Menyuk, “Optical scattering induced noise in RF-photonic systems,” Frequency Control and the European Frequency and Time Forum (FCS), 2011 Joint Conference of the IEEE International , vol., no., pp.1-6, 2-5 May (2011).

[3] L. Brillouin, “Diffusion de la lumiere par un corps transparents homogene,” Ann. Phys. 17, 88 (1922).

[4] R. Y. Chiao, C. H. Townes, and B. P. Stoicheff, “Stimulated Brillouin Scattering and Coherent Generation of Intense Hypersonic Waves,” Phys. Rev. Lett. 12, 592–595 (1964).

[5] A. Kobyakov, M. Sauer, and D. Chowdhury, “Stimulated Brillouin Scattering in Optical Fibers,” Advances in Optics and Photonics, vol. 2, pp. 1-59, (2010).

[6] A.B. Ruffin, “Stimulated brillouin scattering: an overview of measurements, system impairments, and applications,” Optical Fiber Measurements, 2004. Technical Digest: Symposium on , vol., no., pp. 23- 28, (2004).

[7] Marc Niklès, “La diffusion Brillouin dans les fibres optiques: Etude et application aux capteurs distribués,” Ph.D. thesis (Ecole Polytechnique Fédérale de Lausanne, Lausanne, Switzerland, 1997).

[8] R. W. Boyd, “Nonlinear Optics,” 3rd ed., (Academic Press, 2008).

[9] R.B. Jenkins, R.M. Sova, and R.I. Joseph, “Steady-State Noise Analysis of Spontaneous and Stimulated Brillouin Scattering in Optical Fibers,” Lightwave Technology, Journal of , vol.25, no.3, pp.763-770, March (2007).

[10] S. Le Floch, and P. Cambon, “Theoretical evaluation of the Brillouin threshold and the steady-state Brillouin equations in standard single-mode optical fibers,” J. Opt. Soc. Am. A 20, 1132-1137 (2003).

[11] T. Shimizu, K. Nakajima, K. Shiraki, K. Ieda, and I. Sankawa, “Evaluation methods and requirements for the stimulated Brillouin scattering threshold in a single-mode fiber,” Optical Fiber Technology, Volume 14, Issue 1, Pages 10-15, January (2008).

[12] L. F. Stokes, M. Chodorow, and H. J. Shaw, “All-single-mode fiber resonator,” Opt. Lett. 7, 288-290, (1982).

[13] Q. Yu, X. Bao, and L. Chen, “Temperature dependence of Brillouin frequency, power, and bandwidth in panda, bow-tie, and tiger polarization-maintaining fibers,” Opt. Lett. 29, 17-19 (2004).

[14] S. Norcia, S. Tonda-Goldstein, D. Dolfi, J. Huignard, and R. Frey, “Efficient single-mode Brillouin fiber laser for low-noise optical carrier reduction of microwave signals,” Opt. Lett. 28, 1888-1890, (2003).

[15] M. Nikles, L. Thevenaz, and P.A. Robert, “Brillouin gain spectrum characterization in single-mode optical fibers,” Lightwave Technology, Journal of , vol.15, no.10, pp.1842-1851, Oct (1997).

[16] X.S. Yao, “Brillouin selective sideband amplification of microwave photonic signals,” Photonics Technology Letters, IEEE , vol.10, no.1, pp.138-140, Jan. (1998).

[17] A. Debut, S. Randoux, and J. Zemmouri, “Linewidth narrowing in Brillouin lasers: theoretical analysis,” Phys. Rev. A 62(2), 023803 (2000).

[18] J. Geng, S. Staines, Z. Wang, J. Zong, M. Blake, and S. Jiang, “Highly stable low-noise Brillouin fiber laser with ultranarrow spectral linewidth,” Photonics Technology Letters, IEEE , vol.18, no.17, pp.1813-1815, Sept. (2006).

[19] L. Stépien, S. Randoux, and J. Zemmouri, “Intensity noise in Brillouin fiber ring lasers,” J. Opt. Soc. Am. B 19, 1055-1066 (2002).

[20] Y. Song, and X. Zhang, “High power low RIN Brillouin fiber laser with optoelectronic oscillator configuration,” Proc. SPIE 6838, 68380T (2007).

[21] K. Saleh, P.H. Merrer, O. Llopis, and G. Cibiel, “Millimeter Wave Generation Using Brillouin Scattering in a High Q Fiber Ring Resonator,” Proc. of the 2012 IEEE International Topical Meeting on Microwave Photonics (MWP), Noordwjik, (2012).

[22] K. Saleh, P.H. Merrer, O. Llopis, and G. Cibiel, “Optical scattering noise in high Q fiber ring resonators and its effect on optoelectronic oscillator phase noise,” Opt. Lett. 37, 518-520, (2012).

[23] A. Bouchier, K. Saleh, P. H. Merrer, O. Llopis and G. Cibiel, “Theoretical and experimental study of the phase noise of opto-electronic oscillators based on high quality factor optical resonators,” Proc. of the 2010 IEEE-IFCS, pp. 544-548, (2010).

[24] R. M. Herman, and M. A. Gray, “Theoretical Prediction of the Stimulated Thermal Rayleigh Scattering in Liquids,” Phys. Rev. Lett. 19(15), 824–828, (1967).

[25] D. H. Rank, C. W. Cho, N. D. Foltz, and T. A. Wiggins, “Stimulated Thermal Rayleigh Scattering,” Phys. Rev. Lett. 19(15), 828–830, (1967).

[26] T. A. Wiggins, C. W. Cho, D. R. Dietz, and N. D. Foltz, “Stimulated Thermal Rayleigh Scattering in Gases,” Phys. Rev. Lett. 20(16), 831–834, (1968).

[27] T. Zhu, X. Bao, L. Chen, H. Liang, and Y. Dong, “Experimental study on stimulated Rayleigh scattering in optical fibers,” Opt. Express 18, 22958-22963, (2010).

[28] O. Okusaga, J. Cahill, A. Docherty, W. Zhou, and C. Menyuk, “Guided entropy mode Rayleigh scattering in optical fibers,” Opt. Lett. 37, 683-685, (2012).

[29] A. Docherty, C.R. Menyuk, O. Okusaga, and W. Zhou, “Stimulated Rayleigh scattering and amplitude-to-phase conversion as a source of length-dependent phase noise in OEOs,” Frequency Control Symposium (FCS), 2012 IEEE International , vol., no., pp.1-5, 21-24 May (2012).

[30] T. Zhu, X. Bao, and L. Chen, “A Single Longitudinal-Mode Tunable Fiber Ring Laser Based on Stimulated Rayleigh Scattering in a Nonuniform Optical Fiber,” J. Lightwave Technol. 29, 1802-1807, (2011).

[31] M. Borselli, K. Srinivasan, P.E. Barclay, and O. Painter, “Rayleigh scattering, mode coupling, and optical loss in silicon microdisks,” Appl. Phys. Lett. 85, 3693, (2004).

[32] A.I. Filipenko, “End face nonperpendicularity analysis in fiber connectors,” Laser and Fiber-Optical Networks Modeling, 2001. Proceedings of LFNM 2001. 3rd International Workshop on , vol., no., pp.53-55, (2001).

[33] C.M. McIntosh, A.G. Grandpierre, D.N. Christodoulides, J. Toulouse, and J.-M.P. Delavaux, “Eliminating SRS channel depletion in massive WDM systems via optical filtering techniques,” Photonics Technology Letters, IEEE , vol.13, no.4, pp.302-304, Apr (2001).

[34] N. Shibata, R. Braun, and R. Waarts, “Phase-mismatch dependence of efficiency of wave generation through four-wave mixing in a single-mode optical fiber,” Quantum Electronics, IEEE Journal of , vol.23, no.7, pp. 1205- 1210, (1987).

[35] J. Yao, “Microwave Photonics,” Lightwave Technology, Journal of , vol.27, no.3, pp.314-335, Feb.1, (2009).

[36] G. Pillet, L. Morvan, M. Brunel, F. Bretenaker, D. Dolfi, M. Vallet, J.P. Huignard, and A.L. Floch, “Dual-frequency laser at 1.5 lm for optical distribution and generation of high-purity microwave signals,” J. Lightwave Technol., vol. 26, issue 15, pp. 2764-2773, August (2008).

[37] G. J. Simonis, and D. G. Purchase, “Optical generation, distribution, and control of microwaves using laser heterodyne,” IEEE Trans. Microw. Theory Tech., vol. 38, issu 5, pp. 667–669, May (1990).

[38] O. Llopis , P. Martinet, P. H. Merrer, and K. Saleh, “50–60 GHz local oscillator transmission over fiber using optical frequency multiplication,” Microw. Opt. Technol. Lett., vol. 54, issu 5, pp. 1313–1316, May (2012).

[39] M. C. Gross, P. T. Callahan, T. R. Clark, D. Novak, R. B. Waterhouse, and M. L. Dennis, “Tunable millimeter-wave frequency synthesis up to 100 GHz by dual-wavelength Brillouin fiber laser,” Opt. Express, vol 18, no. 13, pp. 13321-13330, June (2010).

[40] O. Okusaga, W. Zhou, J. Cahill, A. Docherty, and C.R. Menyuk, “Fiber-induced degradation in RF-over-fiber links,” Frequency Control Symposium (FCS), 2012 IEEE International , vol., no., pp.1-5, 21-24 May (2012).

[41] Q. Yu, X. Bao, and L. Chen, “Strain dependence of Brillouin frequency, intensity, and bandwidth in polarization-maintaining fibers,” Opt. Lett. 29, 1605-1607 (2004).

[42] T. Parker, M. Farhadiroushan, V. Handerek, and A. Rogers, “Temperature and strain dependence of the power level and frequency of spontaneous Brillouin scattering in optical fibers,” Opt. Lett. 22, 787-789, (1997).

[43] W. Zou, Z. He, and K. Hotate, “Complete discrimination of strain and temperature using Brillouin frequency shift and birefringence in a polarization-maintaining fiber,” Opt. Express 17, 1248-1255, (2009).

[44] S. L. Floch, and P. Cambon, “Study of Brillouin gain spectrum in standard single-mode optical fiber at low temperatures (1.4-370 K) and high hydrostatic pressures (1-250 bars),” Opt. Commun. 219, 395-410, (2003).

[45] J. Hansryd, F. Dross, M. Westlund, P.A. Andrekson, and S.N. Knudsen, “Increase of the SBS threshold in a short highly nonlinear fiber by applying a temperature distribution,” Lightwave Technology, Journal of , vol.19, no.11, pp.1691-1697, Nov (2001).

[46] N. Yoshizawa, T. Horiguchi, and T. Kurashima, “Proposal for stimulated Brillouin scattering suppression by fibre cabling,” Electronics Letters , vol.27, no.12, pp.1100-1101, 6 June (1991).

[47] R. Engelbrecht, M. Mueller, and B. Schmauss, “SBS shaping and suppression by arbitrary strain distributions realized by a fiber coiling machine,” IEEE/LEOS Winter Topicals Meeting Series, 2009, vol., no., pp.248-249, 12-14 Jan. (2009).

[48] J. Cahill, O. Okusaga, and J. White, “Suppression of Stimulated Brillouin Scattering in High Power, Low phase noise RF-Photonic links,” Frequency Control Symposium (FCS), 2012 IEEE International, vol., no., pp. 1-4, (2012).

[49] Y. Takushima, and T. Okoshi, “Suppression of stimulated Brillouin scattering using optical isolators,” Electronics Letters , vol.28, no.12, pp.1155-1157, 4 June (1992).

[50] R. Shelby, M. Levenson, and P. W. Bayer, “Guided acoustic-wave Brillouin scattering,” Physic. Rev. 15, 127-135 (1985).

[51] J. McElhenny, R. Pattnaik, and J. Toulouse, “Dependence of Frequency Shift of Depolarized Guided Acoustic Wave Brillouin Scattering in Photonic Crystal Fibers,” J. Lightwave Technol. 29, 200-208, (2011).

[52] D.B. Leeson, “A simple model of feedback oscillator noise spectrum,” Proc. of the IEEE, vol. 54, no. 2, pp. 329-330, (1966).

[53] D. Eliyahu, and L. Maleki, “Modulation response (S21) of the coupled opto-electronic oscillator,” Frequency Control Symposium and Exposition, 2005. Proceedings of the 2005 IEEE International , vol., no., pp.850-856, August (2005).

Chapter V FRR and OEO: thermal stability and tunability studies

V.1 Introduction

The thermal stability of the OEO is an important parameter to scale as it could affect its frequency stability. This thermal stability is directly linked to the thermal stability of the frequency reference element in the OEO setup, which is the FRR.

Also, in addition to the low phase noise levels that we can achieve using a FRR based OEO, the tunability of the OEO oscillation frequency is a main desired feature for many applications (radars, communications systems…).

In this chapter, the OEO thermal stability is investigated. Theoretical and experimental studies are performed to determine precisely the resonator and the oscillator thermal stability parameter.

Moreover, we have investigated the possibilities of tuning the oscillation frequency of the FRR based OEO. We have therefore studied different techniques to make the FRR completely tunable, which means an independent tuning of its *FSR* and the absolute frequency of its optical resonant modes.

V.2 FRR and OEO thermal stability

One of the critical parameters to scale in a FRR based OEO is the FRR's thermal stability because the FRR is the frequency reference element in the OEO. Its thermal stability directly affects the OEO's thermal stability, and accordingly its frequency stability. More precisely, it is the frequency stability of the FRR's optical modes spacing (the FSR) that has to be studied. The modes' absolute optical frequency stability is also an important factor; however, it does not influence the OEO stability as long as the laser is stabilized onto the FRR via the PDH loop.

We have therefore theoretically and experimentally investigated the thermal stability matter in an OEO system, by first starting a study on the FRR's thermal stability.

V.2.1 Theoretical studies on the FRR and the OEO thermal stability

As we have already mentioned in chapter II, the mode spacing in the resonator frequency comb, the FSR, depends on two parameters of the optical fiber used to fabricate the FRR: its core refractive index *n* and its length L.

Considering that a typical single mode silica fiber experiences a temperature variation (ΔT), the change in the effective refractive index (Δn) versus the temperature will be more important than that of the fiber length (ΔL).

The fiber effective refractive index and its thermal expansion coefficient (α_ϵ) have both a nearly linear dependence on the temperature, [1] - [4]. They are respectively given by:

$$\Delta n = 9.2 \times 10^{-6} \times \Delta T \qquad \textit{(Eq. V. 1)}$$

$$\alpha = \frac{1}{L}\frac{dL}{dT} = 0.5 \times 10^{-6} \qquad (K^{-1}) \qquad \textit{(Eq. V. 2)}$$

Therefore

$$\Delta L = 0.5 \times 10^{-6} \times L \times \Delta T \qquad (m) \qquad \textit{(Eq. V. 3)}$$

In a fiber ring resonator, the optical field phase delay, after propagating though the fiber loop, is given by:

$$\varphi_{res} = \beta L = \frac{2\pi f_{Opt}\, n\, L}{c} \qquad \textit{(Eq. V. 4)}$$

where f_{Opt} is the optical frequency.

When (Eq. V. 4) satisfies $\varphi_{res} = p\ 2\pi$ where ($p = 1,2,3 \ldots$), the resonant frequency f_{Opt_0} is determined by:

$$\frac{2\pi\ f_{Opt_0}\ n\ L}{c} = p\ 2\pi \qquad \textit{(Eq. V. 5)}$$

Therefore

$$f_{Opt_0} = p\frac{c}{n\ L} = p\ FSR \qquad \textit{(Eq. V. 6)}$$

From (Eq. V. 6), we can see that the optical resonant frequency is a multiple p of the resonator free spectral range.

When heating the FRR, n and L will change versus ΔT. As a result, the optical signal inside the resonator will encounter an additional phase delay ($\Delta\varphi_T$), given by:

$$\Delta\varphi_T = -\frac{2\pi\ f_{Opt}\ (\ L\ \Delta n +\ n\ \Delta L)}{c} \qquad \textit{(Eq. V. 7)}$$

And (Eq. V. 4) will be replaced by:

$$\varphi_{res} = \frac{2\pi\ f_{Opt}\ n\ L}{c} + \Delta\varphi_T \qquad \textit{(Eq. V. 8)}$$

From (Eq. V. 5), (Eq. V. 7) and (Eq. V. 8), the p^{th} resonant frequency f_{Opt_p} will then shift by Δf_{Opt_p} as follows:

$$\Delta f_{Opt_p} = -c\ p\frac{(\ L\ \Delta n +\ n\ \Delta L)}{(nL)^2} \qquad (Hz\ K^{-1}) \qquad \textit{(Eq. V. 9)}$$

From (Eq. V. 9), we can see that the first effect of a thermal variation in a FRR will be a uniform shift of the optical frequency comb generated by the FRR (the minus sign indicates a negative frequency shift). Together with this uniform frequency shift, the FSR will change as well. This is the only frequency variation in the optical domain that will be visible in the RF domain. Actually, when the FRR is used for microwave applications, the photodiode output (at the FRR output) will be the resulting RF frequency of the beat-note between at least two optical modes of the FRR's frequency comb. This FSR variation is given by:

$$\Delta FSR = -c\,\frac{(L\,\Delta n + n\,\Delta L)}{(nL)^2} \qquad (Hz\,K^{-1}) \qquad \textit{(Eq. V. 10)}$$

From (Eq. V. 9) and (Eq. V. 10) we get:

$$\Delta f_{Opt_p} = p\,\Delta FSR \qquad (Hz\,K^{-1}) \qquad \textit{(Eq. V. 11)}$$

Fig.V. 1 represents a simple illustration of the relation above. The minus sign in (Eq. V. 10) indicates a contraction in the *FSR* versus the temperature.

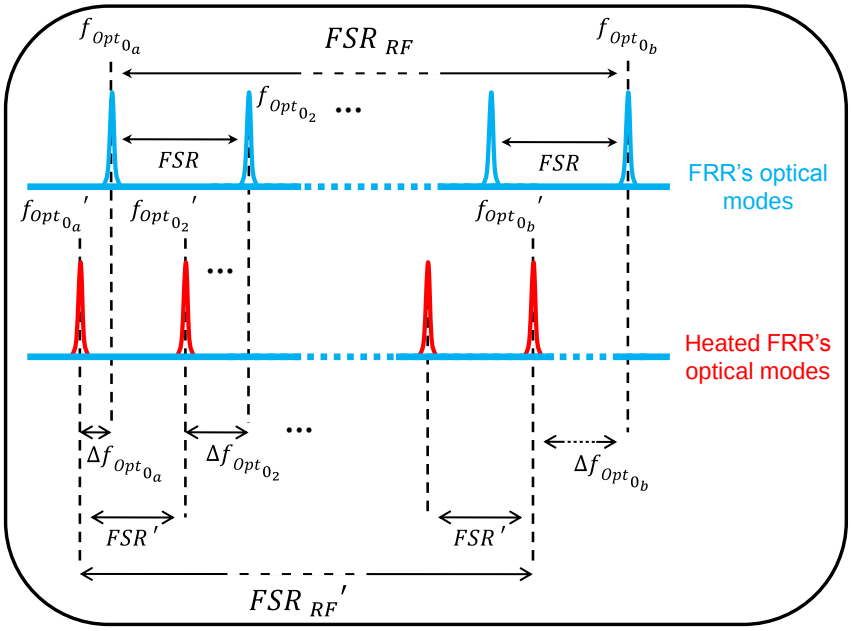

Fig.V. 1. Relation between optical modes' absolute frequency shifts and the FSR variation in a heated FRR

The ΔFSR in (Eq. V. 10) has been calculated for different FRR's lengths and with a temperature variation $\Delta T = 1\,K$. The results are presented in Fig.V. 2 where they show that the *FSR* slightly changes versus the temperature and this variation is inversely proportional to the FRR's length. This being said, the longer the FRR is, the more stable it will be versus the temperature.

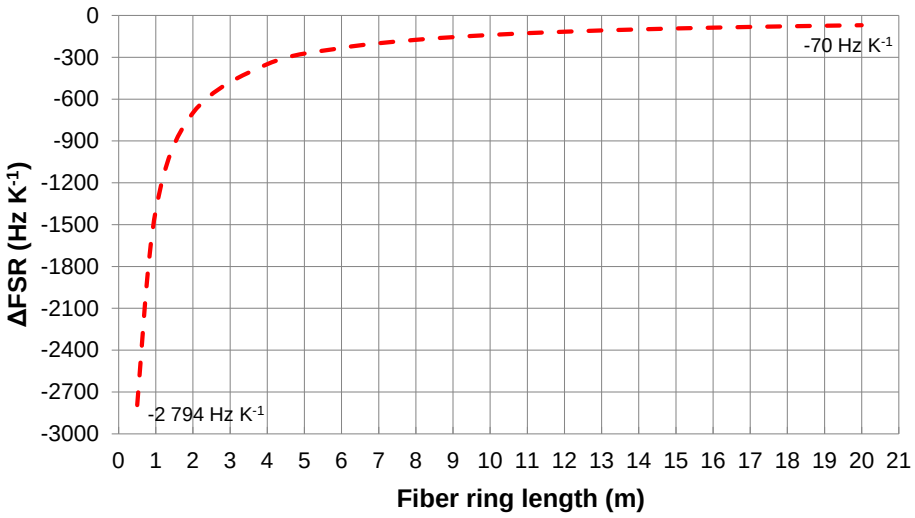

Fig.V. 2. ΔFSR calculated for different FRR's lengths with a temperature variation $\Delta T = 1\ K$. The minus sign in indicates a contraction in the FSR

On the other hand, because in our RF applications using the FRR we utilize two (or even three) modes of the FRR ($f_{Opt_{0_a}}$ and $f_{Opt_{0_b}}$, spaced by the RF application frequency (f_{RF} = FSR_{RF})), we will have to multiply the optical *FSR* variation by a variable *P* equal to the number of "optical" *FSRs* that exist between these two optical modes (see Fig.V. 1 for illustration). Therefore, we will get the global *FSR* variation in the RF domain which will be termed as ΔFSR_{RF}. The variable *P* is given by:

$$P = \frac{f_{Opt_{0_b}} - f_{Opt_{0_a}}}{FSR} = \frac{f_{RF}}{FSR} = \frac{FSR_{RF}}{FSR} \qquad \textit{(Eq. V. 12)}$$

Therefore

$$\Delta FSR_{RF} = P\,\Delta FSR \qquad \textit{(Eq. V. 13)}$$

We can finally conclude that:

$$\Delta FSR_{RF} = \frac{f_{RF}}{FSR}\,\Delta FSR \qquad \textit{(Eq. V. 14)}$$

And

$$\frac{\Delta f_{RF}}{f_{RF}} = \frac{\Delta FSR}{FSR} \qquad \textit{(Eq. V. 15)}$$

These relative fluctuations are therefore a constant equal to -6.8 ppm K^{-1}.

Finally, the global FSR variation in the RF domain, ΔFSR_{RF}, will be given independently from the FRR length, as follows:

$$\Delta FSR_{RF} = f_{RF} \times (-6.8\ 10^{-6}) \quad (Hz\ K^{-1}) \qquad \textit{(Eq. V. 16)}$$

The relative thermal stability of the FRR based OEO is therefore equal to -6.8 ppm K^{-1}. This value is comparable to the typical thermal stability of a conventional microwave dielectric resonator oscillator, which is in the range of 3 ppm K^{-1} for commercial devices.

V.2.2 Experimental results on the FRR and the OEO thermal stability

To validate the theory, the FRR has been fixed on a temperature-calibrated hotplate. 95 % of the 20m-long FRR were in contact with the plate while the two optical couplers were isolated from thermal variations (see Fig.V. 3). Of course, if the optical couplers are exposed to thermal variations, their coupling coefficients may slightly change, leading to a minor modification in the FRR characteristics, especially in its Q_{Opt} and in the *IL*.

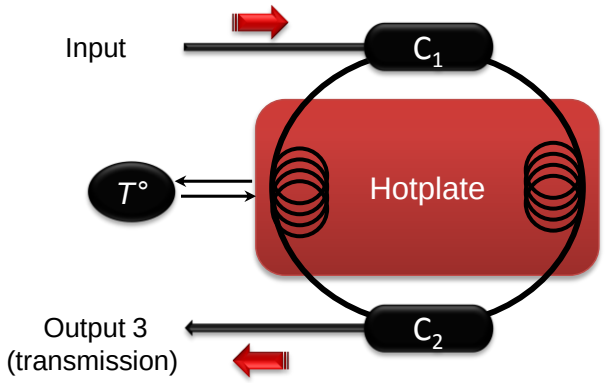

Fig.V. 3. FRR heating using a temperature-calibrated hotplate. The optical couplers were thermally isolated; T: thermoelectric Peltier-junction.

For a $\Delta T = 35\ K$ and a microwave application frequency f_{RF} = 10.2 GHz, the calculation of (Eq. V. 16) gives a ΔFSR_{RF} of (-) 2.4 MHz, taking into account that only 95% of the FRR is exposed to this thermal variation. The minus sign indicates a contraction in the *FSR* versus the temperature. This means a negative shift by 2.4 MHz in the resulting RF frequency if the FRR is used for a microwave domain application.

Experimentally, we have used the microwave domain characterization bench (see chapter II) to measure the FRR transmission response before and after being heated. We have found a frequency shift of 2.5 MHz, as it is shown in Fig.V. 4.

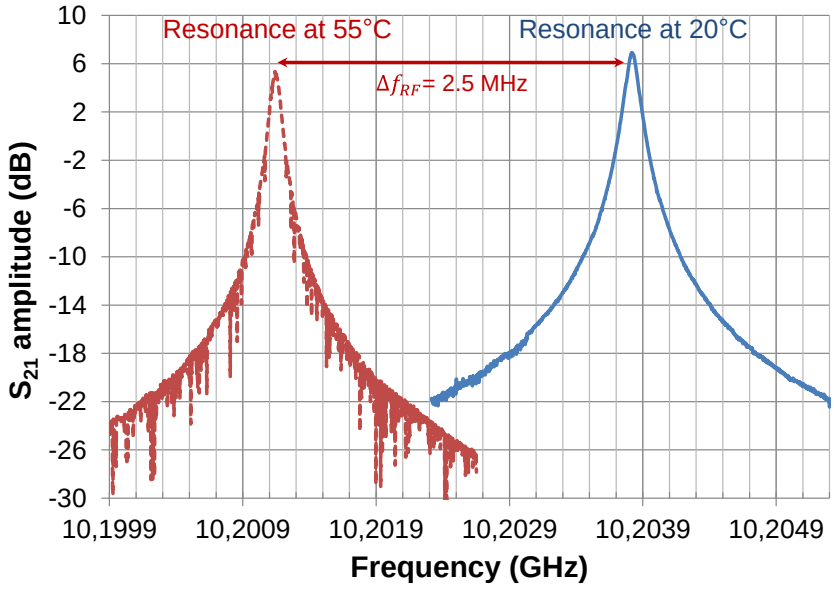

Fig.V. 4. 20m-long FRR's transmission response before and after being heated on 95% of its total length. A RF frequency shift by 2.5 MHz has been obtained when $\Delta T = 35\ K$ and f_{RF} = 10.2 GHz

Furthermore, we have performed the same test on 75% of a one-meter long FRR to validate our theoretical results that expects the same thermal stability for all resonators lengths if the resonators are used for microwave domain applications (like in the OEO case) in the same conditions. The experimental results have validated our theory.

In addition, as we have already mentioned, heating the optical couplers will modify their coupling coefficients, but it marginally modifies the resonant frequency which remains determined by the FRR's loop length.

Finally, the OEO temperature stability can be calculated using the above described approach, providing that the temperature changes remain in a moderate range around the nominal system temperature. Moreover, we have to consider the dielectric resonator bandwidth regarding the FRR's FSR and its Δf_{RF} versus ΔT characteristic to prevent an eventual mode hopping in the OEO oscillation.

V.3 FRR and OEO tunability

Tunability is a desired feature in any optical filter [5]. This also applies to the FRR case due to the high Q_{Opt} that could be obtained using such a resonator structure and the simplicity in its fabrication. Moreover, numerous studies were made (and are still made) to investigate the different possibilities to tune the oscillation frequency in different OEO architectures (in delay-line based OEOs [6]-[9] by using double delay-line loops or adding an optical filter to the OEO loop, or in WGM resonators based OEOs by using tunable WGM resonators made of electro-optic crystalline materials...). This proves that the tunability is an important feature to be studied in our FRR based OEO, and we have therefore investigated the FRR tunability by different means.

Of course, the aforementioned thermal stability study is a first technique which may be used to tune the FRR-OEO oscillation frequency. Nevertheless, we have realized that the FRR response to the temperature is too weak (70 Hz/K for a 20m-long FRR; see Fig.V. 2). Also, temperature tuning is a very slow process and therefore inefficient for many applications. We have therefore searched for other means to tune the FRR frequency response.

V.3.1 Theoretical studies on the tunability of the FRR

Studying the FRR's tunability, we have investigated the possibilities of tuning the absolute frequency of the optical frequency comb generated by the FRR, and also tuning the FRR's *FSR*. Ideally, we have searched to tune both of them independently.

V.3.1.a *Absolute frequency tuning using an optical phase-shifter*

In [11], D. Sadot has reported on an ultra-fast tunable optical filter with a tuning speed of less than one nanosecond. His filter configuration was based on a direct-coupled ring resonator architecture where a phase-shifter (PS) has been inserted within the fiber ring loop. The PS was used to control the phase delay inside the ring loop, and therefore, the phase matching condition in the ring resonator. A change in the phase matching condition leads to an absolute frequency shift in the optical frequency comb generated by the resonator. This frequency shift is proportional to the additional phase-shift added inside the fiber ring loop. The principle can be used to control the absolute frequency of the FRR's optical comb in our case, (see Fig.V. 5 (a)).

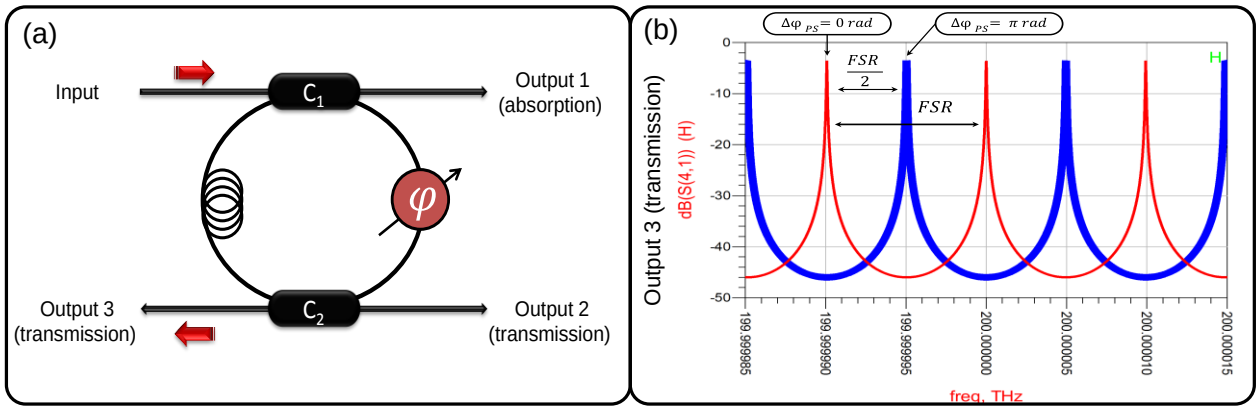

Fig.V. 5. (a) FRR architecture with a phase-shifter used to control the phase delay inside the fiber ring loop. (b) ADS simulation of the optical frequency comb shift in a 20m-long FRR (in blue) when an additional phase-shift $\Delta\varphi_{PS} = \pi$ is added inside the FRR's loop

Similar to the temperature variation case, when the PS is driven by a given DC voltage (ΔV_{PS}), the optical signal inside the FRR will encounter an additional phase delay ($\Delta\varphi_{PS}$), depending on the PS's phase-shift coefficient $\left(\kappa_{\varphi-PS} = \frac{\Delta\varphi_{PS}}{\Delta V_{PS}}\right)$. As a result, the phase matching condition in (Eq. V. 4) will be replaced by:

$$\varphi_{res} = \frac{2\pi\, f_{Opt}\, n\, L}{c} + \Delta\varphi_{PS} \qquad \textit{(Eq. V. 17)}$$

The additional phase delay $\Delta\varphi_{PS}$ is given by:

$$\Delta\varphi_{PS} = -\frac{2\pi\, f_{Opt}\, \Delta n_{PS}\, L_{PS}}{c} \qquad \textit{(Eq. V. 18)}$$

where Δn_{PS} is the PS's refractive index variation and L_{PS} is the PS length. Usually, L_{PS} does not experience any significant change when applying ΔV_{PS} to the PS, therefore its variation could be neglected.

Accordingly, the resonant frequency f_{Opt_0} in (Eq. V. 5) will be replaced by:

$$f_{Opt_0}{}' = f_{Opt_0} + \Delta f_{Opt} \qquad \textit{(Eq. V. 19)}$$

where Δf_{Opt} is the optical resonant frequency shift, proportional to the phase-shift induced by the PS. It is given as follows, [11]:

$$\Delta f_{Opt} = \frac{\Delta\varphi_{PS}}{2\pi} \cdot \frac{c}{n\, L} = \frac{\Delta\varphi_{PS}}{2\pi} \cdot FSR \qquad \textit{(Eq. V. 20)}$$

From (Eq. V. 20), it is clear that when an additional 2π phase-shift is added to the optical signal inside the fiber ring loop, the optical resonant frequency f_{Opt_0} will shift by one *FSR*. Using ADS, we have simulated the transmission and absorption responses of a 20m-long FRR, where a phase-shifter has been inserted within the fiber loop. Changing $\Delta\varphi_{PS}$ from 0 to 2π and monitoring the FRR's responses has confirmed the validity of this tuning principle (see Fig.V. 5 (b)). Furthermore, such a tuning technique does not modify the FRR's transmission characteristics (*IL*, Q_{Opt} etc…).

As we have already mentioned, the frequency shift in the resonator's optical comb will not be visible in the RF domain using our microwave domain characterization technique (this technique can only confirm that no significant change in the FSR occurs). Nevertheless, this frequency shift could be detected using the narrow linewidth laser wavelength scanning method (detailed in chapter II), as we will see in the following.

The tuning principle using a PS has been experimentally tested. We have used a 23m-long FRR with a PS (general optics FPS 001) that has been inserted within the fiber loop. This PS has been characterized using a Mach-Zhender interferometer configuration (see Appendix B), and we have measured a PS's phase-shift coefficient $\kappa_{\varphi-PS}$ = 0.059π rad/V. Therefore, a ΔV_{PS} equal to 18 V will result in a $\Delta\varphi_{PS}$ equal to π rad.

The FRR including a PS (FRR-PS) has been characterized using the narrow linewidth laser wavelength scanning method and the experimental setup illustrated in Fig.V. 6. The second 20m-long FRR in this setup has been used as a spectator FRR to witness on the absolute frequency shift in the 23m-long FRR's optical comb.

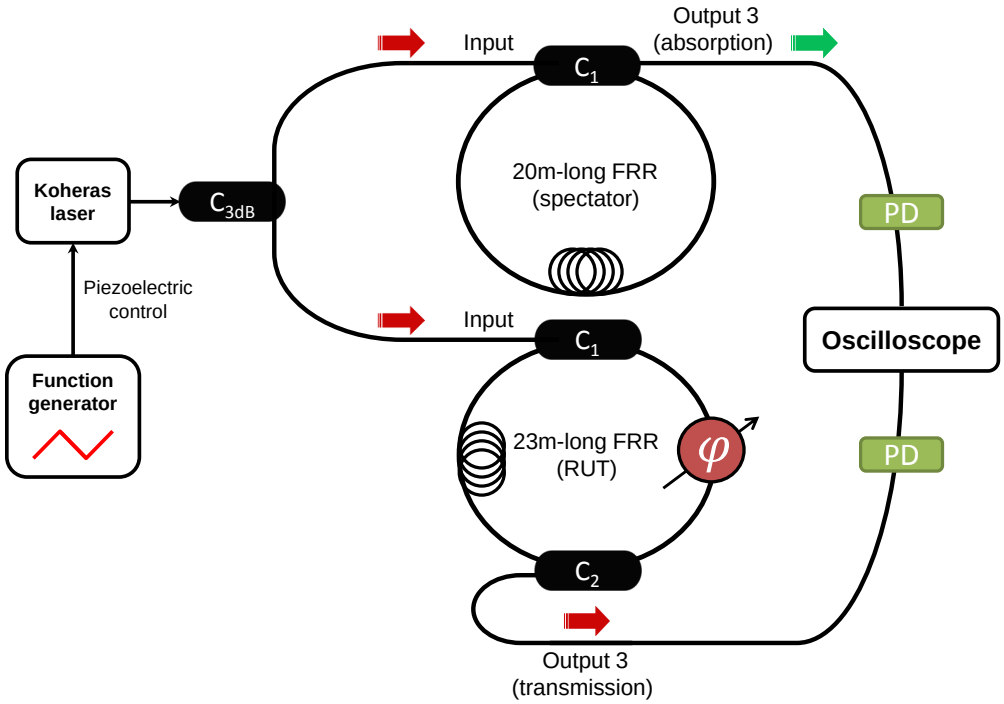

Fig.V. 6. Experimental bench used to detect the frequency shift in a 23m-long FRR's optical comb, caused by an additional phase-shift added inside the ring loop via a phase-shifter. RUT: resonator under test; C_{3dB}: 3dB coupler

The experimental results are depicted in Fig.V. 7. These results confirm that when an additional phase-shift $\Delta\varphi_{PS} = \pi$ is added inside the FRR's loop, its optical frequency comb shifts by the half of the resonator's FSR, $\left(\Delta f_{Opt} = \frac{FSR}{2}\right)$.

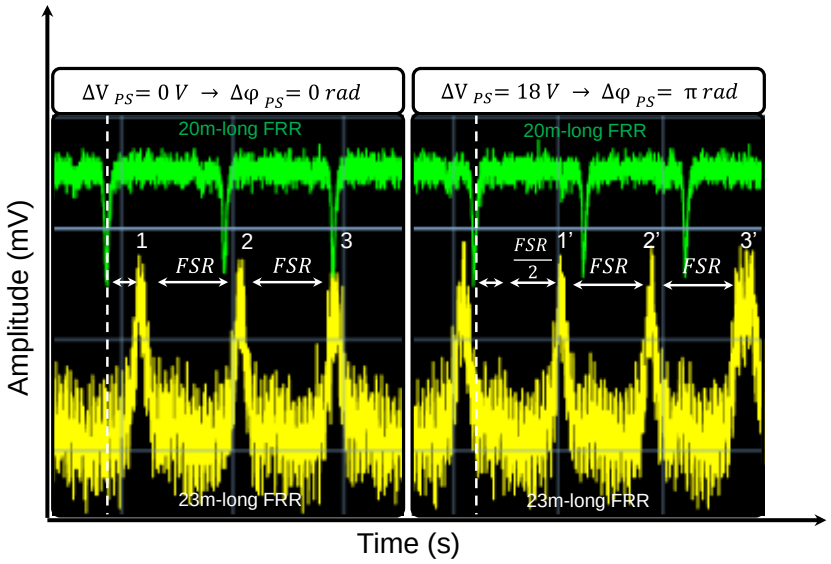

Fig.V. 7. Absolute frequency shift by FSR/2 of the optical comb generated by the 23m-long FRR (in yellow), occurred when an additional phase-shift $\Delta\varphi_{PS} = \pi$ is added inside the FRR's loop. The second 20m-long FRR (in green) has been used as a spectator ring to witness on this absolute frequency shift

V.3.1.b *Free spectral range tuning using a variable optical coupler*

The Sagnac effect, named after French physicist Georges Sagnac who has provided the first experimental demonstration in 1913, manifests itself in a setup called ring interferometer. This setup was capable of indicating the state of rotation of the frame of reference in which it was at rest [12]. In this ring interferometer, the injected light beam is split and the two beams are made to follow a trajectory in opposite directions. The output of this interferometer is sensitive to any phase difference between these two counter-propagating beams.

In our case, the same effect could be used to split the FRR's resonance, thus creating a new and controllable optical frequency comb. This is achieved in a configuration that includes a classical FRR architecture with Sagnac mirror (SM) inside the fiber ring loop. The SM is created by a fiber loop of given length L_{SM} and a tunable optical coupler (TC) (see Fig.V. 8.). This technique has been thoroughly studied by C. Vázquez et al. [13] [14], where analytical expressions describing a similar architecture have been derived (they used a single-direct coupled ring resonator instead of the FRR we are using).

In this architecture, a FRR including a SM (FRR-SM), the optical resonance experiences a split that looks like a creation of a new optical frequency comb. The resonance split value (Δs), or what we can call the new optical comb's absolute frequency shift from the main optical comb, depends on the TC's coupling coefficient (κ_{TC}). By tuning κ_{TC} from 0 to 100 %, we are able to modify Δs from zero to one complete *FSR*.

The FRR-SM's FSR, for both optical frequency combs, is given by:

$$FSR_{FRR-SM} = \frac{c}{n \cdot (L_{FRR} + L_{SM})} \qquad \textit{(Eq. V. 21)}$$

where L_{FRR} is the FRR length.

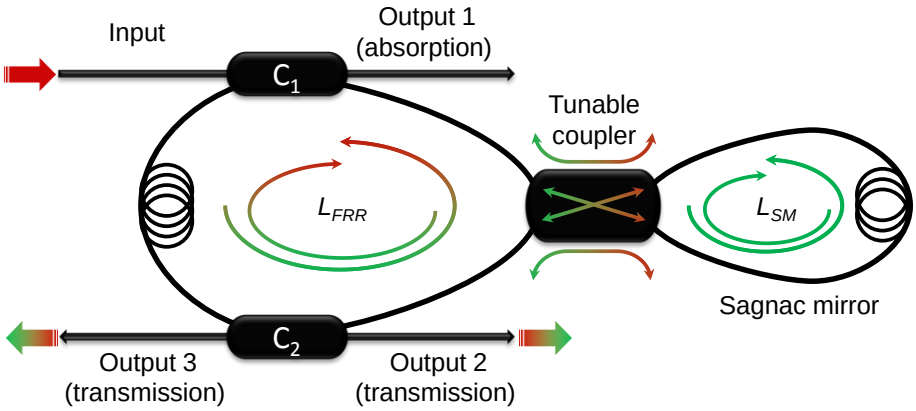

Fig.V. 8. General architecture of the FRR including a Sagnac mirror

Using ADS, we have created a model of the FRR-SM, with an 18m-long FRR and a 2m-long SM. We considered that the fiber attenuation A_f is equal to 0.5 dB/km (P-M fibers) and that the three couplers' excess losses were as follows: $\gamma_1 = \gamma_2 = \gamma_{TC} = 0.03$ dB (all these values can be technically achieved). Furthermore, an optimal optical coupling has been found for couplers C_1 and C_2 ($\kappa_1 = \kappa_2 = 8\%$).

The simulation results of the optical transmission spectrum versus κ_{TC}, at both second and third outputs of the FRR-SM structure, are presented in Fig.V. 9 (we have presented only the results for κ_{TC} = 1% and 50 % for clarity's sake).

From these results we can see that, interestingly, the main optical frequency comb will still be fixed while the new comb is shifted in function of κ_{TC}. This FRR-SM characteristic has not been reported in the work of C. Vázquez et al. [13] [14]. Moreover, a frequency shift by $\frac{FSR_{FRR-SM}}{2}$ can be observed in the new optical comb when κ_{TC} is equal to 50 %.

Furthermore, the resonator's both outputs seem to behave differently. We have therefore compared both outputs' behavior versus κ_{TC}, regarding the main and new resonances' FWHM and transmission loss (see Fig.V. 10 (a) and (b) respectively), and the main and new resonances' worst-case rejection (see Fig.V. 11).

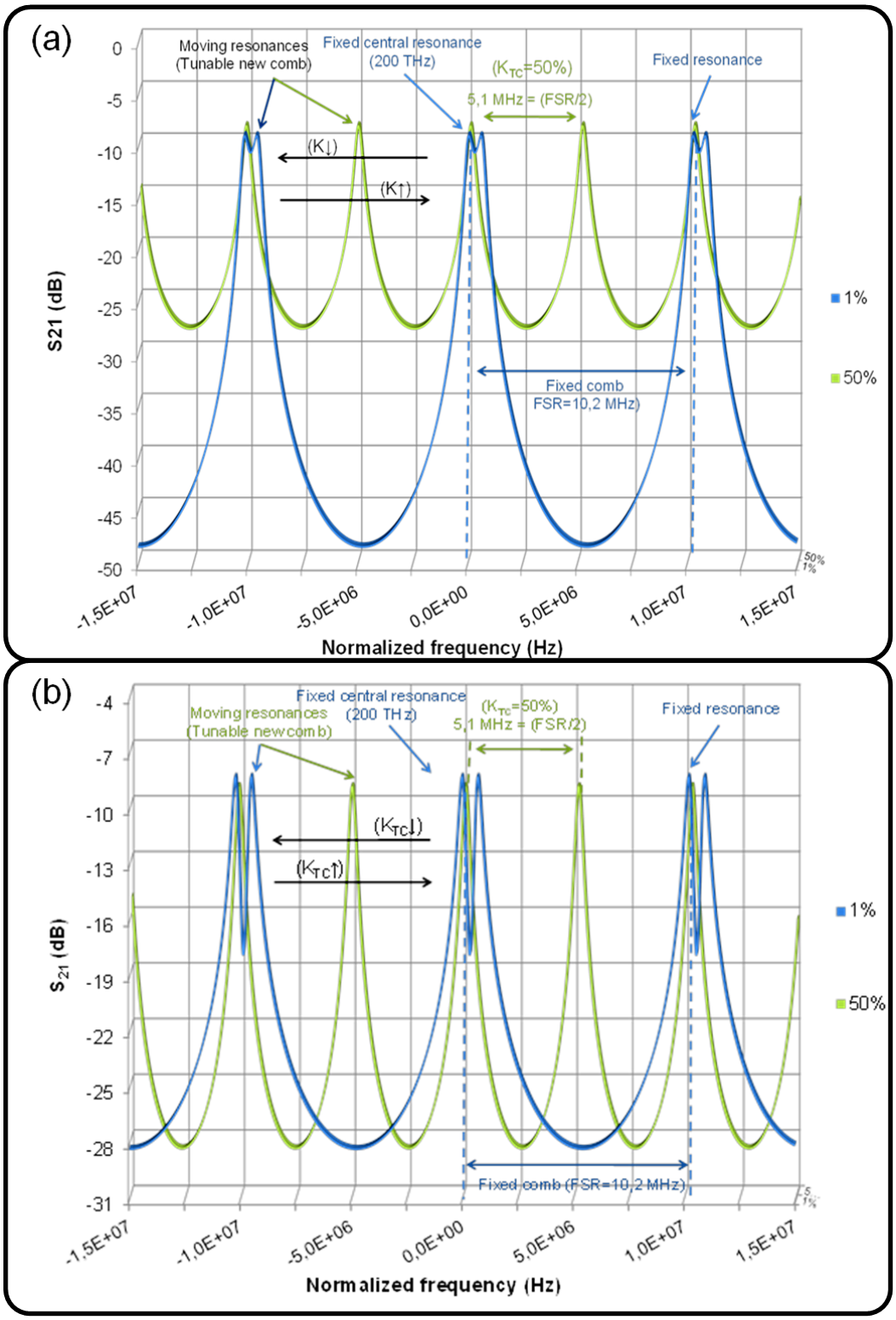

Fig.V. 9. ADS simulation results of the optical transmission spectrum at both second (a) and third (b) outputs of the FRR-SM's versus κ_{TC}. A frequency shift by $\frac{FSR_{FRR-SM}}{2}$ can be observed in the new optical comb when κ_{TC} *is at 50 %.* ↑ and↓ *notations indicate an increasing or a decreasing in* κ_{TC} *value*

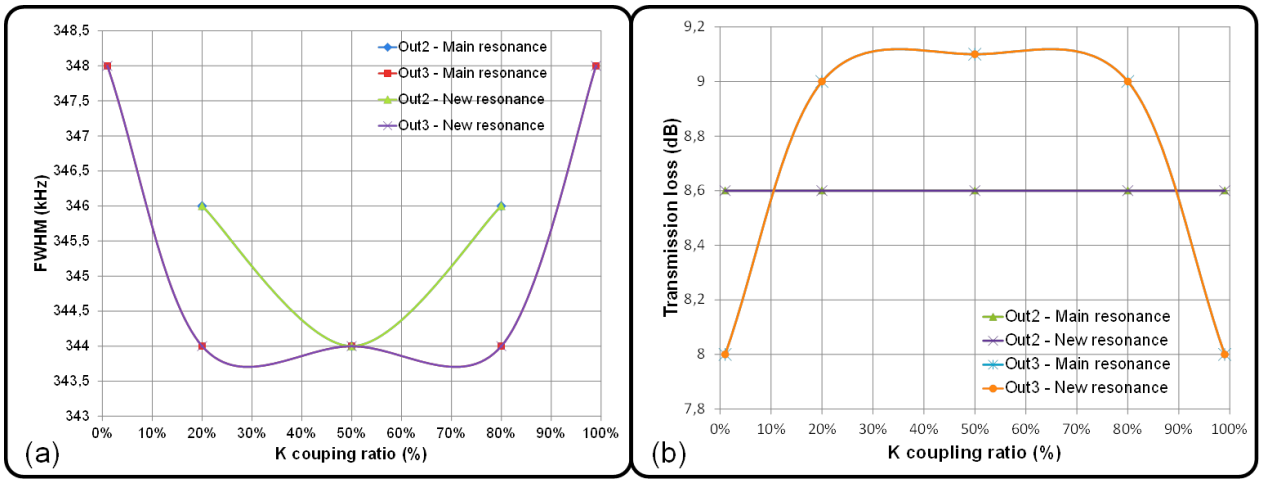

Fig.V. 10. ADS simulation results of the transmission characteristics at the FRR-SM's both second and third outputs' main and new resonances of versus κ_{TC}: (a) FWHM and (b) Transmission loss

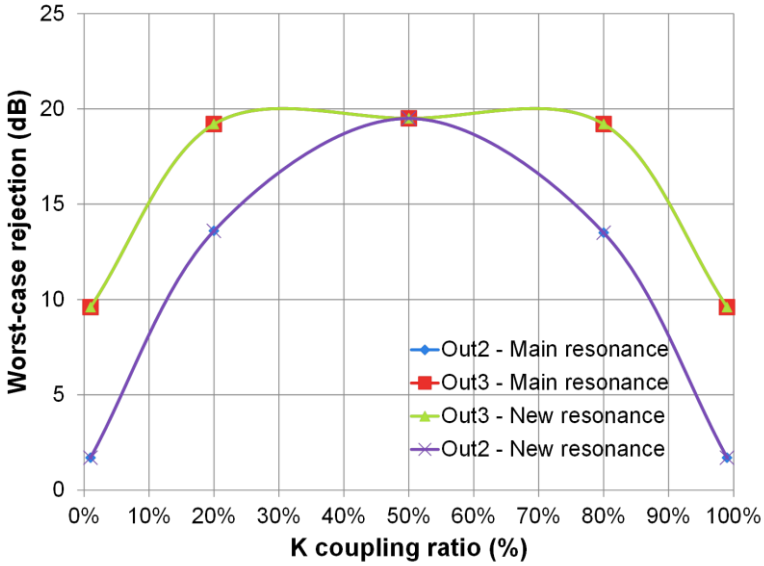

Fig.V. 11. ADS simulation of the worst-case rejection at the FRR-SM's both second and third outputs' main and new resonances versus κ_{TC}

The results in Fig.V. 10 (a) show that for both outputs, the FWHM is the same for the main and the new resonances, however, we can get a narrower FWHM at the FRR-SM's third output and on a wide range of κ_{TC} variations. This FWHM is between 344 kHz and 348 kHz, which means a Q_{Opt} of 5.6×10^8 at 1.55 µm laser wavelength. Identically, the results in Fig.V. 10 (b) show that for both outputs the transmission loss is the same for the main and the new resonances. On the other hand, we can get a constant transmission loss at the second output versus κ_{TC} (transmission loss = 8.6 dB), which is not the case at the third output. Actually, we can see that the transmission loss at the third output varies from 8 dB to 9.1 dB versus κ_{TC}, which is still acceptable if we take into consideration the FWHM behavior and also the worst-case rejection behavior of the resonances at the third output.

Actually, Fig.V. 11 results show that for both outputs, the worst-case rejection is the same for the main and the new resonances, but we can get a higher rejection at the FRR-SM's third output and on a wide range of κ_{TC} variations.

V.3.1.c *All-tunable FRR*

The simulation results of section V.3.1.b are very interesting: they predict, together with section V.3.1.a's simulation and experimental results, that an all-tunable FRR (TFRR) structure is possible if we combine the tunable coupler effect with the phase-shifter effect. This structure will include a SM and a PS as illustrated in Fig.V. 12. It is noteworthy to know that the insertion of the PS either in the SM loop or in the FRR loop will have the same effect on the TFRR response.

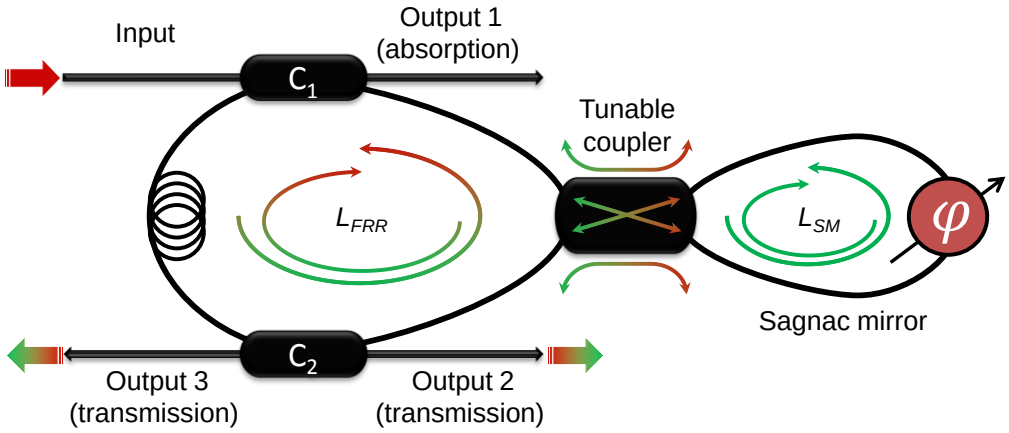

Fig.V. 12. All tunable FRR: a FRR including a Sagnac mirror and a phase shifter

The frequency spectrum at the third output of a 20m-long TFRR has been simulated using ADS. The simulation results presented in Fig.V. 13 show that an independent tuning of the new optical comb, and uniformly both new and main combs, is possible by means of the tunable coupler and the phase-shifter respectively.

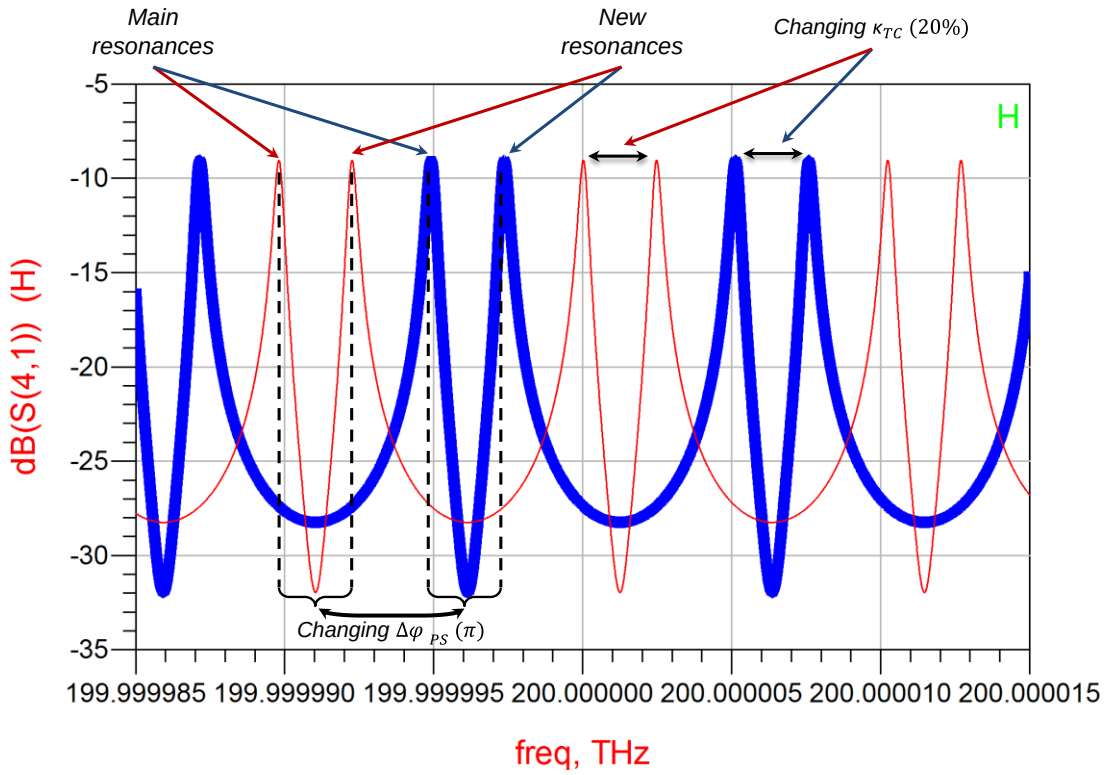

Fig.V. 13. 20m-long all-tunable FRR's third output frequency spectrum simulated using ADS. An independent tuning of the new optical comb and a uniform tuning of both new and main optical combs is respectively obtained by changing the coupling coefficient of the tunable coupler and the phase-shift added by the phase-shifter

V.3.2 Experimental results of an all-tunable FRR

Due to the significance of what ADS is predicting on the TFRR, and in order to confirm these simulation results, we have tried to fabricate a TFRR with some optical devices available at our laboratory.

For this purpose, we have first characterized a polarization maintaining variable ratio optical coupler (905(P)-E from Evanescent Optics Inc.). This coupler's coupling coefficient is adjusted by two different means: a fast tuning accomplished by means of a micrometer screw, and a fine tuning remotely controlled using a piezoelectric actuator. The coupling characteristics of the tunable coupler are presented in Fig.V. 14 versus the DC bias voltage applied to its piezoelectric actuator. They show that the coupler's excess loss is very high, as it can be around 20% (~1 dB). Moreover, both outputs A and B are not equilibrated and also the coupler is not free of hysteresis.

The PS we used has been already mentioned in section V.3.1.a and its characterization is detailed in Appendix B. It has a phase-shift coefficient $\kappa_{\varphi-PS}$ = 0.059π rad/V.

Finally, a TFRR has been fabricated using the aforementioned variable coupler and PS, with FRR's input and output couplers having the following characteristics: κ_1 = κ_2 = 30 % and γ_1 = γ_2 = 0.1 dB. Unfortunately, the whole structure had very high transmission loss (because this was only a test-structure and we were using fiber connectors to connect the different elements instead of splicing

them). Therefore, we have removed the PS from the TFRR structure and we have only tested the FRR-SM behavior. The FRR-SM was 7m-long (L_{FRR} = 5 meter and L_{SM} = 2 meter), thus a 29 MHz FSR_{FRR-SM} is to be expected.

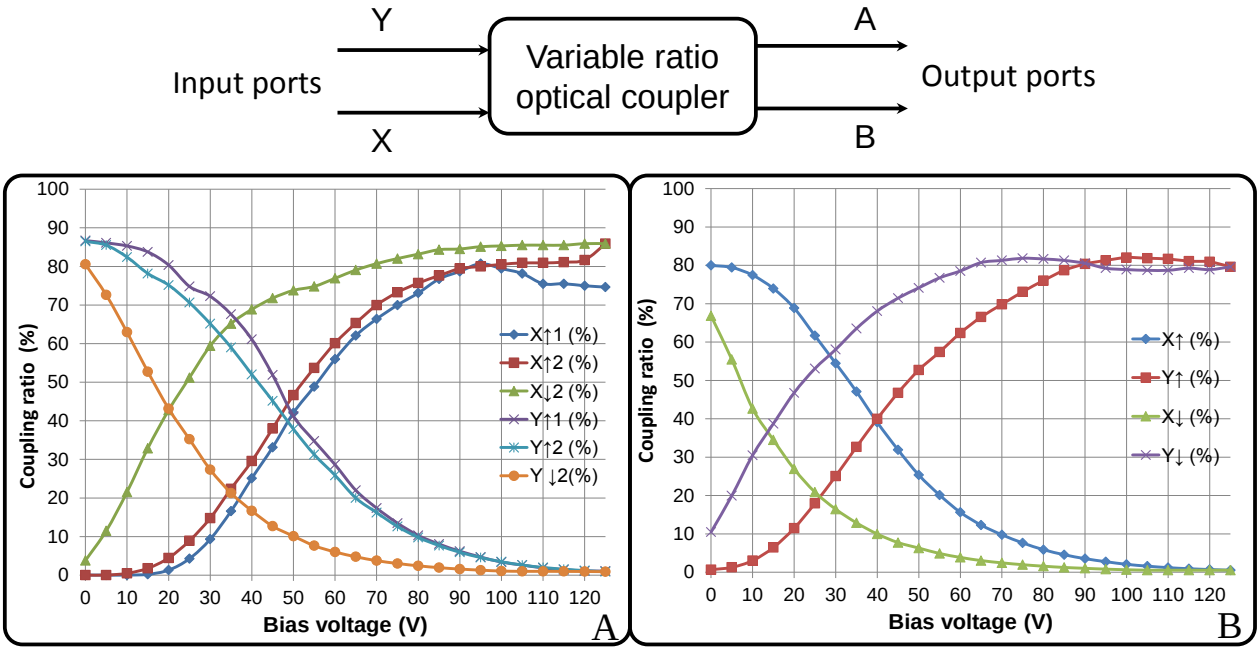

Fig.V. 14. Evanescent Optics (905(P)-E) variable ratio optical coupler scheme and characteristics. A and B notations indicate that the coupler has been characterized at its A or its B output. X and Y notations indicate that the coupler has been characterized with an input optical signal at its X or its Y input. ↑ and↓ notations indicate respectively that the DC bias voltage, applied to the coupler piezoelectric actuator, has been increased from 0 V to 125 V or decreased from 125 V to 0 V (we have done these measurements to scale the coupler's hysteresis)

In spite of removing the PS from the structure, the transmission loss was always high, preventing a correct description of the FRR-SM's transmission characteristics using the microwave domain characterization bench (chapter II). On the other hand, we were able to describe the FRR-SM absorption characteristics using this characterization bench because more optical power can be detected at the absorption port of the structure. The characterization results are presented in Fig.V. 15 and they confirm a total FSR_{FRR-SM} of 31 MHz and a frequency shift in the new comb by the half of FSR_{FRR-SM} when κ_{TC} is around 50%. The difference in the absorption resonances' depths is likely due to the fact that the variable coupler outputs A and B are not equilibrated.

It is noteworthy to point out that when characterizing the FRR-SM structure in the RF domain, we have used a frequency-shifter modulator (FSM; fabricated by our Italian partners at SELEX) instead of a MZM. Actually, the resonances in the two combined frequency combs, generated by the FRR-SM, are not equidistant. This will result in a deformation of the RF response if a linear modulation of the carrier is used because the modulation sidebands will probably not overlap with two optical resonances of the FRR-SM at the same time. On the contrary, the FSM produces only one sideband modulation of the optical carrier. Consequently, it is possible to stabilize the laser carrier on one of the optical resonances

of the main frequency comb (ideally), and the modulation sideband will explore the other resonances of the two combs generated by the FRR-SM and transcribe them accurately in the RF domain.

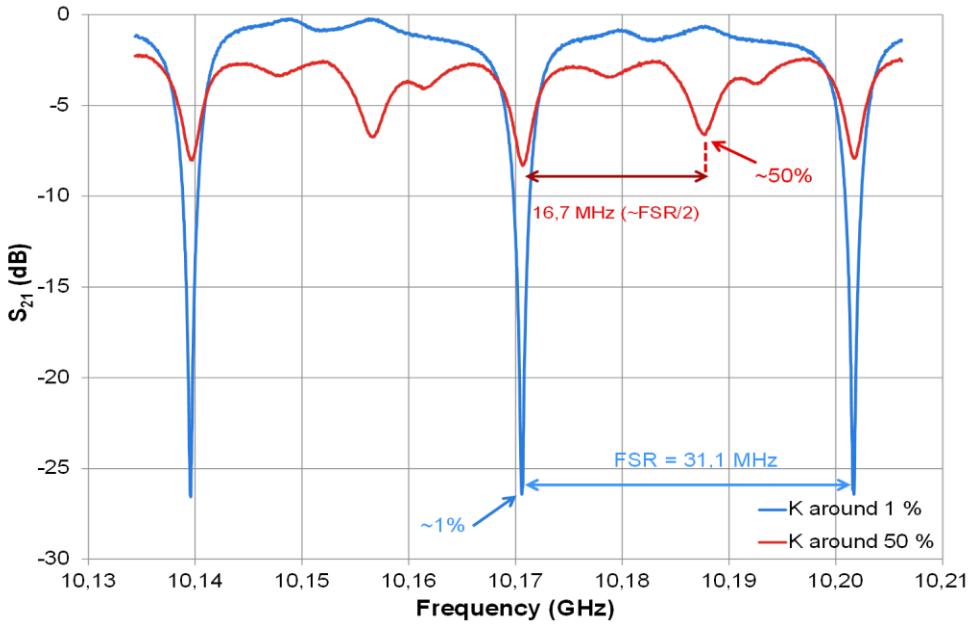

Fig.V. 15. 7m-long FRR-SM tunability characterized at its absorption output using the microwave domain characterization bench. The absorption output was used because the FRR-SM transmission loss was very high, preventing a correct transmission characterization of the structure. The difference in the absorption resonances' depths is likely due to the fact that the variable coupler outputs A and B are not equilibrated

Finally, we have tried to characterize this FRR-SM using the narrow linewidth laser wavelength scanning method (detailed in chapter II), but we were also having the same high transmission loss issue. Using an EDFA, we were able to detect the transmission behavior of the FRR-SM (at its third output) versus some values of κ_{TC} (1%, 30%, 70 % and 87 %). The results are depicted in Fig.V. 16.

In spite of a transmission spectrum where resonances are not equilibrated (due to the couplers outputs which are not equilibrated), the results in Fig.V. 16 fit qualitatively well with our simulation's predictions on the FRR-SM optical comb tunability versus κ_{TC}.

Finally, these different theoretical and experimental studies confirm qualitatively the possibility of having an all-tunable FRR. Of course, the FRR-SM structure we experimentally characterized was only a test-structure that was not optimized. It was used to validate what ADS has predicted on the FRR-SM tunability. Such a tunable structure can be very advantageous for many applications (narrow bandwidth tunable filter, tunable OEO…).

Also, as an example, we can lock two optical modes of the TFRR onto two absorption lines of a hydrogen cyanide reference cell [15], and then we can use these TFRR modes for time-frequency applications in the optical domain or in the RF domain.

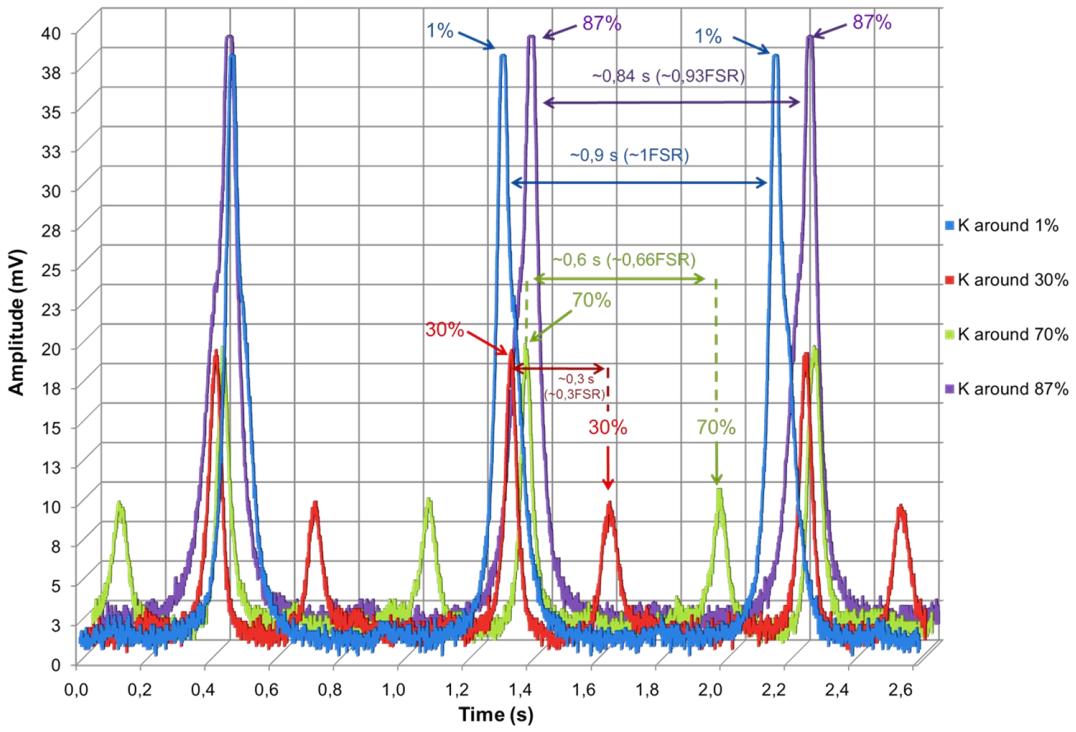

Fig.V. 16. 7m-long FRR-SM tunability characterized at its third transmission output using the narrow linewidth laser wavelength scanning method. The results show a frequency shift in the new comb that can be equal to ~0.93 FSR_{FRR-SM} *if* κ_{TC} *is equal to ~ 87 %. The difference in the absorption resonances' depths is likely due to the fact that the variable coupler's outputs A and B are not equilibrated*

V.4 Conclusion

In this chapter, a theoretical study of the FRR based OEO thermal stability has been presented. The temperature sensitivity of this system, when it uses two optical modes of the FRR for microwave stabilization, is determined by the FRR thermal stability. This thermal stability has been found to be close to -6.8ppm K^{-1} whatever the FRR length is. This relative thermal stability value is comparable to the typical thermal stability of a conventional microwave dielectric resonator oscillator, which is in the range of 3 ppm K^{-1} for commercial devices. Our results have been successfully confirmed through different experimental tests.

In addition to this study, the FRR tunability has been theoretically studied and we have been able to demonstrate the tunability concept of an all-tunable FRR structure. In this structure, the optical frequency comb absolute frequency and the FSR can be both changed independently, respectively by means of a phase shifter and a tunable optical coupler in a Sagnac loop configuration. This structure has been simulated and then qualitatively validated through different experimental tests. Finally, if such a structure can be improved in terms of losses, it could be very useful for many optical and RF applications.

V.5 References

[1] G. Ghosh, "Temperature dispersion of refractive indexes in some silicate fiber glasses," Photonics Technology Letters, IEEE , vol.6, no.3, pp.431-433, March (1994).

[2] S. Chang, C. C. Hsu, T. H. Huang, W. C. Chuang, Y. S. Tsai, J. Y. Shieh, and C. Y. Leung, "Heterodyne inteferometric measurement of the thermo-optic coefficient of single mode fiber," Chin. J. Phys. 38, 437-442, (2000).

[3] H. Choi, H. Taylor, and C. Lee, "High-performance fiber-optic temperature sensor using low-coherence interferometry," Opt. Lett. 22, 1814-1816, (1997).

[4] R. Wynne, J. Daneu, and T. Fan, "Thermal Coefficients of the Expansion and Refractive Index in YAG," Appl. Opt. 38, 3282-3284, (1999).

[5] D. Sadot, and E. Boimovich, "Tunable optical filters for dense WDM networks," Communications Magazine, IEEE , vol.36, no.12, pp.50-55, Dec (1998).

[6] S. Huang, L. Maleki, and T. Le, "A 10 GHz optoelectronic oscillator with continuous frequency tunability and low phase noise," Frequency Control Symposium and PDA Exhibition, 2001. Proceedings of the 2001 IEEE International , vol., no., pp.720-727, (2001).

[7] S. Fedderwitz, A. Stohr, S. Babiel, V. Rymanov, and D. Jäger, "Optoelectronic K-Band Oscillator With Gigahertz Tuning Range and Low Phase Noise," Photonics Technology Letters, IEEE , vol.22, no.20, pp.1497-1499, Oct.15, (2010).

[8] I. Ozdur, D. Mandridis, N. Hoghooghi, and P.J. Delfyett, "Low Noise Optically Tunable Opto-Electronic Oscillator With Fabry–Perot Etalon," Lightwave Technology, Journal of , vol.28, no.21, pp.3100-3106, Nov.1, (2010).

[9] M. E. Belkin, A. V. Loparev, Y. Semenova, G. Farrell, and A. S. Sigov, "Tunable RF-band optoelectronic oscillator and optoelectronic computer-added design model for its simulation," Microw. Opt. Technol. Lett., 53: 2474–2477, (2011).

[10] A. Savchenkov, V. Ilchenko, W. Liang, D. Eliyahu, A. Matsko, D. Seidel, and L. Maleki, "Voltage-controlled photonic oscillator," Opt. Lett. 35, 1572-1574, (2010).

[11] D. Sadot, "Ultra-fast tunable fiber-loop optical filters for dense WDM applications," WDM Technology and Applications IEE Colloquium, pp.13/1-13/5, (1997).

[12] E. J. Post, "Sagnac effect," Rev. Mod. Phys. 39, 475–493, (1967).

[13] C. Vazquez, S. Vargas, J.M.S. Pena, and P. Corredera, "Tunable optical filters using compound ring resonators for DWDM," Photonics Technology Letters, IEEE , vol.15, no.8, pp.1085-1087, (2003).

[14] C. Vazquez, S.E. Vargas, and J.M.S. Pena, "Sagnac loop in ring resonators for tunable optical filters," Lightwave Technology, Journal of , vol.23, no.8, pp. 2555- 2567, (2005).

[15] S. L. Gilbert, W. C. Swann, and C. M. Wang, "Hydrogen cyanide $H^{13}C^{14}N$ absorption reference for 1530–1560 nm wavelength calibration—SRM 2519," NIST Spec. Publ. 260–137 (National Institute of Standards and Technology, Gaithersburg, Md., 1998).

General Conclusion

In this manuscript, we have presented a research work focused on the design of a high spectral purity microwave source using an optoelectronic oscillator (OEO) based on a passive optical resonator, and particularly, on a fiber ring resonator (FRR). This approach is relatively recent and different compared to the one using an optical delay line (DL). The resonator in this case provides simultaneously a large optical delay and a selective signal filtering. It was therefore important for us to point out the efficiency of this approach through many theoretical and experimental studies.

Of course, very high spectral purity sources have been already demonstrated using DL-OEOs. In these systems, contrarily to microwave oscillators, the signals' spectral purity can be possibly better when the RF application frequency increases. On the other hand, DL-OEOs remain bulky and their thermal stabilization is difficult. In addition, they produce spurious modes that need complex configurations to be reduced.

It has been recently found that the use of passive optical resonators can be the solution for many problems encountered in microwave oscillators (e.g. spectral purity at very high frequencies) and in classical DL-OEOs (e.g. size, spurious modes and thermal stability). One of the optical resonators that can be used are the WGM micro-resonators (WGMRs) of mm and sub-mm sizes. They can sharply reduce the oscillator's size and open the path towards integration of such oscillators, with satisfying phase noise levels. Nevertheless, their use in a system is a bit demanding because of the mechanical difficulty in setting up a reliable coupling with a light source and the numerous frequency combs they generate.

Throughout this thesis, a calcium fluoride disk-shaped WGMR has been used to build a 12.5 GHz OEO. We have used a symmetrical coupling technique to couple the laser light-wave onto the resonator. The phase noise spectrum of the generated signal is shown in the figure below. We have found that this phase noise was limited by the WGMR's optical quality factor (Q_{Opt} = 8.4x10^7) and the RF amplifier's noise.

The fact that the FRR is much simpler to use and to fabricate than WGMRs, and that very high Q_{Opt} could be obtained using this resonator, this has made it a very interesting alternative to build an OEO. This optical passive resonator has been therefore thoroughly studied in this manuscript.

During our studies on the FRR, it turned out that such a resonator must be well studied and designed before being used in an OEO setup. In the figure below, we present the phase noise results of the first experiment we made using a 10m-long FRR. This resonator was a test module which has not been well optimized and designed for such application. As a result, and to be able to correctly use a FRR in an OEO setup as the frequency stability element, we have performed multiple modeling studies to simulate the FRR characteristics in function of its different parameters, especially its couplers' coupling coefficients and losses. The obtained simulation results have been then validated experimentally using optical domain and microwave domain characterization benches.

In parallel with these simulations, we have created a FRR model using a microwave CAD software (ADS from Agilent). This FRR model has been implemented in a global OEO model which has been created using the same software. Consequently, open-loop power and frequency simulations have been performed and then validated experimentally. Still, the phase noise simulations using the OEO's ADS model are so far not realistic and noise modeling needs further investigations to make it possible.

These modeling studies have been of great interest in optimizing the different FRRs we have designed and fabricated later during this thesis, and also in our investigations on the tunability of the FRR. Moreover, even if a direct computation of the phase noise is still difficult, the OEO's ADS model has helped us to understand the different noise conversion phenomena occurring inside the FRR based OEO.

One of our optimization studies was based on the evaluation of the white frequency noise contribution to the phase noise of the FRR based OEO. We have shown that there is a trade-off to be made regarding the resonator couplers' coupling coefficients in order to get a satisfying Q_{Opt} and a low noise-to-carrier ratio at the same time. This should finally lead to a low white frequency noise contribution. Thanks to this study, an important reduction of the OEO phase noise has been demonstrated using an optimized 20m-long FRR featuring a Q_{Opt} = 5.1x10^9 (see the figure below).

Despite that, the noise results were always far from our theoretical expectations. We have therefore scrutinized the different noise conversion processes that can take place in the OEO setup. Our noise studies have revealed that the laser frequency noise can be converted into OEO phase noise via the FRR when the laser is not properly stabilized onto the center of the optical resonance. Furthermore, we have found that the laser relative intensity noise (RIN) can be up-converted to microwave amplitude and phase noise via the photodiode nonlinearity. A photodiode optimal optical power working-point, at which the photodiode's RIN-to-RF phase noise conversion factor could approximately vanish, has been identified.

Still, and despite all these studies, another important noise contribution to the OEO phase noise was always present and had to be studied: the nonlinear optical effects generated inside the FRR due to its very high Q_{Opt} and its high intra-cavity power enhancement factor. Among these, the Brillouin scattering and the Rayleigh scattering were the dominating nonlinear effects. These effects are power dependent and we have found that the OEO phase noise can be further improved by working at low optical power (see the figure below). On the other hand, such a low optical power will degrade the noise-to-carrier ratio and also prevent the photodiode from working on its optimal optical power to reduce its nonlinearity.

Therefore, these nonlinear optical effects were deeply studied in the FRR case. Through these studies, we have found a way to completely suppress the Brillouin scattering and to reduce the Rayleigh scattering in a new design of an immunized and high quality factor (Q_{Opt} = 2.1x10^9) 100m-long fiber ring resonator (IFRR). Once this IFRR was used in an OEO setup, considering also the different optimization studies we have made, we have been able to measure a considerably reduced phase noise with a -128 dBc/Hz noise level at 10 kHz offset frequency and a -150 dBc/Hz noise floor (see the figure below).

Aside from its negative effects on the phase noise of the FRR based OEO, investigations have been performed on the generation of millimeter-wave signals using the Brillouin selective sideband amplification process in the 20m-long FRR. The synchronization of the Brillouin selective amplification lines with a 21.7 GHz RF seed signal has resulted in the generation of high power and high spectral purity millimeter-wave signals up to 65 GHz.

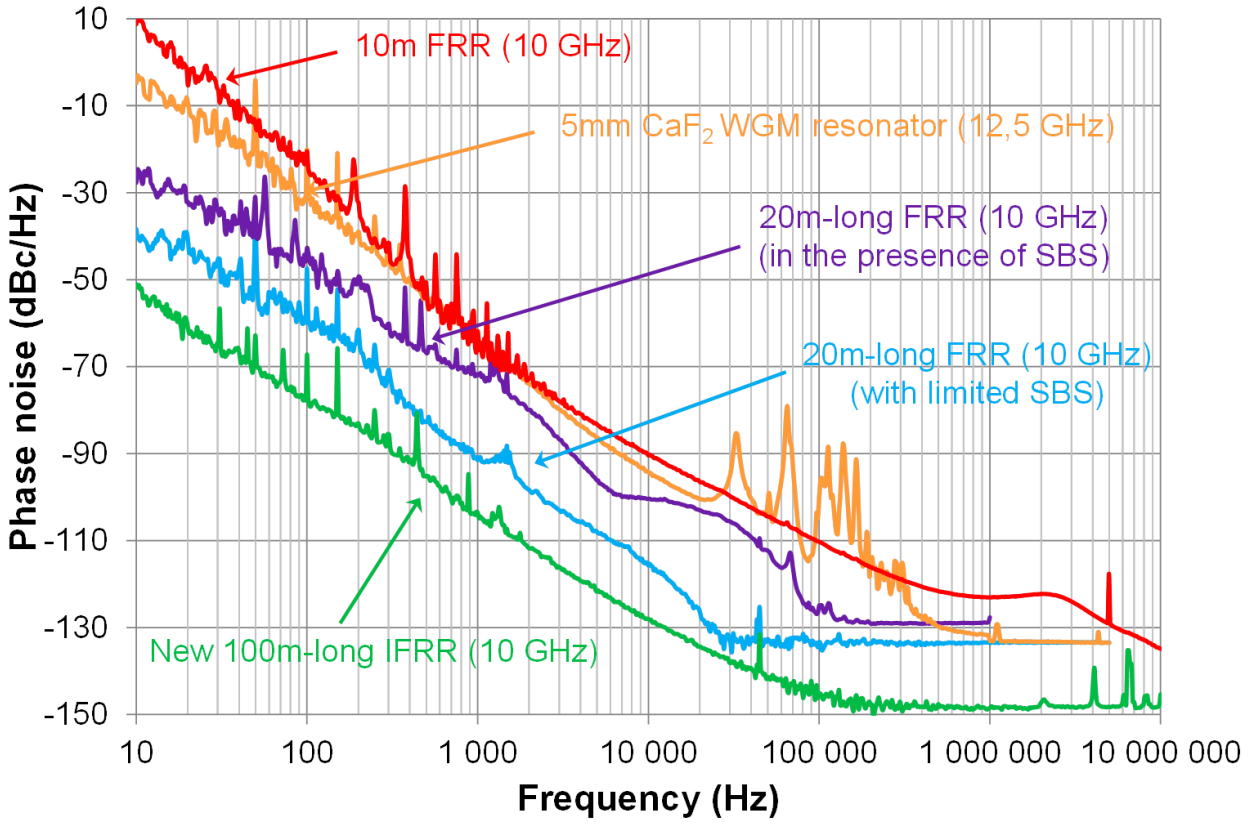

Recall of the phase noise results obtained using the different resonators and oscillators studied throughout this thesis

Finally, we have presented a theoretical study on the thermal stability of the FRR based OEO. This thermal stability has been found to be close to -6.8ppm K^{-1} regardless of the FRR length. Our experimental results have confirmed this proposition. This relative thermal stability value is comparable to the typical thermal stability of a conventional microwave dielectric resonator oscillator, which is in the range of 3 ppm K^{-1} for commercialized devices.

In addition, the FRR tunability has been inspected and we have been able to theoretically demonstrate the tunability efficiency of an all-tunable FRR structure. In this structure, we can independently change the optical frequency comb's absolute frequency and the mode spacing. This structure has been qualitatively validated through different experimental tests and could be very useful for many interesting applications (communications systems, radars…).

Perspectives

The comparison between the phase noise results obtained in the 100m-long IFRR based OEO and those obtained in a 330m-long active cavity based OEO (the COEO commercialized by OEwaves, the well-known company in the field) has shown a slight noise gap between both OEOs, which is in favor of the COEO. However, taking into account the fact that our IFRR is a passive resonator that has more than three times shorter length, this makes our OEO results very encouraging compared to the COEO. Moreover, we can expect to get even better results if the resonator's architecture is further optimized (which is possible if lower loss optical components are used, therefore much better resonator characteristics can be obtained), if other laser stabilization techniques are used (e.g. optical injection lock), if RF amplifiers' noise contribution to the OEO phase noise can be reduced and if lower noise optoelectronic components (laser, photodiode…) are used. The same expectation applies to the case of the calcium fluoride disk-shaped WGMR based OEO we have created (increasing the WGMR's quality factor and reducing the other noise contributions).

Moreover, like in DL-OEOs, passive resonators based OEOs can also benefit from the theory that predicts a better spectral purity of the signals generated by these systems at higher application frequencies (in the millimeter-waves range). Therefore, we think that better performance can be possibly obtained at higher frequencies for both OEOs we have demonstrated: the WGMR based OEO and the 100m-long IFRR based OEO. However, increasing the application frequency involves a large amount of work on the modulation and detection techniques in these frequency ranges to preserve the quality of the generated signals.

Besides that, more understanding of the different noise processes that occur in the OEO setup can be achieved by improving the OEO model we have created using a microwave CAD software. Moreover, and aside from the Brillouin threshold's theoretical prediction we have made, it will be interesting to model the Brillouin scattering efficiency inside the resonator. This will make it proficient to suppress the effect by a different way than the one we used or, on the contrary, it will create FRRs with enhanced nonlinearity for eventual nonlinear optics applications. For example, in the 20m-long FRR we can push the pump power much further than what it was reported in this manuscript to be able to generate high power and high spectral purity millimeter waves far above 100 GHz. Of course, specific optical-electrical detection schemes must be used in this case (wideband photodiodes).

Always in nonlinear optics' field, and even not detected in the 20m-long FRR, four-wave mixing can be used to generate high spectral purity microwave sources if specific managements are done in the FRR structure.

In the 100m-long FRR, we have seen that the insertion of an isolator has completely (optically) suppressed the Brillouin scattering and reduced the Rayleigh scattering. Of course, this technique can be improved by using a lower loss isolator. However, other methods like inducing a thermal difference in the FRR structure can possibly (acoustically) suppress the Brillouin scattering and therefore avoid the

additional optical loss caused by the optical isolator. Moreover, it would be interesting to inspect the FRR's response and nonlinearity at cryogenic temperatures, especially the behavior of the Brillouin scattering and the Rayleigh scattering as they are both spontaneously generated from the optical fiber's thermal instabilities. Can the use of the FRR at cryogenic temperatures suppress these nonlinear effects and increase the FRR's optical quality factor, and therefore reduce the OEO phase noise as in the cryogenic DRO's case?

Finally, the tunability demonstrated in a FRR based structure is very interesting as it can be used to create tunable FRR based OEOs or for an eventual locking of the structure's optical combs to ultra-stable atomic references. Hence, this can be then used for time-frequency metrology or to generate ultra-high stability microwave and optical sources.

Appendix A: Analytical expressions for FRR modeling

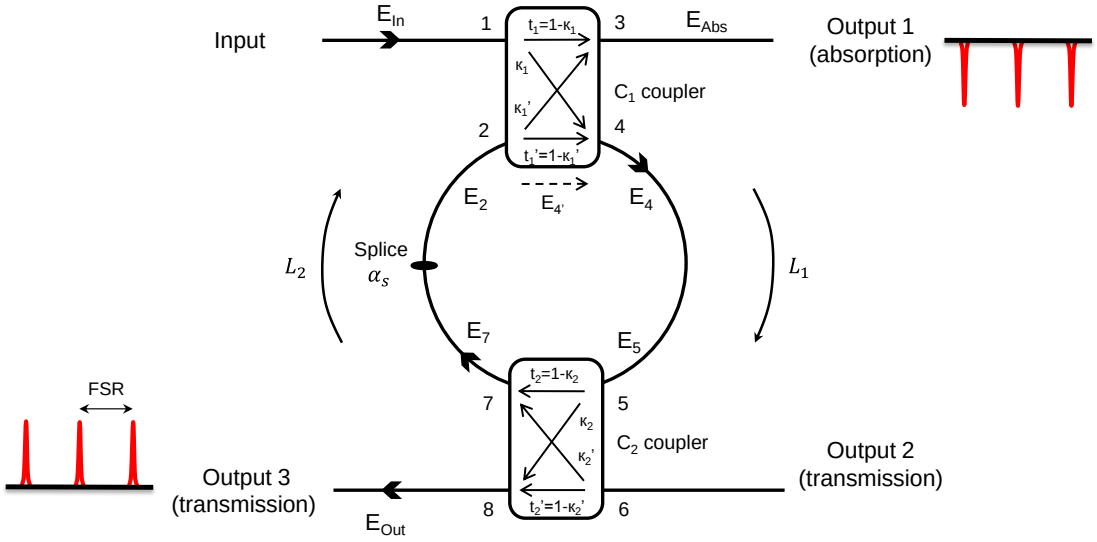

Double directional coupler fiber ring resonator.

To model the FRR parameters separately, we have first extracted analytical expressions for the resonance conditions from a detailed study that have been performed by F. Zhang et al[5] on a single-coupler direct-coupling ring resonator. We have extended their study in order to develop analytical expressions for the different parameters of the FRR, especially its transmission loss, Q_{Opt}, FSR and its intra-cavity power enhancement factor ($IPEF$)…

In these analytical expressions we describe the complex electric field behavior inside the resonator (see the above figure), where couplers C_1 and C_2 are assumed to be reciprocal.

At resonance, the optical circulating wave is in phase with the input light wave, the resonance phase condition is therefore as follows:

$$\beta \cdot L = p\ 2\pi \qquad (p = 1,2,3 \dots) \qquad \textit{(Eq.A.I. 1)}$$

After one turn inside the resonator, the complex electric field at port 2 can be written as follows:

$$E_2 = \sqrt{(1-\gamma_2)} \cdot \sqrt{t_2} \cdot \sqrt{(1-\alpha_s)} \cdot e^{-\alpha_f L} \cdot E_4 \qquad \textit{(Eq.A.I. 2)}$$

[5] F. Zhang and J. Lit, "Direct-coupling single-mode fiber ring resonator," J. Opt. Soc. Am. A 5, 1347-1355 (1988).

The electric field of the wave propagating from port 2 to port 3 will be:

$$E_4' = \sqrt{(1-\gamma_1)} \cdot E_2 = \sqrt{(1-\gamma_1)} \cdot \sqrt{(1-\gamma_2)} \cdot \sqrt{t_2} \cdot \sqrt{(1-\alpha_s)} \cdot e^{-\alpha_f L} \cdot E_4 \quad \textit{(Eq.A.I. 3)}$$

When resonance occurs, the energy lost after one turn inside the resonator is equal to the input energy coming from C_1, this means that:

$$|E_4'|^2 - |E_4|^2 = |\Delta E|^2 \quad \textit{(Eq.A.I. 4)}$$

where $|\Delta E|^2$ is the input time-averaged optical energy from the coupler.

In our approach we assume C_1 and C_2 reciprocity. Therefore, $|\Delta E|^2$ is equal to the energy coupled from port 4 to port 1 in C_1 (no input energy at port 3).

Couplers reciprocity implies that the coupling coefficients κ_1 and κ_2 are as follows:

$$\kappa_1 = \left|\frac{E_4}{E_1}\right|^2_{E_2=0} = \left|\frac{E_1}{E_4}\right|^2_{E_3=0}$$
$$\kappa_2 = \left|\frac{E_8}{E_6}\right|^2_{E_5=0} = \left|\frac{E_6}{E_8}\right|^2_{E_7=0} \quad \textit{(Eq.A.I. 5)}$$

We can thus obtain:

$$|\Delta E|^2 = \kappa_{1_r} \cdot |E_4|^2 \quad \textit{(Eq.A.I. 6)}$$

where κ_{1_r} represents C_1 coupling coefficient at resonance.

By substituting *(Eq.A.I. 3)* and *(Eq.A.I. 6)* into *(Eq.A.I. 4)* we can obtain the resonance amplitude condition:

$$\kappa_{1_r} = 1 - (1-\gamma_1) \cdot (1-\gamma_2) \cdot (t_2) \cdot (1-\alpha_s) \cdot e^{-2\alpha_f L} \quad \textit{(Eq.A.I. 7)}$$

At resonance, the optical circulating wave is in phase with the input light wave, the resonance phase condition can be therefore obtained as follows:

$$\beta \cdot L = p\ 2\pi \qquad (p = 1,2,3 \dots) \quad \textit{(Eq.A.I. 8)}$$

where β is the optical propagation constant ($\beta = \frac{n \cdot 2\pi}{\lambda}$) and p is an integer.

When resonance amplitude and phase conditions are both satisfied, the optimal resonance is established in the FRR (the optimal condition for an absorption line equal to null).

In C_1 and C_2, the excess loss coefficients γ_1 and γ_2 are defined as:

$$1 - \gamma_1 = \frac{|E_3|^2 + |E_4|^2}{|E_1|^2 + |E_2|^2}$$
$$1 - \gamma_2 = \frac{|E_7|^2 + |E_8|^2}{|E_5|^2 + |E_6|^2} \qquad \textit{(Eq.A.I. 9)}$$

where E_i (i=1,2,3,4,5,6,7,8) represents the complex electric field amplitude at port i.

Using coupled-mode theory, the complex amplitudes of the output electric fields in C_1 coupler can be expressed as:

$$E_3 = \sqrt{(1-\gamma_1)} \cdot \left[\left(\sqrt{t_1} \cdot E_1\right) + \left(j\sqrt{\kappa_1} \cdot E_2\right)\right] \qquad \textit{(Eq.A.I. 10)}$$

$$E_4 = \sqrt{(1-\gamma_1)} \cdot \left[\left(j\sqrt{\kappa_1} \cdot E_1\right) + \left(\sqrt{t_1} \cdot E_2\right)\right] \qquad \textit{(Eq.A.I. 11)}$$

E_2 and E_4 are further related by:

$$E_2 = \sqrt{(1-\gamma_2)} \cdot \sqrt{t_2} \cdot \sqrt{(1-\alpha_s)} \cdot e^{-\alpha_f L} \cdot e^{j\beta L} \cdot E_4 \qquad \textit{(Eq.A.I. 12)}$$

From *(Eq.A.I. 10)*, *(Eq.A.I. 11)* and *(Eq.A.I. 12)* we can drive the expression of the intensity ratio at the first output of the FRR (absorption line):

$$\frac{E_3}{E_1} = \sqrt{(1-\gamma_1)} \cdot \sqrt{t_1}\left[1 - \frac{\kappa_1}{1 - \sqrt{t_1} \cdot \sqrt{(1-\gamma_1)} \cdot \sqrt{t_2} \cdot \sqrt{(1-\gamma_2)} \cdot \sqrt{(1-\alpha_s)} \cdot e^{-\alpha_f L} \cdot e^{j\beta L}}\right]$$
$$= \sqrt{(1-\gamma_1)} \cdot \sqrt{t_1}\left[1 - \frac{\kappa_1}{1 - \sqrt{A} \cdot e^{j\beta L}}\right] \qquad \textit{(Eq.A.I. 13)}$$

where $A = t_1 \cdot (1-\gamma_1) \cdot t_2 \cdot (1-\gamma_2) \cdot (1-\alpha_s) \cdot e^{-2\alpha_f L}$ for simplicity.

The output intensity ratio can be therefore written as follows:

$$\left|\frac{E_3}{E_1}\right|^2 = (1-\gamma_1)\left[1 - \left(\frac{\frac{\kappa_1 \cdot (1-\kappa_1-A)}{(1-\kappa_1)}}{1 + A - 2\sqrt{A} \cdot \cos\beta L}\right)\right] \qquad \textit{(Eq.A.I. 14)}$$

By substituting *(Eq.A.I. 12*) into *(Eq.A.I. 11*) we can have:

$$\frac{E_4}{E_1} = \frac{j\sqrt{\kappa_1}\cdot\sqrt{(1-\gamma_1)}}{1-\left(\sqrt{t_1}\cdot\sqrt{(1-\gamma_1)}\cdot\sqrt{t_2}\cdot\sqrt{(1-\gamma_2)}\cdot\sqrt{(1-\alpha_s)}\cdot e^{-\alpha_f L}\cdot e^{j\beta L}\right)} = \frac{j\sqrt{\kappa_1}\cdot\sqrt{(1-\gamma_1)}}{1-\left(\sqrt{A}\cdot e^{j\beta L}\right)} \quad \textit{(Eq.A.I. 15)}$$

We can therefore drive the expression of the intensity ratio of the circulating intensity inside the FRR:

$$\left|\frac{E_4}{E_1}\right|^2 = \frac{\kappa_1\cdot(1-\gamma_1)}{1+A-2\sqrt{A}\cdot\cos\beta L} \quad \textit{(Eq.A.I. 16)}$$

Now if we consider that L_1 separates the output coupler C_2 from the input coupler C_1, we can write E_5 in functions of E_4 as:

$$E_5 = e^{-\alpha_f L_1}\cdot e^{j\beta L_1}\cdot E_4 \quad \textit{(Eq.A.I. 17)}$$

E_8 could be thus written as follows:

$$E_8 = \sqrt{(1-\gamma_2)}\cdot\left[\left(j\sqrt{\kappa_2}\cdot E_5\right)+\left(\sqrt{t_2}\cdot E_6\right)\right] \quad \textit{(Eq.A.I. 18)}$$

Considering that there is no energy input from port 6 we have:

$$E_8 = j\cdot\sqrt{(1-\gamma_2)}\cdot\sqrt{\kappa_2}\cdot e^{-\alpha_f L_1}\cdot e^{j\beta L_1}\cdot E_4 \quad \textit{(Eq.A.I. 19)}$$

Dividing *(Eq.A.I. 19*) by E_1 and substituting *(Eq.II. 8*) in the resulting equation we can get the intensity ratio output at the FRR third output:

$$\left|\frac{E_8}{E_1}\right|^2 = \frac{\kappa_1\cdot(1-\gamma_1)\cdot\kappa_2\cdot(1-\gamma_2)\cdot e^{-\alpha_f L_1}}{1+A-2\sqrt{A}\cdot\cos\beta L} \quad \textit{(Eq.A.I. 20)}$$

Appendix B: Characterization of the optical phase shifter (FPS-001 from general photonics)

Before using the phase-shifter (PS) in our FRR structure including a phase-shifter (FRR-PS), we have to evaluate its phase-shift coefficient ($\kappa_{\varphi-PS}$). This coefficient is given by the following relation:

$$\kappa_{\varphi-PS} = \frac{\Delta\varphi_{PS}}{\Delta V_{PS}} \qquad (rad/V)$$

where $\Delta\varphi_{PS}$ is the additional phase-shift variation (added to the optical signal passing through the PS) caused by the DC bias voltage variation ΔV_{PS} applied to the PS.

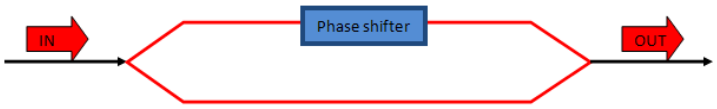

Mach-Zhender Interferometer

The experimental bench used to characterize the PS is depicted in the above figure. It is based on a Mach-Zhender interferometer configuration. To be able to estimate $\kappa_{\varphi-PS}$, we applied a DC bias voltage ramp, varying from 0 to 50 V, to the PS inserted into one of the interferometer's arms. At the same time, we recorded the signal detected by a photodiode (PD) at the interferometer output, using an oscilloscope.

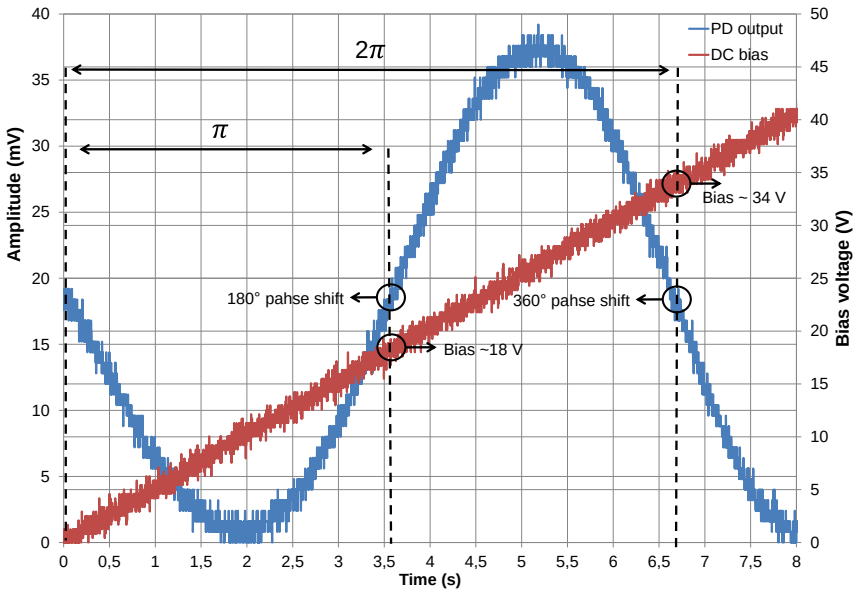

Phase-shifter characteristics

Appendix B: Characterization of the phase shifter (FPS-001 de general photonics)

Looking at the PD output signal in function of the DC bias voltage applied to the PS (see the above figure), we can see that a $\Delta V_{PS} = 18\ V$ causes a phase-shift $\Delta\varphi_{PS} = \pi$. Moreover, a $\Delta V_{PS} = 34\ V$ causes a phase-shift $\Delta\varphi_{PS} = 2\pi$, thereby we get a PS's phase-shift coefficient $\kappa_{\varphi-PS} = 0.059\pi\ rad/V$.

Appendix C: Real images of the different experimental benches

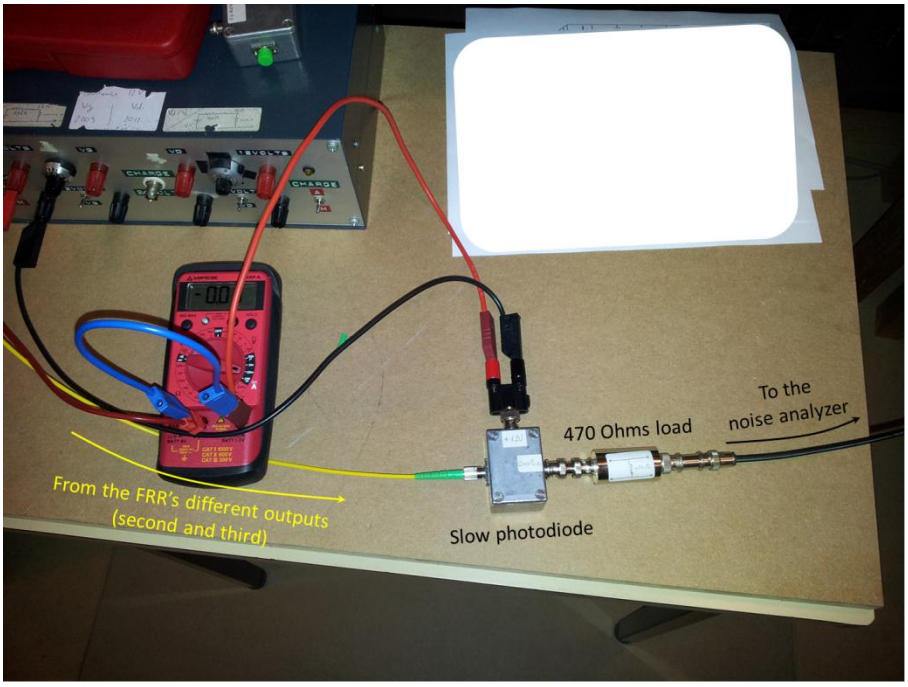

Image 1. Measurement bench used to evaluate the laser RIN degradation

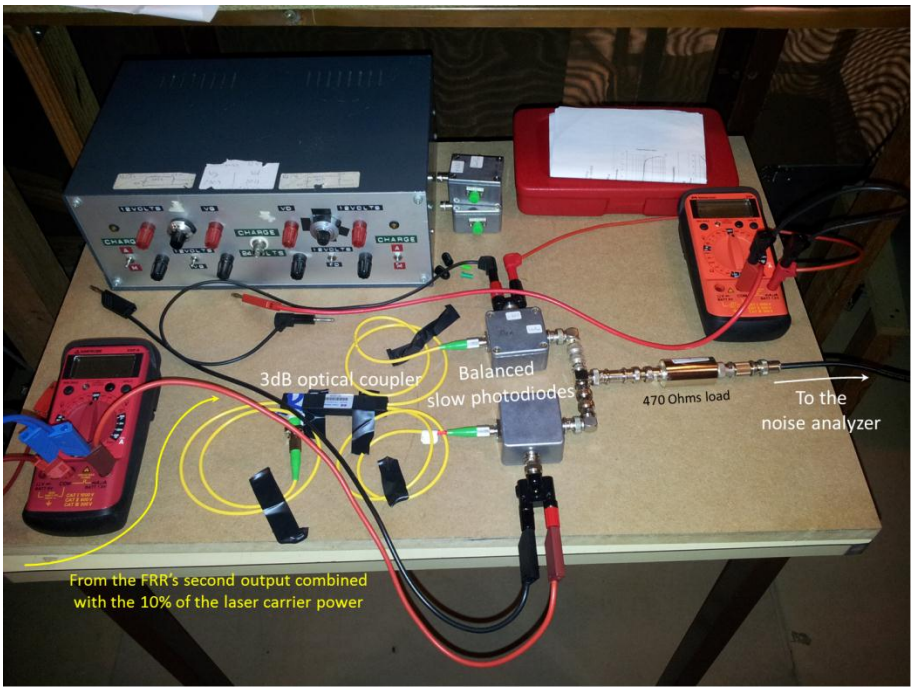

Image 2. Measurement bench used to measure the spectrum of the backscattered stimulated Rayleigh scattering

Appendix C: Real images of the different experimental benches

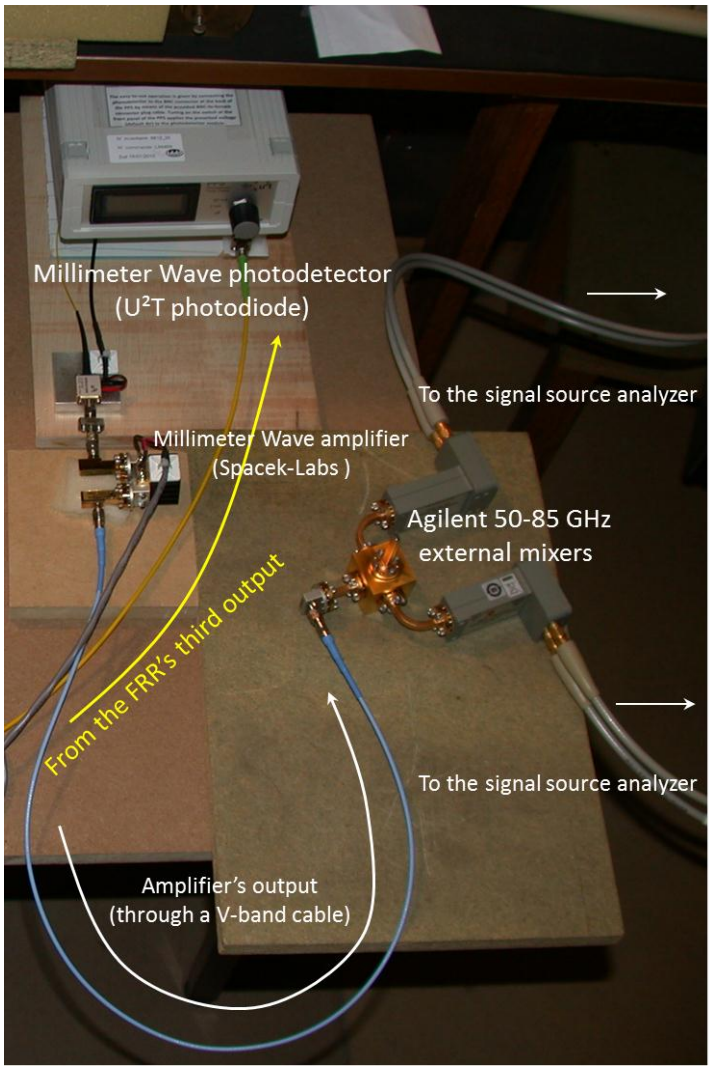

Image 3. Millimeter waves phase noise measurement bench

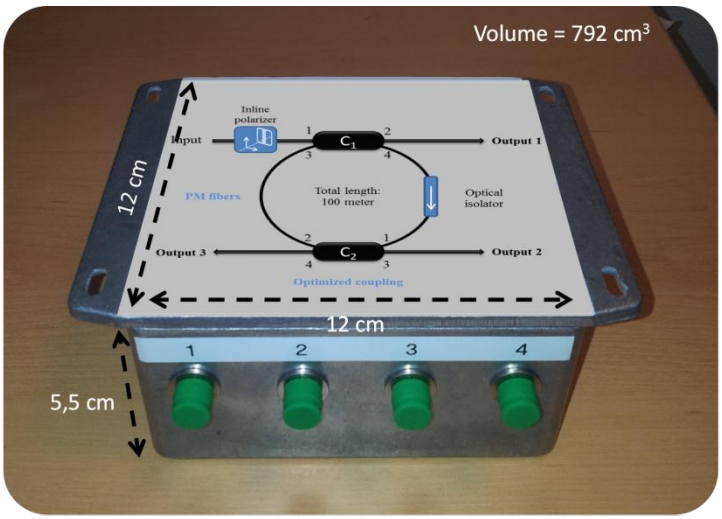

Image 4. 100m-long immunized fiber ring resonator (the FRR inside is very small compared to the package)

Appendix C: Real images of the different experimental benches

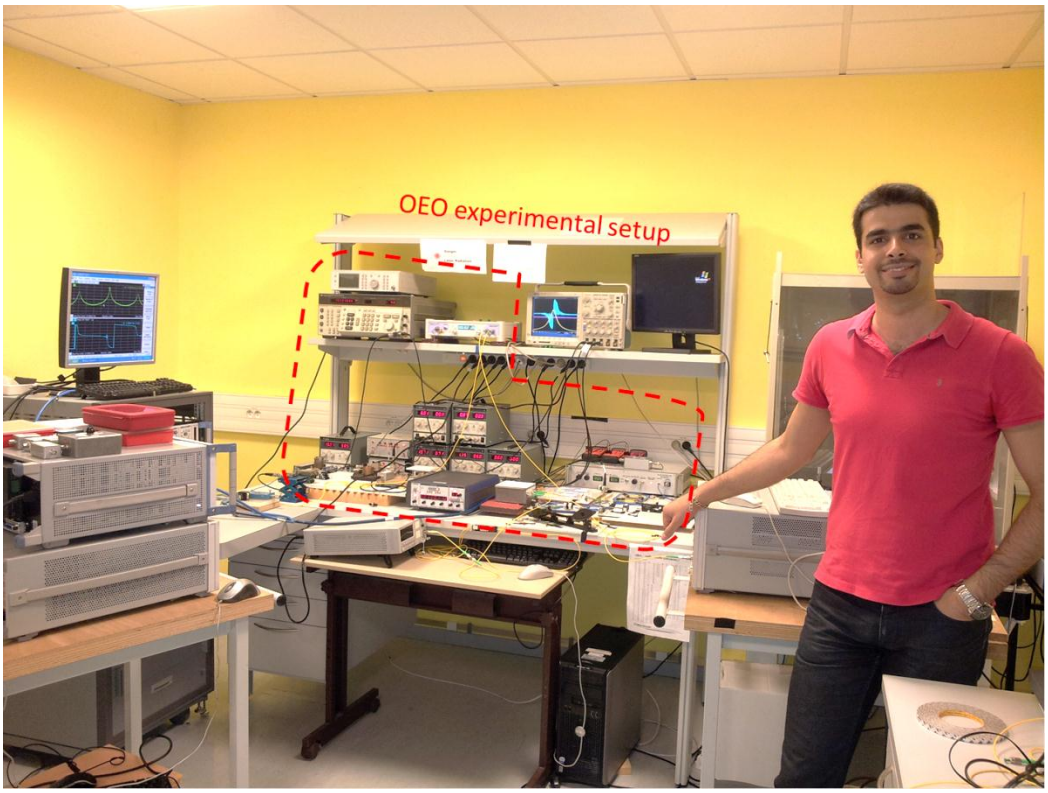

Image 5. Global experimental setup of the optoelectronic oscillator

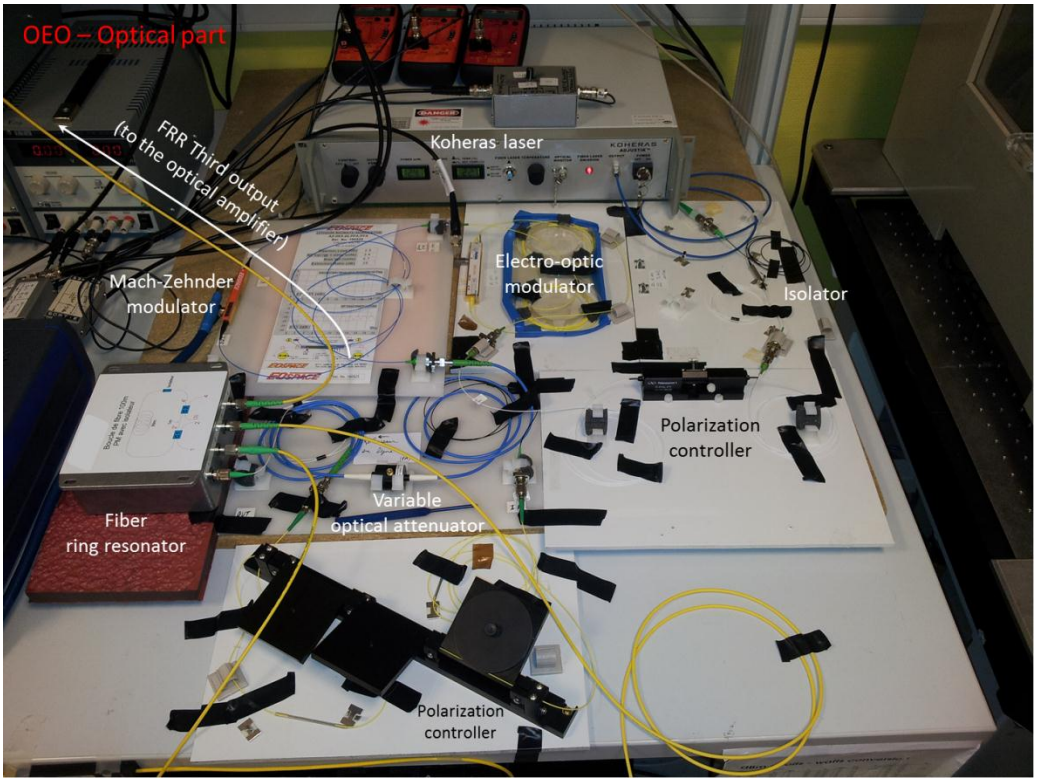

Image 6. Optoelectronic oscillator's optical part

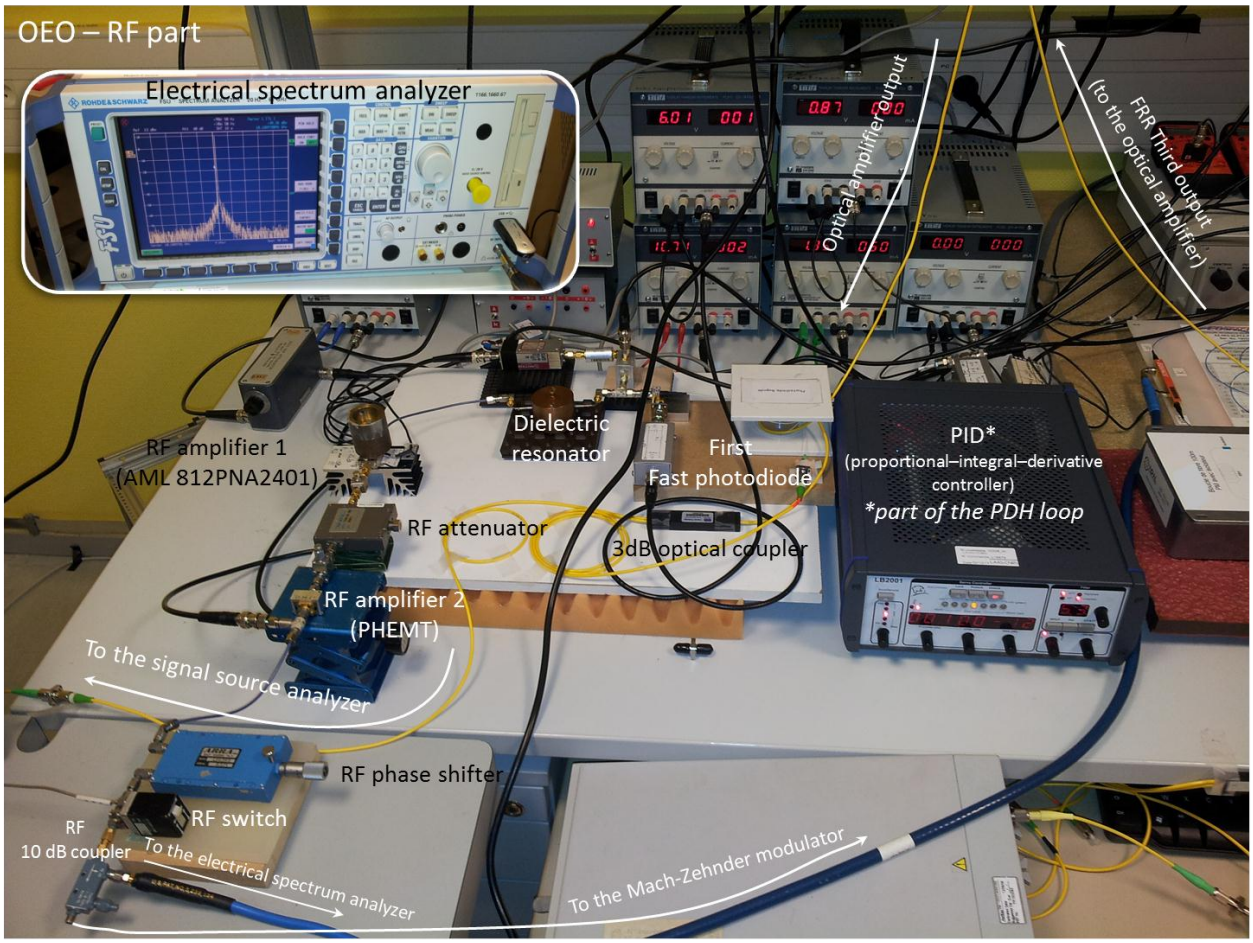

Image 7. Optoelectronic oscillator's RF part

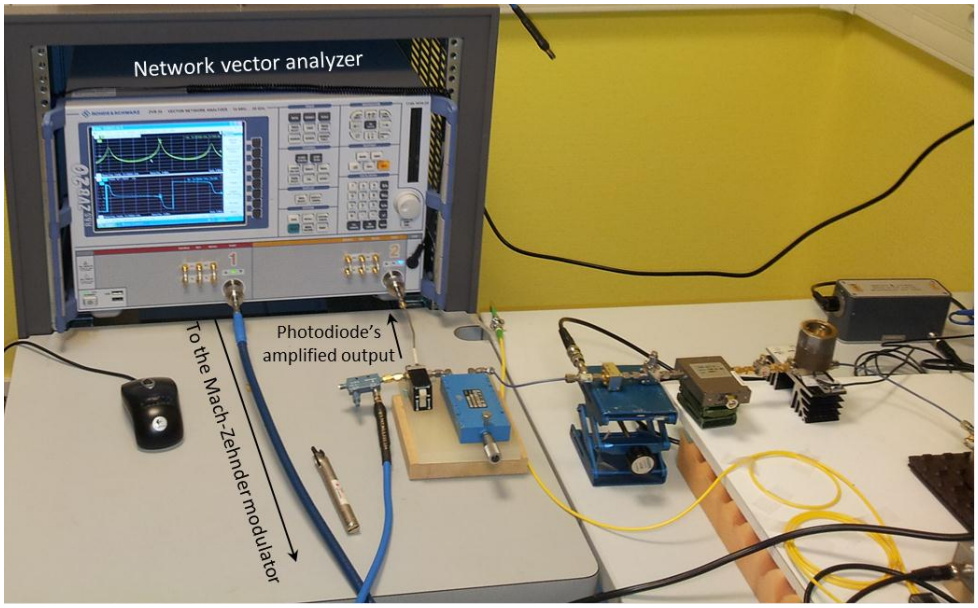

Image 8. OEO open-loop response characterization using a vector network analyzer

Appendix C: Real images of the different experimental benches

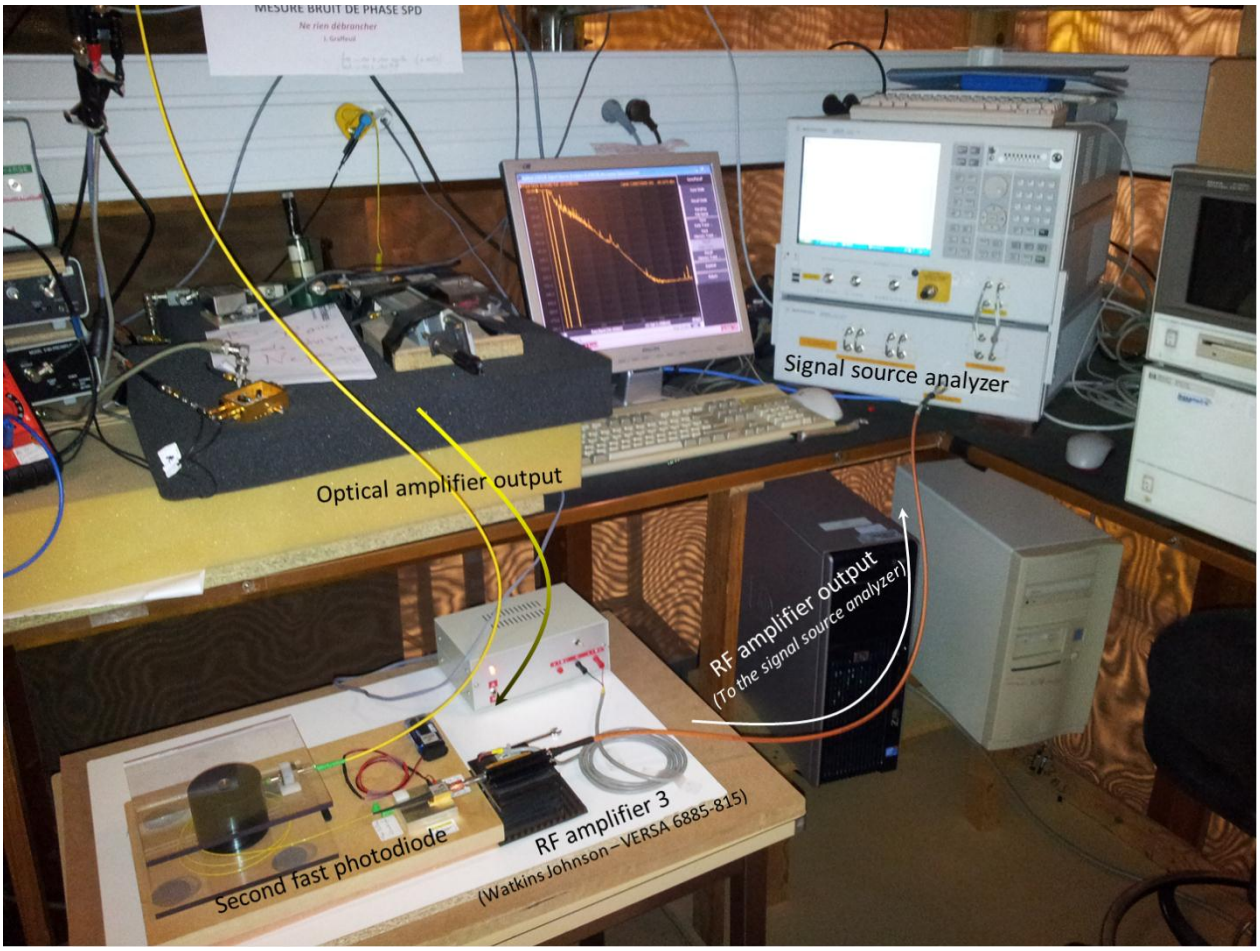

Image 9.OEO phase noise measurements in the Faraday cage

List of publications

Scientific reviews

K.SALEH, P.H.MERRER, O.LLOPIS, G.CIBIEL, Optical scattering noise in high Q fiber ring resonators and its effect on optoelectronic oscillator phase noise. Optics Letters, Vol.37, N°4, pp.518 520, February 2012

P.H.MERRER, **K.SALEH**, O.LLOPIS, G.CIBIEL, Characterization technique of optical whispering gallery mode resonators in the microwave frequency domain for optoelectronic oscillators. Applied Optics. Vol. 51, pp.4742-4748, July 2012.

O.LLOPIS, P.MARTINET, P.H.MERRER, **K.SALEH**, 50 GHz to 60 GHz local oscillator transmission over fiber using optical frequency multiplication. Microw. Opt. Technol. Lett., Vol. 54, N°5, pp.1313–1316, May 2012

O.LLOPIS, P.H.MERRER, H.BRAHIMI, **K.SALEH**, P.LACROIX, Phase noise measurement of a narrow linewidth CW laser using delay lines approaches. Optics Letters, Vol.36, N°14, pp.2713-2715, July 2011

Invited papers

O.LLOPIS, P.H.MERRER, A.BOUCHIER, **K.SALEH**, G.CIBIEL, High-Q optical resonators: characterization and application to stabilization of lasers and high spectral purity microwave oscillators. SPIE Photonics West, San Francisco (USA), 24-27 January 2010, pp.75791B-1-75791B-10

International conferences papers

K.SALEH, P.H.MERRER, O.LLOPIS, G.CIBIEL, Investigations on Noise Processes in Optical Resonator Based Microwave Oscillators: overall system optimization and phase noise reduction. Proc. of the European Microwave Week (EuMW 2012), Amsterdam (The Netherlands), 28 October - 02 November 2012.

K.SALEH, P.H.MERRER, O.LLOPIS, G.CIBIEL, Millimeter Wave Generation Using Brillouin Scattering in a High Q Fiber Ring Resonator. Proc. of the IEEE International Topical Meeting on Microwave Photonics (MWP 2012), Noordwijk, (The Netherlands), 11-14 September 2012.

K.SALEH, P.H.MERRER, O.LLOPIS, G.CIBIEL, Optoelectronic oscillator based on fiber ring resonator: overall system optimization and phase noise reduction. Proc. of the IEEE International Frequency Control Symposium (IFCS 2012), Baltimore (USA), 21-24 May 2012.

K.SALEH, A.BOUCHIER, P.H.MERRER, O.LLOPIS, G.CIBIEL, Fiber ring resonator based opto-electronic oscillator- phase noise optimization and thermal stability study. SPIE Photonics West 2011, San Francisco (USA), 22- 27 January 2011, 10p.

S. AZAIZIA, **K. SALEH**, O. LLOPIS, A. RISSONS, “Evaluation of low cost solutions for the transmission through optical fiber of low phase noise OCXO signals”, Proc. of the IEEE International Frequency Control Symposium (IFCS 2012), Baltimore (USA), 21-24 May 2012.

A.BOUCHIER, **K.SALEH**, P.H.MERRER, O.LLOPIS, Phase noise reduction of narrow linewidth optical fibre-ring based microwave oscillators : modelling and experimental results. Conference on Lasers and Electro-Optics Europe (CLEO 2011), Munich (Germany), 22-26 May 2011, 1p.

A.BOUCHIER, **K.SALEH**, P.H.MERRER, O.LLOPIS, G.CIBIEL, Theoretical and experimental study of the phase noise of opto-electronic oscillators based on high quality factor optical resonators. IEEE International Frequency Control Symposium (IFCS 2010), Newport Beach (USA), 1-4 June 2010, pp.544-548

National conferences papers

K.SALEH, A.BOUCHIER, P.H.MERRER, O.LLOPIS, G.CIBIEL, Etude théorique et expérimentale pour l'amélioration du bruit de phase des oscillateurs optoélectroniques basés sur des résonateurs optiques fibrés et évaluation de la stabilité thermique. Journées Nationales Microondes (JNM 2011), Brest (France), 18-20 May 2011, 4p.

P.MARTINET, H.BRAHIMI, **K.SALEH**, P.H.MERRER, O.LLOPIS, Modélisation CAO de la multiplication de fréquence par l'optique pour la génération de porteuses en gamme millimétrique. Journées Nationales Microondes (JNM 2011), Brest (France), 18-20 May 2011, 4p.

A.BOUCHIER, **K.SALEH**, P.H.MERRER, O.LLOPIS, G.CIBIEL, Etude du bruit de phase des oscillateurs optoélectroniques basés sur des résonateurs optiques à très forts coefficients de qualité. Journées Nationales de l'Optique Guidée 2010, Besançon (France), 19-22 October 2010, 3p.

National conferences without proceedings

K.SALEH, P.H.MERRER, A. ALI SLIMANE, O.LLOPIS, Résonateurs optiques à fort Q et systèmes associés pour la génération micro-onde à haute pureté spectrale. Journée du Club Optique Micro-ondes, Lille (France), 14 June 2012, 2p.

K.SALEH, O.LLOPIS, Sources hyperfréquences à très haute pureté spectrale à base de résonateurs optiques. Journée de l'Ecole doctorale GEET, Toulouse (France), 5 April 2012, 3p.

K.SALEH, A.BOUCHIER, P.H.MERRER, O.LLOPIS, G.CIBIEL, Oscillateurs optoélectroniques basés sur des résonateurs optiques fibrés Etudes, optimisation et modélisations. Journées Nationales du Réseau Doctoral en Micro-nanoélectronique (JNRDM 2011), Cachan (France), 23-25 May 2011, 4p.

A.BOUCHIER, **K.SALEH**, P.H.MERRER, O.LLOPIS, Design et caractérisation d'un résonateur optique à très fort facteur de qualité pour la génération microonde. Journée du Club Optique Micro-ondes, Toulouse (France), 3 June 2010, 1p.

Abstract

Author: Khaldoun SALEH

Title: High spectral purity microwave sources based on optical resonators

Thesis supervisor: Olivier LLOPIS

Place and date of the defence: LAAS-CNRS, the 29th of November 2012

Abstract:
Optics represents an elegant and reliable solution to generate high spectral purity microwave signals, especially the approach using the optoelectronic oscillator (OEO). The spectral purity of these sources is very important for space and military applications and also for time and frequency domain metrology. During this thesis, we have fabricated and studied many types of resonator based OEO in order to optimize the system phase noise. We have especially investigated an original approach using a passive fiber ring resonator (FRR). This resonator type can feature optical quality factors higher than 10^9 when only few meters of optical fibers are used (L ~ 10 m) and it can be easily integrated in a planar setup. Moreover, we have performed an important work on 3D WGM resonators based oscillators.
In the FRR based OEO, spectacular progresses have been achieved thanks to a good understanding of the system intrinsic noise phenomena. Actually, we have found that the most important noise parameters were the laser FM and AM noise conversion into RF phase noise by means of different nonlinearities in the system (like the photodiode nonlinearity), but also by the generation of nonlinear optical effects inside the resonator. By controlling these effects, we have been able to reduce the OEO phase noise level and to reach a -128 dBc/Hz noise level at 10 kHz offset frequency from a 10.2 GHz carrier. This has been achieved using an OEO based on a 100m-long passive FRR, which has been optimized and immunized against different nonlinear optical effects.

Keywords:

High-Q optical resonator, Microwave photonics, Opto-Electronic Oscillator (OEO), Phase noise, Nonlinear optics.

Discipline:

Microwaves, Electromagnetism and Optoelectronics

Résumé

Auteur: Khaldoun SALEH

Titre: Sources hyperfréquences à très haute pureté spectrale à base de résonateurs optiques

Directeur de thèse: Olivier LLOPIS

Lieu et date de la soutenance: LAAS-CNRS, le 29 Novembre 2012

Résumé :
L'optique constitue aujourd'hui une solution performante pour la réalisation de sources très pures en hyperfréquences, en particulier grâce à l'approche de l'oscillateur électro-optique (OEO). La pureté spectrale de ces sources est essentielle pour les applications spatiales, militaires et pour la métrologie du temps et des fréquences. Durant cette thèse, nous avons réalisé et étudié différents types d'OEO à résonateur optique en vue d'optimiser le bruit de phase de ce système. Nous avons en particulier orienté nos travaux vers une approche originale utilisant un anneau résonant fibré (ARF) passif. Ce type de résonateur présente en effet des coefficients de qualité optiques supérieurs à 10^9 pour des longueurs de fibre restant relativement faibles (L ~ 10 m) et facilement intégrables dans un support planaire. En parallèle, nous avons mené un travail important sur les oscillateurs à base de résonateurs optiques 3D.
Concernant l'OEO à ARF, des progrès spectaculaires ont pu être obtenus grâce à une meilleure compréhension des phénomènes de bruit intrinsèques à ce système. Les deux types de bruit prépondérants étaient la conversion du bruit du laser (FM et AM) en bruit de phase RF par différentes non-linéarités (dont la photodiode) et le déclenchement d'effets non-linéaires optiques à l'intérieur du résonateur. Le contrôle de ces effets a permis en particulier d'éliminer des remontées importantes de bruit sur le spectre de l'oscillateur, et d'atteindre un niveau de bruit de phase de -128 dBc/Hz à 10 kHz de la porteuse à 10.2 GHz en utilisant un OEO à base d'un ARF passif de 100 mètres de longueur, optimisé et immunisé contre les effets non-linéaires optiques.

Mots clés :

Résonateur optique à fort Q, Opto-Microonde, Oscillateur Electro-Optique (OEO), Bruit de phase, Optique non-linéaire.

Discipline :

Microondes, Electromagnétisme et Optoélectronique